Evaluation of the Dynamic Fracture Characteristics of Shaped-charge Jets at different Strain-rates and known initial *LINER* and *EXPLOSIVE MICROSTRUCTURES*

by

Fakhree Majiet

Dissertation submitted for the degree Philosophy Doctor (PhD), Physics, at the Stellenbosch University, South Africa

Promoter: Dr. FJ. Mostert, Council of Scientific and Industrial Research

Co-promoter: Prof. E. Rohwer, Stellenbosch University, South Africa

December 2020

Table of Contents

1. INTRODUCTION 1
1.1. Research Goal 1
1.2. Research Background 1
1.3. Originality of Research 3
1.4. Objectives of Research 3
1.5. Hypotheses 3
1.6. Conclusion 4
2. ANALYSIS AND CHARACTERISATION 5
3. LITERATURE REVIEW 6
3.1. Introduction 6
3.2. Factors Influencing shaped-charge Performance 9
3.2.1. Jet Coherency 9
3.2.2. Virtual Origin 9
3.2.3. Stand-off 10
3.2.4. Appendix 10
3.2.5. High Explosive 11
3.2.6. Liner Geometry 12
3.2.7. Initiation System 15
3.2.8. Symmetry 16
3.2.9. Liner Materials 16
3.2.10. Liner Crystal Shape 18
3.2.11. Liner Impurities 19
3.2.12. Liner Microstructure 20
3.2.13. Strain-rate 24
3.2.14. Liner Manufacturing 25
3.3. Break-up-time Models 27
3.3.1. Empirical Formulae 27
3.3.2. Super-plasticity 32
3.4. Strain and Strain-Rate dependence on Shaped-charge performance 36
3.4.1. Analytical Model 36

4. SIMULATIONS ... 40
4.1. Introduction ... 40
4.2. Shaped-charge Collapse Kinetics ... 41
4.3. Hydro code Simulations ... 43
4.4. Studied Explosive Charge Parameters ... 45
4.5. AUTODYN Jet-Formation Model Description ... 46
4.6. Material Modelling Description ... 47
4.6.1. Description of the Explosives used in AUTODYN ... 47
4.6.2. Mie-Gruneisen EOS : ... 49
4.7. Modelling of Strength Effects ... 50
4.7.1. Johnson-Cook Model ... 50
4.7.2. Zerilli-Armstrong Model ... 50
4.7.3. The Steinberg-Guinan Model ... 51
4.8. Explosive Initiation and Wave Propagation ... 55
4.9. Description of the Liner Materials ... 55
4.10. Mesh Sensitivity for the Jet-formation Model ... 56
4.11. Simulation of Experimental Designs ... 56
4.12. Concept Designs ... 57
4.12.1. Preliminary Analysis ... 57
4.12.2. Grid-size analysis ... 58
4.12.3. Design 1 ... 63
4.12.4. Design 2 ... 65
4.12.5. Design 3 ... 66
4.12.6. Design 4 ... 68
4.12.7. Design 5 ... 69
4.12.8. Design 6 ... 71
4.12.9. Simulation Summary ... 72
5. SHAPED-CHARGE MANUFACTURE ... 79
5.1. Liner Manufacture ... 80
5.2. Liner Forging Manufacture ... 80
5.2.1. 60° Liner ... 81

5.2.2. Table 16 explanation 83
5.2.3. 120° Forging 90
5.3. Explosive Manufacture 92
5.3.1. Comp A3 92
5.4. RDX: WAX pressing analysis 95
5.4.1. Smart-Zoom Light Microscopy Analysis 98
5.4.2. Scanning Electron Microscopy 100
5.4.3. Warhead Assembly 103
5.5. 120° Design 104
5.6. Cast PBX Manufacturing Process 105
5.6.1. Cast PBX Process Design 105
5.6.2. Cast PBX Process Manufacture 107

6. EVALUATION 112
6.1. Introduction 112
6.2. Test Set-up 115
6.3. Flash X-ray Evaluation 117
6.4. Digital Image Analysis 120
6.5. The Evaluation of the Dynamic Fracture Characteristics of the Jets from a Specific Design and with known Different Initial *Explosive* Crystal Size 125
6.5.1. Flash X-ray evaluation 125
6.5.2. Results 129
6.6. The Evaluation of the Dynamic Fracture Characteristics of Shaped-charge Jets at different Strain-rates and known initial *LINER MICROSTRUCTURES* 133
6.6.1. Flash X-ray Evaluation 133
6.6.2. Results from Digital Analysis of the Radiographs 152

7. DISCUSSION 170
7.1. Introduction 170
7.2. Strain and Strain-rate determination 170
7.2.1. Strain Determination from Eq. 23 171
7.2.2. L_0 Determination from Simulation 174
7.3. Correlation between numerous analytical models to the experimental data set 179

7.3.1. Breakup times 179

7.3.2. Plasticity 186

7.4. The Evaluation of the Dynamic Fracture Characteristics of Shaped-charge Jets at single Strain-rate and known initial *Explosive* crystal size 187

7.5. Conclusion 187

8. CONCLUSION 188

9. FUTURE WORK 189

10. REFERENCES 190

LIST OF FIGURE..PAGE

Figure 1: Basic shaped-charge concept, with High Explosive (HE, green) and metal liner (red).... 1

Figure 2: Shaped-charge jet-formation process, position time frames presented from initial jet-formation up to jet particulation.. 1

Figure 3: Typical topics within the warhead technology portfolio of which shaped-charge technology is the focus of this research project.. 6

Figure 4: Shaped-charge technology is further divided into numerous categories; this research project focuses mostly on the break-up behavior of jets produced from shaped-charges. 7

Figure 5: Some of the parameters that influence shaped-charge jet-break-up with the focus areas for this research project shown in bold. 7

Figure 6: Bird's-eye view organogram showing some more parameters influencing shaped-charge performance with the focus on jet-break-up and variables used in this research project. 8

Figure 7: Example of the effect of standoff on penetration. [15]. 10

Figure 8: Description of the Appendix for peripheral initiation. 11

Figure 9: Description of the Appendix for point initiation... 11

Figure 10: Penetration versus liner cone angle [13].. 13

Figure 11: Shaped-charge jet profile at different cone angles [18]... 13

Figure 12: Jet and tail velocities as a function of cone angle [13]... 14

Figure 13: The shape of the DW travelling inside the explosive charges with and without waveshaper. [13] These images are section views of a cylindrical charge for ease of description. 15

Figure 14: Air cavity technique for increasing the tip velocity in [22]...................................... 16

Figure 15: Stress-strain curves of 3N, 6N and 8N copper samples at strain-rate of 4.2×10^{-5} s^{-1} [32]. 21

Figure 16: Dog bone samples of the nano copper [43]. 24

Figure 17: The stress-strain curve at different strain-rates [43].................... 25

Figure 18: Description of the break-up time model. [49] 28

Figure 19: The kinematic expression for the jet break-up-time. 36

Figure 20: Geometry of the shaped-charge collapse process, the x-axis representing the symmetry plane for a cylindrical charge, the y-axis representing the charge caliber and positions A and B representing positions within the liner during the collapse process [16]. 42

Figure 21: Jet and slug formation associated with Liner Flow Velocity (V_2) [16]. 42

Figure 22: Comparison between hydro code simulation of jet necking due to instability and flash radiograph of a jet at approximately the same time [81]. 44

Figure 23: Simulation layout including the Euler grid and outflowing boundary. 46

Figure 24: The shock velocity against particle velocity for the EOS of the liner material [17]..... 48

Figure 25: Six concept designs of the shaped charge warheads that were manufactured.......... 57

Figure 26: Material model for design 1. 58

Figure 27: Velocity contours for Design 1 highlighting the differences in tip velocity for three different copper liner material models. 58

Figure 28: Euler model with of 0.1 mm square grids, this was the finest mesh used for the analysis. 59

Figure 29: Grid-size analysis with a 0.1 mm square grid – close-up view of Figure 28. 59

Figure 30: Grid-size analysis with a 0.4 mm square grid – material allocation described in the legend. This image shows the coarse Euler grids. 60

Figure 31: Grid-size analysis with a 0.4 mm square grid – material allocation. Close-up view of Figure 30. 60

Figure 32: Velocity contours for design 1 after 30 µs with an Euler grid-size of 0.1 mm. 61

Figure 33: Velocity contours for design 1 after 30 µs with an Euler grid-size of 0.2 mm. 61

Figure 34: Velocity contours for design 1 after 30 µs with an Euler grid-size of 0.4 mm. 62

Figure 35: Design 1 - Concept layout. 63

Figure 36: Design 1 – collapsed jet, material allocation. 63

Figure 37: Design 1 – collapsed jet, close-up. 64

Figure 38: Design 1 – collapsed jet, velocity contour. 64

Figure 39: Design 2 - Concept layout. 65

Figure 40: Design 2 – collapsed jet, material allocation. 65

Figure 41: Design 2 – collapsed jet, velocity contour. 66

Figure 42: Design 3 - Concept layout. 66

Figure 43: Design 3 – collapsed jet, material allocation. 67

Figure 44: Design 3 – collapsed jet, material allocation – later time. 67

Figure 45: Design 3 – collapsed jet, velocity contour. 67

Figure 46: Design 4 - Concept layout. 68

Figure 47: Design 4 – collapsed jet, material allocation. 68

Figure 48: Design 4 – collapsed jet, velocity contour. 69

Figure 49: Design 5 - Concept layout. 69

Figure 50: Design 5 – collapsed jet, material allocation. 70

Figure 51: Design 5 – collapsed jet, velocity contour. 70

Figure 52: Design 6 - Concept layout. 71

Figure 53: Design 6 – collapsed jet, material allocation. 71

Figure 54: Design 6 – collapsed jet, velocity contour. 72

Figure 55: Correlation between design and tip velocity. 73

Figure 56: Correlation between design and ∆V. 74

Figure 57: Mass distribution for all six designs. 75

Figure 58: Mass distribution for all six designs up to 8 g. 75

Figure 59: Cumulative mass distribution for all six designs. 76

Figure 60: Cumulative mass distribution for all six designs, up to 20 g. 76

Figure 61: Cumulative mass distribution for the 60° liner design. 77

Figure 62: Cumulative mass distribution for 120° liner designs. 77

Figure 63: Cumulative kinetic energy for all six designs. 78

Figure 64: Six concept designs of shaped charge warheads, which were manufactured. 79

Figure 65: Process for manufacturing the 60° forging. 81

Figure 66: Additional forging process considered to obtain an improved microstructure. 81

Figure 67: Sample description: 1, see Figure 65. 82

Figure 68: Sample description: Two, see Figure 65. 82

Figure 69: Sample description 3, see Figure 65. 82

Figure 70: Sample description 4, see Figure 65. 83

Figure 71: Sample 1 as analysed for microstructure and hardness. 84

Figure 72: Sample 2 as analysed for microstructure and hardness. 84

Figure 73: Sample 3 as analysed for microstructure and hardness. 85

Figure 74: Forging process followed for the 120° liner. 90

Figure 75: Forge tooling layout for manufacturing the 120° liner, before forging. 90

Figure 76: Forge tooling layout for manufacturing the 120° liner, after forging. 91

Figure 77: 120° forging first stage sectioned. 92

Figure 78: Four lots of granular Comp A3. 94

Figure 79: Malvern analysis for the respective batches of Comp A3. 95

Figure 80: Summary of the initial pressing analysis at 25 mm diameter. 97

Figure 81: Scanning electron microscope images of RDX 107, 105 & 104 respectively. 98

Figure 82: Photograph of the three explosive batches of Comp A3. 98

Figure 83: Light microscopy for Lot 3 and 4. 99

Figure 84: Light microscopy for Lot 5 and 6. 99

Figure 85: SEM images of a pressed Comp A3 charge. 100

Figure 86: Tools used to press the explosive charges. 101

Figure 87: Machined Comp A3 charges. 103

Figure 88: Components used for Concepts 1 & 2. 103

Figure 89: X-rays for the respective assemblies. 104

Figure 90: Components making up the point and peripheral initiated shaped-charges for 120° liners. 104

Figure 91: Assemblies for the peripheral-initiated assemblies on the left and point-initiated assemblies on the right. 104

Figure 92: Two designs used to evaluate the cast explosive. 105

Figure 93: Tooling design used to manufacture the design 3. 106

Figure 94: Tooling design used to manufacture the design 6. 106

Figure 95: Tooling before casting took place. 107

Figure 96: Split moulds after PBX curing. 108

Figure 97: Split mould disassembly of a single charge. 108

Figure 98: Disassembly of four split moulds. 109

Figure 99: Recovered shaped-charges from split moulds, front view. 109

Figure 100: Recovered shaped-charges from split moulds, top view. 110

Figure 101: Recovered shaped-charges from split moulds, side view. 110

Figure 102: X-ray of cast PBX charge. 111

Figure 103: Cast PBX charge assembly including the booster. 111

Figure 104: Flash X-ray set-up. 115

Figure 105: Flash X-ray set-up. 116

Figure 106: Schematic test set-up. 116

Figure 107: Six shaped-charge warhead concept designs evaluated. 117

Figure 108: Flash X-ray radiographs as shown in JETP. 120

Figure 109: Individual film preparation in terms of position markers and the jet line. 121

Figure 110: A ruler showing the position of particles along the jet. 121

Figure 111: An image showing the digitized particles. 121

Figure 112: A close-up image showing the digitized particles.. 121

Figure 113: Concept design layout used for the RDX crystal size evaluation. 125

Figure 114: 2017-285 Lot 006. 126

Figure 115: 2017-286 Lot 006. 126

Figure 116: 2017-287 Lot 003. 127

Figure 117: 2017-288 Lot 003. 127

Figure 118: 2017-289 Lot 005. 127

Figure 119: 2019-290 Lot 005. 128

Figure 120: Velocity and particle position for all test conducted for the RDX crystal size evaluation.. 130

Figure 121: Flash X-ray Analysis – Cumulative length of the overall shaped-charge jet. 131

Figure 122: Flash X-ray Analysis – Cumulative length of a section of the shaped-charge jet. ... 131

Figure 123: Flash X-ray Analysis - Average break-up-times. 132

Figure 124: Flash X-ray Analysis - average L/D of particles of shaped-charge jets.................... 132

Figure 125: Concept design 1 and matching hardware. 134

Figure 126: FX radiograph for Detonation No: 2017-237, Shot#1.. 135

Figure 127: FX radiograph for Detonation No: 2017-239, Shot#3.. 135

Figure 128: FX radiograph for Detonation No: 2017-240, Shot#4.. 136

Figure 129: FX radiograph for Detonation No: 2017-241, Shot#5. 136

Figure 130: Concept design 2 and matching hardware. 137

Figure 131: FX radiograph for Detonation No: 2017-238, Shot#2. 138

Figure 132: FX radiograph for Detonation No: 2017-242, Shot#6. 138

Figure 133: FX radiograph for Detonation No: 2017-244, Shot#8. 139

Figure 134: FX radiograph for Detonation No: 2017-245, Shot#9. 139

Figure 135: FX radiograph for Detonation No: 2017-284, Shot#10. 139

Figure 136: FX radiograph for Detonation No: 2018-19, Shot#17. 140

Figure 137: FX radiograph for Detonation No: 2018-23, Shot#21. 140

Figure 138: Concept design 3 and matching hardware. 141

Figure 139: FX radiograph for Detonation No: 2018-21, Shot#19. 142

Figure 140: FX radiograph for Detonation No: 2018-24, Shot#22. 142

Figure 141: FX radiograph for Detonation No: 2018-25, Shot#23. 142

Figure 142: Concept design 4 and matching hardware. 143

Figure 143: FX radiograph for Detonation No: 2018-22, Shot#20. 144

Figure 144: FX radiograph for Detonation No: 2018-29, Shot#28. 144

Figure 145: FX radiograph for Detonation No: 2018-30, Shot#29. 144

Figure 146: Concept design 5 and matching hardware. 145

Figure 147: FX radiograph for Detonation No: 2018-20, Shot#18. 147

Figure 148: FX radiograph for Detonation No: 2018-26, Shot#24. 147

Figure 149: FX radiograph for Detonation No: 2018-27, Shot#26. 148

Figure 150: FX radiograph for Detonation No: 2018-28, Shot#27. 148

Figure 151: FX radiograph for Detonation No: 2018-31, Shot#30. 148

Figure 152: Concept design 6 and matching hardware. 149

Figure 153: FX radiograph for Detonation No: 2018-53, Shot#31. 151

Figure 154: FX radiograph for Detonation No: 2018-54, Shot#32. 151

Figure 155: FX radiograph for Detonation No: 2018-55, Shot#33. 151

Figure 156: Velocity - Position graph for design 1 – four test firings. 153

Figure 157: Cumulative Length – Velocity graph for design 1 – four test firings. 153

Figure 158: Average break-up-time - Velocity graph for Design 1 - four test firings. 154

Figure 159: Average velocity difference – Velocity graph for design 1 - four test firings. 154

Figure 160: Velocity - Position graph for design 2 – six test firings. 155

Figure 161: Cumulative Length – Velocity graph for design 2. 156

Figure 162: Average break-up-time - Velocity graph for Design 2. 156

Figure 163: Velocity - Position graph for design 3 – three test firings. 157

Figure 164: Cumulative Length – Velocity graph for design 3. 158

Figure 165: Averaged break-up-time - Velocity graph for Design 3. 158

Figure 166: Velocity - Position graph for design 4 – three test firings. 159

Figure 167: Cumulative Length – Velocity graph for design 4. 160

Figure 168: Averaged break-up-time - Velocity graph for Design 4. 160

Figure 169: Velocity - Position graph for design 5 – five test firings. 161

Figure 170: Cumulative Length – Velocity graph for design 5. 162

Figure 171: Averaged break-up-time - Velocity graph for Design 5. 162

Figure 172: Velocity - Position graph for design 6 – three test firings. 163

Figure 173: Cumulative Length – Velocity graph for design 6. 164

Figure 174: Averaged break-up-time - Velocity graph for Design 6. 164

Figure 175: An illustration of the cumulative length for each particular design. 168

Figure 176: An illustration of the cumulative mass for each particular design. 168

Figure 177: A comparison of the averaged break-up-times for each design. 169

Figure 178: Strain-rate determination from an initial length determined from a constant final strain assumption of 2.3. 173

Figure 179: L_0 determination for Design 1 down to the slug. 174

Figure 180: L_0 determination for Design 1 down to the 2 mm/µs. 174

Figure 181: L_0 determination for Design 2 down to the slug. 175

Figure 182: L_0 determination for Design 2 down to the 2 mm/µs. 175

Figure 183: L_0 determination for Design 3 down to the slug. 175

Figure 184: L_0 determination for Design 3 down to the 2 mm/µs. 176

Figure 185: L_0 determination for Design 4 down to the slug. 176

Figure 186: L_0 determination for Design 4 down to the 2 mm/µs. 176

Figure 187: L_0 determination for Design 5 down to the slug. 177

Figure 188: L_0 determination for Design 5 down to the 2 mm/µs. 177

Figure 189: L_0 determination for Design 6 down to the slug. 177

Figure 190: L_0 determination for Design 6 down to the 2 mm/µs. 178

Figure 191: Graphic representation of strain-rates presented in Table 55 and Table 56, respectively. 179

Figure 192: Measured experimental break-up-times and analytical predictions for design 1. . 182

Figure 193: Measured experimental break-up-times and analytical predictions for design 2. . 182

Figure 194: Measured experimental break-up-times and analytical predictions for design 3. . 183

Figure 195: Measured experimental break-up-times and analytical predictions for design 4. . 183

Figure 196: Measured experimental break-up-times and analytical predictions for design 5. . 184

Figure 197: Measured experimental break-up-times and analytical predictions for design 6. . 184

Figure 198: Plasticity determination of all six designs. 186

LIST OF TABLES **PAGE**

Table 1: Explosive properties for some high explosives. [13], [16], [17] 12

Table 2: Penetration potential ranking of the different liner materials [25]. 17

Table 3: Jet characteristics using different liner materials [29] 18

Table 4: The dependence of the jet-break-up time on the Sulphur content [31]. 19

Table 5: Break-up-time and effective jet length for nine different copper samples [29]. 22

Table 6: The constants of the Zerilli–Armstrong model [35]. 23

Table 7: Typical stacking fault energies for pure face center cubic metals, from Dieter [65] 33

Table 8: Input data to AUTODYN hydro code for the explosive materials. 48

Table 9: The mechanical properties of copper liner materials in the simulations. 49

Table 10: Material properties for OFHC Copper – Steinberg Guinan. 53

Table 11: Material properties for OFHC Copper– Zerilli Armstrong. 54

Table 12 Material properties for OFHC Copper– Johnson Cook 55

Table 13: Tip velocity comparison obtained from design 1 with different grid-sizes. 62

Table 14: Key design variables with tip and tail velocities extracted from the respective simulations. 73

Table 15: Chemical composition for C10100 copper. 80

Table 16: Copper forging sample heat-treatment signature. 86

Table 17: Microstructures summary for copper forgings. 87

Table 18: Copper forging hardness measurements. 89

Table 19: Grain-sizes of new sample “As Forged” – (hardness = 106 HV) 91

Table 20: Grain-sizes of new sample after heat-treatment for 1h @350°C – (hardness = 51 HV). 91

Table 21: Various lots of Comp A3 manufactured with different RDX grades/crystal sizes. 93

Table 22: Particle-size (P) analysis (fines) for four batches of Comp A3 94

Table 23: Initial pressing analysis at diameter 25 mm..... 96

Table 24: Density report for Comp A3 Lot 3. 101

Table 25: Density report for Comp A3 Lot 4. 102

Table 26: Density report for Comp A3 Lot 5. 102

Table 27: Density report for Comp A3 Lot 6. 102

Table 28: Explosive properties of the manufactured explosive and the simulated explosive. .. 105

Table 29 Test Summary of all tests. 118

Table 30: Generic parameter file prepared per test. 120

Table 31: Data generated after digitizing the radiographs. 122

Table 32: Test parameters for the RDX crystal size evaluation. 126

Table 33: Tip velocities and FX delay times for the RDX crystal sizes evaluation. 130

Table 34: Test parameters for design 1. 135

Table 35: Test parameters for design 2. 138

Table 36: Test parameters for design 3. 142

Table 37: Test parameters for design 4. 144

Table 38: Test parameters for design 5. 147

Table 39: Test parameters for design 6. 150

Table 40: Measured tip velocities and FX delay times used for design 1. 152

Table 41: Measured tip velocities and FX delay times used for design 2. 155

Table 42: Measured tip velocities and FX delay times used for design 3. 157

Table 43: Measured tip velocities and FX delay times used for design 4. 159

Table 44: Measured tip velocities and FX delay times used for design 5. 161

Table 45: Measured tip velocities and FX delay times used for design 6. 163

Table 46: Averaged experimental data extracted from FX analysis for design 1. 166

Table 47: Averaged experimental data extracted from FX analysis for design 2. 166

Table 48: Averaged experimental data extracted from FX analysis for design 3. 166

Table 49: Averaged experimental data extracted from FX analysis for design 4. 167

Table 50: Averaged experimental data extracted from FX analysis for design 5. 167

Table 51: Averaged experimental data extracted from FX analysis for design 6. 167

Table 52: Shaped-charge warhead design parameters. 171

Table 53: Strain-rate determination for a constant final strain, εF, of 2.3 from jet tip down to the slug. 172

Table 54: Strain-rate determination for a constant final strain, εF, of 2.3 from jet tip down to the 2 mm/µs. 172

Table 55: Strain and Strain-rate calculations for six concept designs from simulation with L_0 measured down to a velocity of 2 mm/µs. 178

Table 56: Strain and Strain-rate calculations for six concept designs from simulation with L_0 measured down to the slug. 178

ABBREVIATIONS

#	number
°C	Degrees Celsius
µs	microseconds
Ag	Silver
Al	Aluminium
ASTM	American Society for Testing and Materials
bcc	body centered cubic
cc	cubic centimetre
C_D	charge diameter
CJ	Chapmen Jouguet
cm	centimetre
CNC	Computer Numerical Control
Comp	Composition
CSC	conical shaped-charges
Cu	Copper
cum	Cumulative
D	Diameter
D_0	initial diameter
deg	Degrees
Det	Detonator
DRX	Dynamic Recrystallisation
DU	Depleted Uranium
DW	Detonation Wave
EOS	Equations Of State
FCC	face centered cubic
FX	Flash X-ray
g	grams
GPa	Giga Pascal
HE	High Explosive

HERF	High Energy Rate Fabrication
HNS	Hexanitrostilbene
JWL	Jones-Wilkins-Lee
KCl	Potassium Chloride
kg	Kilogram
kJ	kilo Joules
km	kilometers
kPa	Kilo Pascal
kV	kilo Volt
l	Jet length
L	Length
L/D	ratio of Length and Diameter
m	mass
MDBT	Miniaturized Disk Bend Test
mJ	milli Joule
mm	millimeter
Mo	Molybdenum
MPa	Mega Pascal
NA	Not Applicable
Ni	Nickel
nm	Nano-meter
No.	Number
OFHC	Oxygen-free High Conductivity
Pa	Pascal
PBX	Plastic Bonded Explosive
ppm	parts per million
PVE	Pressure, Volume, Energy
Q	Ductility Factor (Plasticity)
r_0	initial radius
RDM	Rheinmetall Denel Munition
RDX	cyclotrimethylenetrinitramine

r_j	radius of jet
s	seconds
SC	Shaped-charge
SCJ	Shaped-charge Jet
SEM	Scanning Electron Microscopy
SO	Stand-off
SU	Stellenbosch University
t	time
Ta	Tantalum
T_B	Break-up-time
Ti	Titanium
T_L	liner element thickness
TMD	Theoretical Maximum Density
U	Uranium
V_0	Tip Velocity
V_{ave}	average velocity
VOD	Velocity of Detonation
V_{PL}	Plastic Velocity
vs	versus
V_{tail}	velocity of the rear end of the jet
W	Tungsten
Zr	Zirconium
ρ	density
ΔV	interparticle velocity difference

Abstract

In the pursuit of continuous improvement within the realm of shaped-charge design, it is the objective of the design to ultimately delay the break-up-time of the produced jets and hence improve the penetration performance.

This research was focused purely on the fracture dynamics of particular jets by monitoring numerous design variables. The design variables varied were carefully selected, namely the initiation system, the explosive type, explosive crystal size and the liner angle. These variables were varied such that the tip velocities of the jets decreased linearly from design 1 to design 6.

This research employed the ANSYS AUTODYN finite difference code to model the behaviour of the shaped-charges in the stages of liner collapse and jet formation. The design parameters were studied quantitatively to identify the effect of each individual parameter on the jet characteristics. All the AUTODYN analyses were validated by means of flash X-ray analysis for all six designs.

The experimental phase of this research project was extensive, quantifying numerous aspects of shape charge design. The data from each experiment was digitally analysed with a sophisticated locally developed software package.

The experimental break-up-times were also compared to the break-up-times predicted by a number of widely used analytical models of which one was found to fit the data optimally.

The main conclusion of this research was established due to the special care in the manufacture of the respective warheads based on six designs. Experimental evidence is presented in support of a parameter, different to the break-up time, to quantify the plasticity of shaped charge jets.

Declaration

I hereby declare that no portion of the work referred to in the thesis has been submitted in support of an application for another degree or qualification of this or any other university or other institute of learning.

Sign …………………

Copyright Statement

1. The author of this thesis (including any appendices and/or schedules to this thesis) owns certain copyright or related rights in it (the "Copyright") and he has given The University of Stellenbosch and Rheinmetall Denel Munition certain rights to use such Copyright, including for administrative purposes.
2. The ownership of certain Copyright, patents, designs, trademarks and other intellectual property (the "Intellectual Property") and any reproductions of copyright works in the thesis, for example graphs and tables ("Reproductions"), which may be described in this thesis, may not be owned by the author and may be owned by third parties. Such Intellectual Property and Reproductions cannot and must not be made available for use without the prior written permission of the owner of the relevant Intellectual Property and/or Reproductions.
3. Further information on the conditions under which disclosure, publication and commercialization of this thesis, the Copyright and any Intellectual Property and/or Reproductions described in it may take place, is available in the University IP Policy.

Dedication

For my parents,

My father – Faeek Majiet

My loving mother – Shahieda Majiet

My wife (Tasneemah) and children (Layaan, Qa’im & Tohaa)

ACKNOWLEDGEMENTS

First, I wish to give all the praise to Almighty Allah for giving me the strength and time to complete this research.

I wish to express my deepest gratitude to my supervisor, Dr. Frederik J Mostert, for his constant encouragement, inspiration, guidance, various helpful advices and comments on the thesis during this research project. He provided me with all kinds of support during my PhD study.

I would like to express my gratitude to Prof. Erich Rohwer for allowing this research to fall under the Stellenbosch University. Also for his assistance, support, helpful advice and time. My past and present colleagues in the Rockets & Missile Subsystems group at Rheinmetall Denel Munition have always been an unfailing source of comfort. I would like to thank all of them for their support and help: Dr. Jean Terblanche DeWet Rautenbach, Walter Seloane, Andrew Nieuwmeyer, Andre Muller, Anwar Salie, Sivuyile Xabanisa, Francois Steyn, Aubrey Simon, Buks Kotze, Francois de Villiers and Rod Keyser.

Special thanks go to Mr. James Manuel as the arming and safety officer during my experimental field-testing.

Dr James Moolman, Mr. Christo du Toit & Melinda Diedericks for all the laboratory and chemical analysis support. Dr Milton Maritz for his continuous support on the continuous improvement on JETP. Max and Carl Ruppert for microstructural and analysis on the copper forgings.

This study would not have been possible without the financial support of Rheinmetall Denel Munition and the Student Development Program, a special acknowledgment to Lorenzo Peterson and Duduzile Letseli.

My special gratitude goes to Dr Pieter König (**KING**) for his tremendous effort in the beginning of my detonics career, also during the initiation of this research project and many valuable discussions during this particular research process.

Finally, I would like to express my deepest gratitude to my **wife** (Tasneemah) and children for bearing with me through this journey, my parents, my sons and daughter, and my brothers and sisters for their constant support, encouragement and love.

PUBLICATIONS

F. Majiet and F. J. Mostert, “Investigation on the influence of the initial RDX crystal size on the performance of shaped-charge warheads,” Defence Technology, vol. 15, no. 5, pp. 802–807, 2019.

F. Majiet and F. J. Mostert, “Evaluation of the Dynamic Fracture Characteristics (Plasticity) of Shaped-charge Jets at Different Strain-rates and Characterized Initial Liner Microstructure,” in 31st International Symposium on Ballistics, 2019.

Neil Griffiths Memorial Award

NEILL GRIFFITHS MEMORIAL AWARD
31st International Symposium on Ballistics
Hyderabad 2019
Presented to the authors of the paper judged to have made the most significant contribution to shaped charge technology at the International Symposium on Ballistics
EVALUATION OF THE DYNAMIC FRACTURE CHARACTERISTICS (PLASTICITY) OF SHAPED CHARGE JETS AT DIFFERENT STRAIN RATES AND CHARACTERISED INITIAL LINER MICROSTRUCTURE
F. Majiet, F. J. Mostert
31st INTERNATIONAL SYMPOSIUM ON BALLISTICS 2019
Ian Cullis
Griffiths Committee Chair
Sidney Chocron
IBS President
IBS INTERNATIONAL BALLISTICS SOCIETY
AERONAUTICAL SOCIETY OF INDIA
QINETIQ

1. INTRODUCTION

1.1. Research Goal

Evaluate the dynamic fracture characteristics of shaped-charge jets at different strain-rates and known initial liner and explosive microstructures

1.2. Research Background

A cylinder of explosive with a hollow cavity on one end and a detonator at the opposite end is known as a shaped-charge as shown in Figure 1. The hollow cavity (which may assume almost any geometric shape such as a hemisphere, cone, tulip, trumpet, or, in fact, any accurate device) is usually lined with a thin layer of metal.

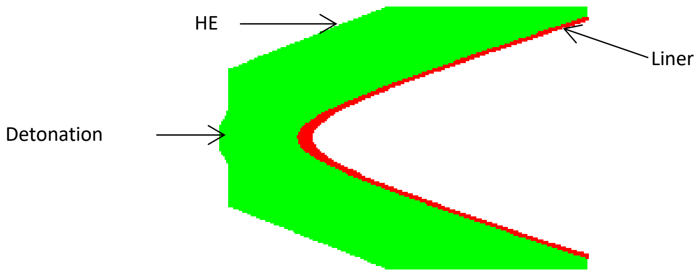

Figure 1: Basic shaped-charge concept, with High Explosive (HE, green) and metal liner (red)

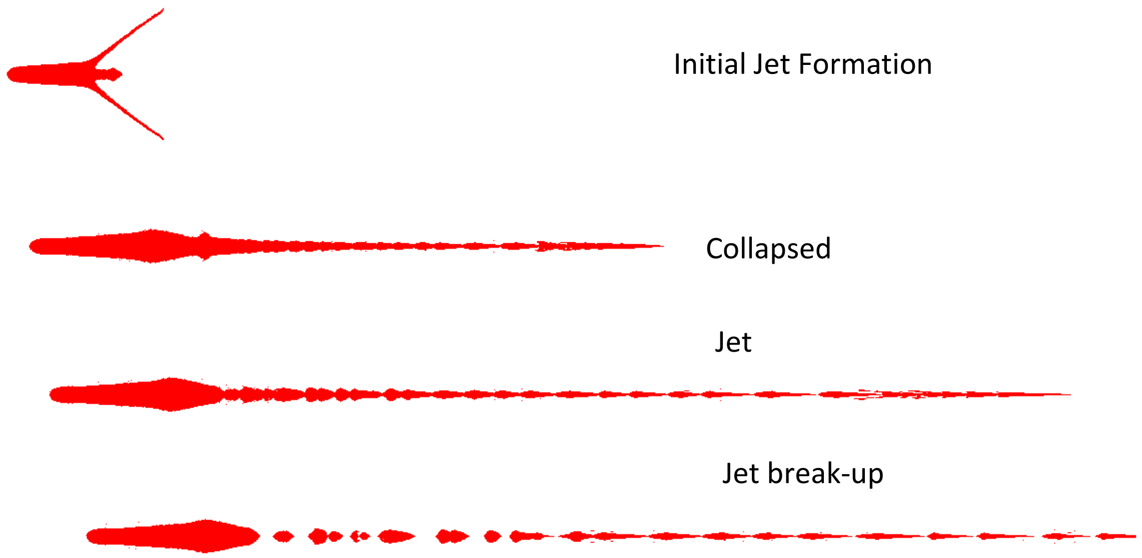

Figure 2: Shaped-charge jet-formation process, position time frames presented from initial jet-formation up to jet particulation.

The liner forms a jet when the explosive charge is detonated. These jets are neither a plasma nor liquid in normal circumstances and have, for typical metals, been experimentally proven to be well below the melting temperature. Upon detonation, a spherical wave propagates outward from the point of initiation or detonation point. This high-pressure shock wave moves at a very high velocity, typically around 8 mm/µs. As the detonation wave engulfs the lined cavity, the material is accelerated under the high detonation pressure, collapsing the liner. During this process the liner material is driven to very violent distortions over very short time intervals at strain-rates of 10^4 - 10^7 s^{-1}[1].

The first jet particle is referred to as the jet tip and the rearmost particle is referred to as the slug. The “Appendix” is a shaped-charge jet section that is located between the end of the tail of the coherent jet and the slug [2]. The appendix is further described and shown in 3.2.4. The stand-off can be defined as the distance from the virtual origin of the shaped-charge to the target. The penetration depth of a shaped-charge jet into most target materials increases to a maximum, then decreases as the stand-off distance increases. This penetration peak occurs just prior to the onset of jet-break-up due to the dispersion, spread, and tumbling of the jet particles after particulation. As a result, it would be advantageous to the shaped-charge designer to predict and control the jet-break-up time.

Dynamic recrystallization (DRX) of various materials was investigated through the microstructural examination of a recovered shaped-charge slug, using both optical and transmission electron microscopy. The microstructure was refined, indicating the DRX process occurred during deformation. No twins or elongated sub grains were observed due to the extremely high strain-rate deformation process. This suggests that the DRX process was dominated by dislocation movements [3], [4].

Hydro code computer programs are limited for use in this instance, because accurate equations of state and constitutive equations are not verifiable under these conditions. In addition, the fracture mechanism and associated algorithm is not well known. Nevertheless, shaped-charge experiments provide an excellent test bed for the study of materials under intense loading conditions.

1.3. **Originality of Research**

The break-up phenomenon in shaped-charge jets has been studied for decades with numerous designs. The focus of this research was to demonstrate the impact of varying strain and strain-rate behaviour on shaped-charge jets with copper liners that have fixed microstructures. The strain and strain-rate was varied by changing the liner angle, explosive output and using different initiation systems. Two liner designs (30^{0} and 60^{0} half angle, respectively) were evaluated with **similar microstructures**. The strain and strain-rate was further modified with two explosives (91% RDX and 55% RDX formulations) and two initiation systems (point initiation and peripheral initiation).

A secondary objective was to quantify the effect of the explosive microstructure on the break-up behaviour of shaped-charge jets. Four different batches of mono-modal Comp A3 (RDX91:WAX9) was manufactured with four different RDX crystal sizes.

1.4. **Objectives of Research**

The objective of this research has been outlined below:

- Quantify the effect of liner angle (30° and 60°, respectively), with a fixed microstructure, on shaped-charge jet break-up
- Quantify the effect of different initiation systems on shaped-charge break-up
- Quantify the effect of explosive microstructure on shaped-charge break-up
- Quantify the effect of different explosive output on shaped-charge break-up
- Establish the distinction between jet plasticity and jet break-up-time

1.5. **Hypotheses**

Various hypotheses were used in the initiation phase of the study. The first hypotheses was that increasing the strain and strain-rate of the shaped-charge jet will increase the break-up-times. That is increasing the liner angle increases the break-up-times.

The second hypotheses of this research was that using larger RDX explosive crystal sizes would form micro jets causing the jets to form differently compared to jets formed from a fine RDX crystal size. The objectives in Section 1.4 are written to address each of the hypotheses.

The two hypotheses are completely independent, but both investigate underlying mechanisms affecting break-up times of shaped-charge jets. The first focusing on aspects of the liner and the second on the explosive.

1.6. **Conclusion**

This research has demonstrated from an experimental perspective some of the underlying mechanisms controlling break-up-times of shaped-charge jets while testing both hypotheses and addressing each objective of this research project. The shaped-charge warheads were manufactured accurately with special care taken with each component used in the products. The research looked at the influence of microstructural defects within the explosives. The research also looked at the shaped-charge design from a strain and strain-rate perspective for a single explosive and a single liner microstructure.

The same microstructure was used for different shaped-charge designs in an experimental study to conclude on jet metallurgy. The data will show that it is the cumulative mass distribution within the shaped-charge jet which is the underlying mechanism affecting the break-up-times.

2. ANALYSIS AND CHARACTERISATION

The research was approached by compiling a set of material properties and performance data understood to be important to shaped-charge kinetics and then developing and executing test plans as required and practicable. In general, the execution involved the thorough characterization of the microstructural and mechanical properties of the liner and explosive variants. This was conducted concurrently with, and guided by, an extensive literature review. The approach and plans were modified with experience and opportunity.

Flash X-ray analysis was used to assess the performance of each concept design. This enabled assessments of jet length, velocity and location over time. Flash X-ray analysis was supplemented with hydro code modelling of liner deformation. Hydro code modeling was used to optimize shaped-charge design variables like initiation system, liner angle, liner thickness and explosive formulation as a means of varying the strain and strain-rate.

Grain morphology was assessed to understand the size and shape of the microstructure.

3. LITERATURE REVIEW

3.1. Introduction

Research within the warhead technology domain may be distributed among the categories as shown in Figure 3. The research is further focused on shaped-charge technology as shown in Figure 4. The research is even further focused on the break-up behaviour of shaped-charge jets as shown in Figure 5. Some parameters that may influence the break-up behaviour of shaped-charge jets are presented in Figure 6.

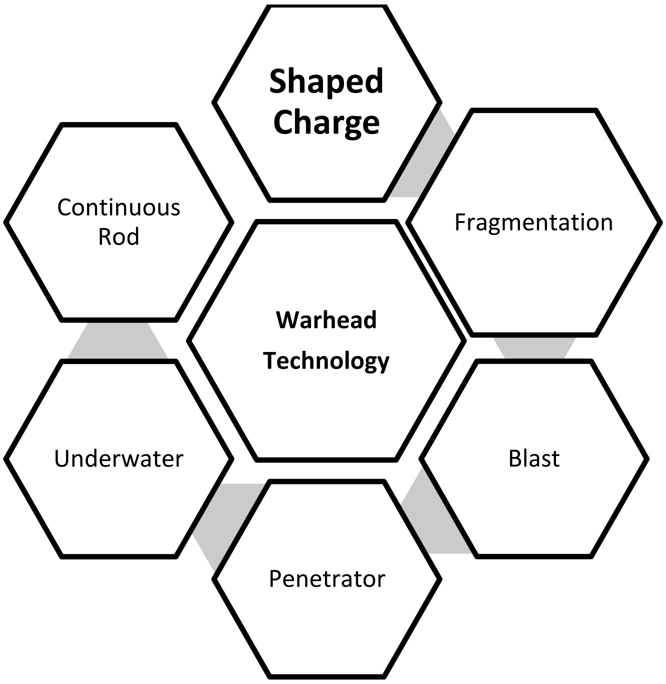

Figure 3: Typical topics within the warhead technology portfolio of which shaped-charge technology is the focus of this research project.

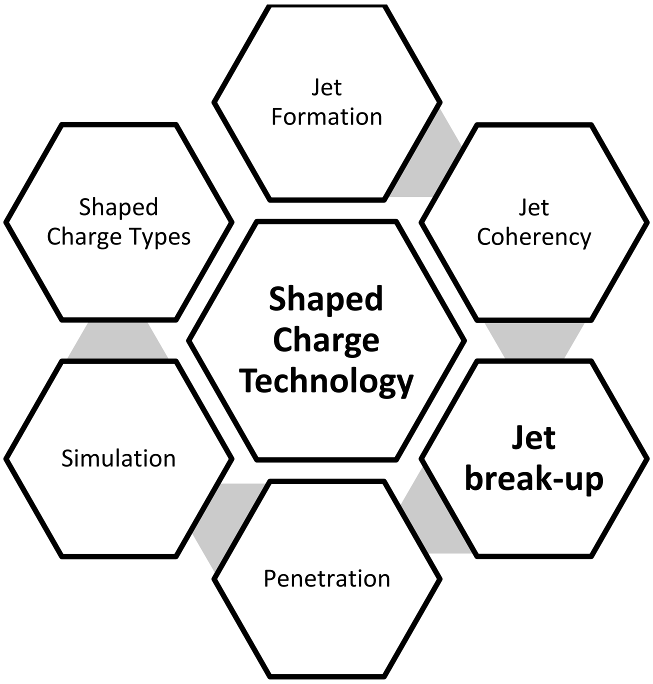

Figure 4: Shaped-charge technology is further divided into numerous categories; this research project focuses mostly on the break-up behavior of jets produced from shaped-charges.

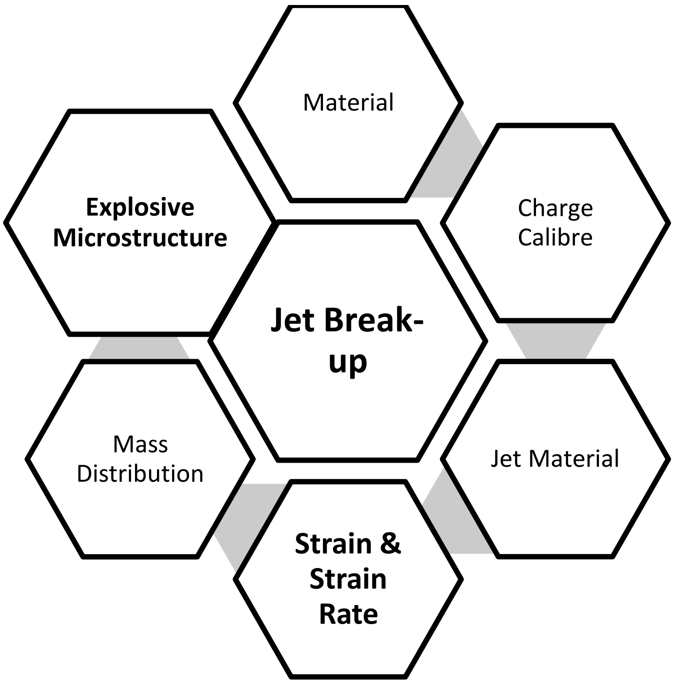

Figure 5: Some of the parameters that influence shaped-charge jet-break-up with the focus areas for this research project shown in bold.

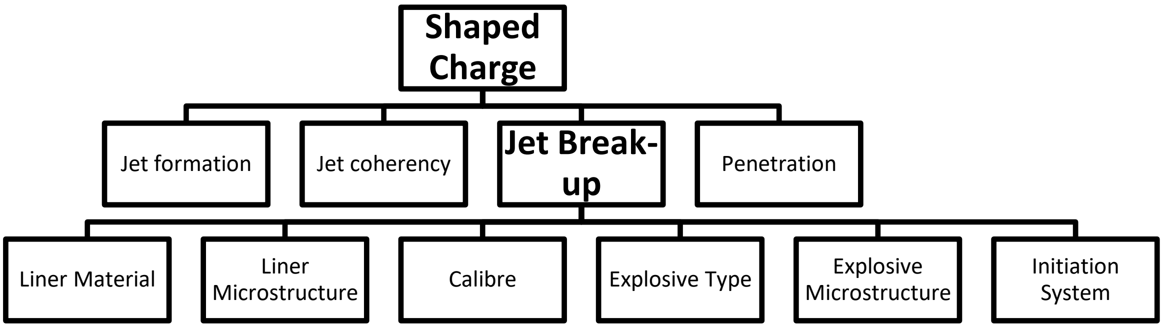

Figure 6: Bird's-eye view organogram showing some more parameters influencing shaped-charge performance with the focus on jet-break-up and variables used in this research project.

The purpose of this chapter is to discuss and criticise some of existing literature relevant to the work presented in this thesis. This has been divided into three principle sections: Modelling of Jet Formation, Current Knowledge of Deformation Mechanisms and The Testing and Characterisation of Materials. The jet-formation section gives a detailed background to the theoretical analysis of high strain-rate deformation. In the final section, practical investigations of material at high strain-rates are discussed and analysed.

3.2. Factors Influencing shaped-charge Performance

This section focuses on a number of factors influencing shaped-charge performance. Jet coherency, virtual origin, stand-off, appendix, explosive, liners design/geometry, detonation wave or initiation system, and more are described below.

3.2.1. Jet Coherency

This phenomena has been extensively studied by Chou et al. [5], [6]. Break-up of a standard jet occurs along its length, the fractures are perpendicular to its axis. When a jet breaks up in parallel to its axis and material then moves radially outwards the effect is described as incoherency.

When the collapse velocity of the liner exceeds the sound velocity of the liner material, the jet becomes incoherent. This is due to the complex interactions of shock waves within the material. As the collapse velocity decreases from the liner's apex to its base, this phenomena is usually only seen in the leading section of the jet. This is the most common cause of incoherency.

It is well known that the velocity of a coherent jet emerging from a shaped-charge is limited. For copper liners, the maximum Mach number for the flow into a coherent jet is 1.23 [7]. In 1974 Harrison, DiPersio, Krapp and Jameson showed that when the flow velocity of the collapsing copper liner becomes larger than $1.23C_0$, where C_0 is the copper bulk sound velocity, the formed jet becomes incoherent. In this case, instead of a straight coherent jet one may get a spray of laterally expanding jet particles (sometimes called bifurcation due to its X-ray shadow) [2]. This observation has since then been verified by other investigators including Chou and Brown, and respective co-workers [5], [8] and others.

3.2.2. Virtual Origin

The concept of virtual origin was first proposed by Allison and Bryan [9] and then developed by Allison and Vitali [10] for the penetration of continuous and particulated jets with the consideration of velocity gradient and the stand-off distance between the virtual origin and target surface. This model has been widely accepted, and can be used to predict the depth of penetration before and after jet-break-up [11], [12].

All jet elements are formed simultaneously at a virtual origin located at a distance from the target surface. Each jet element is emitted from the virtual origin at its own velocity that remains constant during its travelling between the virtual origin and target. The existence of a unique virtual origin location of the entire jet requires that the spatial distribution of jet velocity is linear. [13]

3.2.3. **Stand-off**

The shaped-charge jet does not become fully formed until it has travelled a certain distance. The distance from the virtual origin up to the point that the tip particle has travelled to a particular point is called the stand-off distance, which is usually referenced proportional to the liner or charge diameter. In general the optimum stand-off distance to a target, is between two and eight times that of the liner diameter depending on the design [14]. A proper stand-off distance can increase the penetration depth by 50% in comparison with zero stand-off distance [14]. Figure 7 illustrates the relation between the depth of penetration and the stand-off distance. If this stand-off distance is too large, a coherent unidirectional jet does not exist. Instead, tumbled, deflected and particulated columns of jet particles are observed.

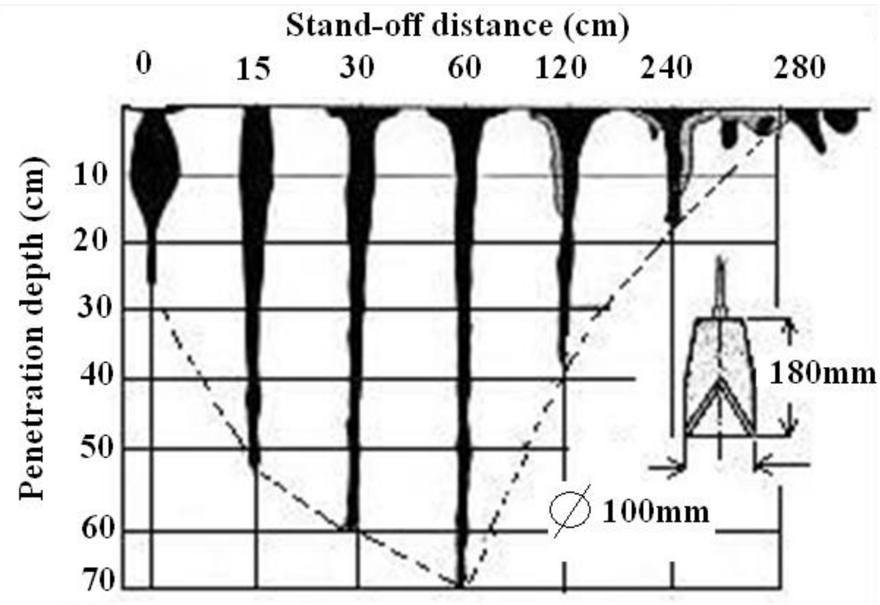

Figure 7: Example of the effect of standoff on penetration. [15].

3.2.4. **Appendix**

The appendix is a shaped-charge jet section that is located between the end of the tail of the coherent jet and the slug [2]. Images from the experimental data set were used to describe the appendix as shown in Figure 8 for peripheral initiation and Figure 9 for point initiation. Figure 8 and Figure 9 are Flash X-ray radiographs of jets produced from point- and peripheral-initiated shaped-charges.

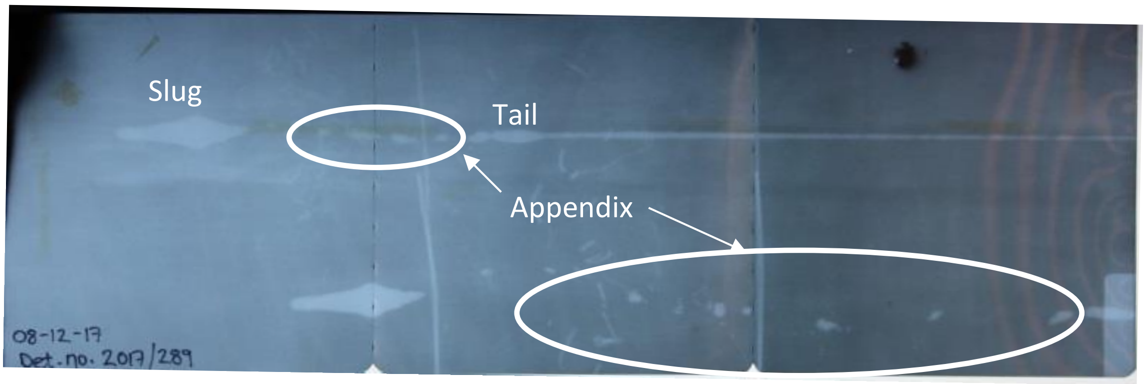

Figure 8: Description of the Appendix for peripheral initiation.

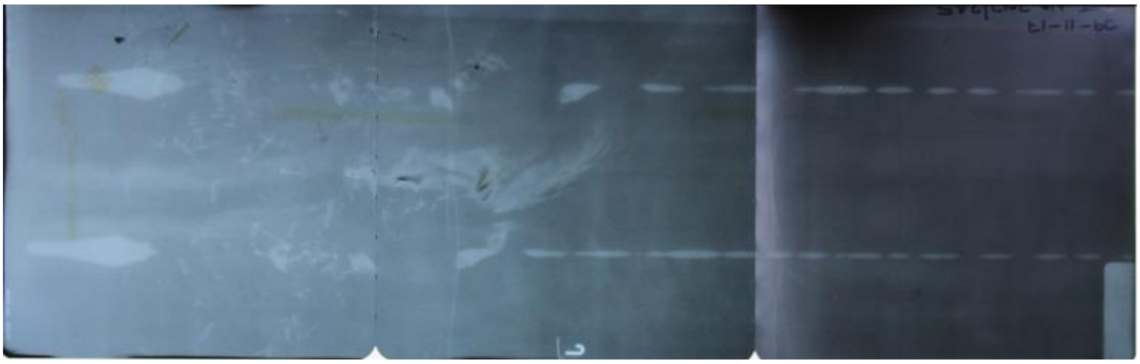

Figure 9: Description of the Appendix for point initiation.

3.2.5. High Explosive

Theoretically, a more energetic explosive produces a faster jet, greater jet kinetic energy and deeper penetration [16]. The energy obtained from the high explosive during its detonation is related to the Gurney velocity of this explosive. This is the energy liberated from the high explosive and transformed into mechanical work imparted to the liner element. Typically, the Gurney velocity increases with the detonation velocity and/or the detonation pressure of the explosive that leads to the increase of the jet tip velocity. As a result, the jet kinetic energy and its penetration potential into the target will be enhanced. Explosive properties for some of the common explosives are listed Table 1.

Table 1: Explosive properties for some high explosives. [13], [16], [17]

HE\Parameter	Density (ρ) (g/cm^3)	Detonation Velocity (m/s)	Gurney Velocity (m/s)	Detonation Pressure (GPa)
HMX	1.891	9100	2960	420
LX-14	1.835	8800	2800	370
RDX	1.730	8489	2870	330
Cyclotol RDX75TNT25	1.754	8250	2790	320
PETN	1.720	8142	2920	220
TNT	1.600	6913	2390	210
Comp A3	1.650	8300	2630	300
Form F	1.400	6000	NA	126

3.2.6. **Liner Geometry**

The liner is considered as the most critical element affecting the dynamic characteristics of the shaped-charge jet and its penetration capability into target materials. There are many liner shapes, which could produce different jet characteristics. These shapes include conical, hemispherical, tulip, trumpet (or bell shape) and bi-conical liners [16].

The liner geometry (shape and thickness) determines the characteristics of the produced jet. For example, the conical liner produces deeper penetration with smaller hole diameters. On the other hand, the bell shape liners produce shallow depth penetration with greater hole diameter [18]. In general, the geometry of the cone is determined by the cone apex angle. If this angle is small, the jet is long, thin and more penetrative. As the cone angle widens, the jet becomes shorter, thicker, and less penetrative [18], as illustrated in Figure 10 and Figure 11.

Various improvements to the liner elements have been made since discovery of application and radiography (1940s). In 1998, Davidson and Pratt, proved [19] that modifying the liner shape of a shaped-charge can increase the jet kinetic energy by 10% and hence can improve the penetration depth by 28%.

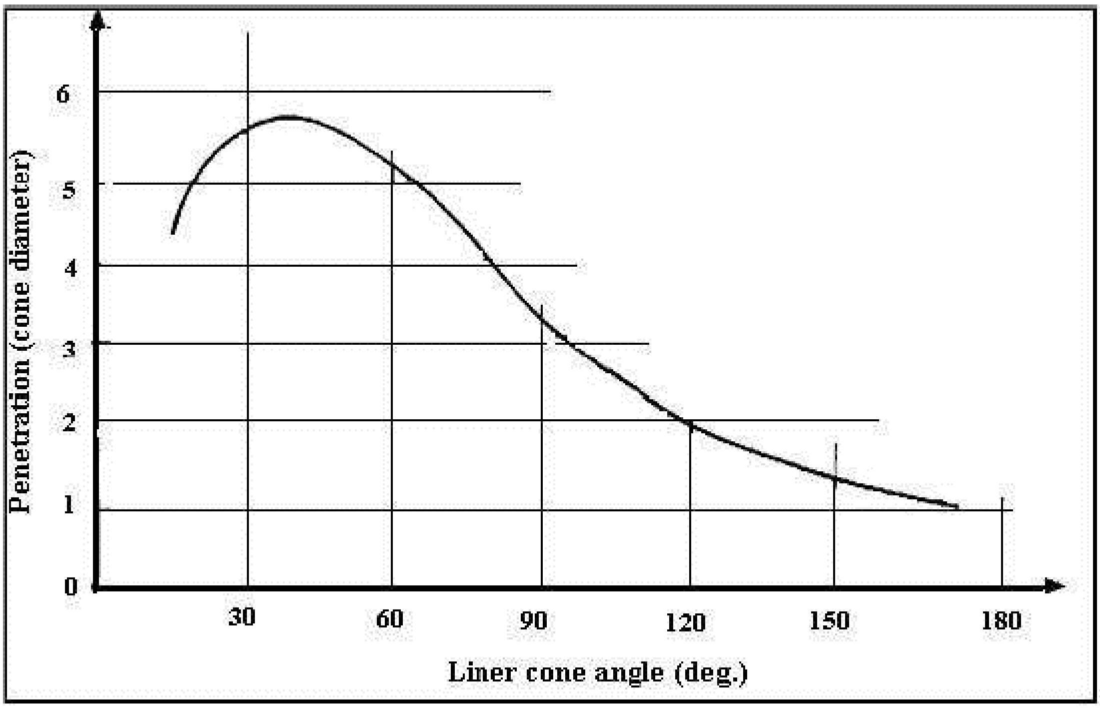

Figure 10: Penetration versus liner cone angle [13].

Figure 10 shows the penetration performance increases to an optimum at approximately 40° then reduces, as the liner angle is further increased. This obviously takes into account numerous assumptions like similar liner thickness, explosive and initiation system.

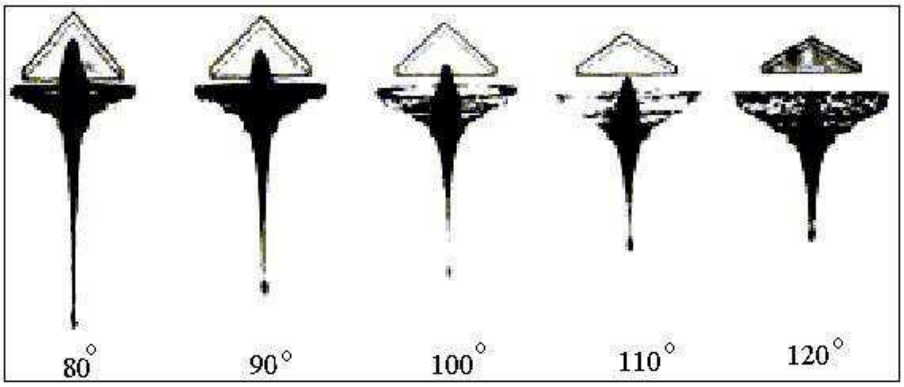

Figure 11: Shaped-charge jet profile at different cone angles [18].

Figure 11 shows the jet profiles for liners of different angles at the same time. These images may be obtained from either simulation or flash X-ray analysis.

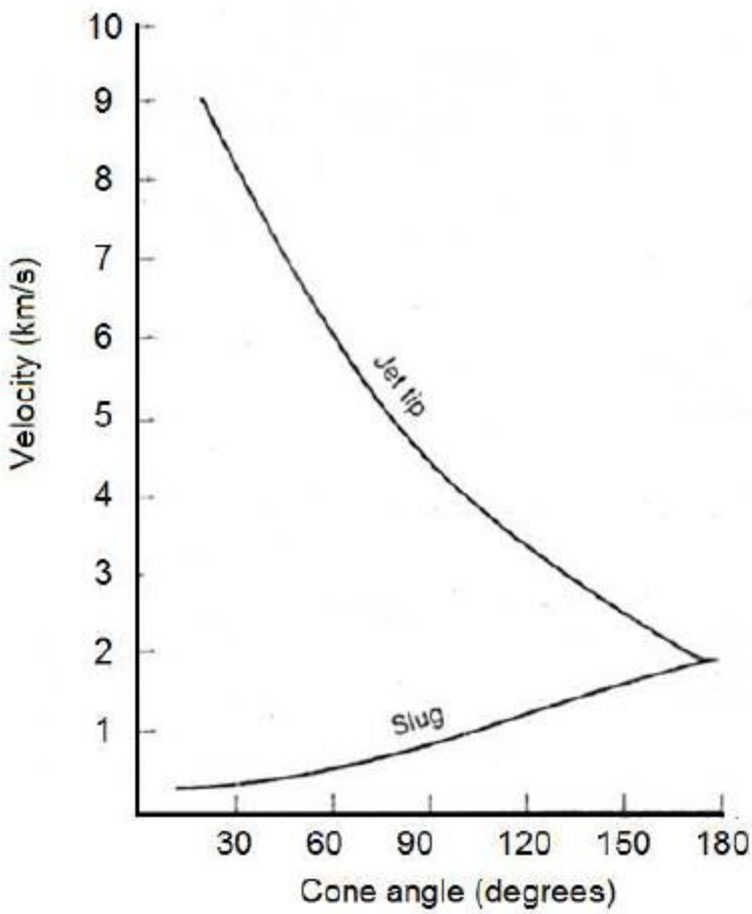

Figure 12: Jet and tail velocities as a function of cone angle [13].

Figure 12 shows the influence of both the jet tip velocities and the slug velocities of similar designs for a particular liner angle. The optimum thickness of a liner has been shown experimentally to be about 2% of the charge or liner diameter [20].

3.2.7. **Initiation System**

The velocity, the length, and the cohesion of the jet, depends on the manner in which the liner collapses, which is strongly influenced by the shape of the detonation wave (DW) when it meets the liner. The DW travels inside the explosive in the form of hemispheres. The angle between the tangent to these hemispheres and the liner defines the value of the deflection angle, which has a large influence on the jet and the slug masses and velocities [21].

Moreover, it will determine the magnitude of the collapse angle, which is the key parameter to determine the jet formation. In general, a faster jet is formed when a smaller angle is induced. This improvement can be achieved using a waveshaper (inert material) in the explosive. This waveshaper is a barrier embedded in the explosive charge between the cavity and the rear initiation point in order to divert the detonation wave. This then changes the implosion angle onto the liner.

Figure 13 shows the plots of the detonation waves of two conical shaped-charges (CSC) indicating the shape of the DW as it meets the liner. The left shaped-charge is without waveshaper, while the right one has a waveshaper of a spherical shape. Smaller incidence inclination angle is preferred for a shaped-charge design improvement as it will increase the real collapse velocity of liner elements and therefore the jet element velocities will be increased [13]. These were one of main techniques used to vary the strain and strain-rate of the shaped-charge jets. Peripheral-initiated shaped-charges contain waveshapers and point-initiated shaped-charges exclude the waveshaper.

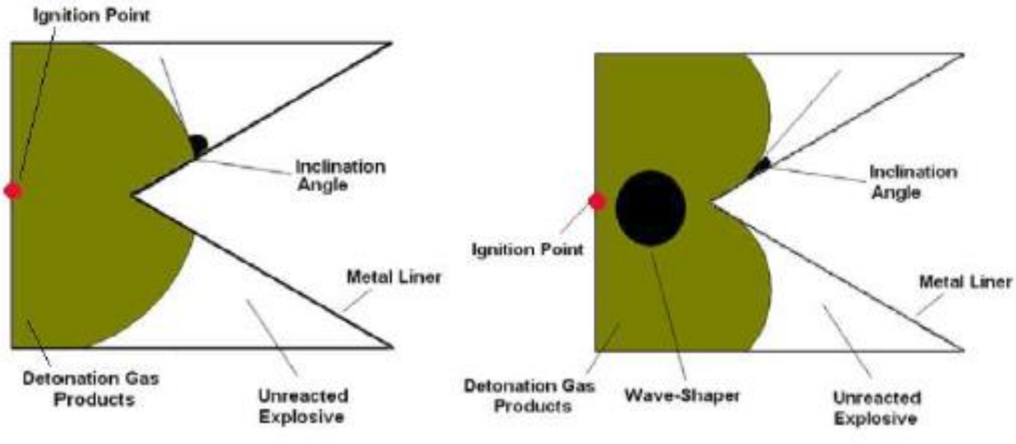

Figure 13: The shape of the DW travelling inside the explosive charges with and without waveshaper. [13] These images are section views of a cylindrical charge for ease of description.

Another technique, i.e. simply leaving an air cavity between the charge and liner instead of an inert material may be used as presented in Figure 14 [22]. This technique has shown similar increases in tip velocity as those used for waveshapers.

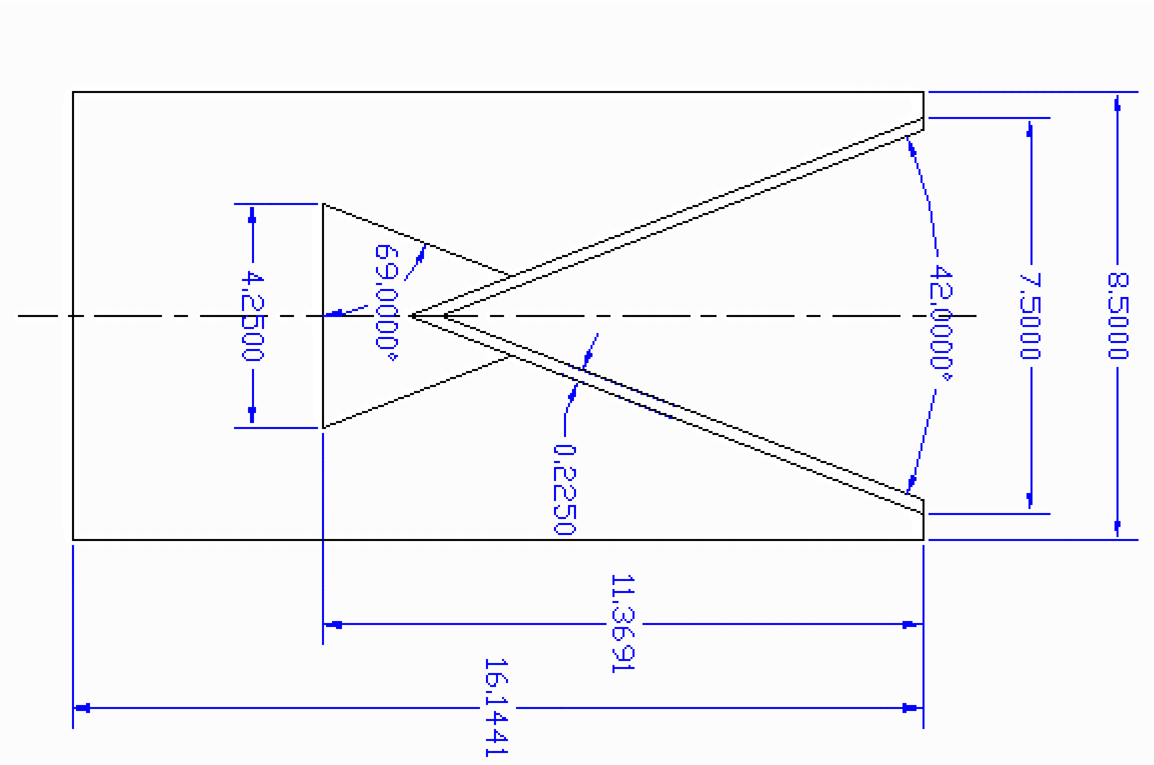

Figure 14: Air cavity technique for increasing the tip velocity in [22].

3.2.8. **Symmetry**

Any change in the shaped-charge symmetry will produce an asymmetric jet, in which curved path and radial velocity components are observed leading to the decrease of the penetration depth [12], [13].

3.2.9. **Liner Materials**

Researchers have shown an increased interest in the different liner materials and their manufacturing techniques. Held [25] showed different materials that could be used as liners and their ranking according to the predicted penetration performance in terms of liner density and jet velocity, as illustrated in Table 2. In general, the characteristics of a good candidate material for shaped-charge liner include [16]:

- high density
- high melt temperature
- high bulk speed of sound
- fine grain and proper grain orientation
- availability and cost
- easiness of fabrication
- high dynamic strength and ductility.

Table 2: Penetration potential ranking of the different liner materials [25].

Liner material	Al	Ni	Cu	Mo	Ta	U	W
Density (g/cm^3)	2.7	8.8	8.9	10.0	16.6	18.5	19.4
Bulk sound speed (mm/µs)	5.4	4.4	4.3	4.9	2.4	2.5	4.0
V_0 (mm/µs)	12.3	10.1	9.8	11.3	5.4	5.7	9.2
Jet performance $V_0\sqrt{\rho_j}(kg/m)^{0.5}/s$	20.2	30.0	29.2	35.7	22.0	22.0	40.5
Ranking	7	3	4	2	6	5	1

Because tungsten has great density exceeding 19 g/cm^3, high melting point of 3410 °C, high sound speed and great ductility, it has been widely used in anti-armour technology as a shaped-charge liner material [26]. Jet ductility is referred to as the ability of a material to remain continuous. The onset of jet break-up is delayed in a jet with a high ductility and consequently the jet stretches more before individual particles form. However, the most commonly used liner material is copper. It flows easily to produce a coherent jet when it is deformed by the detonation wave. This copper material should be oxygen-free with high conductivity and low impurity according to ASTM standard C101OO LAW F68-77 temper 070 [27]. Gold is denser and has greater dynamic ductility than copper. In theory, it should achieve better penetration performance than other materials [13].

Design and experimental studies of advanced high performance trumpet molybdenum-lined shaped-charge warhead technologies are demonstrated with more powerful explosives like CL-20 resulting in ductile jets with coherent tip velocities above 11 mm/µs. [28]

In 2001, Bourne et al. [29] used zirconium, silver, titanium and depleted uranium to study their shaped-charge jet characteristics when same liner masses were used to compare the cumulative jet length produced from these metal liners. They designed a hemispherical liner to test the liner material performance. This design produced a jet containing 80% of the full liner mass. The characteristics of these jets for different liner materials including copper are listed in Table 3 [29]. The ductility factor Q, is an indication of the ductility of the jet (i.e. a higher value is more ductile)

Table 3: Jet characteristics using different liner materials [29].

Metal	Jet Length (mm)	V_{tip} (mm/µs)	V_{tail} (mm/µs)	Break-up time (µs)	Material Ductility Factor (Q)
Silver (Ag)	1456.0	6.48	3.01	419.6	181.90
Zirconium (Zr)	2058.9	6.75	2.34	603.8	246.10
Titanium (Ti)	1327.4	6.34	2.99	396.2	175.70
Depleted Uranium (DU)	1700.0	6.40	3.30	548.4	217.67
Copper (Cu)	1130.5	5.90	2.56	338.5	161.53

3.2.10. **Liner Crystal Shape**

For the fine crystal structure, it is expected that particulation time is longer and the transverse movement of the particulated jet elements can be avoided [25]. It was found that the sharpness or severity texture of the liner material has less influence than the grain-size effect on the jet-break-up time and effective jet length [30].

It was also found that the crystal shape and its deformation due to the manufacturing process affect the particulation (break-up) behaviour during the jet elongation phase, causing transverse movement of the particulated elements or even jet tumbling [25]. Held verified that the shaped-charge jet is very sensitive to the small deviations of the liner structure, which can be amplified in the stage of jet collapse and formation [25]. As a result, tumbling and spinning particulated jet elements around the jet axis can decrease the jet coherency, and therefore, decrease the penetration performance of the shaped-charge jet.

Moreover, the shaped-charge jet undergoes a dynamic recrystallization due to large deformation and dislocation movements of the grain [26].

3.2.11. **Liner Impurities**

Researchers have shown increased interest in the effect of copper material impurities on the ductility of the copper used as shaped-charge liners. In 2004, Schwartz et al. [31] described the dependence of copper ductility on the total type and number of impurity atoms. The copper used was 4N (99.99%) purity and this liner was manufactured by cold forging technique to extrude it to a hollow cone shape. After the cold forging process, the produced liners are annealed at 315 °C for one hour or 400 °C for 10 minutes to stabilize the microstructure of sulphur doping. Table 4 indicates the effect of sulphur content on the break-up-time of the shaped-charge jet at constant grain-size of 40 µm. It has been shown that the total number of impurities decreases the ductility of the copper due to the segregation of the impurities at the grain boundaries [31].

Table 4: The dependence of the jet-break-up time on the Sulphur content [31].

Sulphur concentration (ppm)	Break-up-time (µs)
3	186
4	185
7	147

In 1995, Fujiwara and Abiko [32] performed experiments on the ultra-high-purity copper in order to investigate the effect of impurity presence and operating temperatures on the copper ductility. In this study, the ultra-high-purity copper was produced by electronic beam refining and vacuum melting technique. The tensile test was performed on the ultra-high-purity copper 6N, 8N and compared with commercial purity copper rod 3N (99.9%) under high vacuum of 7×10^{-4} Pa at a strain-rate of 4.2×10^{-5} s^{-1}. The average grain-size for the three copper specimens was 30, 50 and 100 µm for 3N, 6N and 8N, respectively [32]. This implies that the copper impurities have a significant effect on its mechanical properties and performance as a shaped-charge liner.

3.2.12. **Liner Microstructure**

The jet cohesion, break-up-time and effective jet length are the predominant governing parameters affecting the penetration depth of a shaped-charge into target material. These parameters depends on the grain-size and crystal shape of the liner [30]. Many papers have been published to discuss the effect of grain-size of liner material on its mechanical properties and the validity of Hall-Patch relation over wide range of copper grain-size from nanometer to hundred micrometres. For example, Gertsman et al. [33] measured the yield strength of copper with different grain-size particles and compared the measured yield strength with that obtained by the Hall-Patch relation:

$$\sigma_y = \sigma_0 + kd^{-a} \qquad \text{Eq. 1}$$

where σ_y is the yield stress, d is the average grain-size, σ_o and k are material constants and

a = 0.5 [33].

The apparatus used to determine the yield stress was the miniaturized disk bend test (MDBT).

The copper sample with micrometer grain-size was produced from a copper rod of diameter 2 mm and 4N purity (99.99%). The produced sample was 0.2 mm thick and annealed at 300-600°C for 30 minutes to produce different grain-sizes. The nano-crystal copper was produced by the evaporation of pure copper from a tungsten boat under 1 kPa pressure of helium and then compacted under vacuum to produce a pellet of 0.3 mm thickness [33] [34].

It was found that the yield stress of the coarse grain-size could be approximated by Eq 1, where

σ_0 =92(±12) MPa, k=399(±61) MPa/µm and a=0.5.

However, the classic Hall–Patch relation could not be applied to nano-crystal copper because of the lattice dislocation that can move across the crystallite of a polycrystalline material. It was difficult to deduce a global equation governing the dependence of yield strength on the entire grain-size range of the copper material. [4]

Another study of the relationship between average grain-size and mechanical properties of copper used in a shaped-charge liner, was undertaken by Meyers et al. [4]. They performed an experimental investigation on pure (4N purity) oxygen-free high thermal conductivity (OFHC) copper in order to correlate the relation between the average grain-size of copper and the resulting mechanical strength under severe plastic deformation [4]. The experimental work was performed with a flyer plate of 4.7 mm thickness stainless steel accelerated by PBX 9501 explosive to an impact velocity of 2.2 mm/µs. The purpose of this experiment is to create exactly the same conditions of the high pressure and strain-rate as those during the shaped-charge liner ***collapse***. The impact pressure of the flyer plate was approximately 50 GPa, while the pulse time duration was only 2 µs.

In 1995, Fujiwara and Abiko [32] tested the mechanical properties of three copper samples of 3N, 6N and 8N with average grain-size of 30 µm, 50 µm and 100 µm, respectively, under strain-rate of 4.2×10^{-5} s^{-1}. It was found that both yield and maximum stresses in the 3N sample were higher than those of both 6N and 8N samples except that the ductility of 3N (82%) is lower than that of the others (91% and 96% for 6N and 8N respectively) due to the effect of grain-size on the ductility as shown in Figure 15.

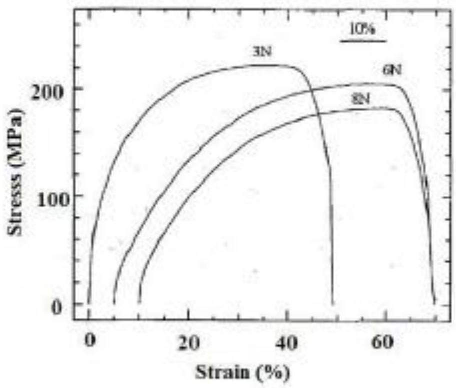

Figure 15: Stress-strain curves of 3N, 6N and 8N copper samples at strain-rate of 4.2×10^{-5} s^{-1} [32].

In 1993, Bourne et al. [30] used a copper liner manufactured by shear forming in order to investigate the effect of both grain-size and texture severity on the jet length and its break-up-time. They used both the Defence Research Agency analytical model JETPEN and flash X-ray diagnostics to determine the fragmentation of shaped-charge jet and particulation time as well as effective jet length. In 1996, Renfre et al. [27] confirmed that the spinning or flow turn machining of the copper material affects not only the liner performance during detonation, but also the grain-shape orientation, which has a direct relation to break-up-time.

Table 5 shows the results of nine copper liner samples that were used to record both effective jet length and break-up-time of the jet. The shaped-charge had a calibre of 102 mm and height of 151 mm. The cone apex angle is 60° and the liner wall thickness is 2 mm. The 3 mm thickness casing is made of aluminium material [29].

Table 5: Break-up-time and effective jet length for nine different copper samples [29].

Liner Code	Average grain diameter (μm)	Break-up-time (μs)	Effective jet length (mm)
ME1A	10	195	1450 – 1500
IE2C	15	172	1300 – 1250
IE2B	20	172	1270 – 1280
IE1B	22	174	1248 – 1330
IE1A	26	182	1400 – 1330
E175A	42	161	1175
IE1C	43	172	1190 – 1350
IE2D	43	149	100 – 1140
IEE1A	48	126	870 – 880

In addition to the well-known Hall-Patch relation between average grain-size and liner mechanical properties, Zerilli–Armstrong model [35], as discussed by Bourne et al. [29], describes the relation among the flow stresses (σ), plastic strain (ε), strain-rate ($\dot{\varepsilon}$), temperature (T) and grain-size (d).

The general form of the Zerilli–Armstrong model is [35]:

$$\sigma = C_1 \varepsilon^n e^{(-C_2 T + C_3 T ln \dot{\varepsilon})} + C_4 + C_5 d^{-0.5} + C_6 \varepsilon^m \qquad \text{Eq. 2}$$

where parameters C_1, C_2, C_3, C_4, C_5, C_6, m and n are constants given in Table 6, d is the average grain-size in (mm) and $\dot{\varepsilon}$ is the strain-rate in (s^{-1}).

The first term represents the effect of the thermal activation on the motion of dislocations. The second and the third terms represent the additional stress due to the grain-size effect (i.e. Hall-Patch effect), while the last term represents the strain hardening. This equation describes the stress-strain behaviour of the bcc (body centred cubic), FCC (face centred cubic) and hcp (hexagonal close packed) materials.

Alkaline metals (Li, Na, K, Rb, and Cs) all have the body centered cubic (bcc) structure. In addition, the vanadium and chromium groups also have the bcc structure. Furthermore, at room temperature, iron has a bcc structure

Metals with the FCC structure include aluminium, copper, nickel, gamma iron, gold, and silver.

Some metals with hexagonal close-packed crystal structures include cobalt, cadmium, zinc, molybdenum and the α phase of titanium.

Table 6: The constants of the Zerilli–Armstrong model [35].

Metal	C_1 (MPa)	C_2 (K^{-1})	C_3 (K^{-1})	C_4 (MPa)	C_5 ($MPa.mm^{0.5}$)	C_6 (MPa)	n	m
Cu	980	0.0028	0.000115	46.5	5	0	0.5	0
Ta	1125	0.00535	0.000327	0	19	310	0	0.440
W	16500	0.591	0.000279	0	25.6	860	0	0.443
Mo	937	0.0036	0.000107	0	22.65	647	0	0.401
Zr	600	0.0024	0.000132	21	7.9	76	0	0.510
Ti	1100	0.00226	0.00017	51	14.86	300	0	0.500
Fe	1033	0.00698	0.000415	0	22	266	0	0.289

As a direct measure of the jet efficiency and its dependence on stress, strain and strain-rate, the break-up-time expression derived based on model by Curtis & Moyes, [36], is:

$$t_B = \frac{\pi r_0}{\Delta V_{Pl}} - \frac{1}{\dot{\varepsilon}_0} \qquad \text{Eq. 3}$$

where r_0 is the radius of the jet and $\dot{\varepsilon}_0$ is the strain-rate of the jet material, ΔV_{PL} is the maximum plastic wave velocity in the metallic liner (i.e. the velocity difference between two neighbouring jet fragments), which is defined as:

$$\Delta V_{Pl} = \sqrt{\frac{1}{\rho_0}\frac{d\sigma}{d\varepsilon}} \qquad \text{Eq. 4}$$

where ρ_o is the original density of the liner.

Both the break-up-time of the jet and the cumulative jet are inverse functions of the plastic wave velocity [29].

In a separate study, Tian et al. [37] found that changes of the liner microstructure and grain-size influence the dynamic behaviour of liner material. Hence, it affects the penetration depth into target materials.

Held (1985) [38], Mostert and König (1987) [39] , Golaski and Duffy (1987) [40], Chokshi and Meyers [41] (1990), and Hirsch (1992) [42] among others comment on the influence of liner metallurgy on the jet ductility. Golaski and Duffy (1987) did not provide a ΔV formula, but showed a direct correlation between liner grain-size and jet-break-up time. Mostert and König (1987) stated that the jet from a shaped-charge elongates to a strain well In excess of 10 before it particulates. They also noted that the micromechanical properties of the liner, as well as its purity, have an Influence on the ductility of the jet, but these factors are not included in any existing models.

3.2.13. **Strain-rate**

It has been demonstrated by Lu et al. [43] that the fracture strain of nano-crystalline copper increases with increasing strain-rate from $6x10^{-5}$ to $1.8x10^{3}$ s^{-1}. This may be attributed to the creep rate and super-plasticity that have been found in the nano-scale metals and alloys at much lower temperatures. The governing deformation mechanism of the nano-scale copper at low temperatures is the grain boundary mechanism rather than lattice dislocation mechanism.

In Ref. [43], nano-crystalline copper was produced by the electro-deposition technique using electro-discharge machining, where the produced copper has an average grain-size of 20 nm, a purity of 99.993% and oxygen content of 24 ppm. Two dog-bone samples of the nano-crystalline copper in Figure 16 were prepared for the tensile test at both low and high strain-rates.

The low strain-rate test at $6x10^{-5}$ to $6x10^{-1}s^{-1}$ were conducted using a standard uniaxial tensile Shimadzu servo-hydraulic test machine (1 kN). The high strain-rate test at $1.8x10^{3}$ s^{-1} was conducted using rotating disk-bar tensile impact apparatus [43].

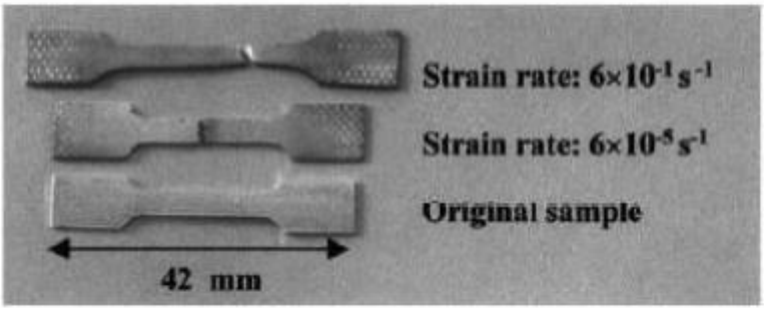

Figure 16: Dog bone samples of the nano copper [43].

It was found from the experiments that the fracture strain increases from 15% to 39% when the strain-rate increases from $6x10^{-5}$ to $6x10^{-1}$ s^{-1} and increased to 55% at the high strain-rate of $1.8x10^{3}$ s^{-1}. This is different from the behaviour of coarse-grain copper, in which the fracture strain decreases slightly at higher strain-rates [43].

The general relation between material yield stress and strain-rate is given by:

$$\sigma \propto \dot{\varepsilon}^{m} \qquad \text{Eq. 5}$$

where m is the strain-rate coefficient. For nano-crystalline copper, m= 0.036 within the strain-rate range of $6x10^{-5}$ to $1.8x10^{3}$ s^{-1}. For coarse-grain copper, this coefficient was 0.011 in the same strain-rate range [43].

The nano-grain copper exhibits much sensitivity of its mechanical properties to the strain-rate because of lattice dislocation activities, grain boundary effects and high resistance to crack nucleation [43].

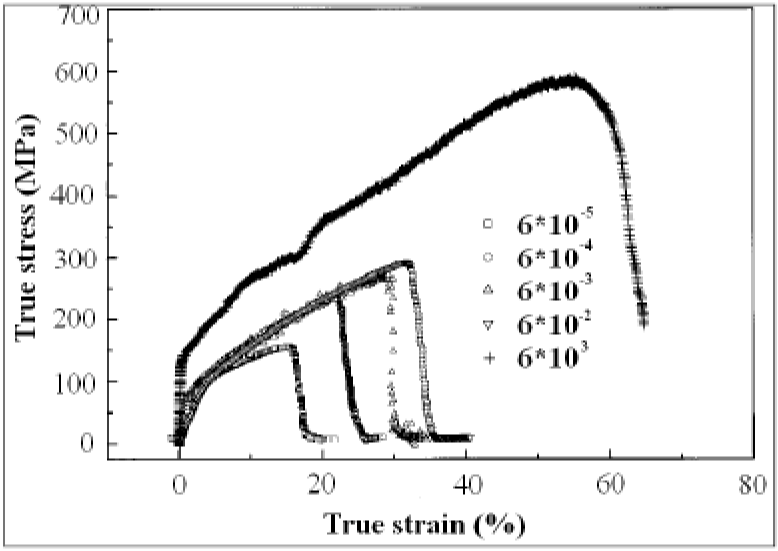

Figure 17: The stress-strain curve at different strain-rates [43].

3.2.14. **Liner Manufacturing**

Many methods can be used to manufacture the shaped-charge liner element. The manufacturing technique is determined according to the applications of the shaped-charge. For military warhead applications, high precision and accuracy liners are required, therefore high cost precision forging and flow turn techniques are normally applied. During high volume production, the low cost manufacturing is the predominant feature of liner production, and thus most liners are made by powder-metal technology and a low-precision forging technique [14]. A list of liner manufacturing techniques are mentioned below:

- flow turning (spinning or shear forming);
- high energy rate fabrication (HERF);
- deep drawing;
- cold forging;
- warm forging;
- hot forging;
- electroforming copper;
- infiltrating technology and
- press moulding or powder metallurgy technique.

Another recent technique observed is that of an ECAP (equal channel angular pressing) technique where the copper billet is pressed into a die vertically and the sample is bent ninety degrees within the die and removed in the horizontal direction. Lee et al. [38] has manufactured copper samples with grain-sizes as small as 3 μm with this technique.

3.3. Break-up-time Models

Since shaped-charge jet elements have a velocity gradient from its tip to its tail or slug, the shaped-charge jet breaks up into small elements at large travelling distances. In the break-up stage, the penetration efficiency of the shaped-charge starts to decrease steadily due to the decrease of the effective jet length prior to impact and the presence of the air gaps between the jet segments or particles. Therefore, the understanding of the jet-break-up phenomenon and the methods of delaying the onset of jet-break-up are the major interests of the shaped-charge designer. Many investigators studied this phenomenon, e.g. Cowan [45], Hirsch [46], Hennequin [47], Walters & Summers [48]. They used empirical formulae, hydro code simulations and one-dimensional analytical models to determine the jet-break-up time. This section focuses on some of the empirical formulae and analytical models used to measure and predict break-up-times of shaped-charge jets. This section also touches on the concept of super plasticity.

3.3.1. Empirical Formulae

The jet-break-up time t_{nB} presents the time at which the separation between any two adjacent jet particles n and n-1 is zero. This time may be obtained from the particulated jets in flight obtained from flash-X-ray radiography. The formula that is presented below uses the initiation time of the charge, i.e. trigger signal, as reference time. Hence, either the applicable values for the first FXR exposure time t_{FX1}, or the second, t_{FX2} can be used to calculate the experimental break-up-time. The formula used to calculate this value is:

$$t_{nB} = \frac{\left(P_{n-1}(t_{FX1}) - L_{n-1} - P_n(t_{FX1})\right)}{V_{n-1} - V_n} \qquad \text{Eq. 6}$$

where P_n is the position of particle "n", P_{n-1} is the position of previous particle, V_n is the velocity of particle "n" and V_{n-1} is the velocity of the velocity of the previous particle.

The data presented for the numerous designs are essentially the average break-up-times per velocity segment. In this present work, the average break-up-time per velocity segment was measured for three firings and the average of three firings are presented below.

The other parameters like the velocity difference between neighbouring jet particles, the cumulative jet particle length as function of velocity are self-explanatory and need no further discussion.

This break-up time model is further described graphically below. It is assumed that the jet originated at the virtual origin S_0 and T_0. Consider the jth particle with its tip at s_j^b and its end at s_j^e at the time of the second flash, T_2. This particle is followed by the jth gap that spans the interval $[s_{j-1}^b, s_j^e]$. The (j-1)th particle lies in the interval $[s_{j-1}^e, s_{j-1}^b]$.

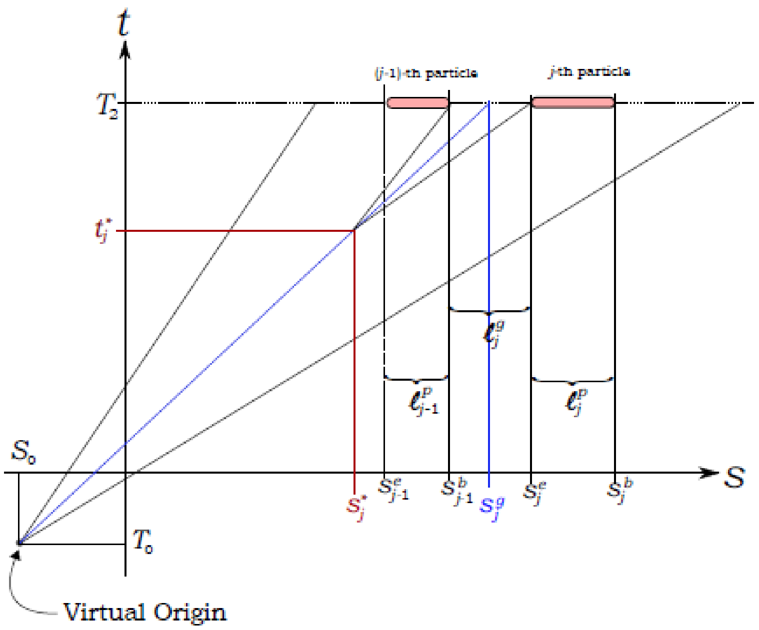

Figure 18: Description of the break-up time model. [49]

<u>Lengths</u>

The length of the jth particle is:

$$l_j^p = s_j^b - s_j^e.$$

The length of the jth gap is:

$$l_j^g = s_j^e - s_{j-1}^b.$$

<u>Midpoints and velocities</u>

The midpoint of the jth particle is at:

$$s_j^p = \frac{s_j^b - s_j^e}{2},$$

And it travels with velocity:

$$v_j^p = \frac{s_j^p - S_0}{T_2 - T_0}.$$

The midpoint of the jth gap is at:

$$s_j^g = \frac{s_j^e - s_{j-1}^b}{2},$$

and it travels with velocity

$$v_j^g = \frac{s_j^g - S_0}{T_2 - T_0}.$$

Gap Growth

The separation velocity between the j[th] and the (j-1)[th] particle (this is the velocity at which the gap grows) is given by:

$$\Delta v_j^g = v_j^p - v_{j-1}^p.$$

The gap is therefore in existence for a time $\frac{l_j^g}{\Delta v_j^g}$, and therefore the break-up-time for the gap is given by:

$$t_j^* = T_2 - \frac{l_j^g}{\Delta v_j^g}.$$

It is assumed that the gap originated on the line connecting its midpoint with the virtual origin, that is, its midpoint maintained a constant velocity. Therefore it must have originated at time t_j^*, at the position:

$$s_j^* = S_0 + \left(\frac{s_j^g - S_0}{T_2 - T_0}\right)\left(t_j^* - T_0\right).$$

A few empirical formulae are presented below:

Hirsch [50] further used the SCAN code and a set of experiments with charges of varying liner thicknesses to study the break-up-time, in which V_{PL} was found to be a function of liner thickness and charge diameter. $1/V_{PL}$ was named as specific break-up-time of the liner and was given by:

$$\frac{1}{V_{PL}} = 13.886 - 101.49\frac{T_L}{C_D} \qquad \text{Eq. 7}$$

where C_D is the charge diameter and T_L is the liner element thickness. Eq. 7 predicts reasonable jet-break-up times for certain shaped-charges.

$$V_{Pl} = \frac{v_{max} - v_{min}}{no.of\ particles} \qquad V_{Pl} \approx \Delta V \qquad \text{Eq. 8}$$

where ΔV is the average interparticle velocity difference measured from FX radiographs and V_{Pl} is the plastic velocity taking the tip and tail velocities of the jets. It should be noted that there are slight differences between the V_{Pl} and ΔV and some models are sensitive to those differences (this will be further highlighted in the analysis of experimental data from this study).

Chou and Carleone [51] deduced a formula predicting the break-up-time. The break-up times predicted from this formula had good agreement with the experimental measurements and has the following expression:

$$t_b = \frac{r_0}{C_p}\left[3.75 - 0.125\frac{r_0\eta_0}{C_p} + \frac{C_p}{r_0\eta_0}\right] \quad \text{Eq. 9}$$

where t_b is the break-up-time, r_0 is the initial jet radius, η_0 is the initial strain-rate of the jet, $C_P = \sqrt{\frac{Y}{\rho_0}}$, where ρ_0 is the initial jet density, Y is the jet yield strength (270 MPa for OFHC copper) [16]. Held [38] defined the average break-up-time of several shaped-charges using flash X-rays to calculate the fragments length. He defined the break-up-time by

$$t_b = \frac{\sum l}{V_{TIP} - V_{jcut}} \quad \text{Eq. 10}$$

where $\sum l$ is the summation of broken-up jet elements, V_{jo} and V_{jcut} are the velocities of the jet tip (V_{TIP}) and the cut-off element (i.e. the velocity of last penetrating element), respectively. Held's model was not used in this study since the cut-off velocities of each design was not measured.

Baker mentions in [52] that Walsh, J.M. (1984), theorized that the dependence of jet length would take a particular form based on his determination of a dimensionless parameter for the problem and numerical experiments in which initial perturbation strengths were varied [53]. Baker further discusses that Mostert (1995) [54], suggested that break-up-time is proportional to the ratio of the cube root of the shaped-charge jet cumulative mass (Δm) and the plastic velocity (Δv). $\left(\frac{\Delta m}{\Delta v}\right)^{\frac{1}{3}}$,Baker then assigns a proportionality constant linked to a jet plasticity/jet ductility parameter by:

$$t_b = Q\left(\frac{\Delta m}{\Delta v}\right)^{\frac{1}{3}} \quad \text{Eq. 11}$$

An expression from the MK model originally published in 1987 [39] and then in 2016 [55] is presented below:

$$t_b^{\frac{3}{2}} = \frac{\alpha r_0 l_0^{\frac{1}{2}}}{\gamma \Delta v^{\frac{1}{2}}} ln\left(\frac{N}{N_c}\right) \quad \text{Eq. 12}$$

where α, γ and N_c are constants and N is the initial dislocation density

The MK expression rewritten as Baker presents it below is an attempt at deciphering the physics of this constant. According to Mostert & König, this constant may be attributed to dislocation theory, and according to Baker, it is attributed to jet plasticity:

$$t_b = C\left(\frac{\acute{\Delta m}}{\Delta v}\right)^{\frac{1}{3}} \qquad \text{Eq. 13}$$

where C is a proportionality constant, Δm is the cumulative mass and Δv is the plastic velocity of interparticle velocity difference.

The investigation of break-up phenomena, in general, has been an undertaking. Mott [56] carried out the first analysis of fragmenting shell cases as early as 1947. The first model able to predict jet-break-up with reasonable accuracy was derived by Hirsch [46] [57] [58] who used an empirically calculated constant, V_{Pl}, the "plastic velocity" - to calculate the break-up-time, t_b.

$$t_b = \frac{D_o}{V_{Pl}} \qquad \text{Eq. 14}$$

where D_o is the initial diameter of jet element when the elongation starts and V_{PL} is the characteristic plastic velocity, manifesting as the velocity difference between successive fragments.

The term V_{Pl} is derived from some of the jets characteristics. For a given design of charge, the velocity distribution along the length of the jet is found to be approximately linear. The range of the velocity profile is given by the difference in velocity between the jets tip and its tail. The number of particles into which these jets break-up is approximately constant. The plastic velocity is derived by dividing the velocity range by the number of jet particles. [59]

Various attempts have been made at hydro code modelling of the break-up phenomena. Chou and Carleone [51], [60], [61] have carried out a comprehensive study using the Lagrangian based hydro code HEMP. Their results show that variations in the jets yield strength or velocity could cause plastic instabilities to occur. Miller [62] has used the PISCES code and included constitutive models for strain hardening and thermal softening. The occurrence of instabilities was in this case attributed to the point during the deformation process at which thermal softening becomes dominant over strain hardening. These hydro codes suffer similar criticisms as analytical models. Given some arbitrary initial perturbation, the profiles of necks are predicted to develop in a very similar manner to those seen in radiographs. There is, though, no description included in the model that takes into account the mechanism of deformation.

The break-up-time of shaped-charge jets have been studied extensively. However, none of the studies examined the effect of the initiation method on the break-up-time specifically. This study compares two types of jets – jets emanating from a point-initiated charge and jets from a peripherally-initiated charge. The study includes numerical simulations, analytical modelling and an experimental program.

The higher liner collapse velocity of the peripherally initiated charge creates a jet that stretches with a higher strain-rate and temperature. The higher strain-rate tends to reduce the break-up-time, according to an analysis performed by Chou and Flis [6] while the higher temperature tends to increase the break-up-time because the yield strength is reduced. Which one of these effects dominates the break-up process is still an open question. It was found that the change of the initiation mode from point to peripheral causes an increase in the jet-break-up time due to the reduction of the V_{pl} parameter that yields the best fit to the data. [63]

3.3.2. **Super-plasticity**

Alloys which are superplastic at low strain rates have been known for some time. They are often binary alloys that utilise a eutectoid or similar feature in their phase equilibrium diagram to develop a fine grain-size. This is necessary as super-plasticity relies on grain-boundary diffusion. A fine grain-size increases the area of grain boundary per unit volume material and therefore the amount of deformation possible per unit volume material. Detailed discussion on superplastic deformation is given by Ridley and Pilling [64].

One feature of super-plasticity, that the amount of deformation per unit volume of material is increased, may apply to high strain-rate deformation. This could be achieved in two ways: the dislocation density in a cell wall could increase - possibly causing a local failure if the material formed an adiabatic shear band - or the cell size could be reduced - thus increasing the overall dislocation density of the material without increasing it greatly in a localised area. Reduced dislocation cell size has been reported in explosively shocked material. There is no proof that very small dislocation cells form at the strain-rates involved in the jetting processes, however the theory appears plausible.

It has been postulated that the amount of deformation that occurs per unit volume affects the jetting performance. However, this theory is incomplete, as it does not explain why jetting performance should be related to grain-size. This observation suggests the grain boundaries may be an important source of dislocations required in the formation of either adiabatic shear bands or fine dislocation cell structures. Decreasing the grain-size would increase the area of grain boundary per unit volume of material. Therefore, if grain boundaries act as dislocation sources, the number of dislocations generated per unit volume of material would also increase.

Superplastic properties at high rate of strain are not realistic as the ultra-fine grain-sizes required are not currently attainable. Ultra-fine grain-size liners have been produced in the laboratory, but it is impossible to control in high volume production. However, it may be useful to consider the process of dynamic recrystallisation. This mechanism is in some respects analogous to that described by super-plasticity theory if it is considered in the context of the dislocation phenomena for cell formation.

Dislocation cells or sub grains are formed within individual grains and consist of dislocation-free regions separated by walls of high dislocation density. The size of these cells is found to be related to the size of voids formed during ductile deformation and fracture. As the dislocation cell size decreases the void size also decreases and the materials ductility increases – Vecchio et al. [3]. It would be anticipated that with decreasing stacking fault energy of a pure material, the size and extent of voids would decrease because stacking fault energy is a critical parameter in the formation of dislocation cells. The stacking fault energies for some pure metals are given in Table 7.

Table 7: Typical stacking fault energies for pure face center cubic metals, from Dieter [65].

Pure Metal	Stacking fault metal energy (mJ m^{-2})
Aluminium	200
Copper	80
Gold	50

It is known that superplastic materials form sub grains. Whether they are formed by dislocations moving by climb or glide is not known. However, sub grain formation causes small volumes of a crystal to become reoriented with respect to each other: a process analogous to the larger scale re-organisation of grains associated with superplastic flow. An attempt has been made to consider how sub grain formation could form the basis of a deformation mechanism capable of operating at high strain-rates. Dieter [66] and Holtzman and Cowan [67] found that shock loaded materials form sub grains and as the magnitude of the shock is increased the size of the sub grains is reduced. It was also found that the smaller sub grains have more tightly packed dislocation walls. The shock experienced by a shaped-charge liner is severe and from this, it may be anticipated that the sub grains would be very small and their walls have very high dislocation density. This may result in the formation of adiabatic shear bands. Adiabatic shear bands are regions of very intense shear that operate at a high temperature. The surrounding material remains virtually un-deformed and does not experience the increase in temperature.

The existence of these phenomena has not yet been verified in recovered slug or jet material. It is likely that thermal effects occurring after high speed deformation has taken place, such as heating of the material due to air resistance while in flight, would anneal out any such regions of high dislocation density and cause grain growth. It is interesting to note that Jamet [68] reported the grain-size of recovered slug material to be about 20 µm.

Chokshi and Meyers [41] have considered the possibilities for dynamic recrystallisation. This involves the development of a dislocation cell structure and the transformation of low-angle grain boundaries to high-angle grain boundaries during plastic deformation. The process is repeated continually during deformation, resulting in a steady-state recrystallized grain-size, d_s. They have used a relationship developed by Derby and Ashby [69] which relates the steady state grain-size to the strain-rate

$$d_s \propto \dot{\varepsilon}^{-0.5}. \qquad \text{Eq. 15}$$

Using an empirical route, they estimated the value of d_s at high strain-rates. This was compared to the theoretical value of grain-size required for diffusion-controlled super-plasticity at similar strain-rates and was found to be less than 10 nm. The values were of a similar magnitude and from this; they deduced that super-plasticity resulting from dynamic recrystallisation was a potential mechanism for very high strain-rate deformation. Although an interesting analysis, some of the numerical values used by Chokshi and Meyers are questionable. Of particular concern is the critical value for d_s at high strain-rates. The method they describe for finding this value uses a graphical extrapolation on a limited amount of data.

Carleone and Chou [70] studied the jet-break-up phenomenon using a one-dimensional model. They focused on the influences of jet material strength and its inertia force and showed that the ratio of jet flow stress to its material density controls the growth of the instability. They predicted that the break-up-time increases with the decrease of this ratio.

The one-dimensional model was extended by Chou and Carleone [60] in order to include the stress concentration at the jet necks. The solution of their equation showed that the critical wavelength was independent of the jet-stretching rate, where it had a value of “2.22” in terms of the jet diameter at the beginning of the jet instability. However, a two dimensional hydro code simulation by Carleone and Chou [60] predicted that the critical wavelength was a function of the jet-stretching rate. The correct number of jet segments was also determined from the two-dimensional solution.

Miller [71] also developed a one-dimensional model to study the jet necking problem. The model was based on the separation of variables and Fourier integral technique. Miller [71] assumed that a long and nearly cylindrical jet with a small neck at the centre of the jet has a linear velocity gradient. A perfectly plastic constitutive equation was used. Although the predicted results were in good agreement with experiments, the initial material conditions such as temperature and flow stress had to be assumed. The results obtained by the one-dimensional model in [71] using the perfectly plastic constitutive equation were similar to that obtained using Steinberg-Guinan constitutive equation as in [16].

Walsh [53] developed an analytical model to perform a detailed analysis of the effects of surface roughness, the non-uniform initial velocity gradients and the non-uniform yield strength on jet-break-up. The predicted results were similar to those of Chou and Carleone [60]. The model predicted that the break-up-time was only mildly dependent on the amplitude of the initial disturbance. Walsh [53] also concluded that the jet-break-up time could be delayed by reducing the shaped-charge fabrication tolerances or increasing the homogeneity of the shaped-charge elements.

In 1993, Backofen [72] used an analytical model to calculate the different parameters of the produced jet. These parameters include the virtual origin, the break-up-time and jet penetration capability into different target materials. It was found that the used analytical model gives reasonable results to the break-up-time estimated by using flash X-ray during the detonation of the shaped-charge.

3.4. Strain and Strain-Rate dependence on Shaped-charge performance

This section focuses on the analytical models used to describe and predict break-up-times of shaped-charge jets.

3.4.1. Analytical Model

An analytical model was developed for the break-up-time of the jet from a shaped-charge liner. The model is based on three assumptions. First, a kinematic expression for the break-up-time; second an expression related to plastic stability; and finally, a material-based constitutive equation relating the stress, strain and strain-rate, and temperature. In other words, the jet from a shaped-charge liner will particulate when it becomes plastically unstable, and the break-up-time will depend on the stress, strain and strain-rate, and temperature at failure or particulation. [16]

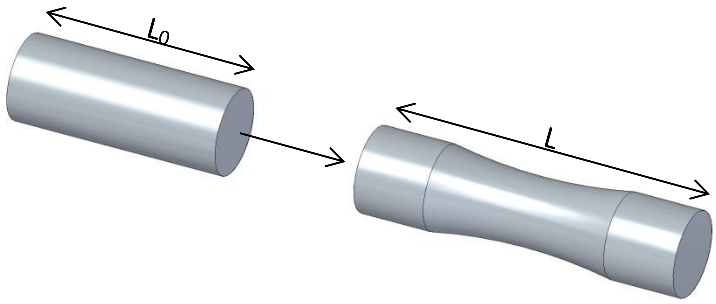

Figure 19: The kinematic expression for the jet break-up-time.

Figure 19 illustrates the kinematic expression for the jet-break-up time. An initial length of jet, L_0, eventually stretches to length, L, where it begins to neck at the break-up-time, τ, then

$$L = L_0 + \tau(v_t - v_r) \qquad \text{Eq. 16}$$

where v_t is the tip velocity of the jet and v_r is the rear or tail velocity of the jet. Dividing Eq. 16 by L_0 yields

$$\varepsilon = \frac{L - L_0}{L_0} = \frac{\Delta L}{L_0} = \frac{\tau(v_t - v_r)}{L_0} \qquad \text{Eq. 17}$$

$$\dot{\varepsilon} = \frac{d\varepsilon}{\mathrm{d}\tau} = \frac{d}{\mathrm{d}\tau}\left(\frac{\Delta L}{L_0}\right) = \frac{(v_t - v_r)}{L_0} \qquad \text{Eq. 18}$$

where ε is strain, τ is the time, $\dot{\varepsilon}$ is the strain-rate, v_t is the jet tip velocity and v_r is the velocity of the rear section of the jet. The plastic stability criterion requires that for stability, otherwise the jet necks and eventually breaks:

$$\frac{d\sigma}{d\varepsilon} \geq \sigma \quad \text{Eq. 19}$$

where σ is the liner metal dynamic yield stress.

Miller showed that a one-dimensional theory applied to a perfectly plastic stretching metal rod, or applied to a stretching metal rod governed by the Steinberg-Guinan-Cochran constitutive model, predicts the generation of a progression of new necks from an existing neck. Two-dimensional finite-difference calculations predict the same behaviour. [71]

A few empirical formulae are presented herein. Hirsch [58] suggested a phenomenological formula for the jet-break-up time. This formula calculates the break-up-time (t_b) as

$$t_{b=}\frac{d_{j0}}{V_{pl}} \quad \text{Eq. 14}$$

where d_{jo} is the initial diameter of jet element when the elongation starts and V_{pl} is the characteristic plastic velocity or the velocity difference between successive fragments.

Hirsch's formula for break-up-time based on Eq. 14 and the liner geometry is

$$t_{b=}\frac{1}{V_{pl}}\sqrt{8RT_L}sin\left(\frac{\beta}{2}\right) \quad \text{Eq. 20}$$

where T_L is the original liner thickness, β is the collapse angle and R is the radius of each element from the liner axis.

Hirsch attempted to express the plastic velocity as

$$V_{pl} = \sqrt{\frac{\sigma}{\rho}} \quad \text{Eq. 21}$$

where σ is the liner metal dynamic yield stress and ρ is the density of the liner material, from microscopic metallurgical conditions [74]. Hirsch employed the Mott fragmentation model [74] and provided a description of the break-up-time model as arising from shear bands according to:

$$V_{pl} = \sqrt{\frac{d\sigma_m}{\rho}} \quad \text{Eq. 22}$$

where $d\sigma_m$ represents the difference between the isothermal and adiabatic stress vs strain characteristics of the metal at the point where adiabatic stress becomes a maximum. Hirsch quotes strains of one to two at a strain-rate of 10^5 s^{-1} for OFHC copper. Hirsch further qualified the plastic velocity by suggesting a break-up mechanism, where holes caused by a pile up of vacancies are formed at the metal surface and gradually increase until breaking is caused by the formation of voids in the jet [74].

Hirsch also predicted the existence of a strain-rate threshold below which other mechanisms dominate the break-up process. Hirsch states that even perfectly symmetrical and homogeneous shaped-charge configurations have transverse velocity components in the jet [58]. This means that the break-up process starts during the liner collapse and the transverse velocity influences the jet-break-up. Hirsch relates the plastic velocity to the processes which affect the liner metallurgical state during the initial stages of jet-formation [74]. Hirsch shows how both the deformation energy heating the sliding shear bands during the localization process and the rate of the instability growing in the plastic flow during this process, combine to determine the plastic velocity parameter. This velocity is shown to be related to both the velocity due to the plastic deformation and the component of the maximum slide velocity allowable to form shear bands in the elongation direction. Hirsch thus attempts to include the influence of the metallurgical structure of the liner on the break-up-time [74]. Held advocates a calculation of the break-up distance instead of the break-up-time [75]. The various analytical models do not agree with each other or with the experimental data. In fact, the method of calculating jet-break-up time distribution from the experimentally obtained flash radiographs varies from institution to institution. Nevertheless, significant insight has been gained from the analytical break-up-time models, namely, the existence of a critical wavelength, the effect of jet strength and density, and the dependence on strain-rate. It is known experimentally that the jet microstructure, notably the grain-size (and probably the grain-size distribution, the grain orientation, the metal chemistry or purity, and the material texture) strongly affects the jet-break-up time.

Chokshi and Meyers point out that high strain-rate deformation leads to an increase in temperature, which, in conjunction with the large strains involved, leads to a very fine grain-size microstructure due to dynamic recrystallization. Subsequently, it appears that the fine grain-size leads to super plasticity at high strain-rates, which in turn leads to large tensile strains to failure [41].

These factors are not included in the analytical or theoretical break-up-time models and including them is not straightforward. In fact, the underlying mechanisms behind jet-break-up are not understood. If a known perturbation is applied to a stretching jet in a numerical simulation, the jet will neck at a critical wavelength and break. The exact nature and origin of this critical perturbation(s) is unknown, but may be due to irregularities in the liner material yield strength or other material or micromechanical properties, non-uniformities in the initial jet velocity gradient, jet surface roughness, or due to inherent perturbations in the fabrication of the shaped-charge. Example, material anisotropies, liner-wall thickness variations, the quality of the liner inner surface and exterior surface and inhomogeneity in the explosive fill. The exact nature or the fracture process (at a critical value of strain, pressure, stress, plastic work, or internal energy) is unknown. Furthermore, models that account explicitly for the nucleation and growth of voids, cracks, and shear bands have not yet matured to the extent that they can be readily incorporated into the hydro code models.

Factors which are known to affect jet-break-up time are given by Held [75]and Walters and Zukas [16]. In general, the jet-break-up time can be increased by decreasing the jet-stretching rate, increasing the jet radius, increasing the jet density, decreasing the jet strength, and increasing the ductility of the jet under the dynamic conditions described above. Thus, the liner design, liner geometry, liner material, and method of fabrication or the shaped-charge liner are all pertinent factors to be considered in assessing the jet-break-up time distribution.

Walters and Summers used flash X-ray experimental results of various liner designs to determine the strainto failure of jet segments [48]. It is stated that copper is used as the liner material. The results were based on the experimental jet length L and calculated initial jet length L0. They stated that the average final true strain of the jet has a constant value of 2.3, calculated as,

$$\varepsilon_F = ln\left(\frac{L}{L_0}\right) \approx 2.3 \qquad \text{Eq. 23}$$

This amount of elongation corresponds to a necking ratio of 0.32, which is the ratio of the jet radius at the failure to the initial radius. During their studies, the cumulative break-up-time is measured as 147.8 µs and calculated as 153.0 µs, using final true-strain value of 2.3 as a failure criterion in break-up calculations [48].

Various factors influencing shaped-charge performance were discussed and were considered during the manufacturing and experimental phases. The analytical and empirical models were used during the data analysis phase discussed later.

4. SIMULATIONS

4.1. Introduction

Besides the analytical formulae given in the previous sections, highly nonlinear and time-dependent events, like shaped-charge jet-formation and penetration, can also be simulated using transient, dynamic wave propagation codes, called hydro codes [76]. The name “hydro code” refers to the codes that are generally used for the problems involving large pressures so that material strength can be neglected. Recent and most commonly used commercial hydro codes are AUTODYN, LS-DYNA and DYTRAN. AUTODYN is used for the numerical simulations in this study. It utilizes the differential equations governing unsteady material dynamic motion expressed as the conservation of mass, momentum and energy [17].

AUTODYN has different solver types corresponding to different numerical solution methods. The solver types are Lagrange, Euler, Arbitrary Lagrange Euler and Smoothed Particle Hydrodynamics. In the current study, the Euler solver is used for jet-formation problems. The Euler solver provides accurate jet and velocity profiles as well as the mass distributions.

In the following sections numerical solver types are discussed briefly, based on the AUTODYN Theory Manual [17].

AUTODYN hydro code is based on the solving of the mass, momentum and energy conservation equations for given boundary values/conditions, where the materials can be defined by its equation of state and its strength model [77]. This hydro code is capable of performing the shaped-charge jetting analysis, jet-formation and penetration.

In the Euler solver, a control volume method is used to solve the differential equations that govern conservation of mass, momentum and energy. The integral and discrete forms of these equations are expressed in conservation form to obtain accurate and stable solutions. A two-step numerical procedure is used to solve the finite-difference equations. In the first step, which is the called the Lagrangian step, the Lagrangian form of the equations are updated or advanced one time interval (time step). In the second step, the Euler step, updated variables are mapped onto the Eulerian mesh. Multiple materials are handled through a volume fraction technique or an interface capturing technique. All variables are stored in a cell-centered fashion.

Euler solver is suitable for handling problems including large deformations and fluid flow. However, it is difficult to track free surfaces, material interfaces and history-dependent material behaviour. Euler solver is computationally less efficient in a way that the mesh of the problem needs to be extended beyond the initial physical material limits since material is allowed to flow out of these initial limits. The inefficiency of the Euler solver is overlooked within the shaped-charge formation problem since it may be solved in a 2D axisymmetric model, which drastically reduces computational time.

In this thesis work, the Euler solver is used to simulate jet-formation problems. Further extension of the results produced from jet-formation in Euler may be further analysed by analytical expressions, as it is done in analytical break-up calculations.

The jet-formation is simulated using the Euler method based on continuum mechanics to obtain the jet profiles at different time stages. In this scheme, the explosive, the charge casing and the liner materials are filled into the global Euler multi-material part [77]. The Euler solver is suitable in the early jet-formation stages, where large distortions of the explosive charge cause extremely high strain-rates of the order of 10^7 s^{-1}. These distortions will cause the solver to stop working if a Lagrange solver is selected for the jet formation. The Euler multi-material processor describes the detonation wave propagation inside the charge and shows the jet profile as it elongates with time. The jet is allowed to move on the Euler grids up to the moment when it just impacts the target. At this moment, the formed jet may be remapped as a Lagrangian mass having non-uniform velocity distribution.

4.2. **Shaped-charge Collapse Kinetics**

Several well-established shaped-charge collapse models are available. The primary models were developed by Birkhoff et al. [78], Visco-Plastic Jet-formation and Pugh, Eichelberger and Rostoker (PER) [79]. Birkhoff et al. was chosen over PER because this study focused on early collapse where the simplification of assuming constant collapse velocity is appropriate, whereas the PER method accounts for variable collapse velocities according to [16].

The Birkhoff, MacDougall, Pugh and Taylor model describes the geometry and velocity of a collapsing shaped-charge liner into the central axis and resulting jet. It is the first published fundamental theory of jet-formation and recognizes that as the detonation pressure is much greater than the strength of the liner, the liner is treated as an inviscid fluid [6]. The variables are velocities, angles and locations. The conditions are assumed constant and symmetric about the charge axis. The modelled equations are presented in Eq. 24 and Eq. 25 and geometry are described in Figure 20 and Figure 21, respectively.

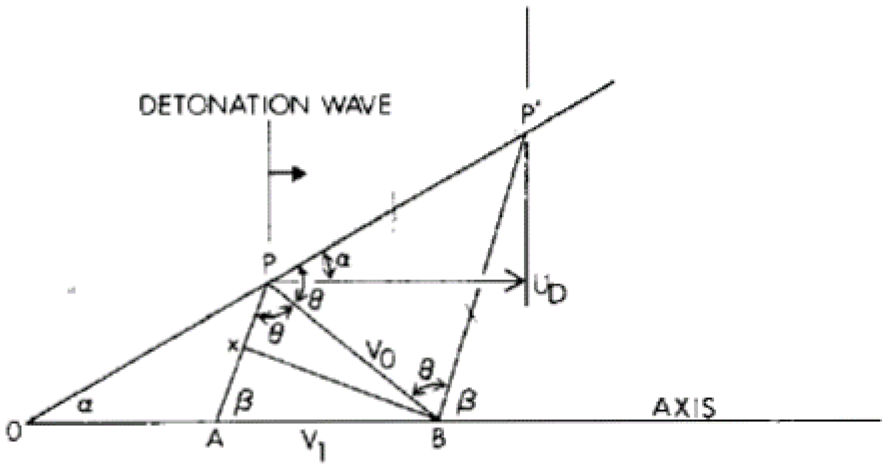

Figure 20: Geometry of the shaped-charge collapse process, the x-axis representing the symmetry plane for a cylindrical charge, the y-axis representing the charge caliber and positions A and B representing positions within the liner during the collapse process [16].

The pertinent information illustrated in Figure 20 are liner-collapse velocity (V_0), velocity along the liner axis (V_1), the original half angle of the liner (α), the liner-collapse angle (β) and the locations associated with the vector equations A to B and P to B. Interrelated with this is liner flow velocity (V_2) as shown in Figure 21. The locations of A, B (and P) along with assumptions of constant, symmetric conditions are consistent with Figure 20.

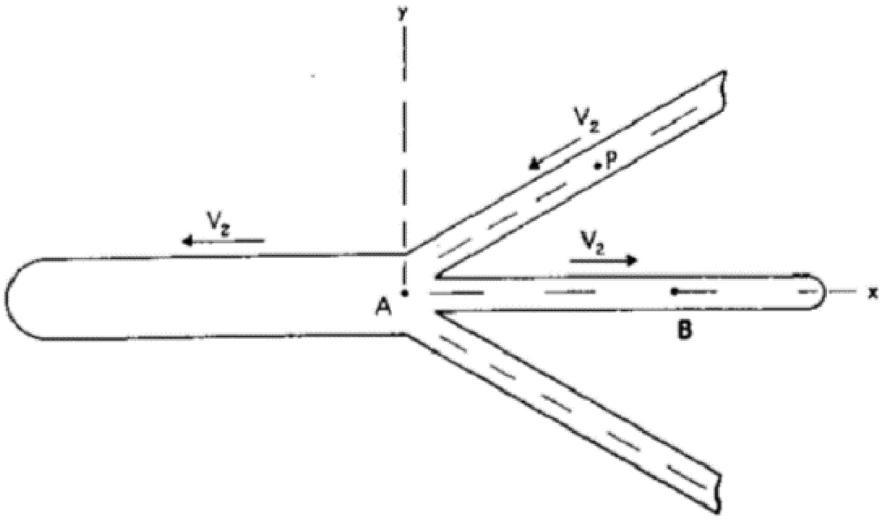

Figure 21: Jet and slug formation associated with Liner Flow Velocity (V_2) [16].

The relevant equations associated with Birkhoff et al. define V_0 and V_2 as functions of V_1, and liner geometry. Liner velocity (V_0), vector PB (Figure 20), is a component of the velocity along the X axis (V_1) as given by Eq. 24 [16].

$$V_0 = \frac{V_1 sin\beta}{cos[(\beta - \alpha)/2]}$$ Eq. 24

V_1 is relatable to the jet velocity (V_j) at any location along material moving on the axis. In considering V_1 synonymous with V_j, it is noted that some texts set $V_j = V_1 + V_2$ [16] , while others set V_1 to V_j [80]. Regardless, vector AB is identical with V_1 in the chosen model as V_1 = 0. V_2 is the velocity of the material in the liner wall as it flows into the collapse point and is a function of liner angle (α) liner collapse angle (β) and V_0, see Eq. 25 [16].

$$V_2 = V_0 \left\{ \frac{cos[(\beta - \alpha)/2]}{tan\beta} + sin\left(\frac{\beta - \alpha}{2}\right) \right\}$$ Eq. 25

4.3. Hydro code Simulations

Using the Lagrangian code HEMP, Chou and Carleone [81], Karpp and Simon [82] determined the jet-break-up time by following the jet profile changes with time. Karpp and Simon [82] demonstrated that a jet with a uniform initial radius under continuous stretching eventually developed necking, which depends on the wavelength of the initial surface perturbation. They also estimated the strength of copper under dynamic conditions, which was found to be 0.1 GPa or 100 MPa. This is needed for the prediction of the jet-break-up time. Chou and Carleone [81] used the same code to predict the effects of the yield strength, jet density, the initial disturbance wavelength and its amplitude on jet-break-up time. They showed that the perturbation in jet strength or velocity causes plastic instability. The critical wavelength seems independent of the perturbed physical quantity that initiates the instability. Figure 22 shows a comparison of their hydro code simulation with the flash radiograph of a typical jet.

In 1981, Miller [62] used the two-dimensional hydro code named PISCES in order to predict the break-up-time of the copper jet. Miller used the Steinberg-Guinan constitutive equation in the hydro code in order to account for the strain hardening and thermal softening by considering the effect of temperature, pressure and large plastic strain. Miller [62] used an unconfined Ballistics Research laboratory (BRL)-105 mm diameter 42° conical shaped-charge to compare the experimental results with the numerical results. It was found that the predicted break-up-time for the subsequent elements is longer than that calculated by the hydro code. Later in 1982, Miller [71] concluded that the difference between the hydro code simulation and the experimental test was attributed to the random necking of the jet due to imperfect formation of the jet.

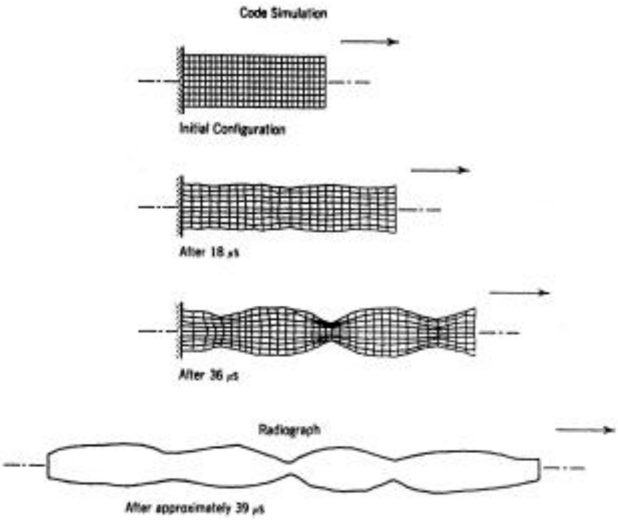

Figure 22: Comparison between hydro code simulation of jet necking due to instability and flash radiograph of a jet at approximately the same time [81].

According to Walter [16], Osborn used the two-dimensional code named TOODY to study the jet-break-up problem while Pfeiffer simulated the jet-break-up using the STRESS-2 to study the same phenomena.

Petit J. et al. [83] designed a combined numerical/analytical technique to describe shaped-charge jet-break-up. The method overcomes drawbacks from exclusively numerical or analytical approaches, such as mesh sensitivity or oversimplified description. It yields predictions for break-up-time, total number, and cumulative length of fragments in good agreement with the experimental data. Simulations were performed with the OURANOS code. An explicit Eulerian finite-difference scheme was employed for numerical simulations. Predictions display pronounced mesh sensitivity. Coarse grids lead to overestimates in the break-up-time at the jet tip, and conversely to underestimates at the tail. Fine grids reduce overestimates, but these are evenly spread out along the jet. Finding a mesh leading to some acceptable overall agreement with experimental data on all three aspects investigated: number of fragments, cumulative length of fragments, and break-up-time is viewed as impossible with Euler meshes. Indeed, the origin of fragmentation is found in mesh imperfections taking effect during the liner collapse. Results therefore lack sound physical justification [83]. The author has performed a grid-size analysis on the jet-formation stage and shown differences in tip velocity. Similar observations as seen by Petit with the OURANOS code are seen with AUTODYN as well. The jet-formation was simulated using the Euler method based on continuum mechanics to obtain the jet profiles at different time stages. In this scheme, the explosive and the liner materials are filled into the global Euler multi-material part [77]. This processor is suitable in the early jet-formation stages, where large distortions will be caused by extremely high strain-rate in the order of 10^7 s^{-1} [25] [31]. These distortions will cause the solver to stop working if a Lagrange solver is selected for the jet formation. The Euler multi-material processor describes the detonation wave propagation inside the charge and shows the jet profile as it elongates with time. If the jet is allowed to move on the Euler grids up to the moment when it just impacts the target, the penetration phase of the simulation may be set-up differently. At this moment, the formed jet may be remapped as a Lagrangian mass having non-uniform velocity distribution if penetration calculations are necessary.

4.4. **Studied Explosive Charge Parameters**

This section focuses on the variables used in the simulations for consideration of varying the strain and strain-rates. The variables were the high explosive type, liner angle and thickness, liner material, charge confinement and the initiation system. They are further elaborated below:

high explosive type: two different explosives were used to study the effect of detonation characteristics of explosive on the formed jet characteristics and its effects on the shaped-charge jet properties. These explosives were Comp A3 and HNS1.4. The Jones Wilkins Lee (JWL) equation of state parameters for these explosives were available in the AUTODYN built-in library;

- liner angle: cone apex angles were 60° and 120° with the same explosive charge. The liner thickness was kept constant for simplicity of manufacture. Hence, the jet characteristics are presented as a dependence on the explosive type, liner angle and initiation system. Furthermore, numerical simulations were conducted for constant liner thickness of 1.7 mm with both of these liner angles;
- fixed liner material and thickness: the selected materials for the liner were OFHC solid copper;
- degree of confinement: No confinement was used for the charges. This eliminated possible adverse mechanical influences on the jet parameters originating from a casing and simplified the experimental set-up and execution; and
- initiation system: the behaviour of the detonation wave inside the explosive charge was studied by selecting two different initiation methods, i.e. a central point on the charge axis and a point on the side of charge (peripheral initiation). This could be done with built-in selections from the AUTODYN code.

4.5. AUTODYN Jet-Formation Model Description

The jet-formation model was set-up in order to obtain the jet profile, the contours of different jet parameters and the jet-break-up phenomena, which were needed to analyse the jet properties. The model uses Euler solver with outflow boundary condition, which allows the detonation gaseous products to expand smoothly towards the Euler (flow-out) boundary and prevents pressure build up in the grid that will influence the jet-formation process, as shown in Figure 23. Some of the detonation gaseous products still flow around the base of the liner onto the jet axis. This is tolerated within the simulation up to the stage when the jet is completely formed. Energy is removed from the grid when the gasses flow through the boundary, but this is similar to what will happen in real life when the gasses are expanded far enough away from the liner not to influence its acceleration. The explosive material is removed from the simulation once the jet is completely formed to allow the jet to stretch up to the length provided. The simulations presented in this section were produced by the author within this research project.

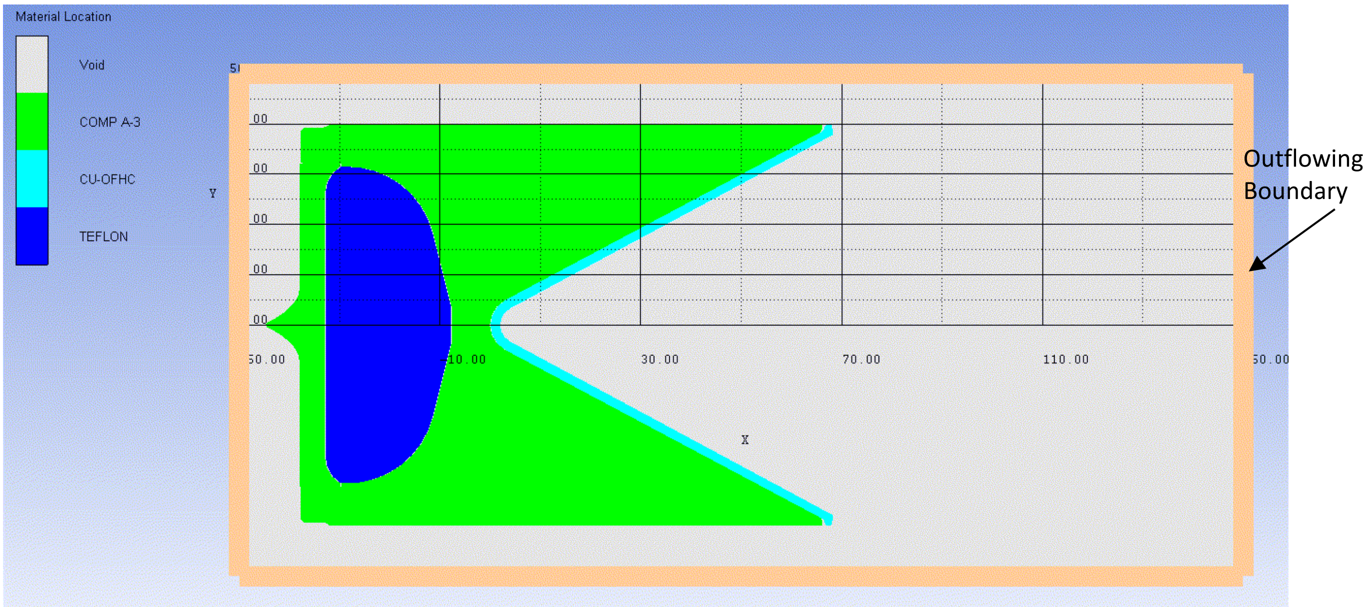

Figure 23: Simulation layout including the Euler grid and outflowing boundary.

With detonation pressures in excess of 20 GPa, it is obvious that large deformation occurs inside the liner. The Euler (fixed grid) mesh allows for this distortion of jet formation and a continuous jet of highly distorted material is formed. The code output from the Euler solver creates jet and slug profiles according to the shaped-charge design. This jet may be remapped to a new Lagrange model at any stage, which is suitable for simulating the jet penetration into various targets. The physical parameters of the jet, such as its kinetic energy will be almost unchanged during the remapping and exporting process.

4.6. Material Modelling Description

4.6.1. Description of the Explosives used in AUTODYN

The explosive required for shaped-charges must have high velocity of detonation and high density to provide a high detonation pressure, which results in a high jet tip velocity and consequently a larger depth of penetration [16]. The explosive materials used for filling shaped-charges were CompA3 and HNS1.4 within the simulations. The equation of state for the used explosives is "Jones-Wilkins-Lee" (JWL) equation, which is a simple pressure, volume, energy (PVE) relation that has been developed to describe the adiabatic expansion of the detonation products [84]:

$$p = A\left(1 - \frac{\omega}{r_1 v}\right)e^{-r_1 v} + B\left(1 - \frac{\omega}{r_2 v}\right)e^{-r_2 v} + \frac{\omega E}{v} \qquad \text{Eq. 26}$$

where p is the pressure, v is the relative volume ($1/\rho$), E is the energy, A, B, r_1, r_2, and ω are constants [85]. The values of the experimental constants for some explosives have been determined from sideways plate-push dynamic test experiments [86]. These values were determined experimentally by the cylinder expansion test [17] and may be found in the AUTODYN materials library. For the listed explosives, the values of the above-mentioned constants are available in the material library of AUTODYN. The input data to AUTODYN hydro code for the explosive materials are listed in Table 8.

Table 8: Input data to AUTODYN hydro code for the explosive materials.

Parameter	Explosive Type	
	Comp-A3	HNS1.4
Density (g/cm^3)	1.650	1.400
Parameter A (kPa)	6.113×10^8	3.665×10^8
Parameter B (kPa)	1.065×10^7	6.750×10^6
Parameter r_1	4.4	4.8
Parameter r_2	1.2	1.4
Parameter ω	0.32	0.32
C-J detonation velocity (m/s)	8300	6340
C-J Energy/unit volume (kJ/m^3)	8.900×10^6	6.000×10^6
C-J pressure (kPa)	3.000×10^7	1.450×10^7

The material that has been used for the liner element was solid copper-OFHC. The equations of state (EOS) of this material was shock and linear [17].

It has been shown experimentally that, for most solids and liquids that do not undergo a phase change, the shock Hugonoit values of shock velocity (U) and material velocity behind the shock (U_p) can be adequately fitted to a straight line

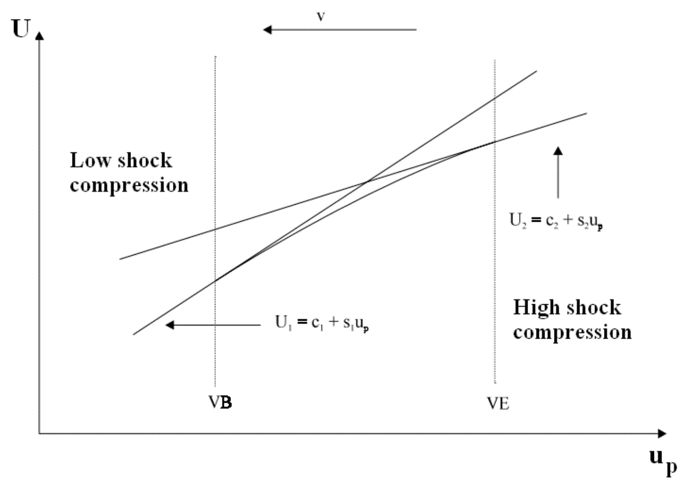

Figure 24: The shock velocity against particle velocity for the EOS of the liner material [17].

4.6.2. **Mie-Gruneisen EOS:**

The Mie-Gruneisen EOS is based on the shock Hugoniot representation of the thermodynamic parameters of the material and is expressed as:

$$\mathrm{p} = p_H + \Gamma_\rho (e - e_H) \qquad \text{Eq. 27}$$

where Γ_σ is the Gruneisen Gamma coefficient and equal to $\mathrm{B}_0/(1+u)$ where B_0 is a constant, $\Gamma_\rho = \Gamma_0 \rho_0 = constant$ is assumed; and ρ is the density. The terms p_H and e_H are the Hugoniot pressure and energy, respectively, given by

$$p_H = \frac{\rho_0 C_0^2 \mu (1+\mu)}{[1-(S-1)\mu]^2} \qquad \text{Eq. 28}$$

and

$$e_H = \frac{1}{2}\frac{p_H}{\rho_0}\left(\frac{\mu}{1+\mu}\right) \qquad \text{Eq. 29}$$

where

$$\mu = \left(\frac{\rho}{\rho_0}\right) - 1 \qquad \text{Eq. 30}$$

is the compressibility, C_o is the sound speed in the material and s is a constant giving the slope of shock velocity-particle velocity relationship. The mechanical properties of these materials are given in Table 9, where the constants in the previous equations were taken from the material library.

Table 9: The mechanical properties of copper liner materials in the simulations.

Name	OFHC - Steinberg Guinan
Reference Density	8.93
Equation of State	Shock
Gruneisen coefficient	2.02
C_o (m/s)	3940
S	1.489
Reference Temperature (K)	300

4.7. Modelling of Strength Effects

4.7.1. Johnson-Cook Model

This constitutive model aims to model the strength behaviour of materials subjected to large strains, high strain-rates and high temperatures. Such behaviour might arise in problems of intense impulsive loading due to high velocity impact and explosive detonation. The model defines the yield stress Y as

$$Y = [A + B\varepsilon_P^n][1 + Clog\varepsilon_P^*][1 - T_H^m] \qquad \text{Eq. 31}$$

where

ε_P^n= effective plastic strain;

ε_P^*= normalized effective plastic strain-rate;

T_H^m= homologous temperature = $\frac{T - T_{Room}}{T_{melt} - T_{Room}}$; and

The five material constants are A, B, C, n and m.

The expression in the first set of brackets gives the stress as a function of strain when $\varepsilon_P^* = 1sec^{-1}$ and $T_H = 0$ (i.e. for laboratoryoratory experiments at room temperature). The constant A is the basic yield stress at low strains while B and n represent the effect of strain hardening. The expressions in the second and third sets of brackets represent the effects of strain-rate and temperature, respectively. In particular, the latter relationship models the thermal softening so that the yield stress drops to zero at the melting temperature T_{melt}. The constants in these expressions were obtained by Johnson and Cook empirically by means of dynamic Hopkinson bar tensile tests over a range of temperatures and other tests and checked by calculations of Taylor tests where metal cylinders impact rigid metal targets which provided strain-rates in excess of 10^5 sec^{-1} and strains in excess of 2.0.

4.7.2. Zerilli-Armstrong Model

While the Johnson-Cook model predicts the behaviour of most materials tested in the Taylor tests well, it is acknowledged that the results for OFHC (oxygen-free high conductivity) copper does not agree well [17]. In an approach seeking to improve on Johnson-Cook, Zerilli and Armstrong proposed a more sophisticated constitutive relation obtained through the use of dislocation dynamics[17]. The effects of strain hardening, strain-rate hardening and thermal softening (based on thermal activation analysis) have been incorporated into the formulation. The effect of grain-size has also been included. The relation is a relatively simple expression and should be applicable to a wide range of FCC (face-centered cubic) materials. A relation for iron has also been developed and is applicable to other bcc (body-centered cubic) materials. An important point made by Zerilli and Armstrong is that each material structure type (FCC, bcc, hcp) will have its own constitutive behaviour, dependent on the dislocation characteristics for that particular structure. For example, a stronger dependence of the plastic yield stress on temperature and strain-rate is known to result for bcc metals as compared with FCC metals. Their formulation attempts to model these differences and therefore has much to commend it if experiments using different metals of these types are being modelled.

The equations for the yield stress are [17]:

(for FCC metals)

$$Y = Y_0 + C_2 \varepsilon e[-C_3 T + C_4 T log \dot{\varepsilon}] \qquad \text{Eq. 32}$$

where

ε = effective plastic strain

$\dot{\varepsilon}$ = normalized effective plastic strain-rate

T = temperature (K)

and Y_0, C_2, C_3, C_4 are constants.

4.7.3. **The Steinberg-Guinan Model**

In this formulation, the authors have assumed that while yield stress initially increases with strain-rate, experimental data on shock-induced free surface velocity versus time records indicate that at high strain-rates (greater than 10^5 sec^{-1}) strain-rate effects become insignificant compared to other effects and that the yield stress reaches a maximum value which is subsequently strain-rate independent. They have also postulated that the shear modulus increases with increasing pressure and decreases with increasing temperature and in doing this they have attempted to include modelling of the Bauschinger effect into their calculations. The Bauschinger effect is that elastic-plastic materials behave differently upon stress unloading and reverse loading than when they are stress loaded [87].

They have therefore produced expressions for the shear modulus and yield strength as functions of effective plastic strain, pressure and internal energy (temperature) and constants for 14 metals. They have demonstrated that, using this model, their computer calculations have successfully reproduced measured stress and free surface velocity versus time data for a number of shock wave experiments.

The constitutive relations for shear modulus G and yield stress Y for high strain-rates are[17]:

$$G = G_0\left(1 + \left(\frac{G_p'}{G_0}\right)\frac{p}{\eta^{1/3}} + \left(\frac{G_T'}{G_0}\right)(T - 300)\right) \quad \text{Eq. 33}$$

$$Y = Y_0\left(1 + \left(\frac{Y_p'}{Y_0}\right)\frac{p}{\eta^{1/3}} + \left(\frac{G_T'}{G_0}\right)(T - 300)\right)(1 + \beta\varepsilon)^n \quad \text{Eq. 34}$$

subject to $Y_0(1 + \beta\varepsilon)^n \leq Y_{max}$, β - constant

where

ε = effective plastic strain

T = temperature (K)

η =compression = v_0/v (volume or density ratio with the starting material volume or density)

and the primed parameters with the subscripts p and T are derivatives of that parameter with respect to pressure and temperature at the reference state (T = 300 K, p = 0, ε = 0). The subscript zero also refers to values of G and Y at the reference state.

The respective material model parameters used for the simulations in this work presented in Figure 27 are shown in Table 10, Table 11 and Table 12, respectively.

Table 10: Material properties for OFHC Copper – Steinberg Guinan.

Name	OFHC Copper
Reference Density	8.93
Equation of State	Shock
Gruneisen coefficient	2.02
C_o (m/s)	3940
s	1.489
Reference Temperature (K)	300
Specific Heat (J/kgK)	383
Thermal Conductivity	0
Strength	Steinberg Guinan
Shear Modulus (kPa)	4.77×10^7
Yield Stress (kPa)	1.20×10^5
Maximum Yield Stress	6.40×10^5
Hardening Constant	36
Hardening Exponent	0.45
Derivative dG/dP	1.35
Derivative dG/dT (kPa/K)	-1.798×10^4
Derivative dY/dP	0.003396
Melting Temperature (K)	1790

Table 11: Material properties for OFHC Copper– Zerilli Armstrong.

Material	OFHC Copper– Zerilli Armstrong
Equation of State	Linear
Reference Temperature (K)	300
Specific Heat (J/kgK)	383
Thermal Conductivity (J/mKs)	0
Strength	Zerilli Armstrong
Shear Modulus (kPa)	4.60×10^{7}
Yield Stress (kPa)	6.5×10^{4}
Hardening Constant #1 (kPa)	0
Hardening Constant #2 (kPa)	8.9×10^{5}
Hardening Constant #3	0.0028
Hardening Constant #4	1.15×10^{4}
Hardening Constant #5 (kPa)	0
Hardening Constant #6	0
Ref. Strain-rate (/s)	1

Table 12 Material properties for OFHC Copper– Johnson Cook.

Material	OFHC Copper– Johnson Cook
Equation of State	Linear
Bulk Modulus (kPa)	1.2910^8
Reference Temperature (K)	300
Specific Heat (J/kgK)	383
Thermal Conductivity (J/mKs)	0
Strength	Johnson Cook
Shear Modulus (kPa)	4.60×10^7
Yield Stress (kPa)	9.00×10^4
Hardening Constant (kPa)	2.92×10^5
Hardening Exponent	0.31
Strain-rate Constant	0.025
Thermal Softening Constant	1.090
Melting Temperature (K)	1356
Ref. Strain-rate (/s)	1

4.8. **Explosive Initiation and Wave Propagation**

The detonation wave is assumed to travel at the prescribed detonation velocity U_D and its path from the predefined initiation point can be determined. The detonation wave propagates in the spherical direction to engulf the entire un-burnt explosive cells in the mesh. The use of JWL constitutive model assumes instantaneous energy release when the detonation wave reaches a particular cell and an immediate transition to the CJ state (detonation pressure, density and temperature) is achieved. At this state, the full reaction of the explosive is completed and the full energy of the explosive is liberated, after which the detonation gaseous products will start to expand.

4.9. **Description of the Liner Materials**

The material that have been used for liner element was OFHC-copper. The equations of state (EOS) of this materials was the Shock-EOS, while the strength model selected was the Steinberg-Guinan material Model [17]. The strength model selection was made after computation results with various models were compared with experimental results (see section 4.12.1)

4.10. Mesh Sensitivity for the Jet-formation Model

It is well known that the shape and the density of the mesh affect the simulation results. Generally, computations with fine meshes produce a more accurate solution; but it is more time-consuming than that needed for coarse meshing computations. The mesh sensitivity study for the jet analysis was performed on an apex angle of 60° and copper liner. The Euler grids containing the explosive charge had four uniform square cells with different sizes of 0.1, 0.2, and 0.4 mm, respectively. The shaped-charge models with different mesh sizes were allowed to run until the liner completely collapsed for the entire liner elements. A square mesh size of 0.1 mm was selected for all simulations.

4.11. Simulation of Experimental Designs

In the following, the predicted parameters associated with the different simulation studies herein are listed.

Output of jet-formation model (Euler)

The histories of the following parameters from the jet-formation model are predicted:

- jet profile at different times;
- mass distribution; and
- kinetic energy distribution.

4.12. **Concept Designs**

Six charge designs were defined for producing jets of various magnitudes of strain and strain-rate. This comprised of two liner designs, two initiation modes and two explosive types. All six concepts were simulated in AUTODYN. The six concept designs are presented in Figure 25 below.

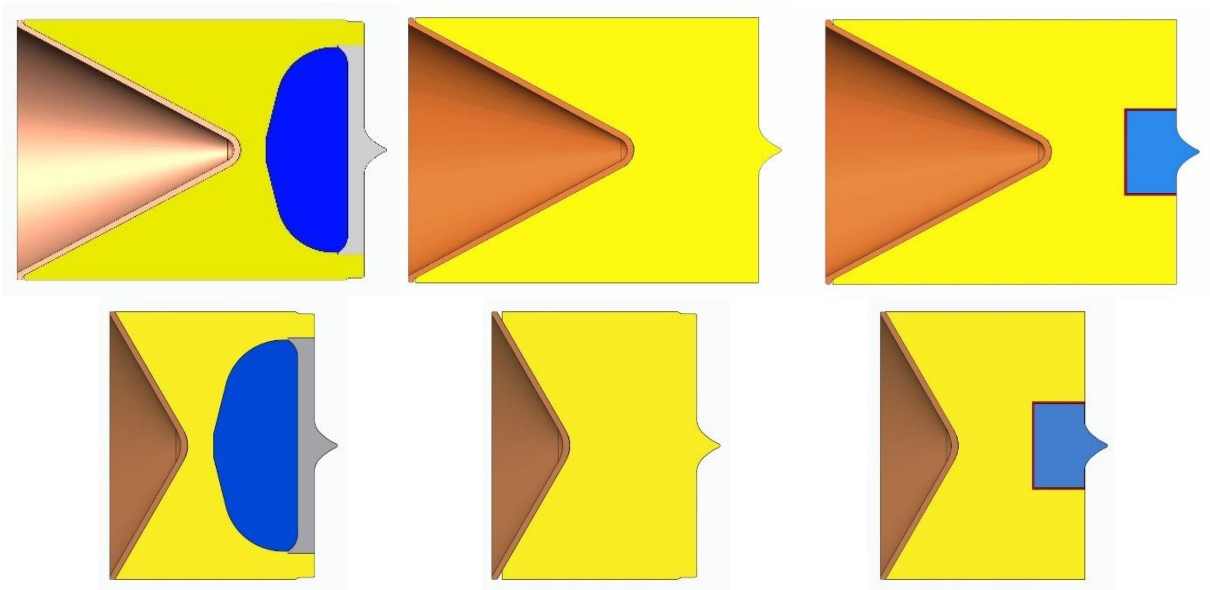

Figure 25: Six concept designs of the shaped charge warheads that were manufactured.

4.12.1. **Preliminary Analysis**

The initial simulations and calibration to experiments were done with the high strain-rate design (Design 1), as shown in Figure 26, which is explosive formulation, Comp-A3, including peripheral initiation with a waveshaper. Various copper models exist in the AUTODYN library. The simulations were conducted with three copper strength models, respectively. This means the simulation was repeated for the exact same model and replacing the liner material with Copper: Steinberg Guinan, Zerilli Armstrong & Johnson Cook strength models of which the material models may be found in the AUTODYN materials library [17]. The velocity contours are shown with a highlight of the tip velocity in Figure 27. Simulations with peripheral initiation were executed excluding the relay charge allowing peripheral initiation of the main charge as shown in Figure 35. The copper material model which best matched the tip velocity as observed in experimental data was that of Steinberg Guinan as shown in Figure 27. These initial simulations were computed with a grid-size of 0.2 mm square grid-sizes. Later simulations with grid-sizes of 0.1 mm will show a closer correlation in terms of tip velocity for all six-concept designs. Further description on the grid-size evaluation is shown in 4.12.2.

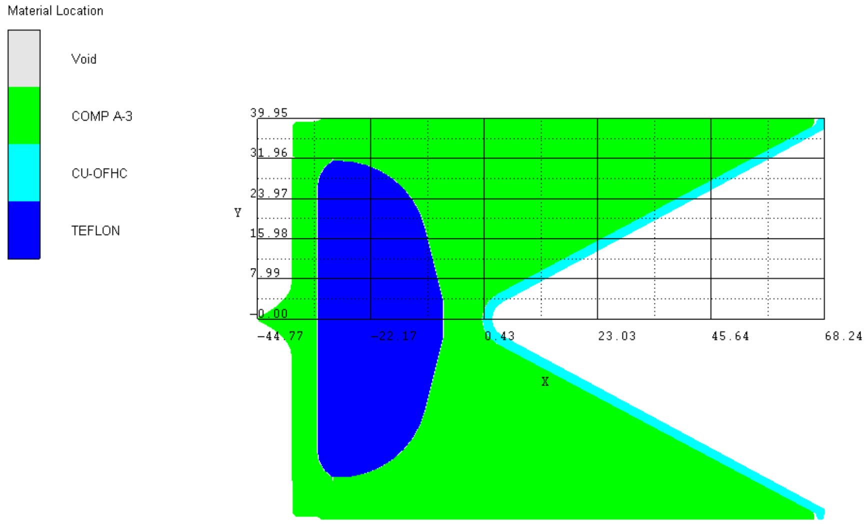

Figure 26: Material model for design 1.

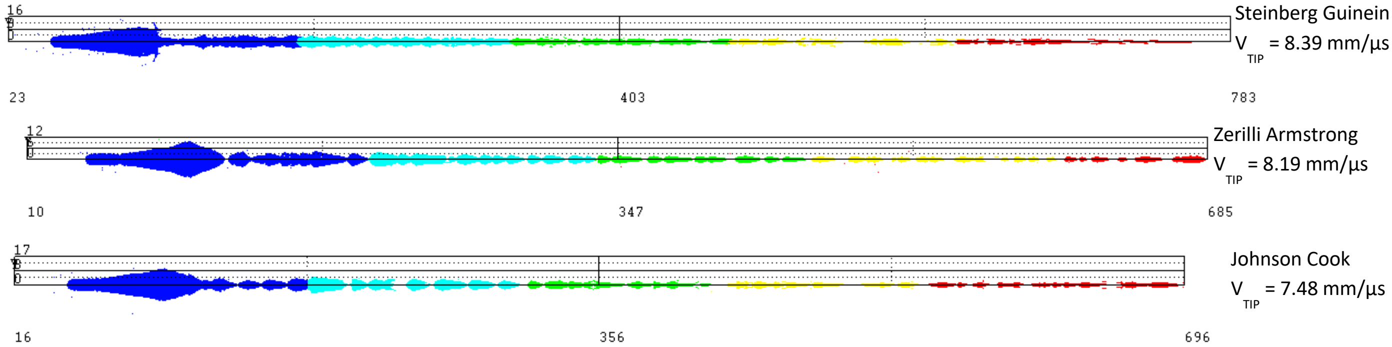

Figure 27: Velocity contours for Design 1 highlighting the differences in tip velocity for three different copper liner material models.

4.12.2. **Grid-size analysis**

Design 1 was used as the concept for evaluating the grid-size sensitivity of the jet-formation phase. The grid view for design 1 is shown in Figure 28 with a closer view shown in Figure 29. A clear profile is observed for the liner with finer grid-sizes. The material model for design 1 with grid-sizes of 0.4 mm is shown in Figure 30 with a closer view in Figure 31. The coarse liner profile is observed in Figure 31. The velocity contours for design 1 is shown Figure 32, Figure 33 and Figure 34 for grid-sizes 0.1 mm, 0.2 mm and 0.4 mm, respectively. All three simulations were left to run up to 30 µs. The tip velocity was recorded for each grid-size and reported in Table 13.

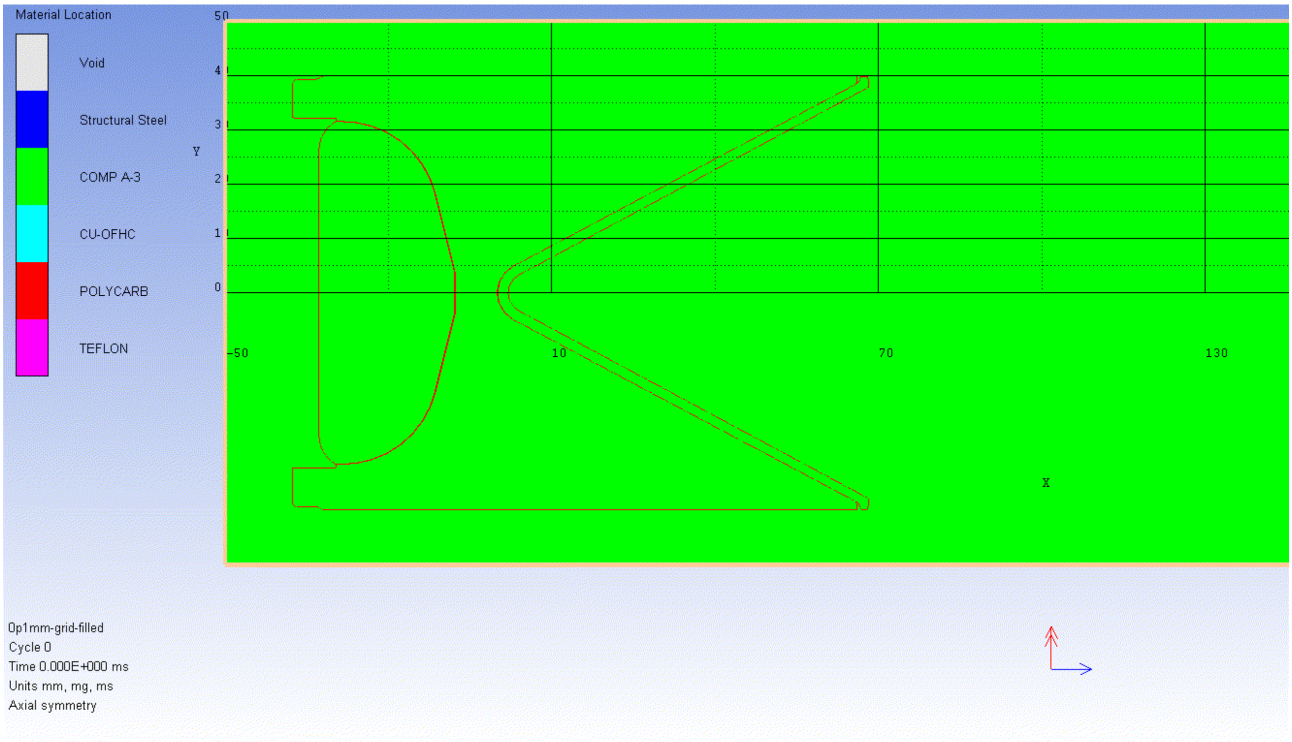

Figure 28: Euler model with of 0.1 mm square grids, this was the finest mesh used for the analysis.

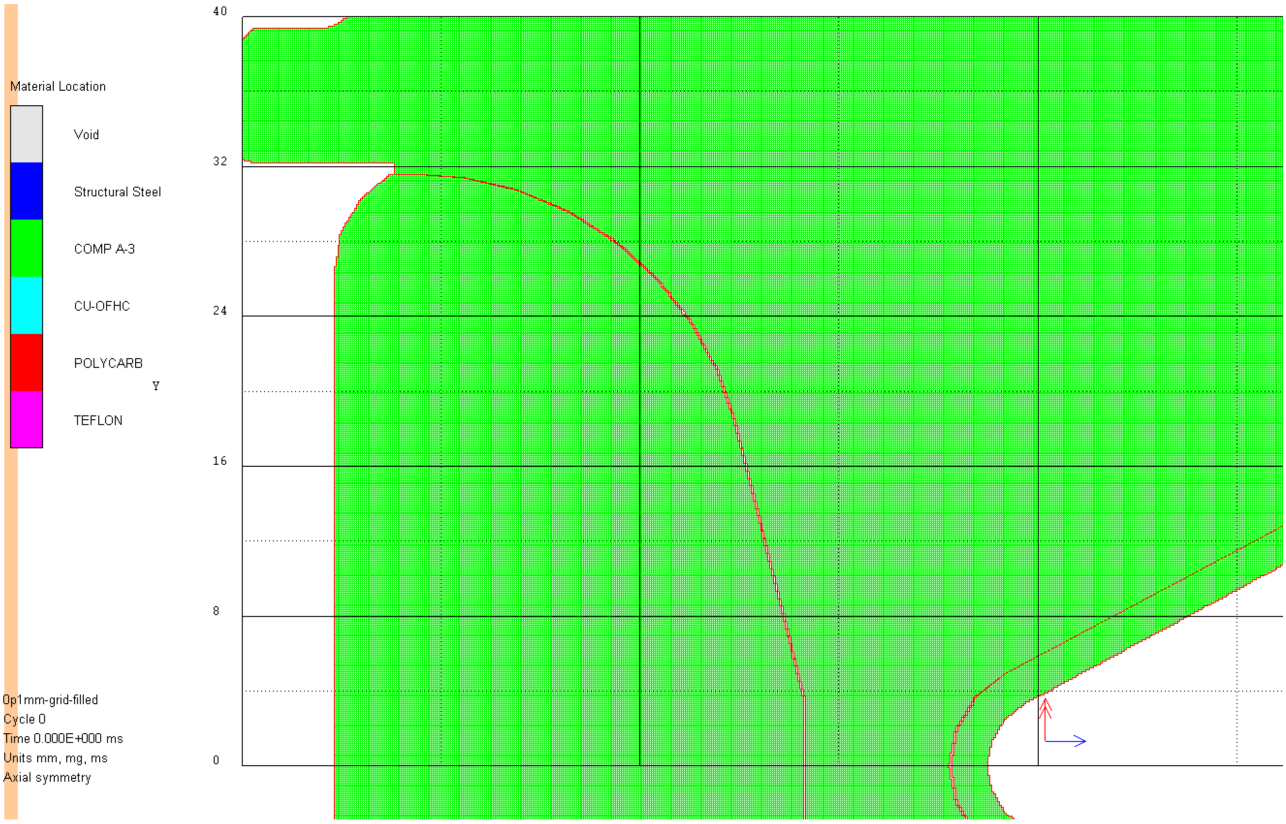

Figure 29: Grid-size analysis with a 0.1 mm square grid – close-up view of Figure 28.

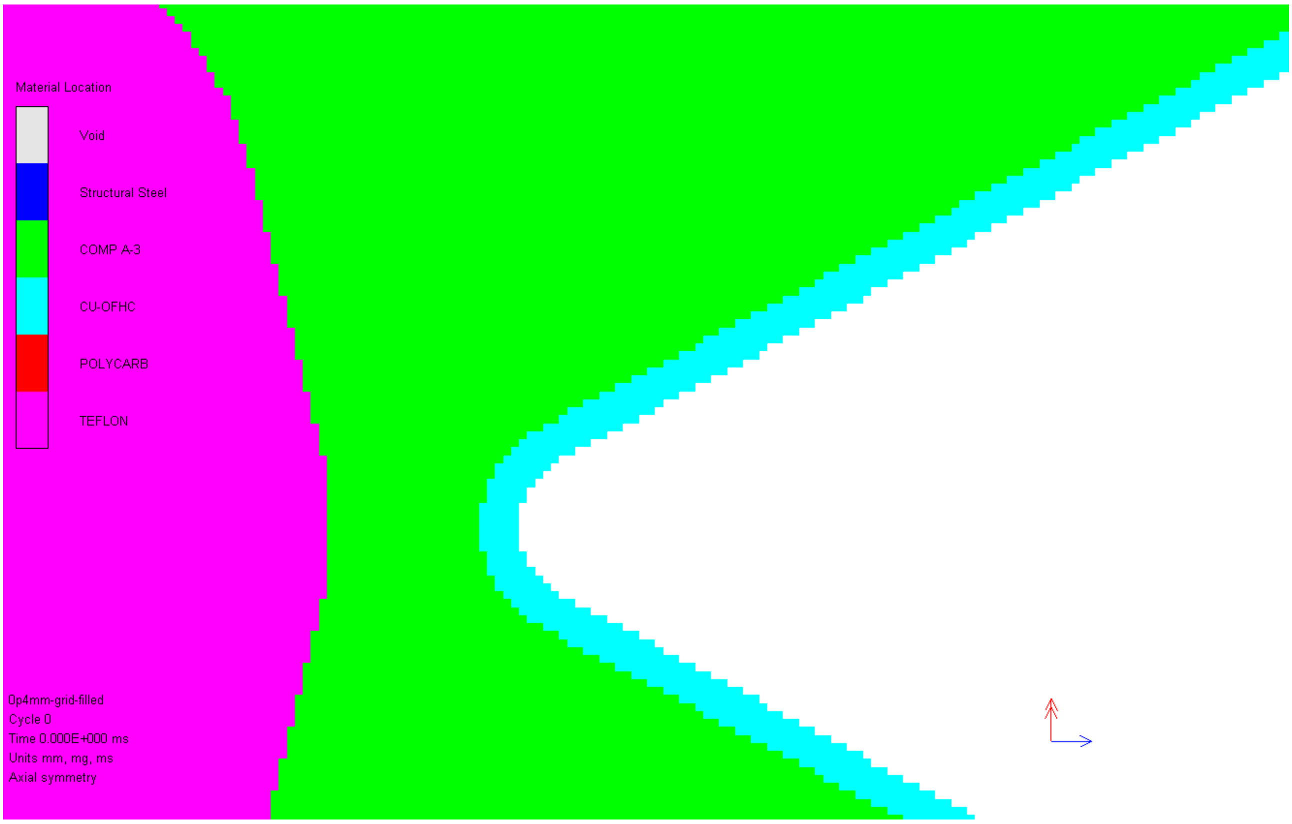

Figure 30: Grid-size analysis with a 0.4 mm square grid – material allocation described in the legend. This image shows the coarse Euler grids.

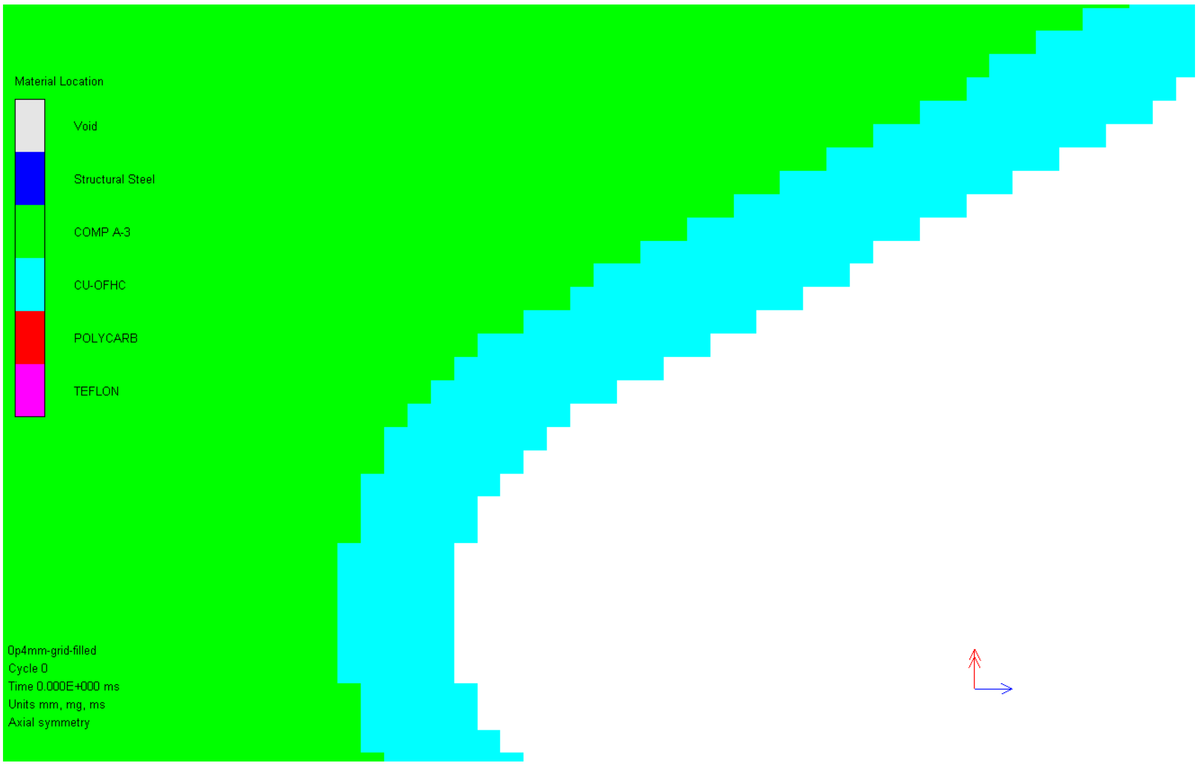

Figure 31: Grid-size analysis with a 0.4 mm square grid – material allocation. Close-up view of Figure 30.

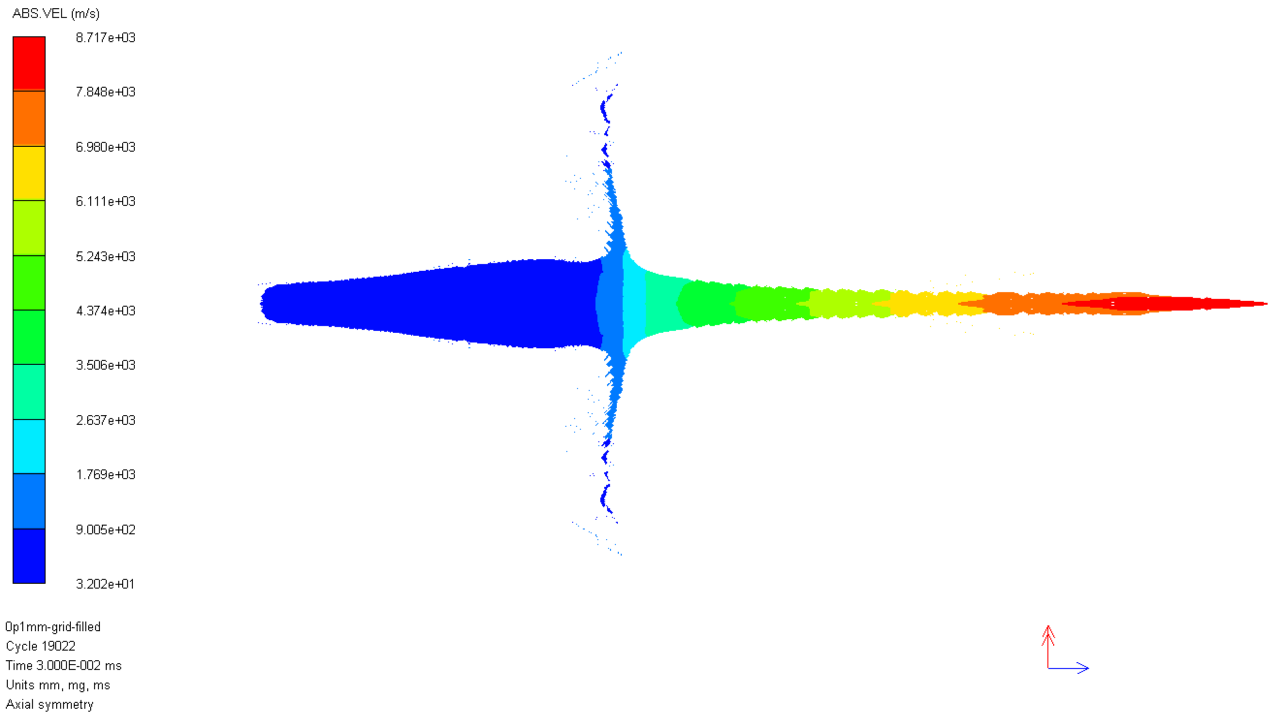

Figure 32: Velocity contours for design 1 after 30 µs with an Euler grid-size of 0.1 mm.

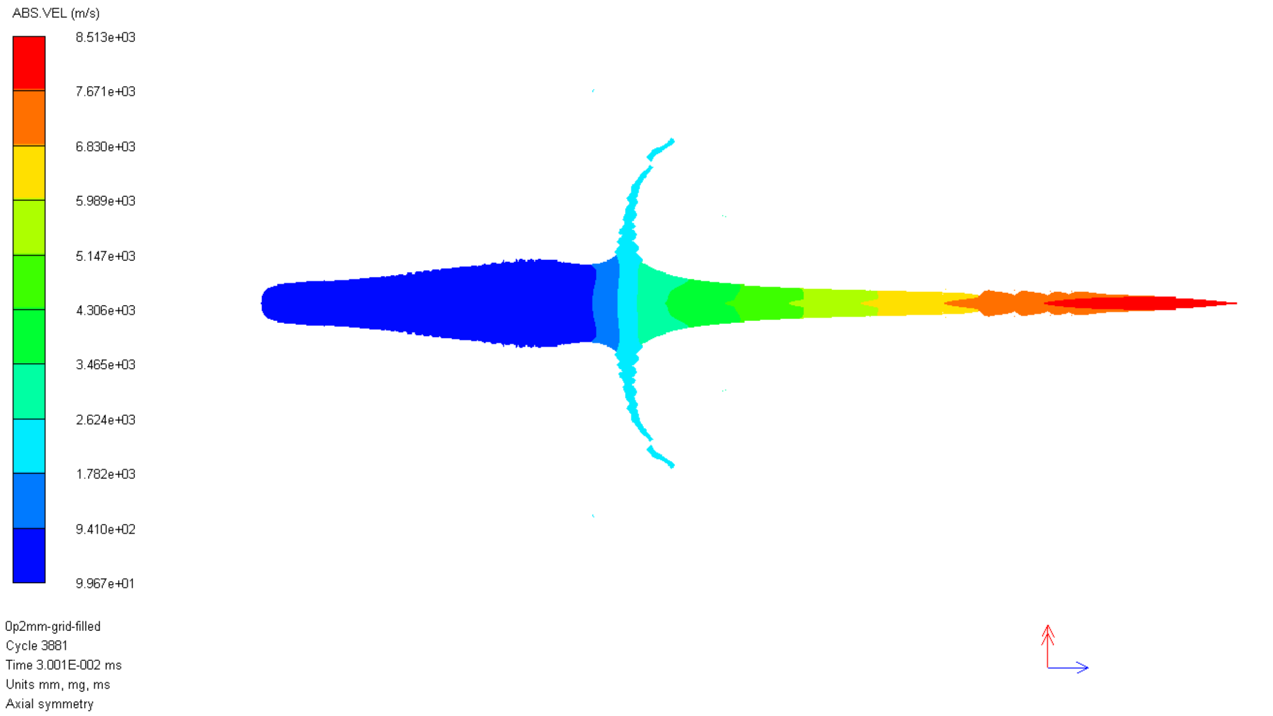

Figure 33: Velocity contours for design 1 after 30 µs with an Euler grid-size of 0.2 mm.

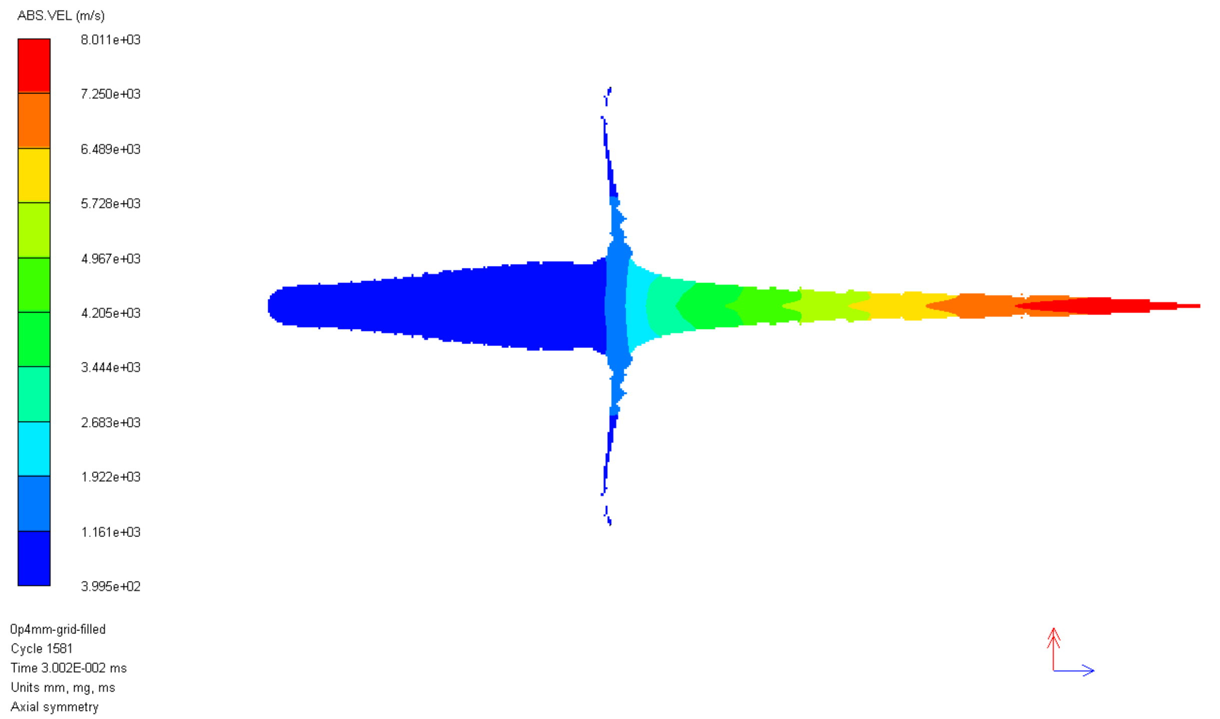

Figure 34: Velocity contours for design 1 after 30 µs with an Euler grid-size of 0.4 mm.

Table 13: Tip velocity comparison obtained from design 1 with different grid-sizes.

Grid-size (mm)	Tip velocity (mm/µs) @ 30 µs
0.1	8.72
0.2	8.51
0.4	8.01

For all the following simulations the grid size will be 0.1 mm.

4.12.3. **Design 1**

Design 1 consisted of a 60° liner and Comp A3 for the explosive formulation including a waveshaper for peripheral initiation. The concept layout presented in Figure 35 shows the liner consisting of exactly the same material but labelled C1 to C8, respectively to show which part of the liner is distributed to which part of the jet. The material properties are exactly that of the Steinberg Guinan material model. The liner was subdivided into sections such that the researcher may gain insight as to which part of the liner moves into which part of the jet. This technique was utilised in [16] and applied to all the designs in this work. The velocity contours in Figure 38 show a tip velocity of 8.71 mm/μs.

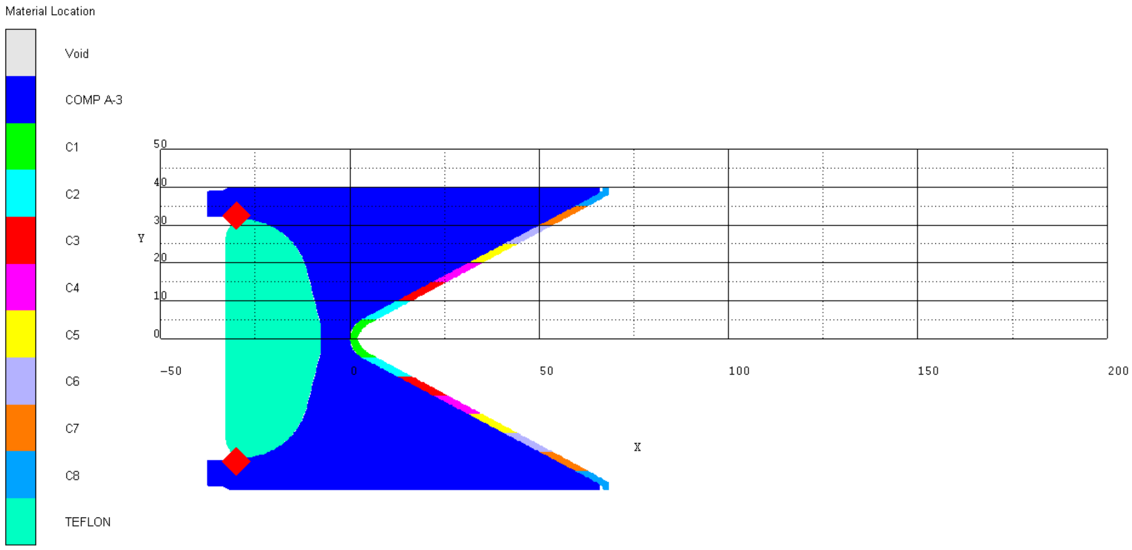

Figure 35: Design 1 - Concept layout.

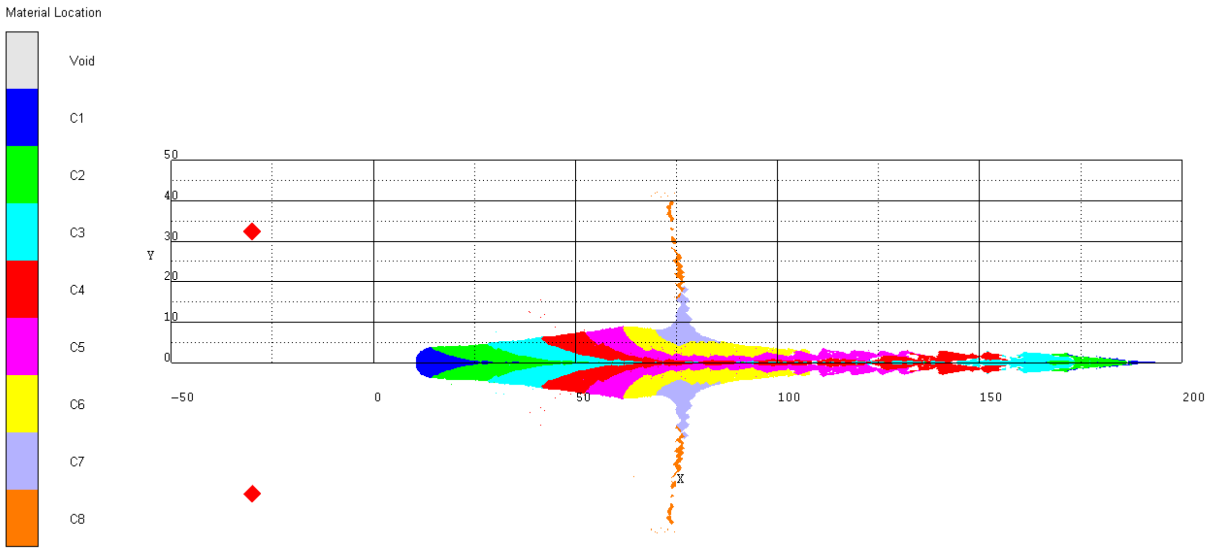

Figure 36: Design 1 – collapsed jet, material allocation.

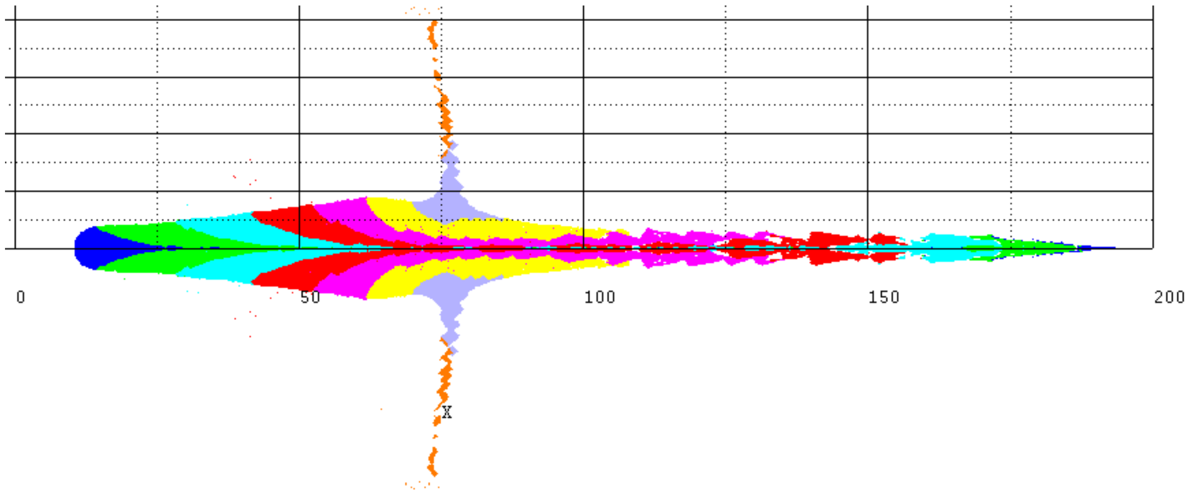

Figure 37: Design 1 – collapsed jet, close-up.

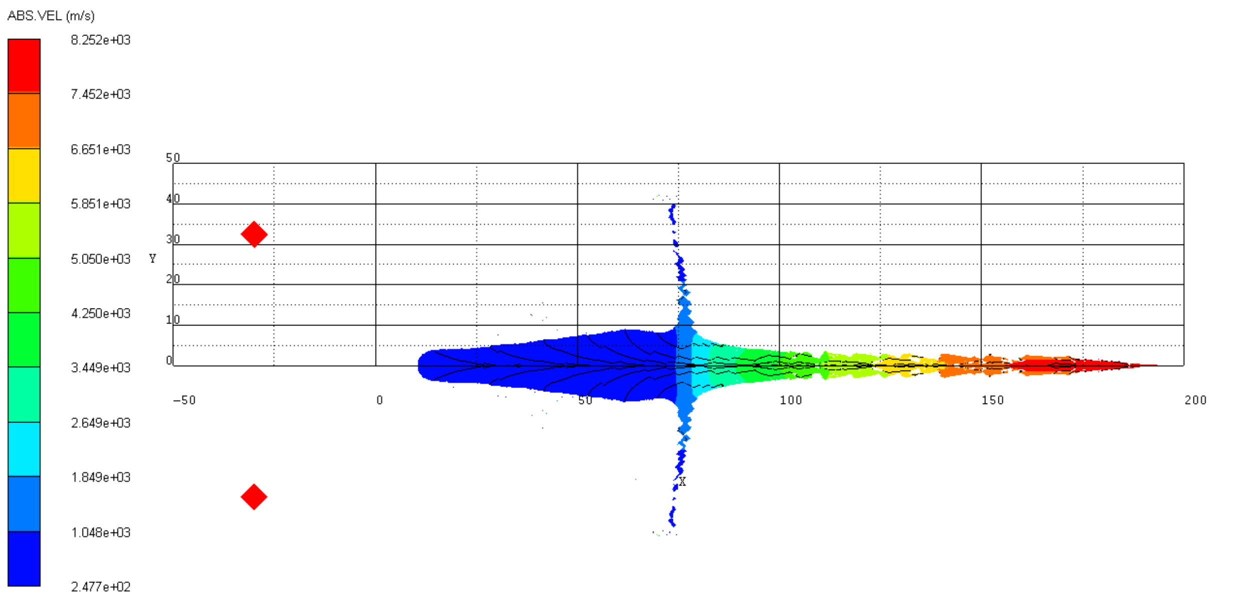

Figure 38: Design 1 – collapsed jet, velocity contour.

4.12.4. **Design 2**

Design 2 is similar to design 1 but in this case, the waveshaper is excluded. The concept layout is presented in Figure 39. That is, the same explosive formulation, Comp-A3, but point-initiated and without a waveshaper. The liner material contours for the collapsed jet are shown in Figure 40. The velocity contours are shown in Figure 41 revealing a tip velocity of 6.87 mm/µs.

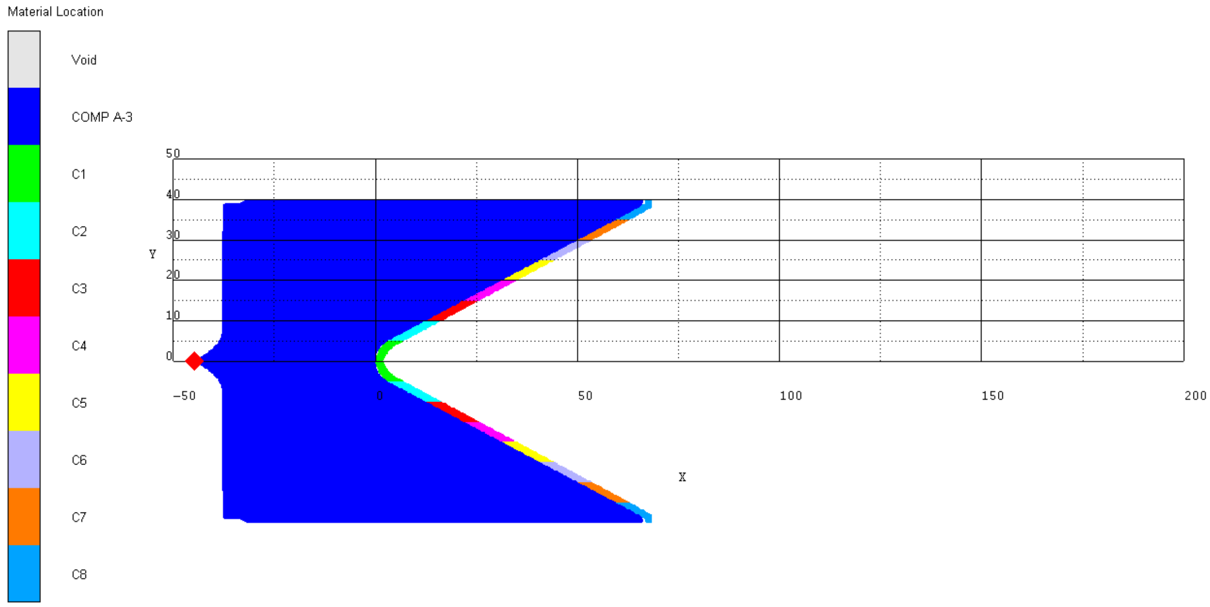

Figure 39: Design 2 - Concept layout.

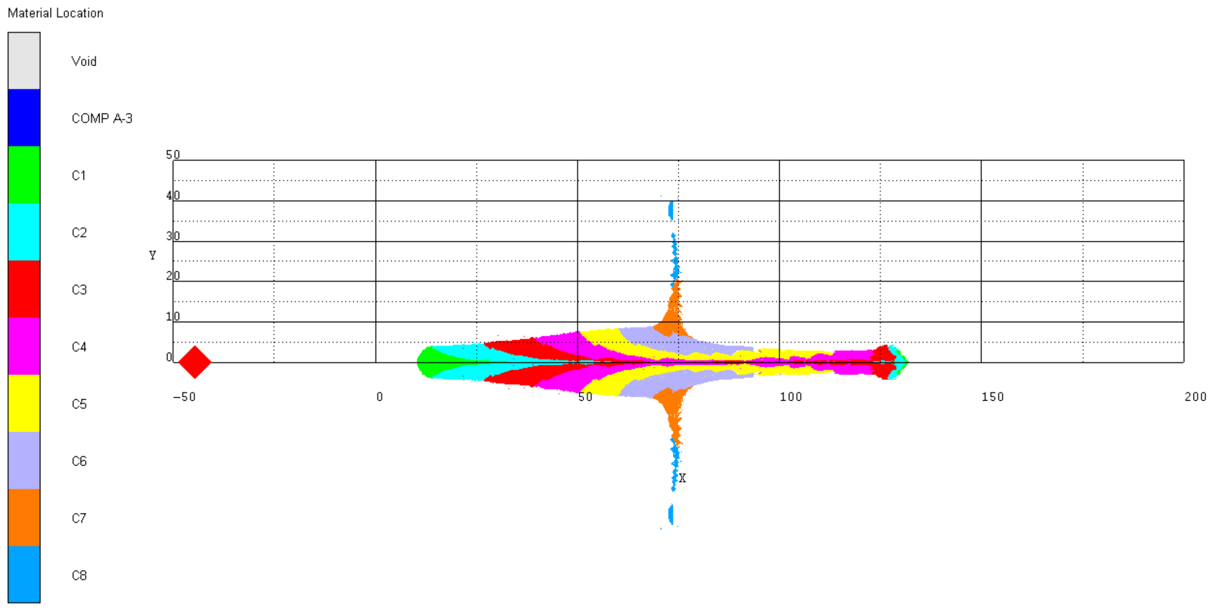

Figure 40: Design 2 – collapsed jet, material allocation.

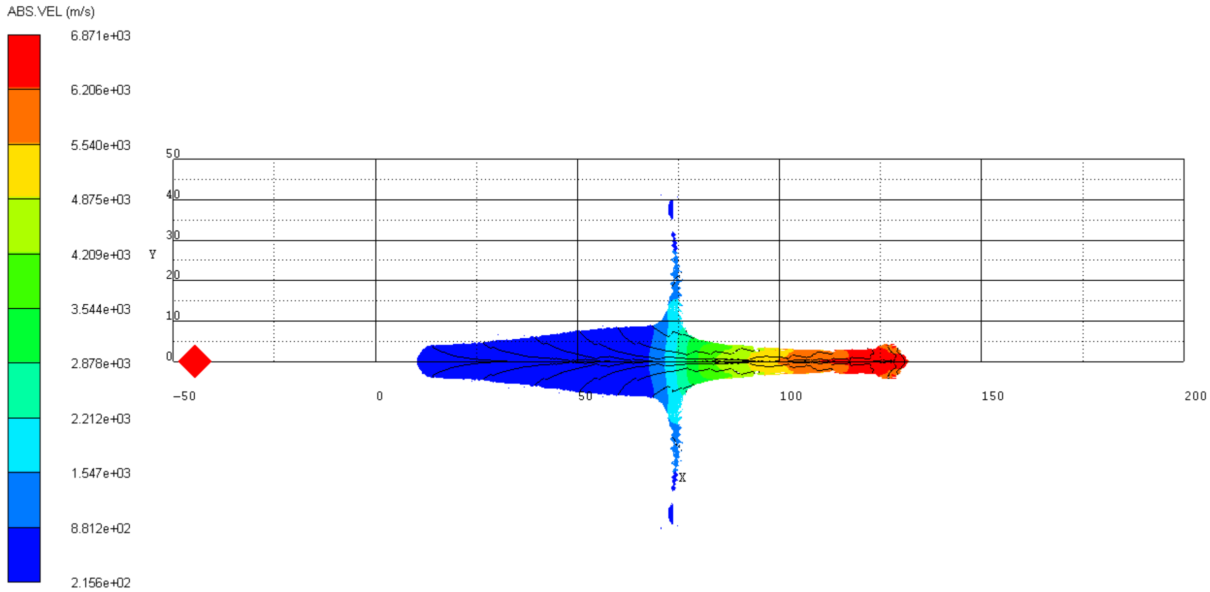

Figure 41: Design 2 – collapsed jet, velocity contour.

4.12.5. **Design 3**

Design 3 is similar to design two, but substituting the Comp A3 with a reduced output explosive. The concept layout is presented in Figure 42. That is explosive formulation, HNS 1.4, is point-initiated and there is no waveshaper. The liner material contours for the collapsed jet are shown in Figure 43 and Figure 44, respectively. The velocity contours are shown in Figure 45 revealing a tip velocity of 4.66 mm/µs. HNS at 1.40 g/cm^3 was used since it had similar explosive characteristics to an in-house cast explosive formulation. The point of this specific formulation was the reduced Velocity of Detonation (VOD) and detonation pressure, resulting in a much lower strain-rate for the design.

- Simulation - 60^0 liner with HNS
- HNS Detonation velocity = 6.34 mm/µs @ 1.4 g/cm^3
- Explosive requirement - VOD < 6.34 mm/µs.

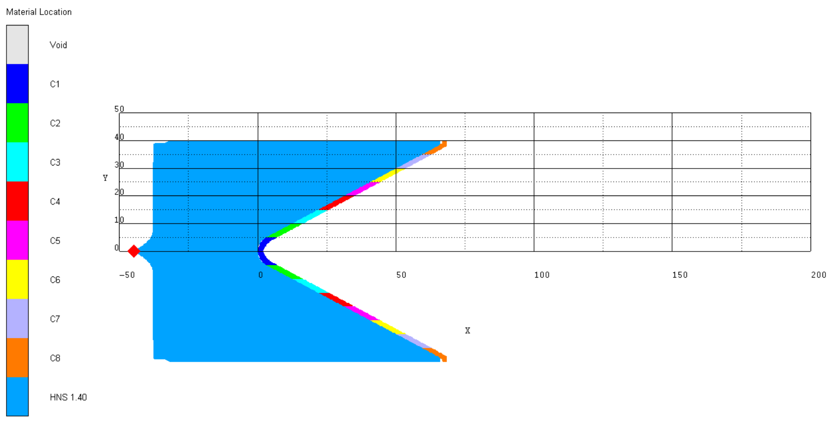

Figure 42: Design 3 - Concept layout.

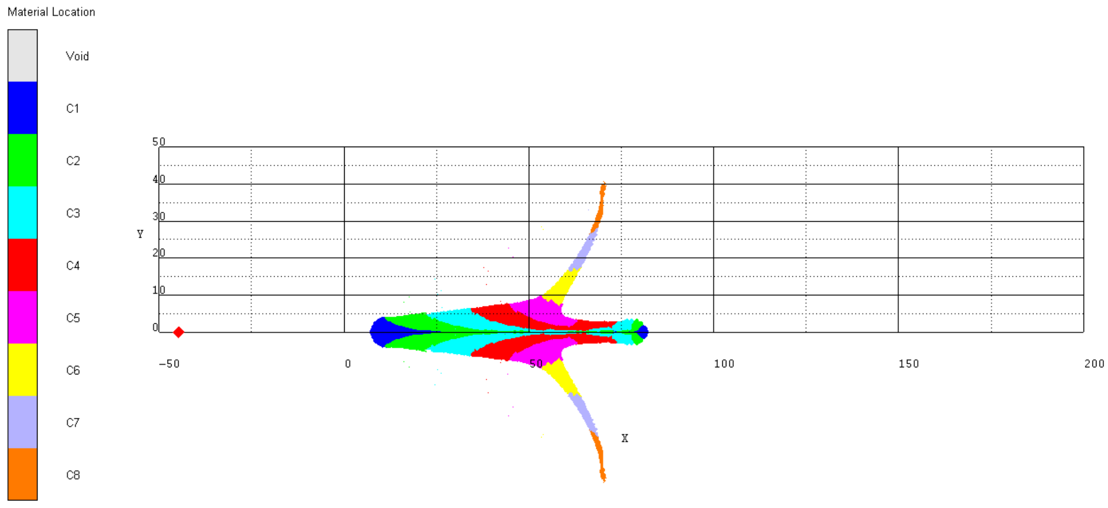

Figure 43: Design 3 – collapsed jet, material allocation.

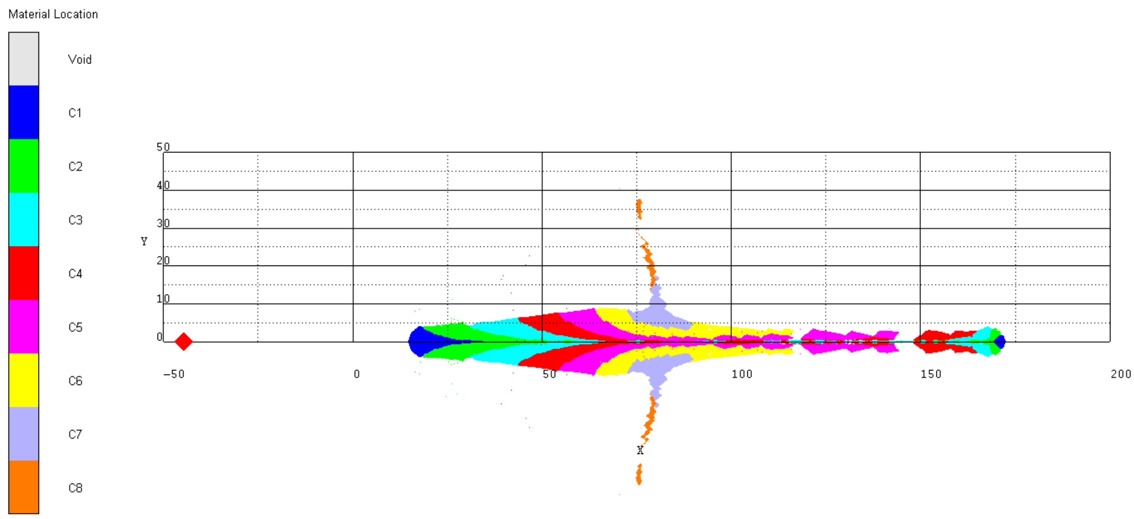

Figure 44: Design 3 – collapsed jet, material allocation – later time.

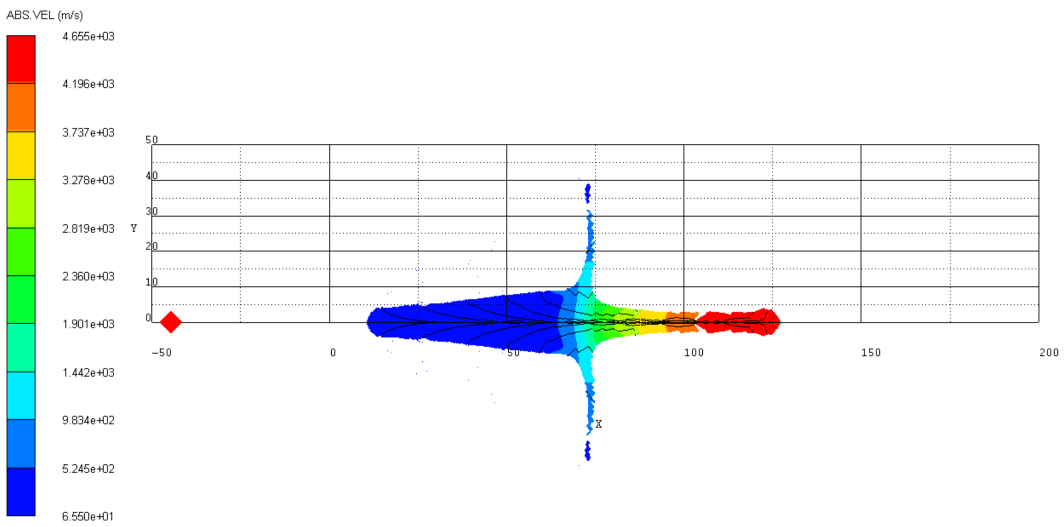

Figure 45: Design 3 – collapsed jet, velocity contour.

4.12.6. **Design 4**

Design 4 is similar to design one, this time using a 120° liner instead of the 60° liner. The concept layout is shown in Figure 46, which is explosive formulation, Comp-A3, peripherally initiated and including a waveshaper. The liner material contours for the collapsed jet are shown in Figure 47. The velocity contours are shown in Figure 48 revealing a tip velocity of 4.76 mm/µs.

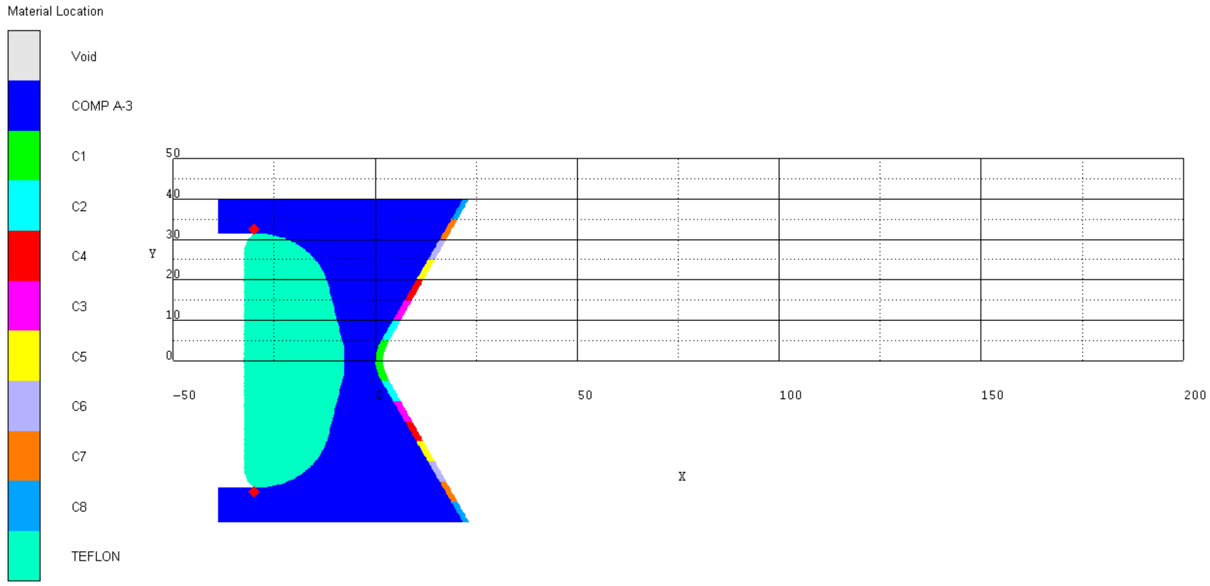

Figure 46: Design 4 - Concept layout.

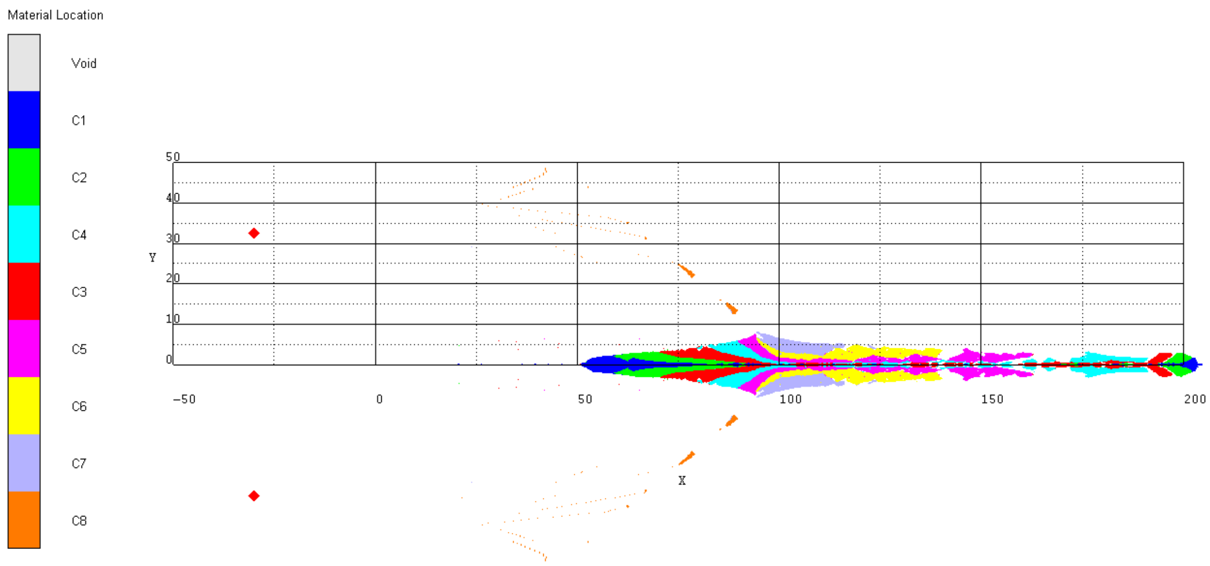

Figure 47: Design 4 – collapsed jet, material allocation.

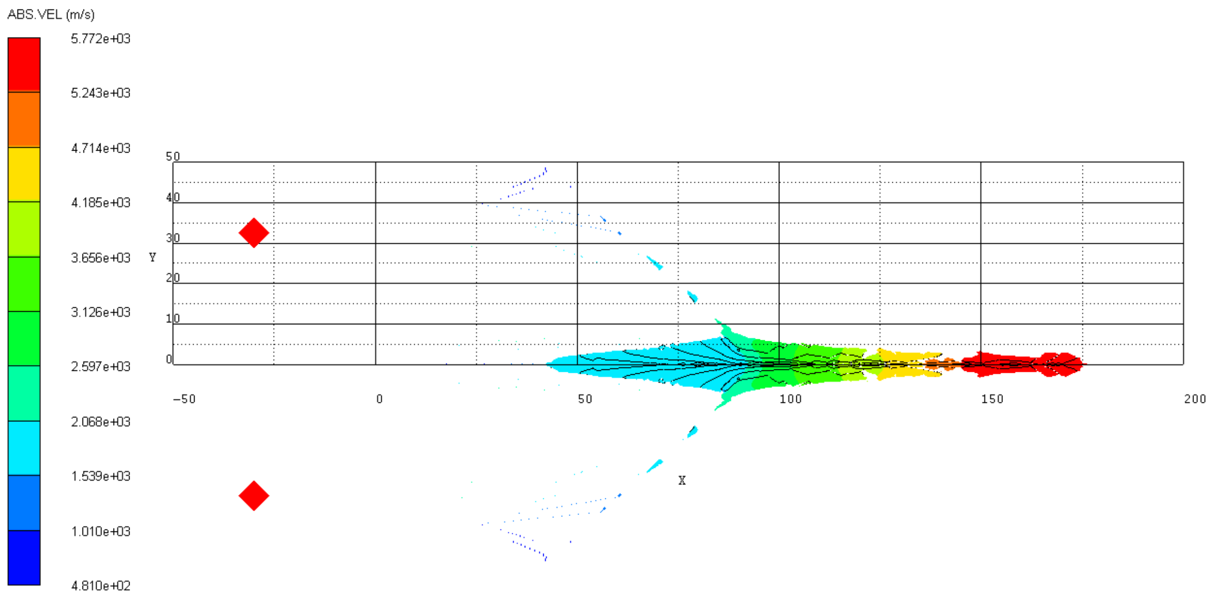

Figure 48: Design 4 – collapsed jet, velocity contour.

4.12.7. **Design 5**

Design 5 is similar to design 4, this time excluding a waveshaper. The concept layout is presented in Figure 49; which is explosive formulation, Comp-A3, point-initiated excluding a waveshaper. The Steinberg Guinan material was used for the liner material based on the analysis done with design 1. The liner material contours for the collapsed jet are shown in Figure 50. The velocity contours are shown in Figure 51 revealing a tip velocity of 3.80 mm/µs.

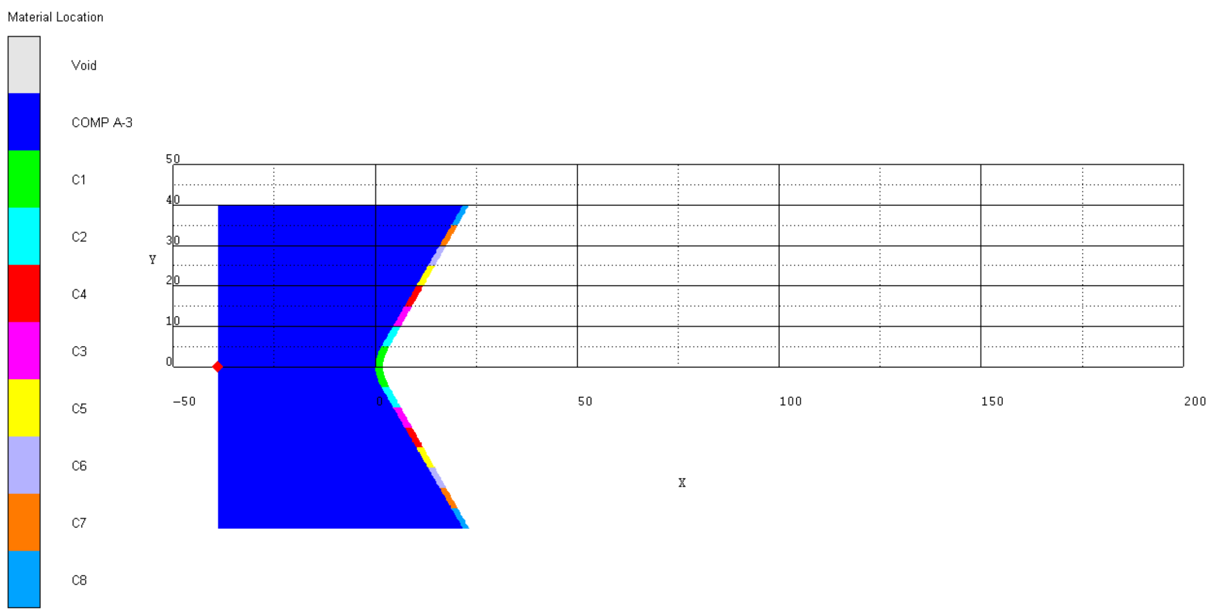

Figure 49: Design 5 - Concept layout.

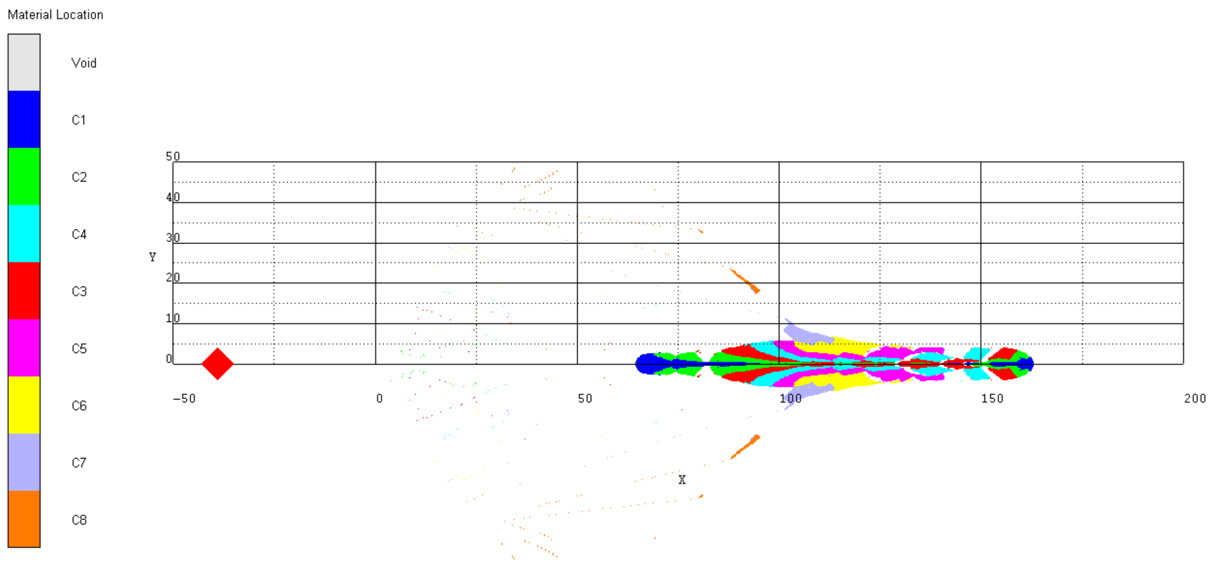

Figure 50: Design 5 – collapsed jet, material allocation.

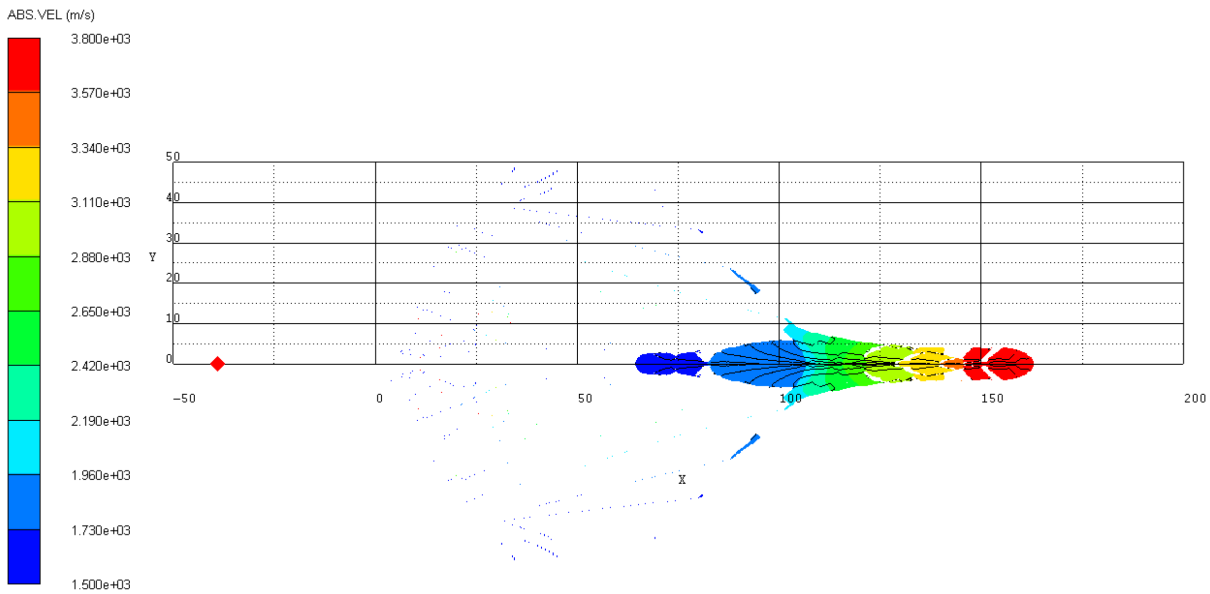

Figure 51: Design 5 – collapsed jet, velocity contour.

4.12.8. **Design 6**

Design 6 is similar to design 5, this time substituting the explosive formulation with HNS 1.4 (similar to what was done with design 3). The concept layout is presented in Figure 52, which is explosive formulation, HNS, point-initiated and without a waveshaper. The liner material contours for the collapsed jet are shown in Figure 53. The velocity contours are shown in Figure 54 revealing a tip velocity of 2.66 mm/µs.

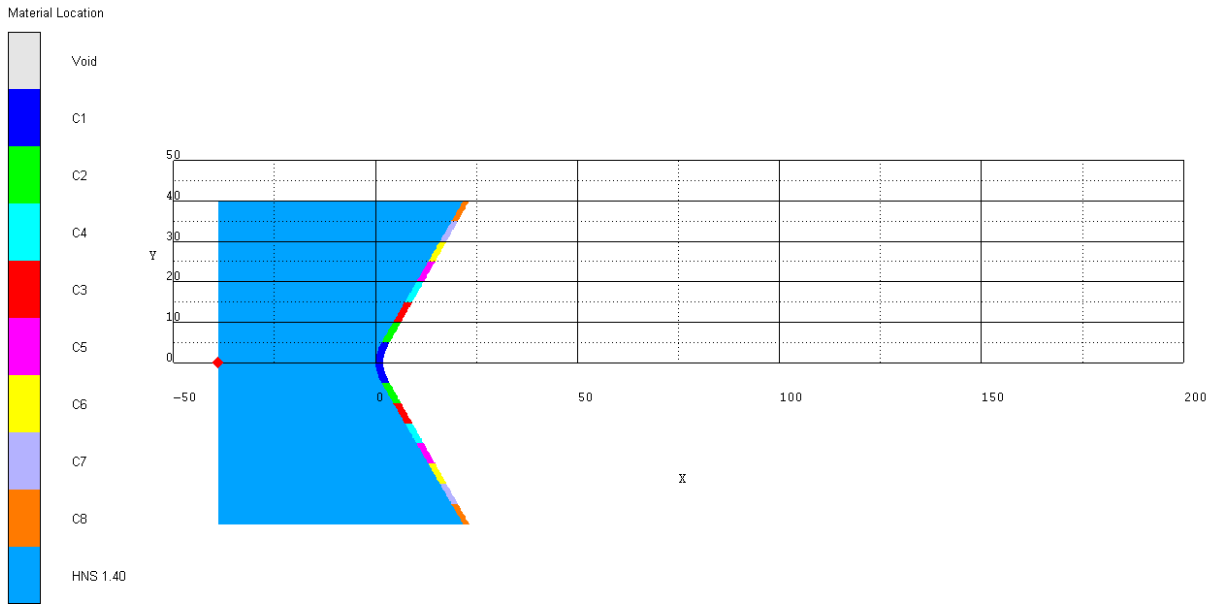

Figure 52: Design 6 - Concept layout.

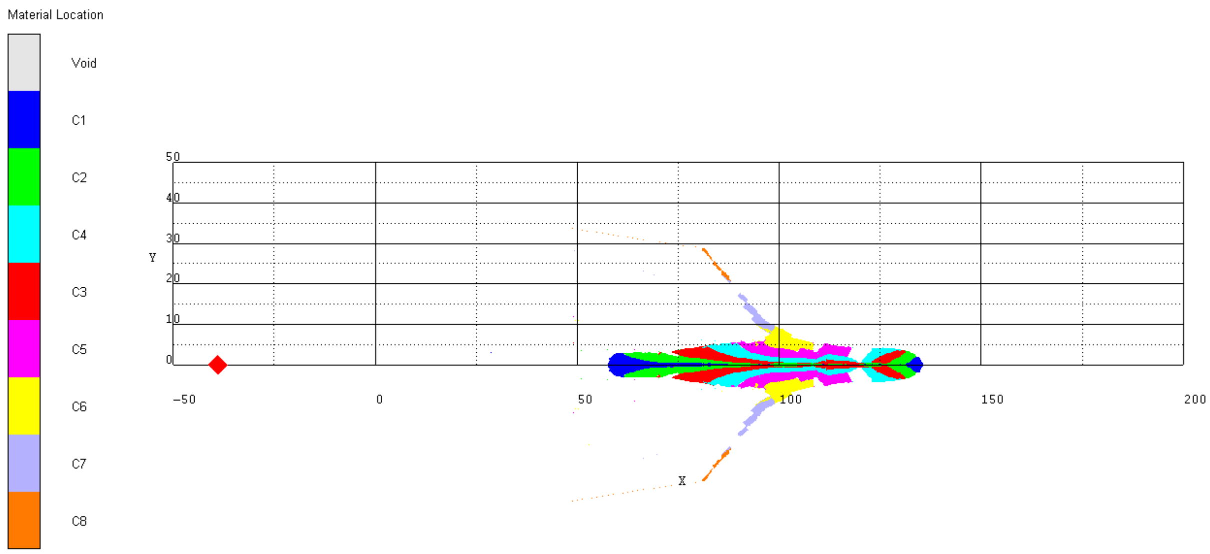

Figure 53: Design 6 – collapsed jet, material allocation.

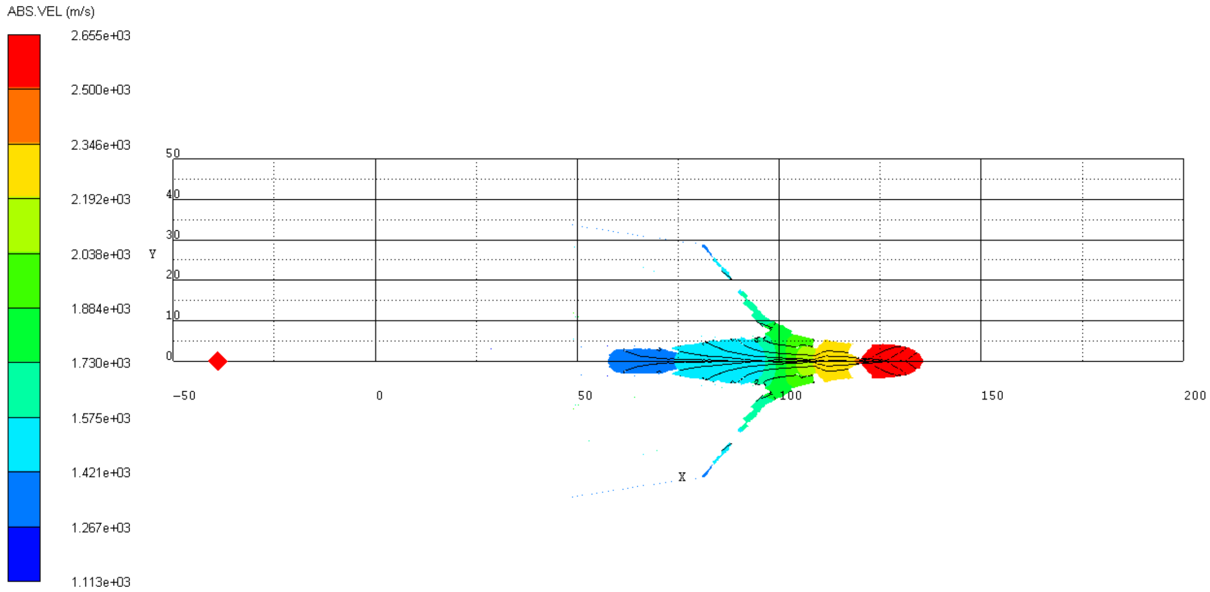

Figure 54: Design 6 – collapsed jet, velocity contour.

4.12.9. **Simulation Summary**

The summary of the key design variables and the tip and tail velocities are presented in Table 14. The data, graphically presented in Figure 55 and Figure 56 respectively, was proof that the various design changes were successful in terms of varying strain and strain-rate of the jets. Both, jet tip velocities and the velocity gradient (ΔV) linearly decreased as the designs changed from one to three for a 60° liner and similarly for designs four to six with a 120° liner. The design changes referred to here are the use of point and peripheral initiation and the use of an explosive containing 91% RDX and 55% RDX. Although different strategies were considered such as different liner thicknesses, different explosive charges, with and without confinement and different explosives, the variation in the initiation system and this specific explosive selection, made this linear change in velocity regime.

Table 14: Key design variables with tip and tail velocities extracted from the respective simulations.

Design	Explosive	Initiation Mode	% RDX	Liner Angle (deg)	Tip Velocity (mm/µs)	Slug Velocity (mm/µs)	ΔV (Tip & Slug) (mm/µs)
1	RDX: WAX	Peripheral	91	60	8.7	0.5	8.2
2	RDX: WAX	Point	91	60	6.7	0.5	6.2
3	Cast Formulation	Point	55	60	4.8	0.5	4.3
4	RDX: WAX	Peripheral	91	120	4.8	1.4	3.4
5	RDX: WAX	Point	91	120	3.9	1.4	2.5
6	Cast Formulation	Point	55	120	2.5	1.1	1.4

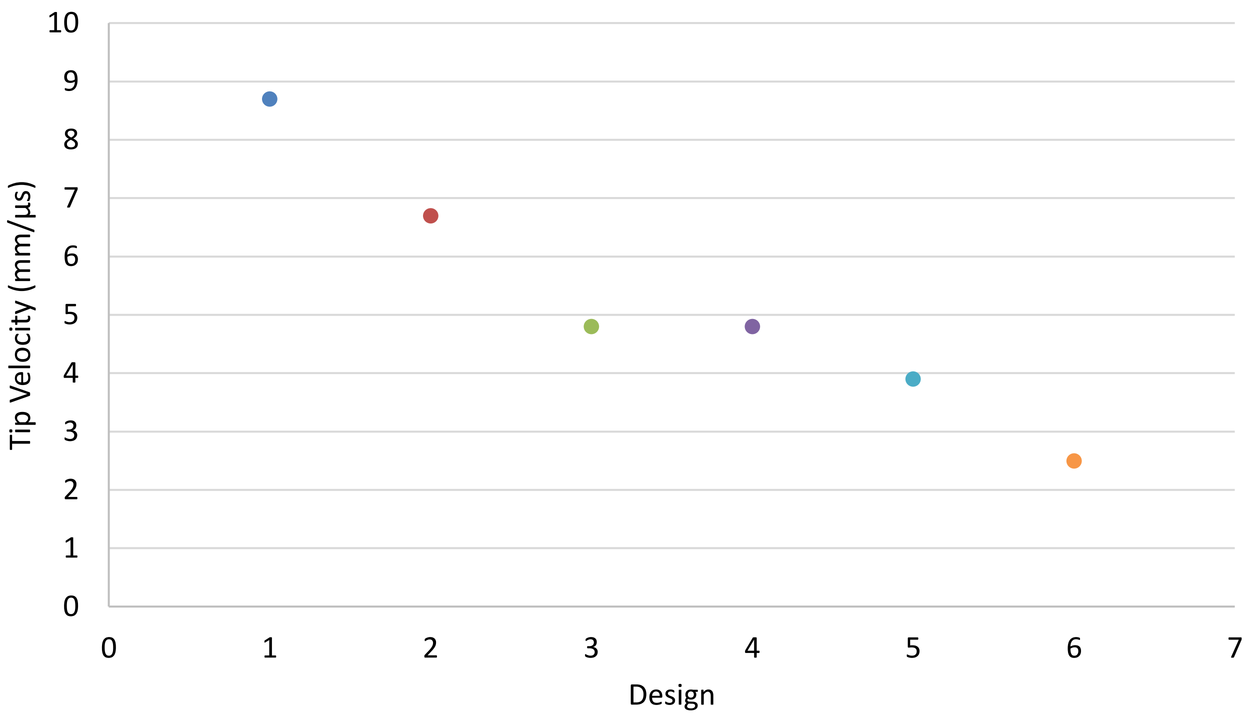

Figure 55: Correlation between design and tip velocity.

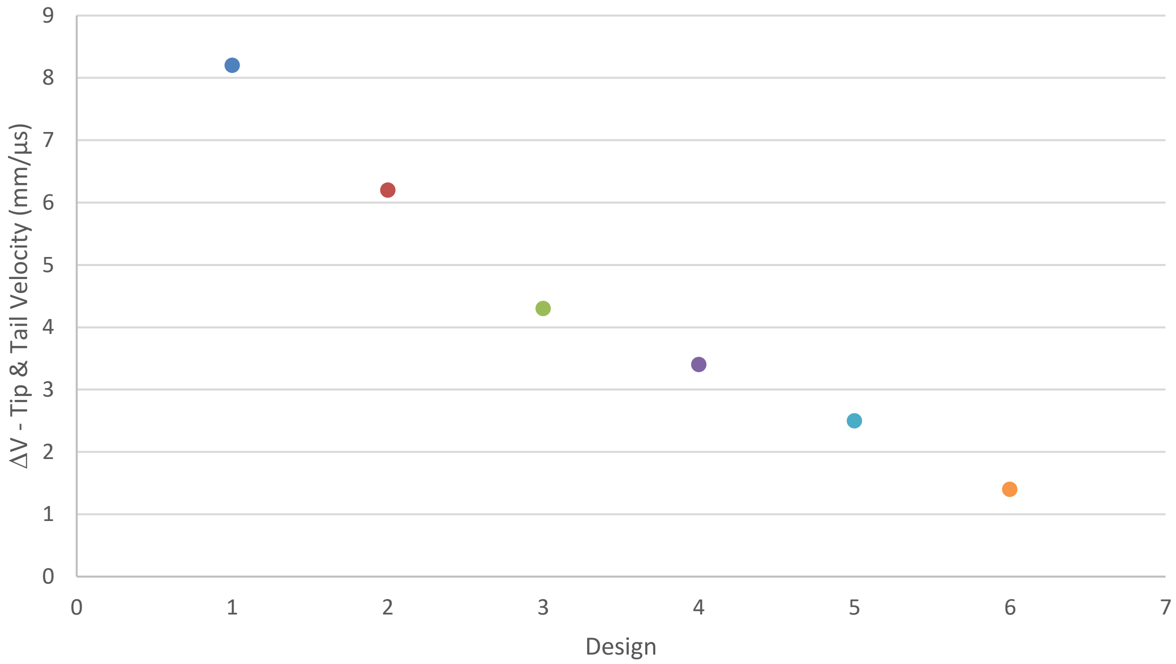

Figure 56: Correlation between design and ΔV.

The mass distributions per velocity segment in 0.5 mm/µs segments from a typical 2D axisymmetric simulation in AUTODYN are presented in Figure 57. A close-up view of the mass distributions are presented Figure 58. These mass distributions have not been integrated to present the actual jet masses. These are the masses as generated in the PRINT grid data option. Ansys AUTODYN has the option of writing out data for each grid point in an Euler grid. The cumulative mass distributions are presented in Figure 59 and Figure 60. The effects of peripheral initiation is clearly observed when analysing the cumulative mass distribution from design 1 to design 2 with an increase in tip velocity, but a nearly identical mass distribution from the intersection point of the tip velocity of design 2. The trend in mass distribution for design 3 is similar to design 1 & 2 due to the identical liner design but an offset in velocity is observed due to the reduced output explosive. The cumulative mass distribution for the 60° liners are shown in Figure 61. Similar observations may be seen in Figure 62 where peripheral initiation of design 4 increases the tip velocity to an identical mass distribution at the tip velocity of design 5 down to the rear of the jet. An offset is then again observed for Design 6 due to the reduced output explosive.

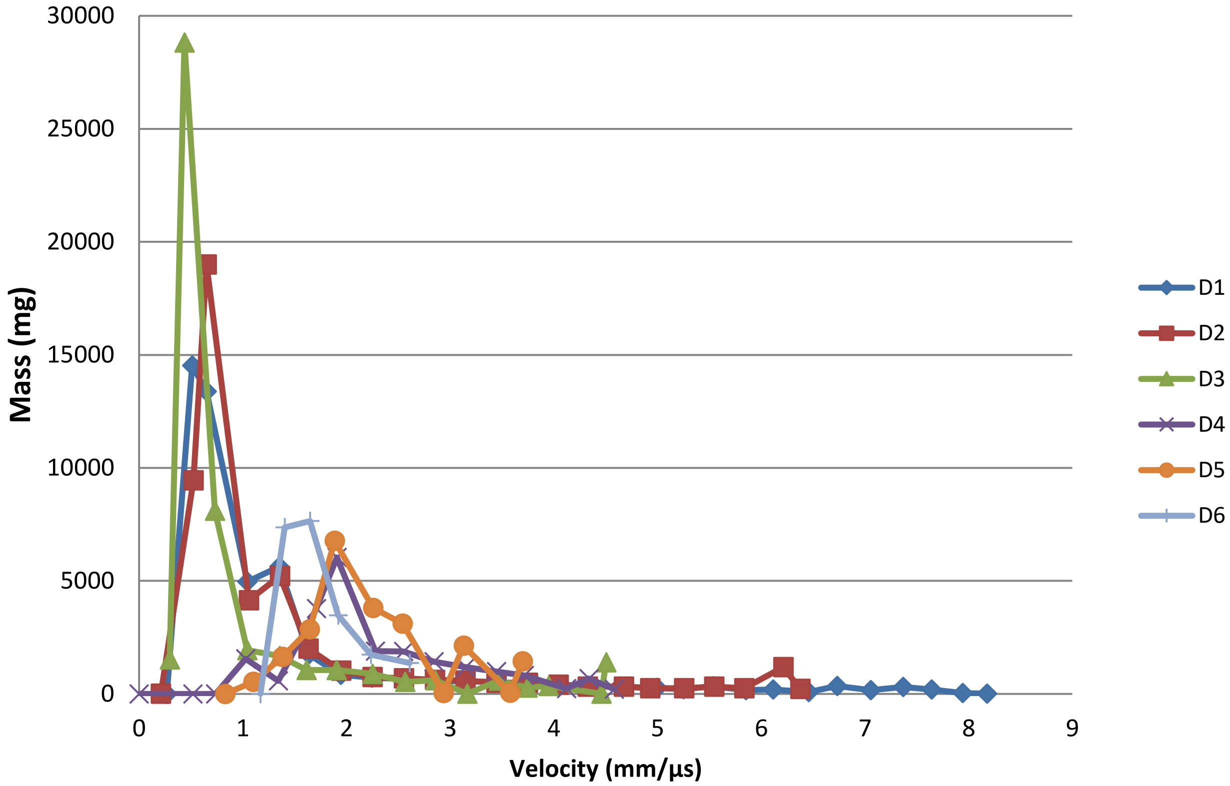

Figure 57: Mass distribution for all six designs.

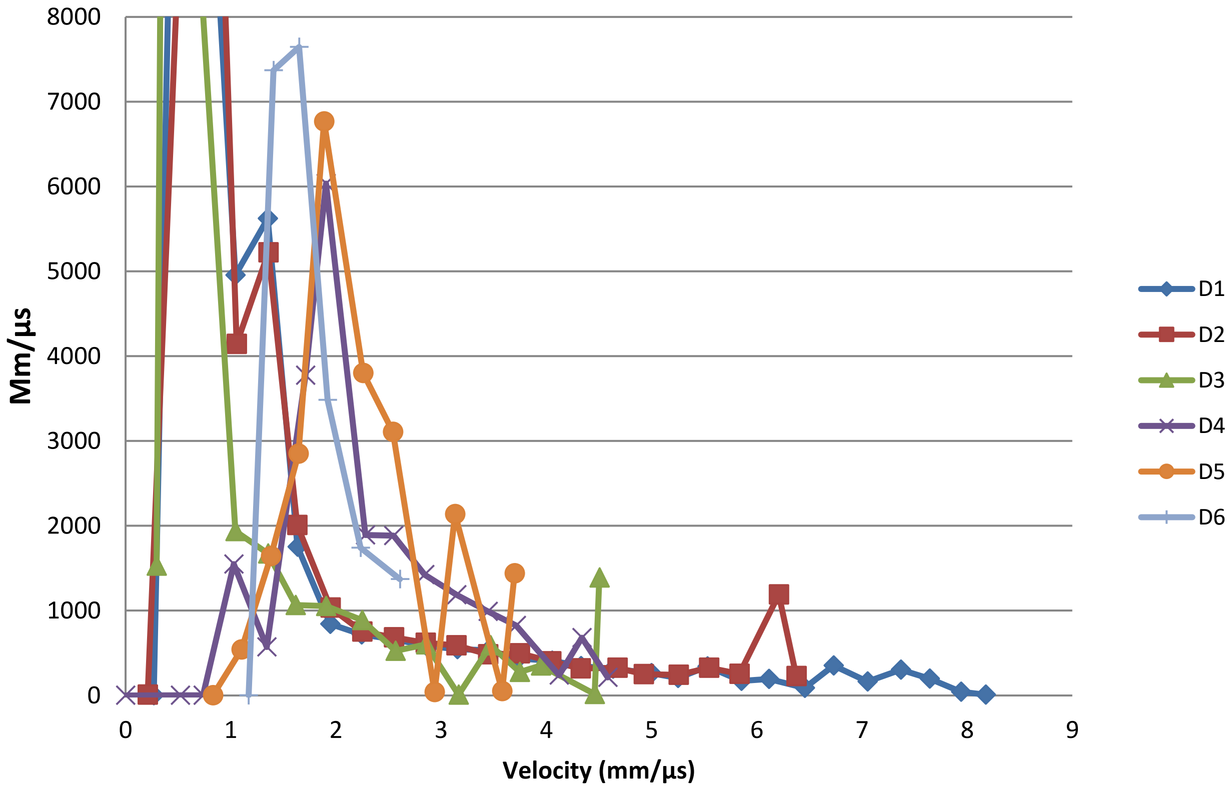

Figure 58: Mass distribution for all six designs up to 8 g.

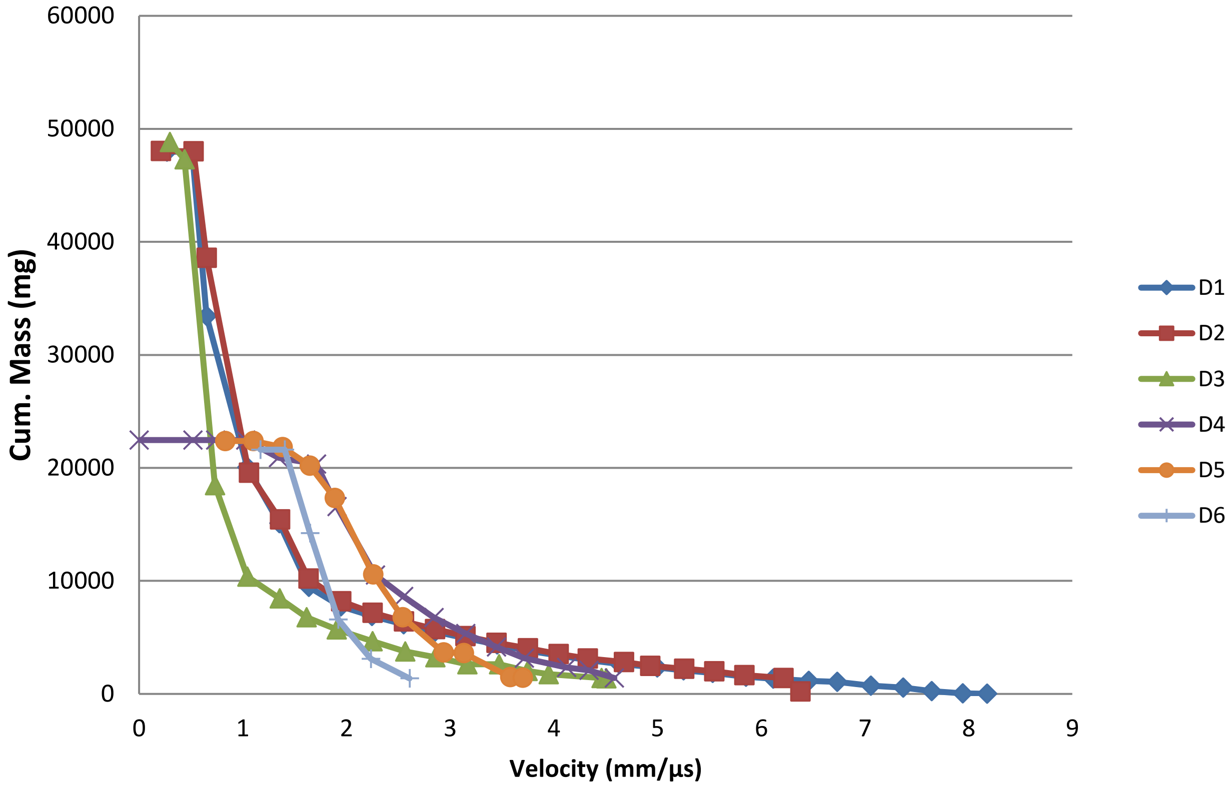

Figure 59: Cumulative mass distribution for all six designs.

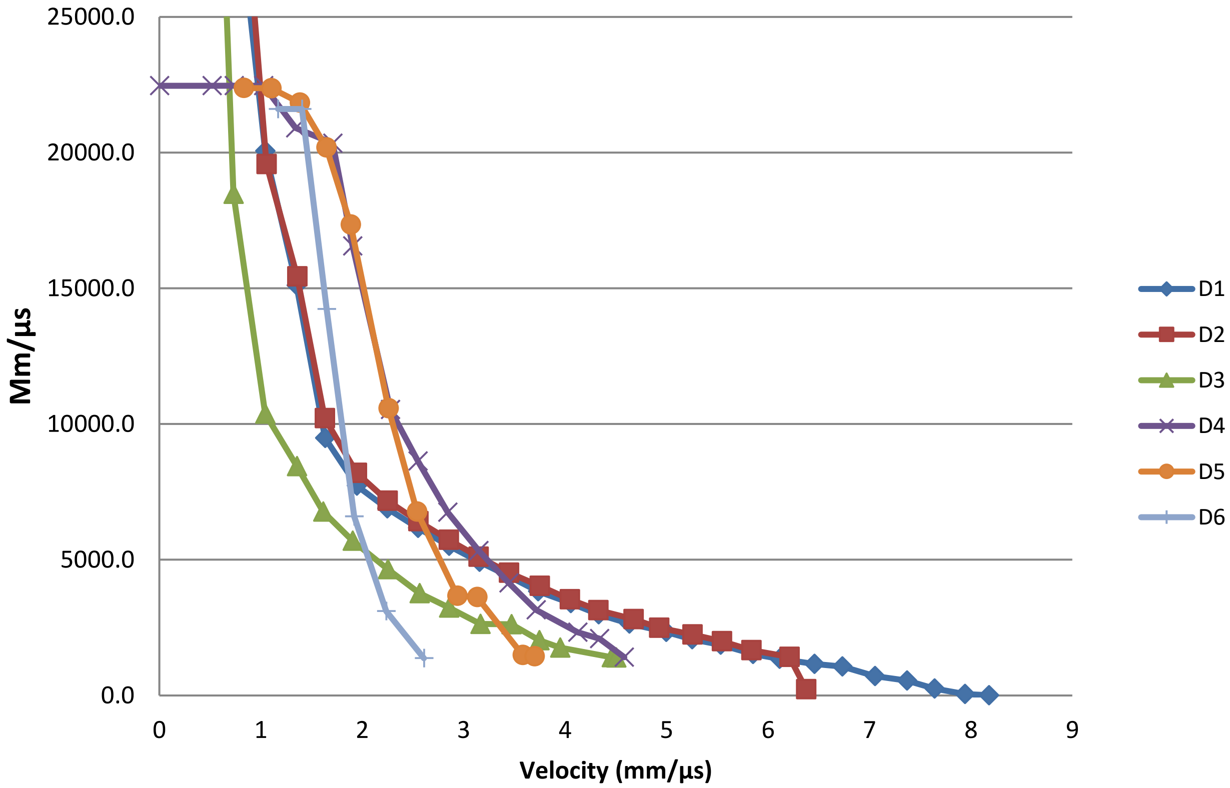

Figure 60: Cumulative mass distribution for all six designs, up to 20 g.

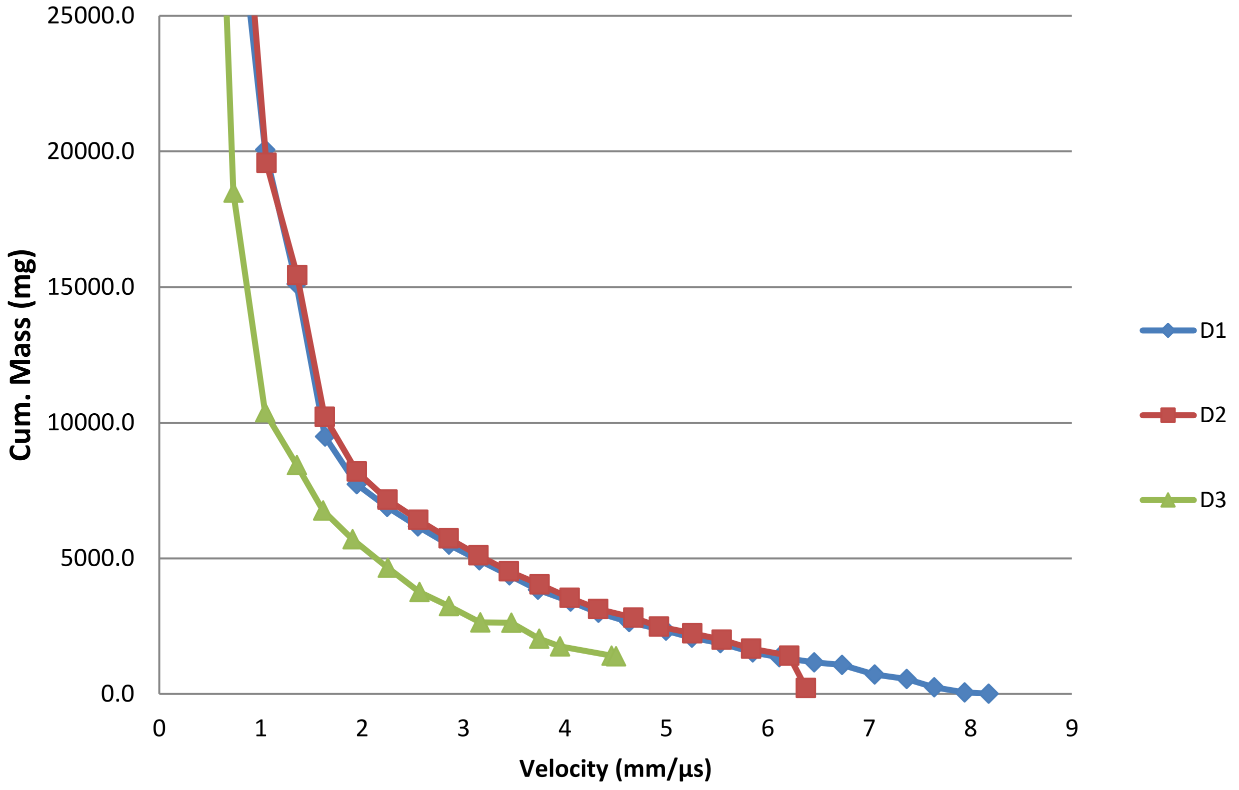

Figure 61: Cumulative mass distribution for the 60° liner design.

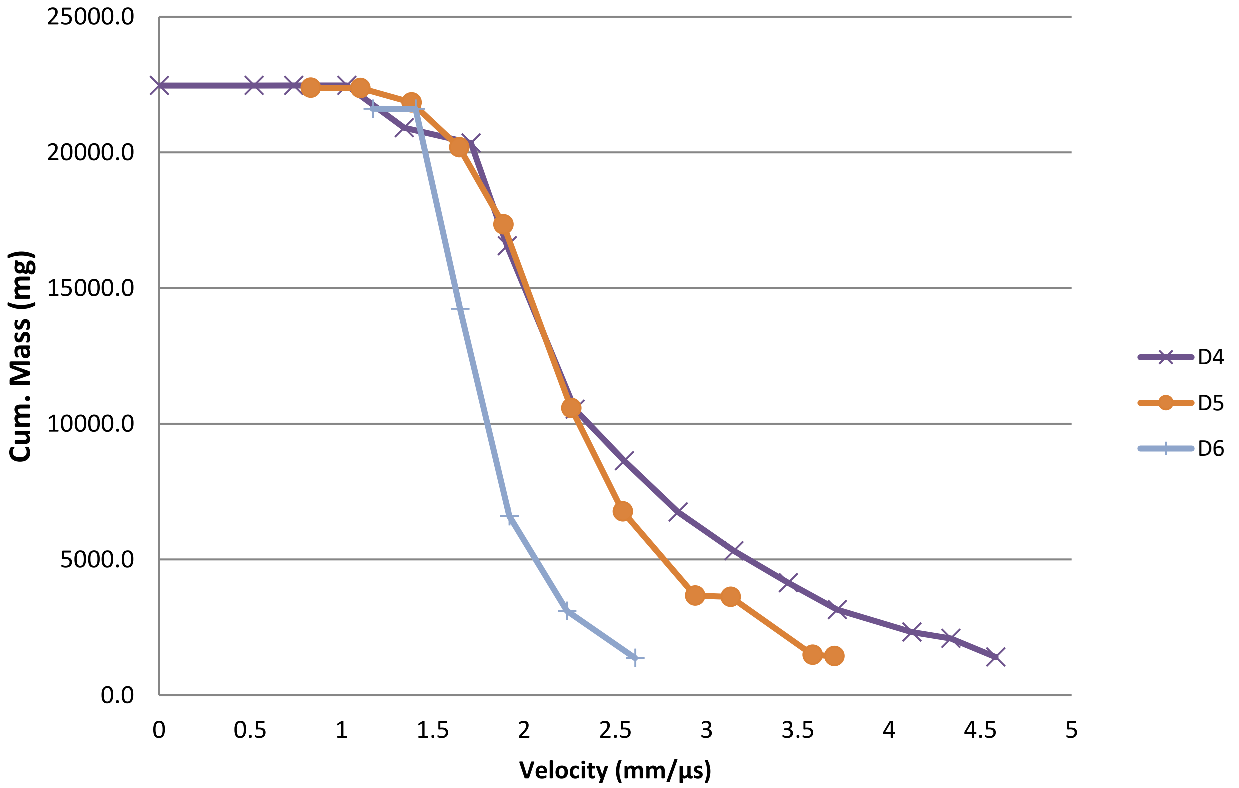

Figure 62: Cumulative mass distribution for 120° liner designs.

The simulations have shown the influence of the initiation where peripheral initiation increases the tip velocity. It has also shown the influence of the explosive used onto a particular liner design. Reduced energy explosive resulted in reduced output in terms of velocities but showed similar trends in terms of kinetic energy and mass distributions towards the rear.

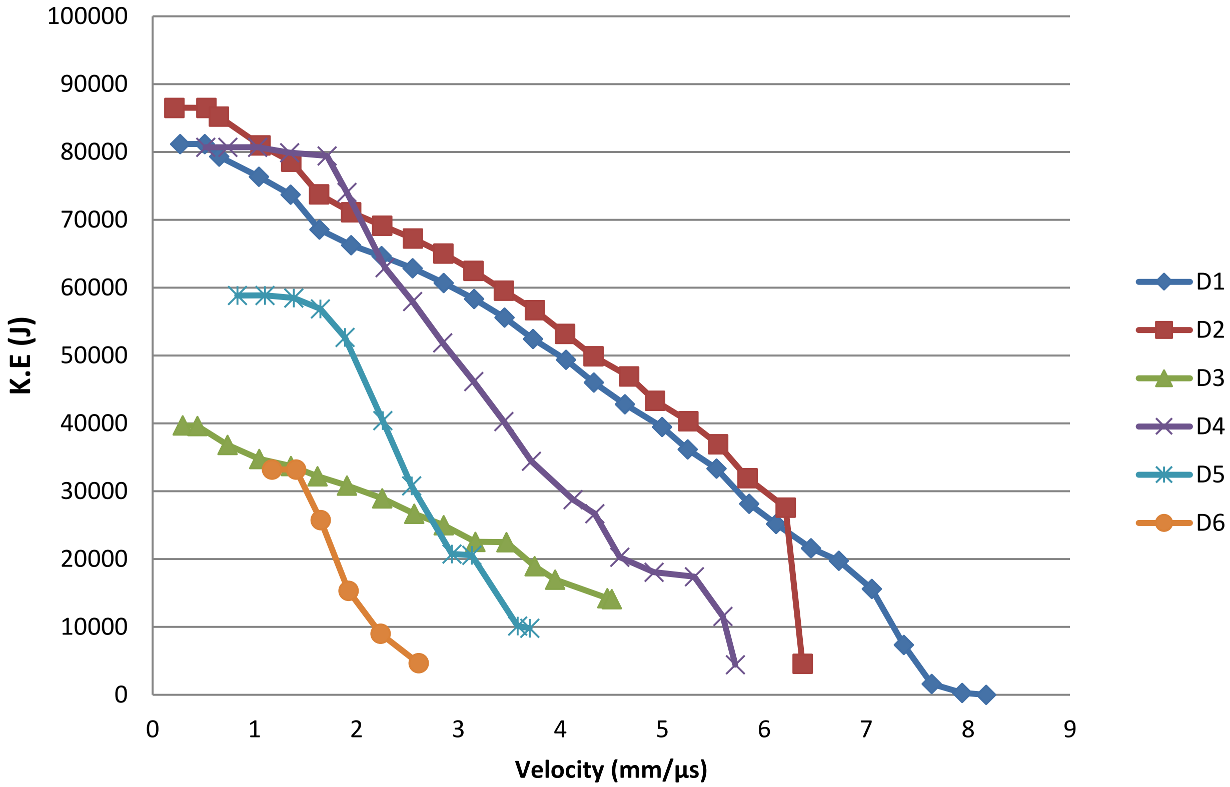

Figure 63: Cumulative kinetic energy for all six designs.

The next chapter focuses on the manufacture of the designs presented above.

5. SHAPED-CHARGE MANUFACTURE

The shaped-charge warheads were manufactured with utmost care in most respects. The manufacturing may contribute marginally in the scientific context, but if great care was not taken thereof, scientific observations and deductions may not have been possible. This chapter will demonstrate all aspects that were required to acquire adequate hardware for use in this this project. Shaped charge warheads were manufactured using six concept designs from a combination of two liner designs, two explosive charge designs and two explosive formulations. A new liner design required the design of new tooling since these copper forgings were manufactured in a large press. Two explosive types were used, which entailed two completely different manufacturing and assembly processes. Two initiation systems were used for the pressed explosive type as well. The two concepts on the right with the larger boosters are the concepts representing the cast PBX formulation.

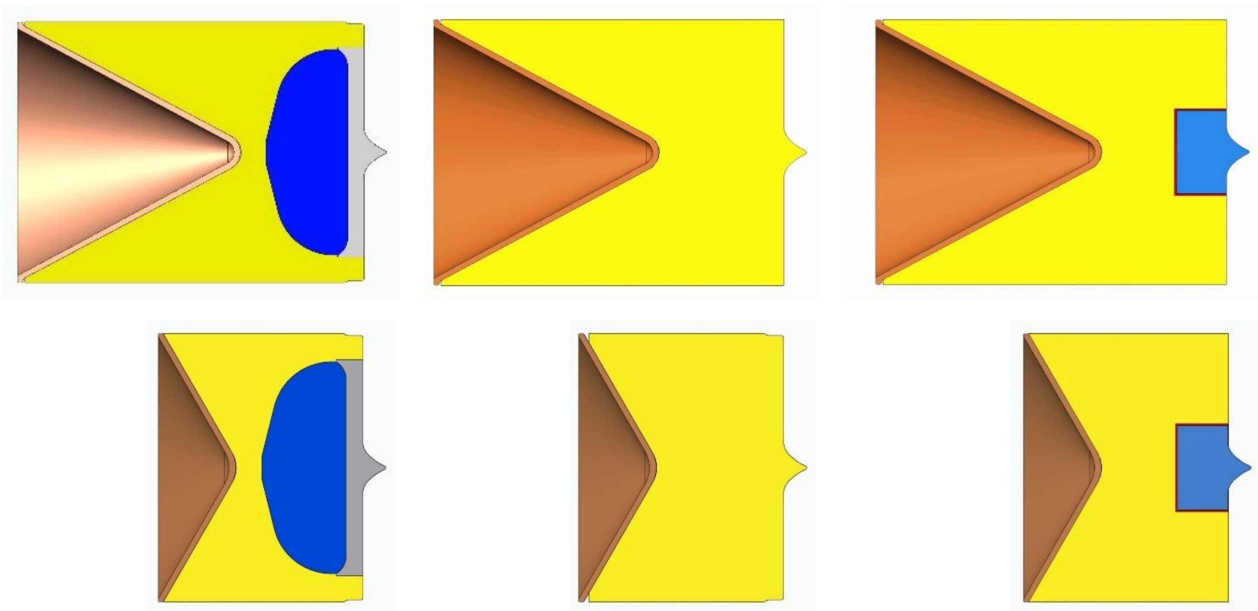

Figure 64: Six concept designs of shaped charge warheads, which were manufactured.

5.1. Liner Manufacture

5.2. Liner Forging Manufacture

One of the main focus points of the research was to evaluate/quantify the effect of various strain and strain-rates on shaped-charge liners with **fixed microstructures**. Since extraordinary emphasis was placed on the microstructure of the liners, a major effort was placed on the forging manufacturing process. Two liner designs were evaluated, 30° and 60° half angle respectively. The final microstructure of both samples had to be of comparable size in order to be certain that comparative analyses could be made from the different designs in terms of strain and strain-rate behaviour. It was essential to minimize the uncertainties that could arise from manufacturing differences. In particular, it was very important to ensure that comparable metallurgical starting material is present in all the liners, as it is known that jet parameters is sensitive for the starting microstructure in the liner.

The copper used for all samples were C10100, that is high-purity oxygen-free copper. The chemical composition is presented in Table 15. This is a high conductivity copper, which has, in the annealed condition, a minimum conductivity of 100%. Cu is determined by the difference between the impurity total and 100 %. For alloy C10100, the Cu value is exclusive of Ag. The following additional impurity maximum limits shall apply: Bi 1ppm (0.0001%); Cd 1ppm (0.0001%); Mn 0.5ppm (0.00005%); Ni 10ppm (0.0010%); Se 3ppm (0.0003%); S 15ppm (0.0015%); Sn 2ppm (0.0002).

Table 15: Chemical composition for C10100 copper.

Chemical Composition										
	Element									
	Cu	**Pb**	**Zn**	**Fe**	**P**	**Ag**	**As**	**O**	**Sb**	**Te**
Min (%)	99.99									
Max (%)		0.0005	0.0001	0.0010	0.0003	0.0025	0.0005	0.0005	0.0004	0.0002

The copper billets were forged; heat-treated and then forged again in various stages up to profiles comparable to that of the final liner shape. A detailed microstructural analysis was performed at each stage to quantify the effects of the cold working process on the microstructure and the various heat-treatment processes in between. Once the forgings met the microstructure and hardness requirements, they were sent for CNC machining and inspections. Liners were inspected by mass, thickness variations and roundness variation before used in the experiments. The liner thickness and roundness variations had to be below 30 µm.

5.2.1. **60° Liner**

The 60° liner was manufactured with the existing tooling process. The initial billet in (1), refer to Figure 65, was heat-treated and water quenched. The microstructural analysis was performed before and after heat-treatment. Thereafter it goes through each forging cycle with and without a heat-treatment cycle.

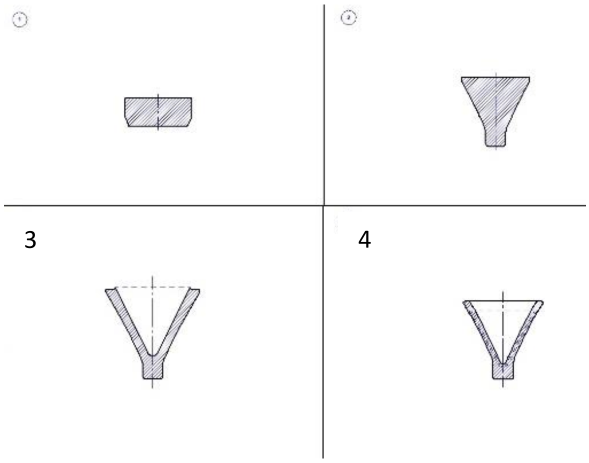

Figure 65: Process for manufacturing the 60° forging.

An additional process was considered using more copper as shown in Figure 66. This allowed the copper billet to be worked more in the axial direction. Sample number two & three already had microstructures comparable to the final forging of the process followed in Figure 65.

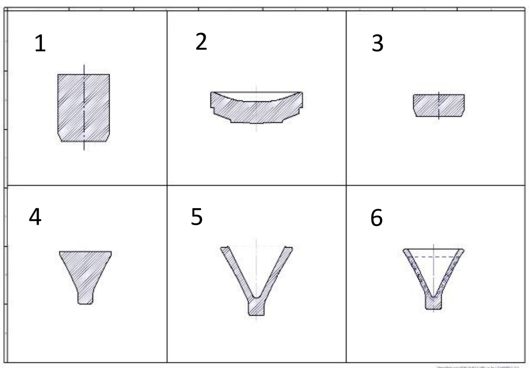

Figure 66: Additional forging process considered to obtain an improved microstructure.

The process followed in the end was that presented in Figure 65 due to the availability of copper and due to its comparability to the 60° forging.

Figure 67: Sample description: 1, see Figure 65.

Figure 68: Sample description: Two, see Figure 65.

Figure 69: Sample description 3, see Figure 65.

Figure 70: Sample description 4, see Figure 65.

The heat-treatment recipe in Table 16 should be read together with the sample description in Figure 65. The respective samples were manufactured according to the process outlined in Figure 65, but the heat-treatment was included at different stages. The samples were analysed for microstructure and hardness after each process.

5.2.2. **Table 16 explanation**

Twenty-two samples were analysed for the 60° liner alone. Each sample had a minimum of 10 points analysed for both hardness and microstructure. Nearly 300 images representing microstructure were generated in this study and its corresponding hardness measurement was conducted. This section will discuss the overall understanding regarding the microstructural trends and hardness measurements rather than presenting 300 images of micrographs and hardness measurements. The information attained was important from a product-manufacturing context, but is not relevant to the thesis.

5.2.2.1. Sample 1

The initial billet microstructure was between 400 µm and 600 µm thick. Sample 1 was machined to size then heat treated at 540 °C then water quenched; this process brought the microstructure down to an average of 200 µm with a range of between 50 µm and 350 µm at various positions within the sample. The hardness was measured to be 55 Vickers

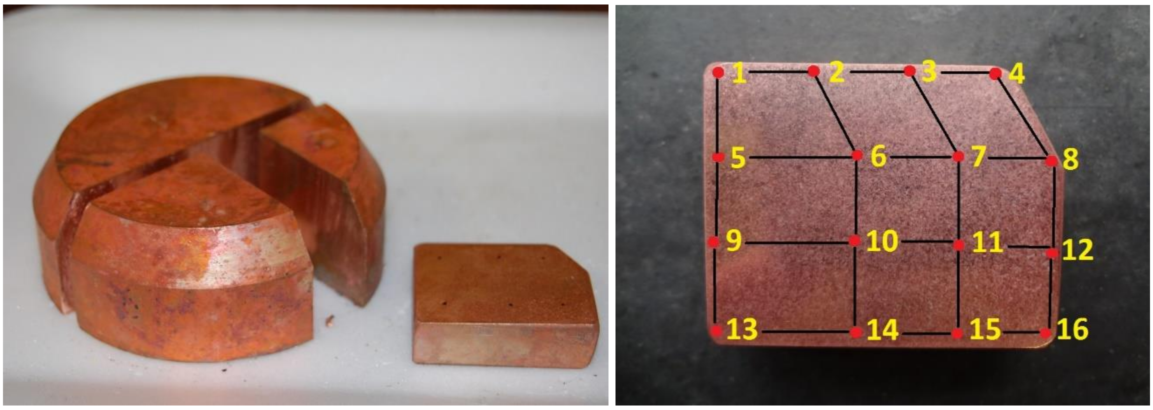

Figure 71: Sample 1 as analysed for microstructure and hardness.

5.2.2.1. Sample 2

Sample 2 was taken from the first stage of the forging process. This process was more about allowing the forging to locate well within the die/tool. Very little material flow was induced in this process; therefore, not much improvement to the microstructure was achieved. This process was rather important to allow uniform flow for the process to follow. This sample was analysed after forging without the heat-treatment and had elongated grains and a hardness of 128 Vickers. After heat-treatment, the sample had an average grain-size of 80 µm and a hardness of 50-55 Vickers.

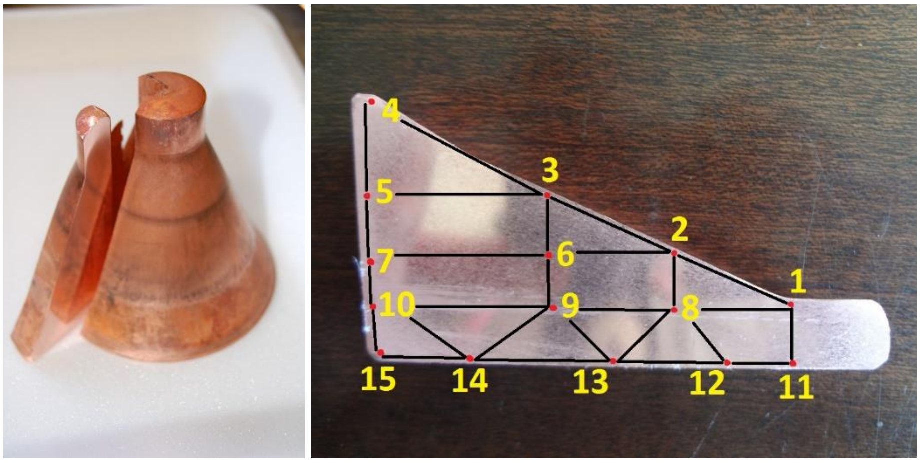

Figure 72: Sample 2 as analysed for microstructure and hardness.

5.2.2.2. Sample 3

Sample 3 was forged in a manner that allowed the material to flow. This sample was analysed after forging without any heat-treatment and had elongated grains and a hardness of 128 - 135 Vickers. After heat-treatment, the sample had an average grain-size of 30 µm and a hardness of 50-58 Vickers.

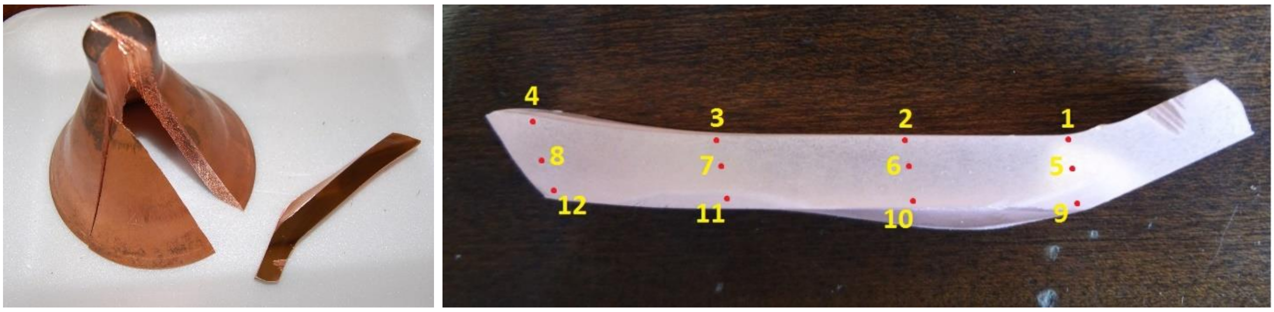

Figure 73: Sample 3 as analysed for microstructure and hardness.

5.2.2.3. Sample 4

Sample 4 was forged further, which allowed the material to flow more and meet the physical dimensions of the required liner. This sample was analysed after forging without the any heat-treatment and had elongated grains and a hardness of 128 - 135 Vickers. Numerous temperatures were attempted with the final forging ranging from 230 – 300 °C. The heat-treated sample had an average grain-size of 30 µm with a heat-treatment of 300 °C and a hardness of 45 Vickers. The lower heat-treatment of 230°C resulted in a hardness of 57 – 70 Vickers and the intermediate heat-treatment of 280°C also had a hardness of 46 Vickers.

Table 16: Copper forging sample heat-treatment signature.

Sample Number	Sample Description	HT_0 540°C Water Quenched	Forging 1	HT1 350°C Air Cooled	Forging 2	HT2 350°C Air Cooled	Forging 3	HT3 350°C Air Cooled
1	1	■						
2	2	■	■					
3	3	■	■	■				
4	4	■	■	■	■			
5	5	■	■	■	■	■		
6	8	■	■	■	■	■		
7	7.1	■	■	■	■	■	■	
8	7.2-300°C/1h	■	■	■	■	■	■	■
9	7.3-280°C/1h	■	■	■	■	■	■	■
10	7.4-230°C/1h	■	■	■	■	■	■	■
11	9	■	■	■	■	■	■	■
12	12	■	■		■			
13	15	■	■		■	■		
14	14	■	■		■		■	
15	13	■	■		■		■	■
16	6	■	■	■	■		■	
17	10	■	■	■	■		■	■
18	11	■	■	■				
19	2-2	■	■	■	■	■	■	■
20	3-2	■	■	■	■	■	■	■
21	Shock Treatment	■	■	■	■	■	■	■
22	30							

Table 17: Microstructures summary for copper forgings.

Sample Number	Sample Description	Grain-sizes (micron)					Comments
		Top (Apex)	**75%**	**50%**	**25%**	**Bottom**	
1	1	200 (50 - 350)	200 (50 - 350)	200 (50 - 350)	200 (50 - 350)	200 (50 - 350)	The same all over
2	2	Severe along.	Increasing along from bottom to apex	150(50-300) Slight elongation			
3	3	80 (40 - 200)	80 (40 - 200)	80 (40 - 200)	80 (40 - 200)	80 (40 - 200)	Fairly similar all over. All recrystallized.
4	4	40(20 - 120) Some oriented/elongated grains	Smaller, mildly elongated grains	Varied sizes elongated grains	Varied sizes elongated grains	50-60(20-150)	
5	5	20 - 90	30 (10 60)	30 (10 60)	30 (10 60)	40(20-80)	All re-crystallized. Very fine on inside. Good overall structure
6	8	50(20-150) RX, but many oriented grains	25-30(10-80) RX, good overall structure	30(10-80) RX, good overall structure	25-30(10-70) RX, good overall structure	40(20-70) RX, good overall structure	Good structure
7	7.1	40(20-150), some oriented grains	25(10-80), some oriented grains	25(10-70), some oriented grains	25(10-70), few oriented grains	25(10-50), few oriented grains	Relatively small grains, but with a fair amount of oriented grains
8	7.2-300°C/1h	70 (30-180)	35 (10-100)	30 (10-100)	35 (10-100)	-	
9	7.3-280°C/1h	80 (30-200)	40 (10-100)	40 (10-100)	40 (10-100)	-	

10	7.4-230°C/1h	50 (10-150)	50 (10-100)	30 (10-80)	30 (10-80)	-	
11	9	50 (10-90)	30 (10-90)	30 (10-90)	25 (10-80)	30 (10-80)	Fairly homogenous - good structure
12	12	Large elong grains	Large, severely elong grains	Large, severely elong grains	Large, severely elong grains	100(60 - 300) Mild elongation	
13	15	40 (10 140)	30- 40 (10 140)	30- 40 (10 140)	30- 40 (10 140)	45 (10 - 170)	All recrystallized, but with few long grains
14	14	Large, varied elong grains	Large, severely elong grains	Large, severely elong grains	Large, severely elong grains	100(60 - 300) Mild elongation	
15	13	30/40 (10-120) some elongated	25/30 (10-100) some elongated	30 (10-100) some elongated	30 (10-100) some elongated	30 (10-150)	
16	6	No results for this	sample	Sample	Resulted	In cracks	Failed
17	10	70(30 - 170), RX	20(<10 - 50), RX	20(<10 - 50), RX	20(<10 - 50), RX	30(10 - 60), RX	Best overall structure. Fine grains, mostly equiaxed and sizes more uniform
18	11	Similar to Sample 3					
19	2-2	40 (20 - 100)	25 (10 - 60)	30 (10 - 50)	25 (10 - 50)	20 (10 - 50)	
20	3-2	40 (10 - 100)	30 (10 - 60)	25/30 (10 - 50)	25 (10 - 60)	25 (10 - 40)	
21	Shock Trea.	120 (50-300)	60 (20-160)	50 (10-100)	40 (10-80)	60 (30-180)	
22	30	90 (30-200)	25 (10-60)	20 (10-40)	25 (10-40)	-	

Table 18: Copper forging hardness measurements.

Sample Number	Sample Description	Hardness (Vickers 5kg load)
		Apex----> Base
1	1	55.2
2	2	128.4
3	3	55.2 - 52.6 - 50.2 - 47.9
4	4	128.4 - 128.4 - 135.0 - 135.0
5	5	55.2 - 58.0 - 58.0 - 58.0
6	8	52.6 - 58.0 - 58.0 - 58.0
7	7.1	121.9
8	300°C/1h	46.5 - 46.5 - 45.5 - 44.5
9	280°C/1h	46.5 - 46.0 - 46.0 - 65.5
10	230°C/1h	69.6 - 56.5 - 57.9 - 65.9
11	9	55.2 - 58.0 - 58.0 - 58.0
12	12	151.4
13	15	52.6
14	14	128.4
15	13	58.0 - 55.3 - 58.0 - 58.0
16	6	
17	10	64.2
18	11	
19	2-2	71.6 - 75.7 - 64.2 - 64.2
20	3-2	61.0 - 64.2 - 67.7 - 64.2
21	Shock Treated	65.8 - 77.2 - 48.0 - 43.9
22	30	45.8 - 51.3 - 46.8 - 53.8

5.2.3. **120° Forging**

The process used for manufacturing the 120° forging is presented in Figure 74. The process first started with sample 3, which resulted in sample four not meeting the microstructure requirement. The longer initial billet strategy was then used for the 120° liner process to match up the microstructures of the two forging designs

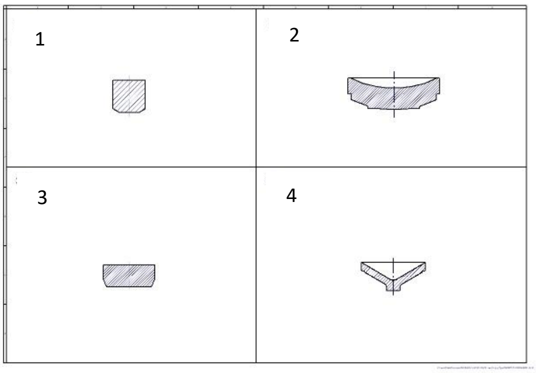

Figure 74: Forging process followed for the 120° liner.

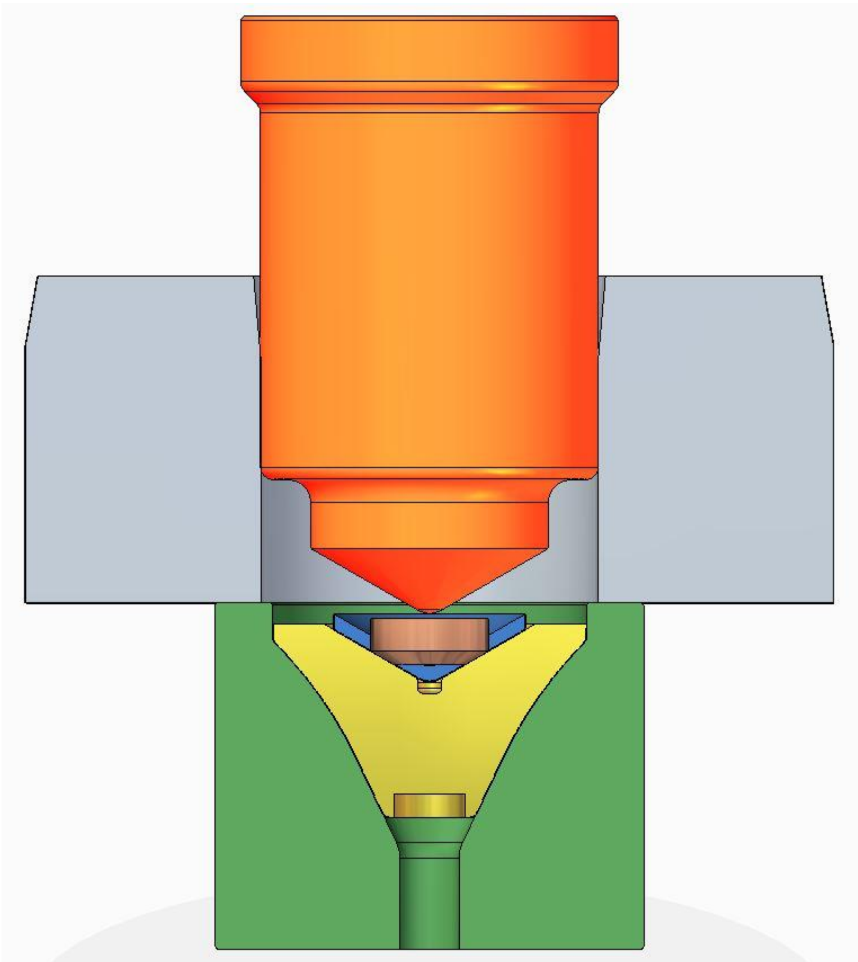

Figure 75: Forge tooling layout for manufacturing the 120° liner, before forging.

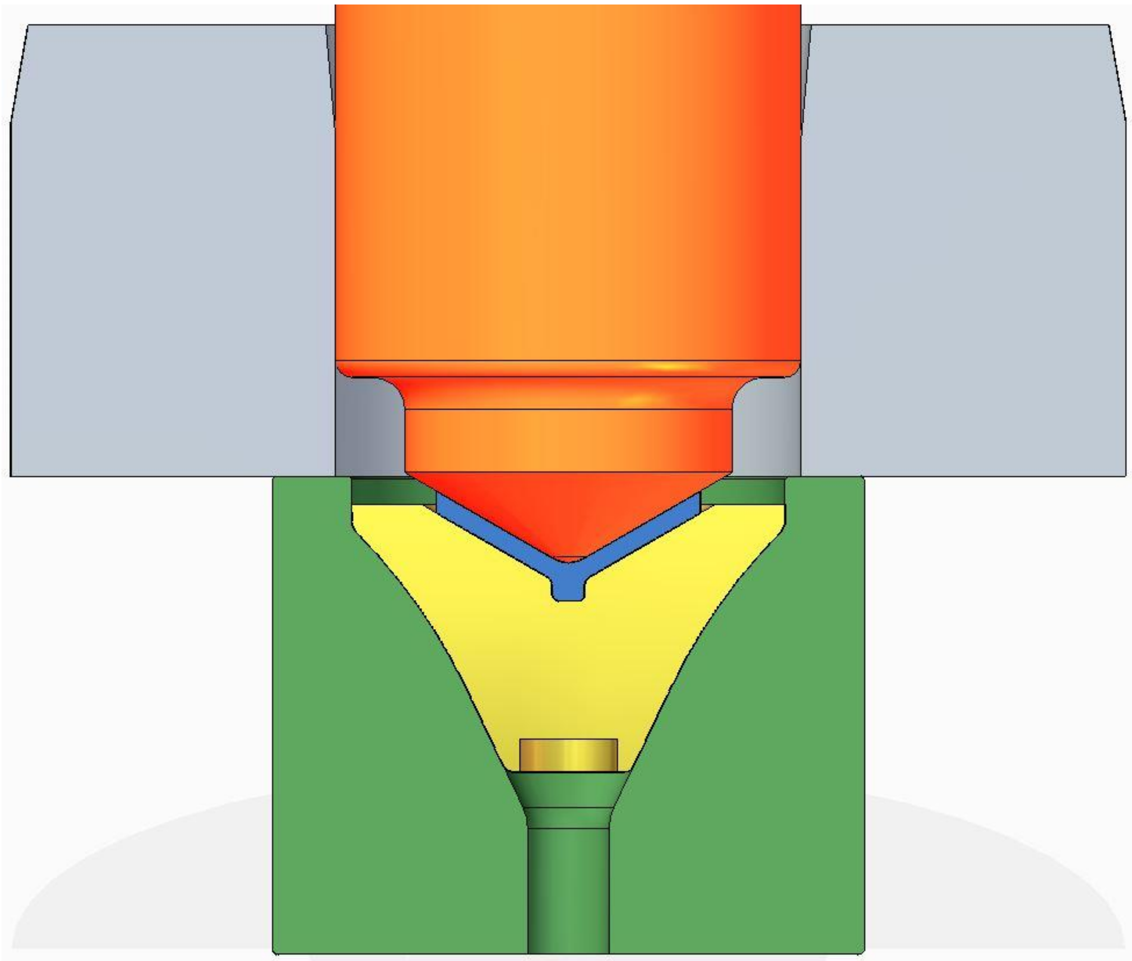

Figure 76: Forge tooling layout for manufacturing the 120° liner, after forging.

Table 19: Grain-sizes of new sample "As Forged" – (hardness = 106 HV).

Sample Position	Grain-size (µm)	Comment
Liner Base	±180	Range (50 – 250 µm)
33%	NA	(Large, severely elongated grains)
66%	NA	(Large, severely elongated grains)
Liner Apex	±80	Range (30 – 190 µm)

Table 20: Grain-sizes of new sample after heat-treatment for 1h @350°C – (hardness = 51 HV).

Sample Position	Grain-size (µm)	Comment
Liner Base	±20	Range (10 – 30 µm)
33%	±15	Range (10 – 30 µm)
66%	±35	Range (10 – 50 µm)
Liner Apex	±60	Range (30 – 100 µm)

Figure 77: 120° forging first stage sectioned.

5.3. Explosive Manufacture

Two explosive types were selected for this research, the first being a pressed Comp A3 (RDX: WAX 91:9) formulation and the second being a cast PBX formulation containing 55% RDX. These explosives were selected due to the availability of the raw materials and because the detonation parameters were favourable to induce strain-rate differences into the jet.

5.3.1. Comp A3

Four batches of Comp A3 were specially manufactured for this research. These batches of explosives were manufactured with specific characteristics addressing the objectives of this research. The four batches of Comp A3 comprised of the standard optimised RDM Comp A3 and another three batches controlling the initial RDX crystal sizes. The initial pressing parameters were evaluated with a small press. Charge diameters of 25 mm were used. A summary is presented in Table 23 and graphically presented in Figure 80.

Crystal sizes of 30, 100, 200 – 300 µm and 300 – 400 µm were selected for this investigation. The fine crystal size was selected to be comparable to the average grain-size of the copper liners. The larger crystals were selected three and ten times larger to ensure good variation in the three explosive batches.

This particular project made use of Comp A3: RDX 91% - Wax 9%. Three batches of RDX were manufactured with different crystal sizes at RDM's pilot plants. These three batches of explosives were placed behind OFHC copper liners with a fixed average grain-size of 30 µm. This section focusses on quantifying the effects of RDX particle-size on the break-up behaviour of the shaped-charge jets.

Four batches of the Comp A3 (RDX/WAX 91/9, ρ = 1.63 g/cm^3) with the different RDX particle-sizes were manufactured within a pilot plant as shown in Table 21. Scanning Electron Microscope (SEM) images of the respective RDX types are presented in Figure 81. Images of the three different Comp A3 batches are shown in Figure 78. By visual inspection, it was already noted that the granular material produced after coating with wax, showed particle-size differentiation. Moulding powder granules of PBX were prepared using the standard slurry coating process [88]–[90]. Gravimetric analysis were conducted on the three Comp A3 batches to ensure the RDX/WAX ratio was obtained. The results are presented in Table 22, and revealed all three were within specification with a variation of less than 1%.

5.3.1.1. RDX: WAX granular product manufacture

The respective batches of Comp A3 with RDX types are mentioned in Table 21. A photograph of all four batches are shown in Figure 78. The particle-size analysis of the four respective batches are presented in Table 22. The particle size distribution was conducted with a manual sieving process. A Malvern particle size analysis was also performed on the various batches of Comp A3 as shown in Figure 79. The Malvern Mastersizer 2000 is a laser diffractionparticle size analyzer, suitable for measuring particle sizes 0.021 mm – 2 mm. A small amount of sample (~0.25g) is required for analysis.

Table 21: Various lots of Comp A3 manufactured with different RDX grades/crystal sizes.

RDX grading	**Coarse**	**Standard**	**Medium**	**Fine**
Lot	**003**	**004**	**005**	**006**
RDX Name	107	101	105	104
RDX Grain Size (µm)	300 - 400	200 - 300	100	20 - 30

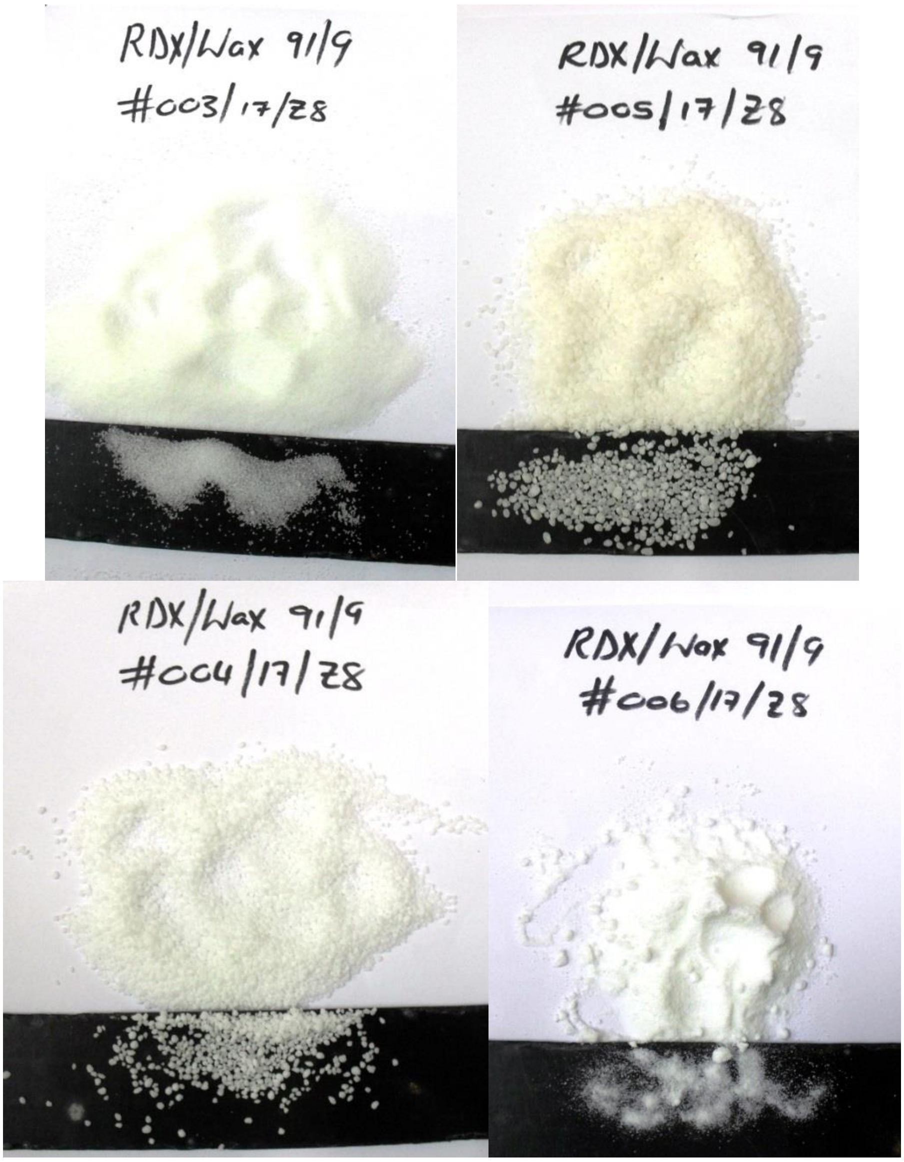

Figure 78: Four lots of granular Comp A3.

Table 22: Particle-size (P) analysis (fines) for four batches of Comp A3

Characteristics	Lot 003		Lot 004		Lot 005		Lot 006	
RDX%	91.8		90.4		90.3		90.5	
Wax%	8.5		9.6		9.7		9.5	
Wax content of fractions	Fraction	Wax Content	Fraction	Wax Content	Fraction	Wax Content	Fraction	Wax Content
425 µm <P	Balance		Balance		Balance		Balance	
425 µm<P<250 µm	49.4	7.8	1.8	7.5	3.0	6.4	17.5	14.4
250 µm<P<150 µm	5.1	7.4	1.2	5.2	2.4	5.7	14.6	10.2
P<150 µm	0.5	7.2	1.2	4.9	2.9	5.6	45.6	3.7

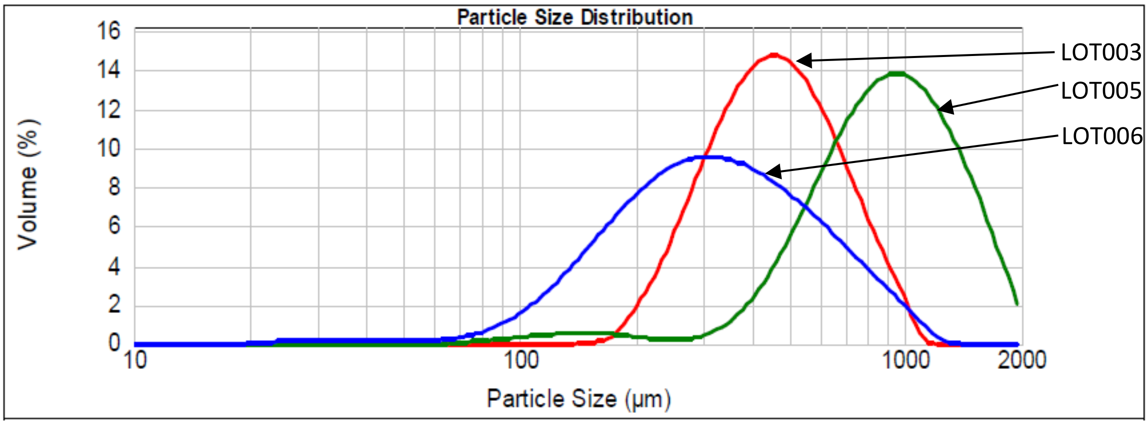

Figure 79: Malvern analysis for the respective batches of Comp A3.

5.4. **RDX: WAX pressing analysis**

The standard Comp A3 formulation, Lot 004, was used to conduct a pressing analysis. Charges were pressed at room temperature of 21°C and an elevated temperature of 70°C at 100, 150 and 200 MPa effective pressure. The size of the charges pressed for the Comp A3 pressing analysis was 25 mm in diameter and 25 mm long. A summary of the initial pressing analysis at 25 mm diameter is presented in Table 23 and Figure 80. The data is also presented in the form of its theoretical maximum density (TMD).

Table 23: Initial pressing analysis at diameter 25 mm.

Lot	Pellet No	Diameter	Length	Mass	Density	TMD	Pressure
		mm	mm	g	g/cc	%	MPa
		Room Temperature					
3	1	25.08	25.27	20.22	1.620	96.93	100
	2	25.09	25.22	20.23	1.622	97.09	150
	3	25.10	25.14	20.22	1.625	97.28	200
4	1	25.08	25.44	20.21	1.608	96.23	100
	2	25.09	25.35	20.21	1.612	96.50	150
	3	25.10	25.32	20.21	1.613	96.54	200
5	1	25.08	25.36	20.20	1.612	96.49	100
	2	25.08	25.28	20.21	1.618	96.84	150
	3	25.09	25.22	20.18	1.618	96.85	200
6	1	25.08	26.60	20.22	1.539	92.08	100
	2	25.08	26.08	20.22	1.569	93.92	150
	3	25.08	25.78	20.23	1.588	95.06	200
		Temperature - 70°c					
3 Hot	1	24.98	25.18	20.25	1.641	98.20	100
	2	24.97	25.16	20.24	1.643	98.31	150
	3	24.97	25.15	20.25	1.644	98.40	200
4 Hot	1	24.96	25.33	20.24	1.633	97.73	100
	2	24.96	25.25	20.23	1.637	97.99	150
	3	24.96	25.25	20.24	1.638	98.04	200
5 Hot	1	24.95	25.24	20.23	1.639	98.11	100
	2	24.95	25.22	20.22	1.640	98.14	150
	3	24.96	25.22	20.21	1.638	98.01	200
6 Hot	1	24.97	25.45	20.25	1.625	97.24	100
	2	24.98	25.31	20.21	1.629	97.50	150
	3	24.98	25.30	20.24	1.632	97.69	200

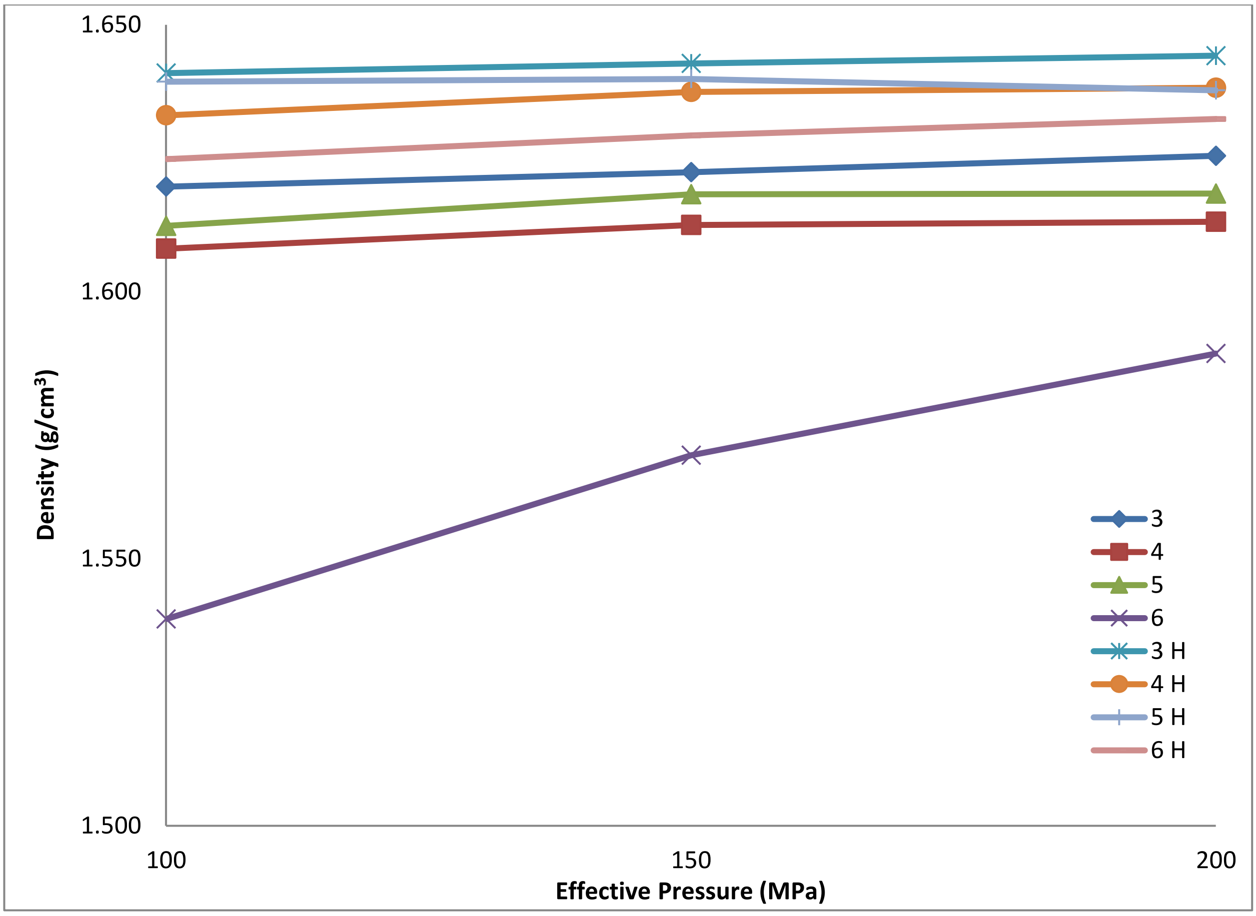

Figure 80: Summary of the initial pressing analysis at 25 mm diameter.

The pressing analysis shows an increase in density at 21°C from 94.1% TMD up to 95.67% TMD with an increase in effective pressure from 100 to 200 MPa. The press was heated to 68.6 °C and new charges were pressed at similar pressures. A more uniform density was then measured across a variety of pressures. This can be explained due to the binder softening at 68.6 ^{0}C. The density at elevated temperature was within 1% TMD from 100 to 200 MPa effective pressure. Refer to Table 19 and Table 20 for lot grain sizes.

5.4.1. **Smart-Zoom Light Microscopy Analysis**

Light and electron microscopy was used to evaluate differences between the pressed explosive charges manufactured with different initial crystal sizes. Figure 83 and Figure 84 shows the images from a typical light microscope. An in house Zeiss Smartzoom 5 digital light microscope was used. Electron Microscopy gave excellent images of the coated RDX wax crystals as shown in Figure 81 and corresponding photograph of the granular material in Figure 82. An in house Zeiss EVO MA15 electron microscope was used for used. The images were magnified 100 times.

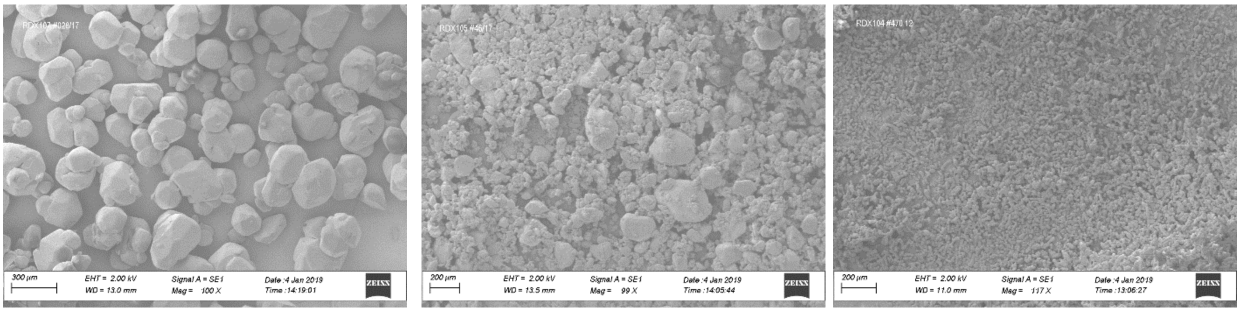

Figure 81: Scanning electron microscope images of RDX 107, 105 & 104 respectively.

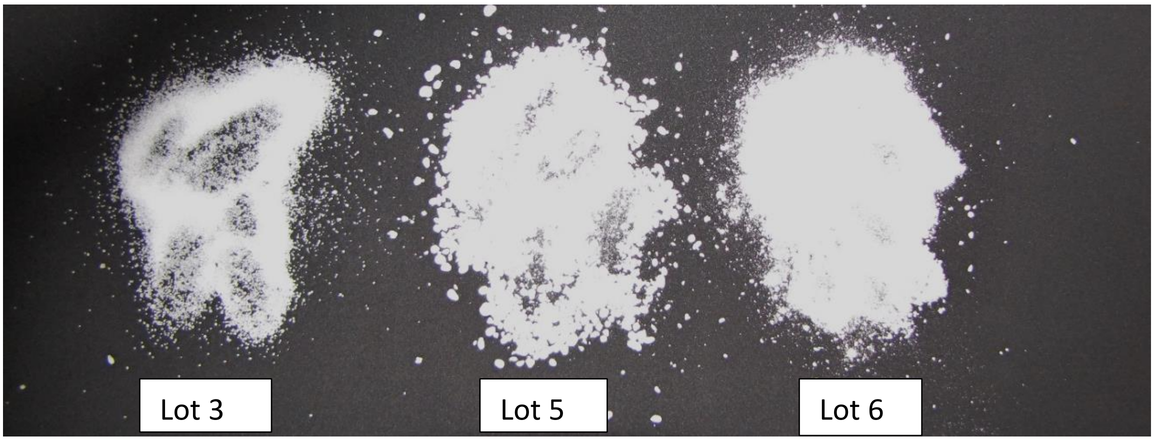

Figure 82: Photograph of the three explosive batches of Comp A3.

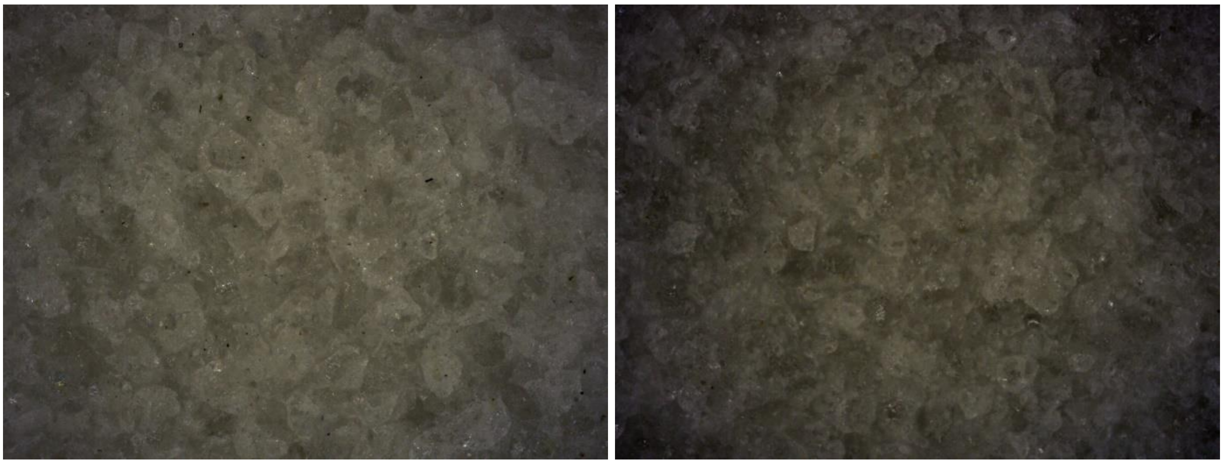

Figure 83: Light microscopy for Lot 3 and 4.

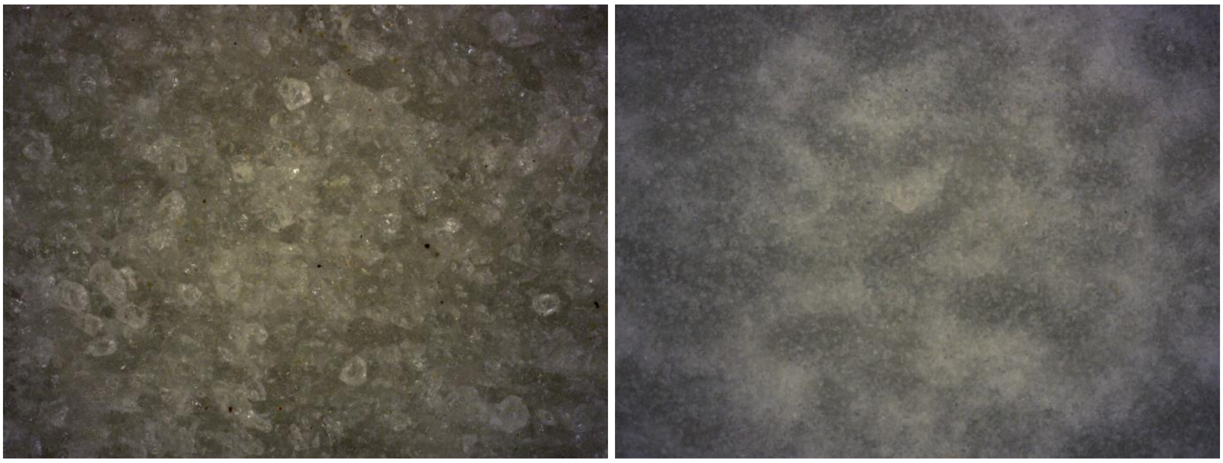

Figure 84: Light microscopy for Lot 5 and 6.

5.4.2. **Scanning Electron Microscopy**

SEM images were attempted after pressing the Comp A3. This was an attempt at quantifying the average crystal size after pressing from the hypotheses perspective of crystal breakage. This investigation was paused for now since an extensive exercise involving sample preparation is required.

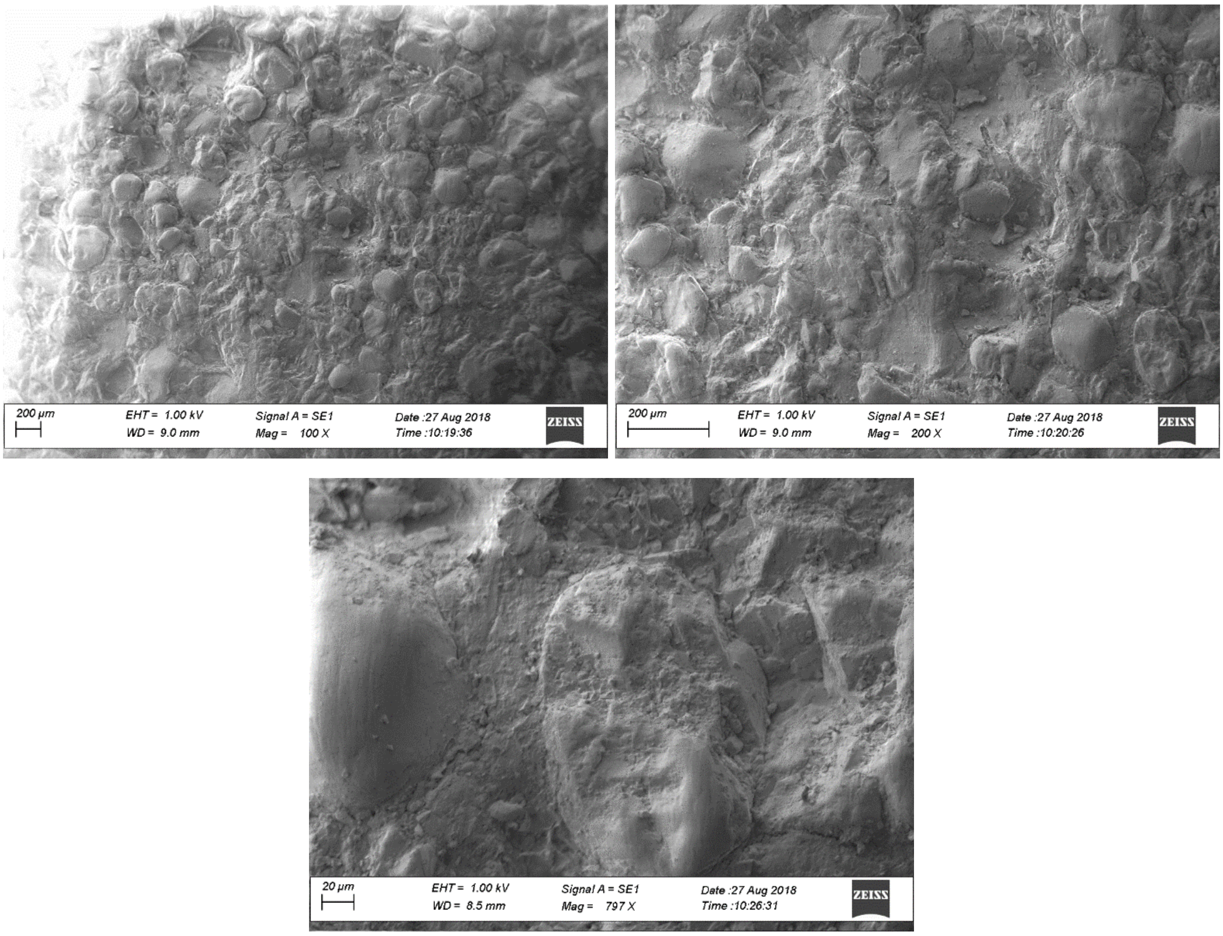

Figure 85: SEM images of a pressed Comp A3 charge.

Part of the press explosive investigation was to quantify the effect of RDX crystal size on the break-up-time of jets. Four lots of Comp A3 was manufactured with different crystal sizes. The 100% theoretical maximum density (TMD) was used as 1.671 g/cm^3.

5.4.2.1. **Press Reports**

A layout of the press tool used to press the explosive charges are shown in Figure 86. Explosive Press reports for each explosive Lot is presented in Table 24 to Table 27. All four batches were pressed at the same pressure and resulted in densities within ± 0.01 g/cm^3.

Figure 86: Tools used to press the explosive charges.

Table 24: Density report for Comp A3 Lot 3.

Charge No	Diameter 1	Diameter 2	Height	Mass	Diameter ave	Density	TMD	Accept
	mm	mm	mm	g	mm	g/cc	%	
1	85.90	85.96	136.63	1310.9	85.93	1.654	99.0	Yes
2	85.85	85.93	136.85	1311.0	85.89	1.653	98.9	Yes
3	85.90	85.97	136.80	1311.1	85.94	1.652	98.9	Yes
4	85.91	85.93	136.89	1310.3	85.92	1.651	98.8	Yes
5	85.91	86.00	136.68	1310.5	85.96	1.652	98.9	Yes
6	85.87	85.97	136.68	1310.6	85.92	1.654	99.0	Yes
7	85.89	85.98	136.69	1310.8	85.94	1.653	98.9	Yes
8	85.90	85.94	136.69	1310.7	85.92	1.654	99.0	Yes
9	85.85	85.96	136.73	1310.7	85.91	1.654	99.0	Yes
10	85.84	85.93	136.75	1310.6	85.89	1.654	99.0	Yes
11	85.88	85.98	136.73	1310.5	85.93	1.653	98.9	Yes

Table 25: Density report for Comp A3 Lot 4.

Charge No	Diameter 1	Diameter 2	Height	Mass	Diameter ave	Density	TMD	Accept
	mm	mm	mm	g	mm	g/cc	%	
1	85.85	85.86	137.85	1310.7	85.86	1.642	98.3	Yes
2	85.85	85.87	137.92	1310.7	85.86	1.641	98.2	Yes
3	85.84	85.88	137.94	1310.7	85.86	1.641	98.2	Yes
4	85.83	85.87	137.96	1310.8	85.85	1.641	98.2	Yes
5	85.83	85.86	137.68	1310.6	85.85	1.645	98.4	Yes
6	85.82	85.87	141.59	1344.5	85.85	1.641	98.2	Yes
7	85.81	85.87	141.60	1344.5	85.84	1.641	98.2	Yes
8	85.83	85.85	141.58	1344.6	85.84	1.641	98.2	Yes
9	85.82	85.88	141.54	1344.8	85.85	1.641	98.2	Yes
10	85.85	85.85	141.48	1344.8	85.85	1.642	98.3	Yes

Table 26: Density report for Comp A3 Lot 5.

Charge No	Diameter 1	Diameter 2	Height	Mass	Diameter ave	Density	TMD	Accept
	mm	mm	mm	g	mm	g/cc	%	
1	85.77	85.79	137.76	1310.3	85.78	1.646	98.5	Yes
2	85.76	85.79	141.49	1344.2	85.78	1.644	98.4	Yes
3	85.72	85.79	141.46	1344.3	85.76	1.645	98.5	Yes
4	85.78	85.80	141.35	1344.8	85.79	1.646	98.5	Yes
5	85.77	85.80	141.33	1344.2	85.79	1.646	98.5	Yes
6	85.76	85.80	141.47	1344.4	85.78	1.644	98.4	Yes
7	85.77	85.83	141.45	1344.1	85.80	1.643	98.4	Yes
8	85.76	85.77	141.43	1344.1	85.77	1.645	98.4	Yes
9	85.76	85.77	141.31	1344.2	85.77	1.647	98.5	Yes
10	85.75	85.78	141.27	1344.0	85.77	1.647	98.6	Yes

Table 27: Density report for Comp A3 Lot 6.

Charge No	Diameter 1	Diameter 2	Height	Mass	Diameter ave	Density	TMD	Accept
	mm	mm	mm	g	mm	g/cc	%	
1	85.84	85.86	141.14	1342.5	85.85	1.643	98.3	Yes
2	85.82	85.86	141.35	1344.0	85.84	1.643	98.3	Yes
3	85.84	85.90	141.63	1343.8	85.87	1.638	98.0	Yes
4	85.77	85.82	141.73	1344.1	85.80	1.640	98.2	Yes
5	85.80	85.85	141.43	1344.1	85.83	1.643	98.3	Yes
6	85.82	85.89	141.38	1343.5	85.86	1.641	98.2	Yes
7	85.79	85.82	141.54	1344.2	85.81	1.642	98.3	Yes
8	85.80	85.85	141.45	1344.0	85.83	1.642	98.3	Yes
9	85.81	85.89	141.38	1343.8	85.85	1.642	98.3	Yes
10	85.77	85.80	141.43	1344.0	85.79	1.644	98.4	Yes

An image of the pressed and machined Comp A3 charges are shown in Figure 87.

Figure 87: Machined Comp A3 charges.

5.4.3. **Warhead Assembly**

The individual components used to make up the two concepts with 60° liners with point and peripheral initiation systems are presented in Figure 88.

Figure 88: Components used for Concepts 1 & 2.

The X-ray images (used for quality control) for the respective assemblies are presented in Figure 89. The X-ray apparatus used was a Phillips 420 kV X-ray system and General Electric DXR500 digital flat panels.

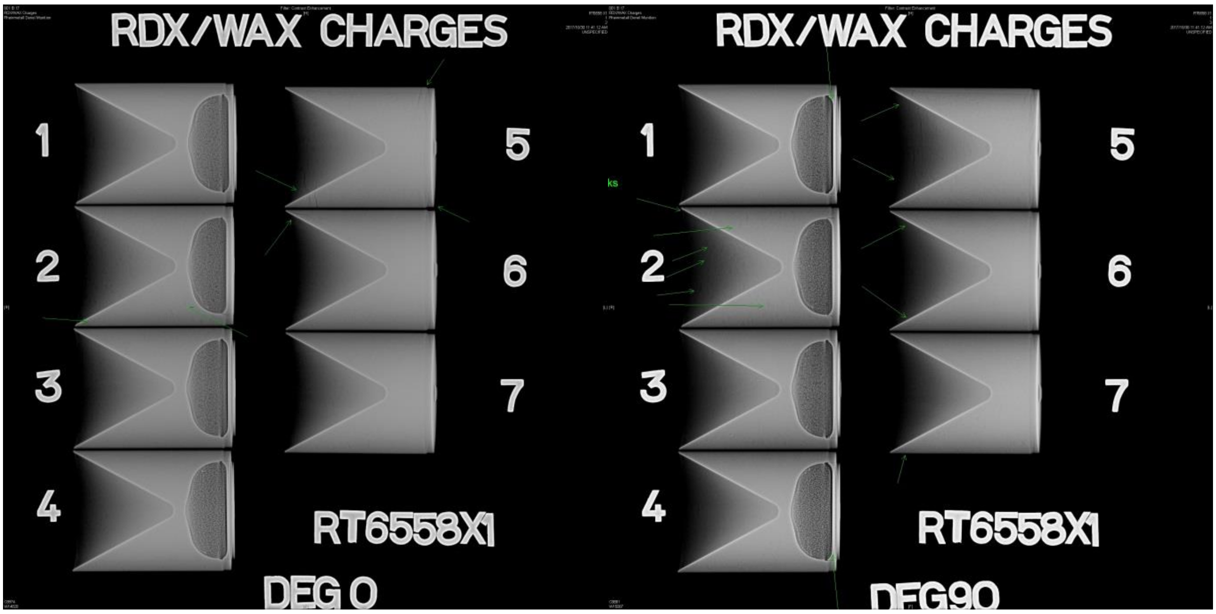

Figure 89: X-rays for the respective assemblies.

5.5. **120° Design**

The Individual components making up the point- and peripheral-initiated shaped-charges for 120° liners with Comp A3 are presented in Figure 90.

Figure 90: Components making up the point and peripheral initiated shaped-charges for 120° liners.

Figure 91: Assemblies for the peripheral-initiated assemblies on the left and point-initiated assemblies on the right.

5.6. Cast PBX Manufacturing Process

5.6.1. Cast PBX Process Design

Initial simulations indicated that an explosive with low VOD would generate an additional data point in terms of strain and strain-rate. That is by further reducing the tip and tail velocity of the shaped-charge jet. The simulations were done with HNS at 1.4 g/cm^3. A cost analysis of this formulation showed that experimentation was not feasible. An experimental formulation within the RDM database was then selected with similar explosive properties. Formulation F, a cast PBX, was selected for use in the experimental evaluation. The explosive properties of the simulated formulation (HNS) vs the manufactured formulation is presented in Table 28. The processibility of cast PBX vs a pressed explosive is completely different. The cast explosive was prepared in fluid or paste form and then poured into a container to cure. It was decided to design tooling in such a way that the casting process is conducted into the final shape required, i.e. without further modification or machining. The shaped-charge design for both liners are presented in Figure 92. The split mould designs used for manufacturing the concepts containing cast PBX are presented in Figure 93 and Figure 94. Split moulds were the preferred tooling design since bare charges were required for the shaped-charge evaluation.

Table 28: Explosive properties of the manufactured explosive and the simulated explosive.

Formulation	VOD (mm/µs)	Density (g/cc)	Detonation Pressure (kbar)
			(calculated: $P = 2.5\phi V^2$)
F (55% RDX & 15% KCl)	6.00	1.40	126
HNS 1.4	6.34	1.40	141

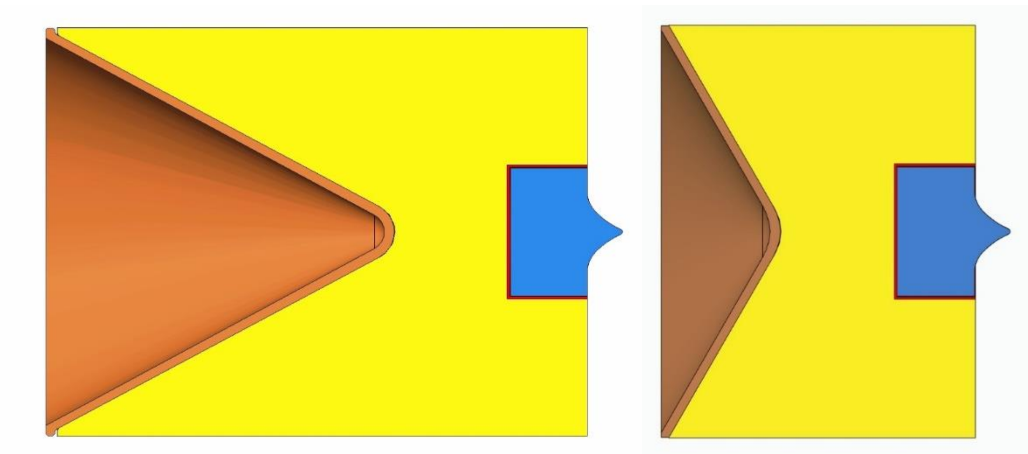

Figure 92: Two designs used to evaluate the cast explosive.

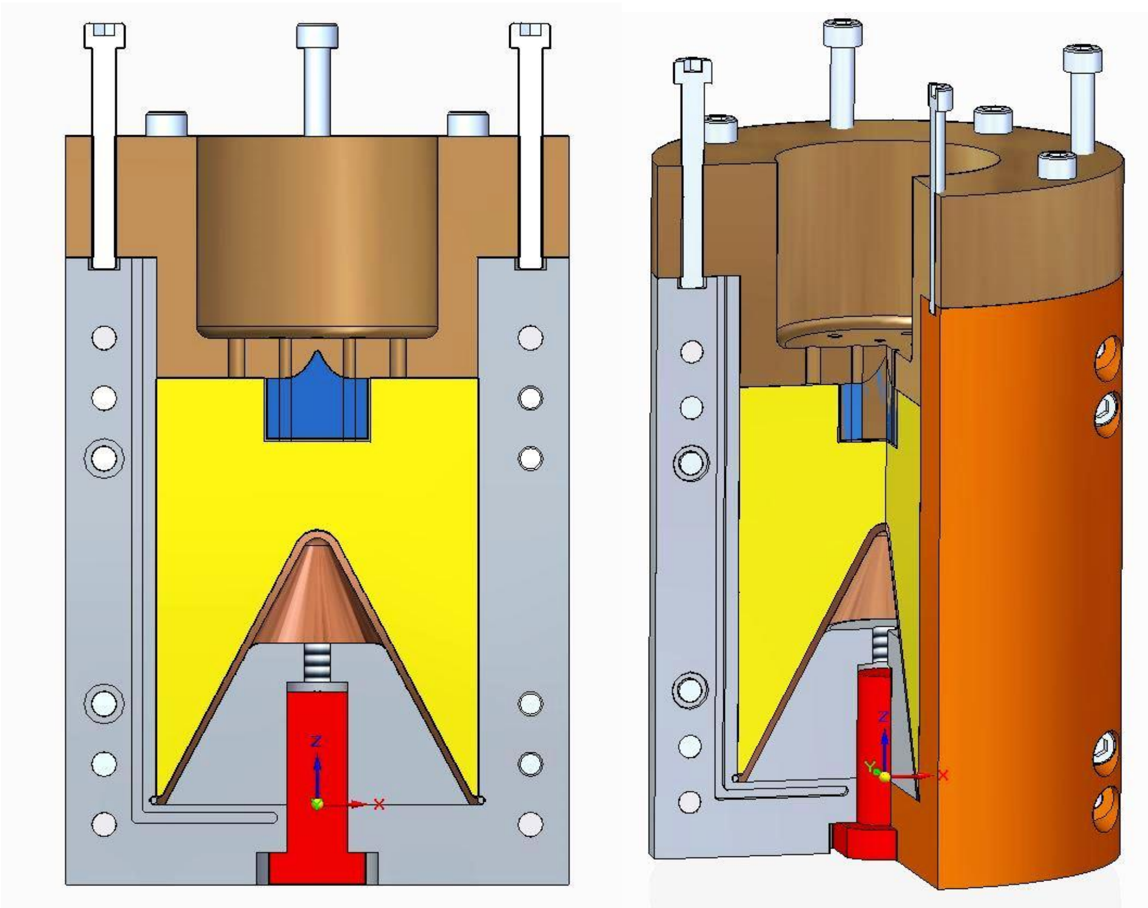

Figure 93: Tooling design used to manufacture the design 3.

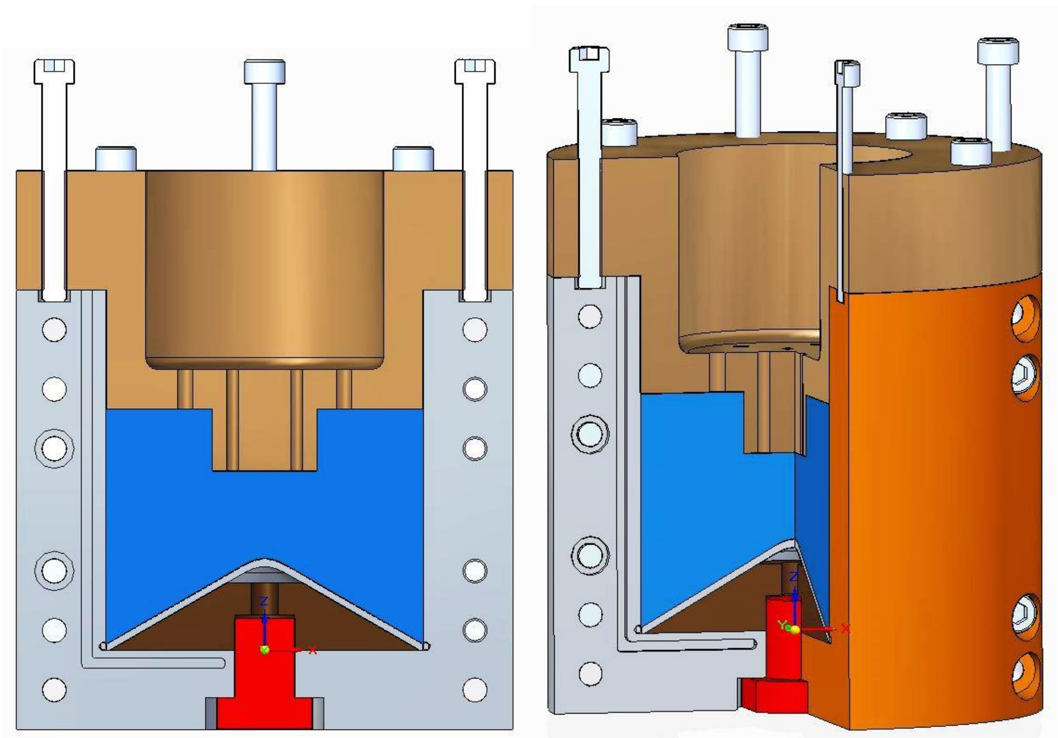

Figure 94: Tooling design used to manufacture the design 6.

5.6.2. **Cast PBX Process Manufacture**

The manufacturing tooling design was a rather niche concept within this project. The split mould feature allowed for casting to the final diameter, casting straight on the liner has numerous benefits. The use of Teflon coating resulted in the perfect finish of the explosive. The ram tool which took into account the booster cavity and length of the booster was well selected taking the settling binder layer into account considering an experimental (not optimised) formulation was used. The hardware before casting is presented in Figure 95. The hardware after curing is shown in Figure 96. The procedure of dismantling is shown in Figure 97. Figure 98 shows the dismantled moulds, while Figure 100 and Figure 101 shows the recovered shaped-charge warheads with cast PBX in direct contact the copper liners. A settling binder layer is observed in Figure 101. This was expected considering an experimental formulation was used. Non-optimised formulations have this defect during casting explosives and was taken into account by accommodating for a booster to be positioned 25 mm deep into the charge assembly. The X-rays for the respective assemblies are presented in Figure 102. A photograph of the charge is presented in Figure 103.

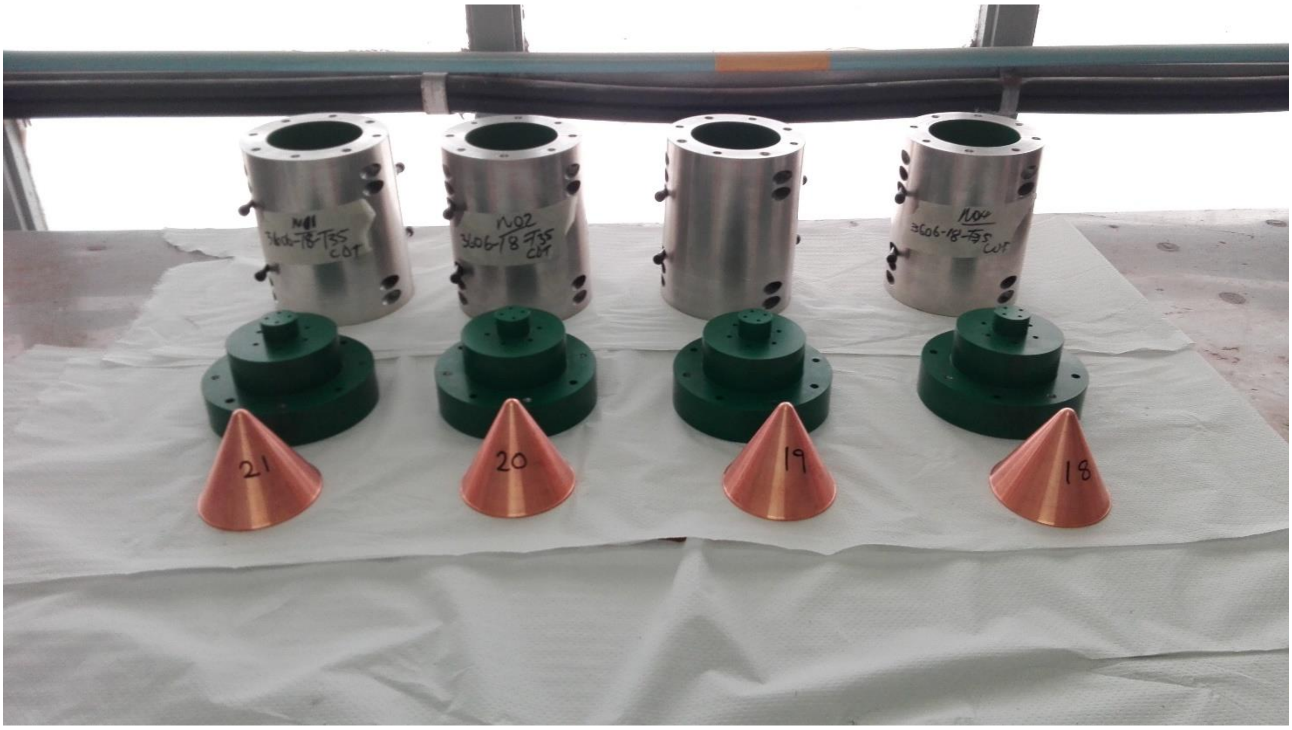

Figure 95: Tooling before casting took place.

Figure 96: Split moulds after PBX curing.

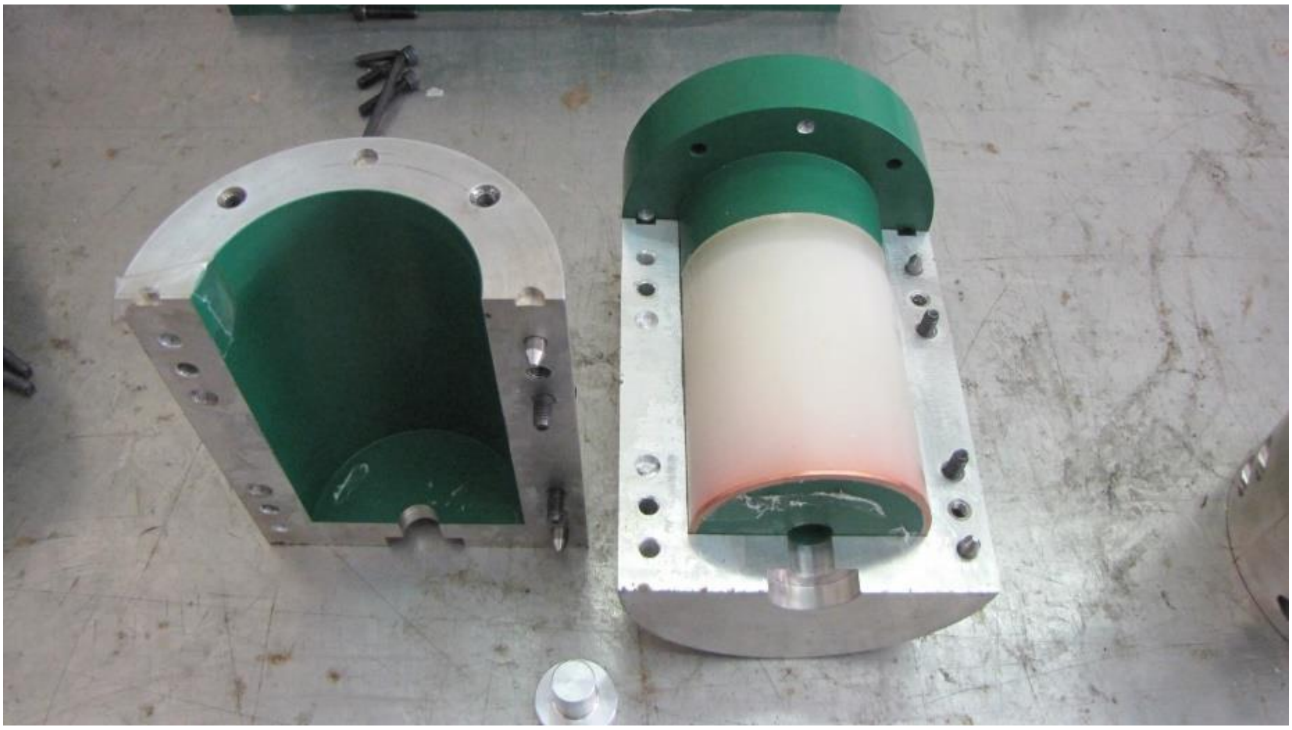

Figure 97: Split mould disassembly of a single charge.

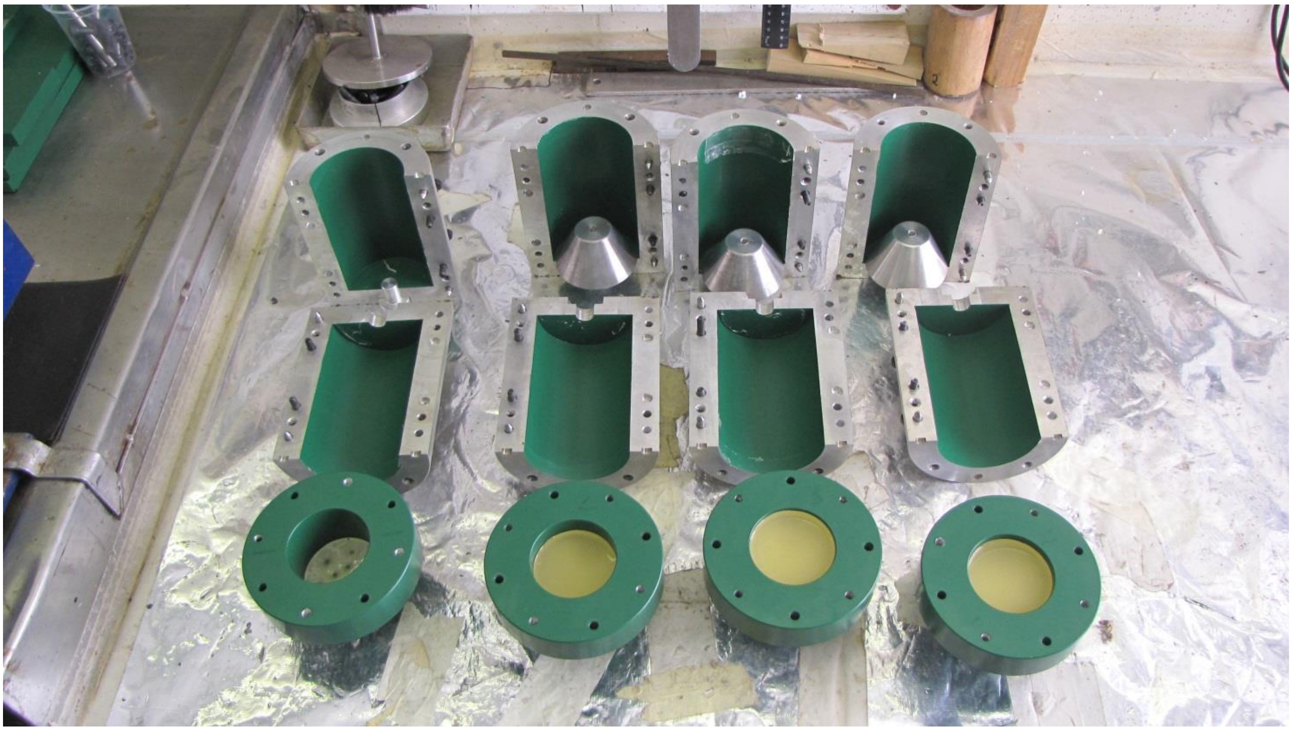

Figure 98: Disassembly of four split moulds.

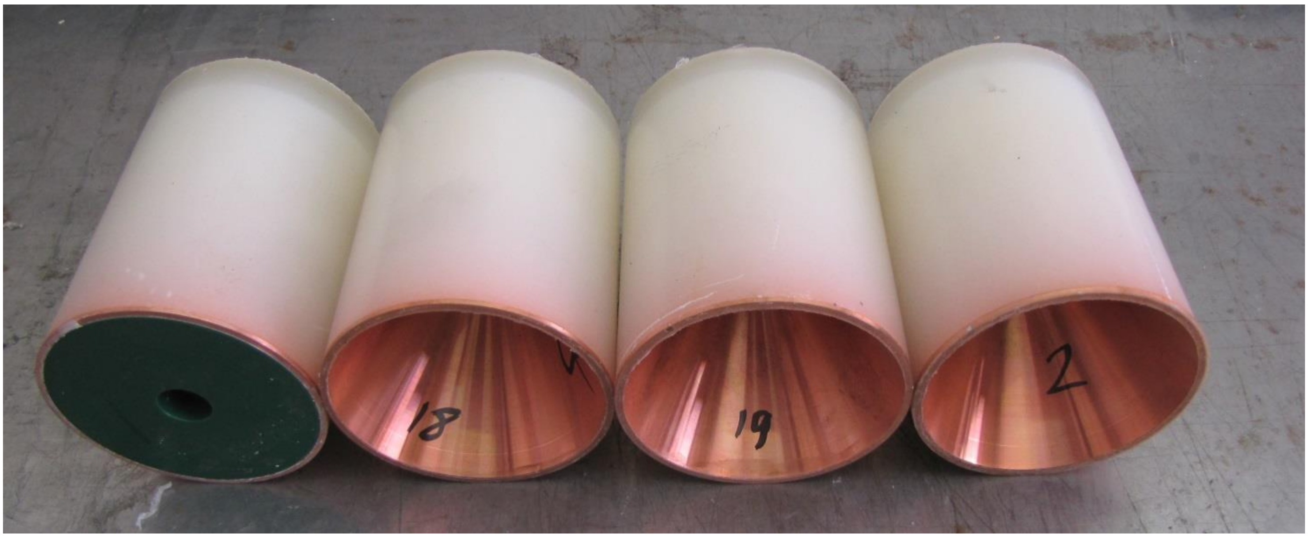

Figure 99: Recovered shaped-charges from split moulds, front view.

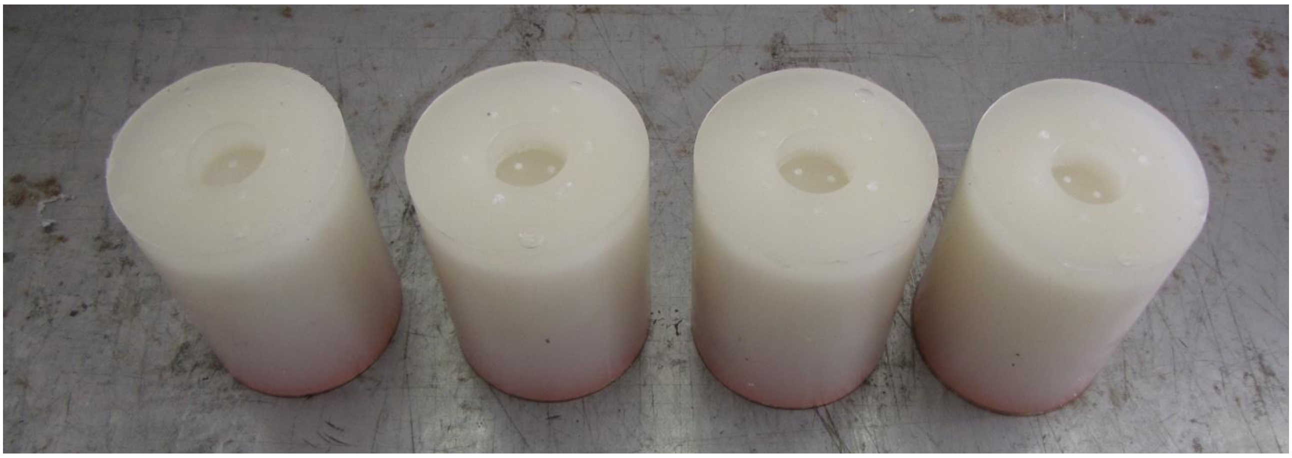

Figure 100: Recovered shaped-charges from split moulds, top view.

Figure 101: Recovered shaped-charges from split moulds, side view.

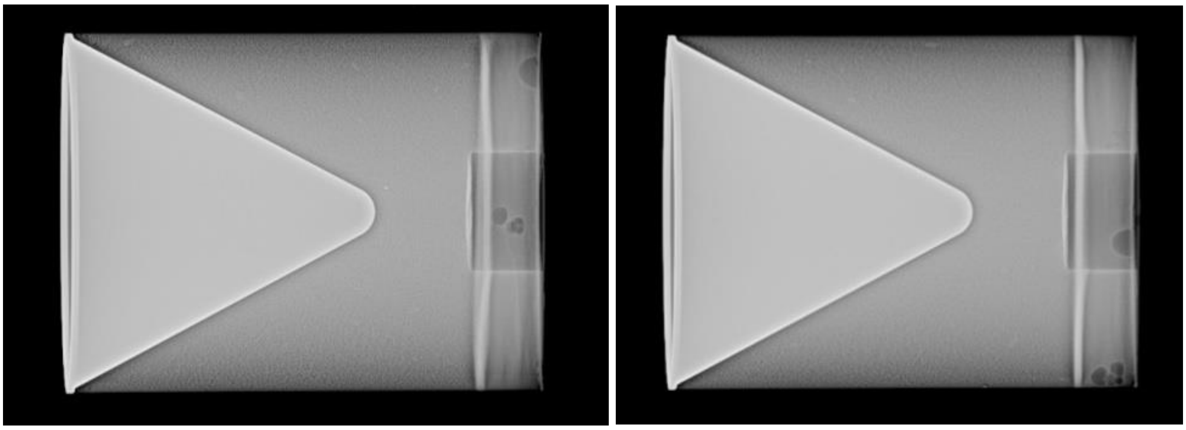

Figure 102: X-ray of cast PBX charge.

Figure 103: Cast PBX charge assembly including the booster.

6. EVALUATION

6.1. Introduction

An X-ray is an electromagnetic wave of high energy and very short wavelength, which is able to pass through many materials opaque to light. X-ray photography for observing the jets produced by shaped-charges has become an important research tool to explain jet behaviour. The obstructing cloud of smoke and flame, which detracts from ordinary photographic processes, does not affect flash-radiographs, which produce clear, sharp outlines of the jet material with exposure times of the order of 0.1 microsecond [91].

Flash X-ray radiography is useful in studies of macroscopic properties during extremely short time intervals. It is essentially the X-ray equivalent of optical strobe photography. The fact that the pulse length of a flash X-ray system is in the region of 30 ns makes it ideally suited to the task of examining material that is changing or moving very rapidly through air or opaque material. A typical radiograph set-up consists of the object or event to be studied placed as far as possible from the flash X-ray machine diode. The X-ray photographic plate is then placed closely behind the specimen. The distance is necessary to approximate an incident X-ray plane wave as closely as possible to avoid edge effects. These detector systems can become more complex by using intensifying screens or optical image intensifiers prior to the X-ray film. Since the event under study is explosive in nature, special protection boxes/blast deflectors were designed to prevent damage to the detection system[92].

A double flash X-ray radiographic system has been in operation at the Warhead Testing Facility for a number of decades. Each X-ray tube is positioned at an angle with respect to its immediate neighbour. The film holder, receiving radiation from its corresponding X-ray tube is orthogonal to the direction of jet flight. This arrangement allows both flashes to emit at different positions on a single X-ray film. Each film holder contains three X-ray films with dimensions 300 mm by 900 mm, laid end to end for a total length of 2700 mm. The round is detonated right next to the first cassette holder in front of a blast protection plate, made of plywood in this case. The jet travels parallel to the length of the three film cassettes. The X-ray tubes are triggered at pre-determined and set time intervals after charge initiation. RP83 detonators with known delays were used to initiate the shaped-charges. Shaped-charge jets are also characterised by double –orthogonal synchro streak technique as discussed in [93]. This facility was not available for evaluation.

For a short time interval after collapse of the shaped-charge liner walls, the material from the inside of the liner forms a continuous axial jet. The gradient in velocity between the front and rear of the jet causes the jet to increase in length with time. This produces stress on the solid jet material, which causes it to neck, and then break-up into many individual particles. With all other conditions equal, the time of initial jet-break-up depends upon the physical properties of the metal used to form the liner. Jets formed by ductile metal liners remain in the continuous state for longer than those obtained from less ductile liners do. For example, a steel jet breaks up sooner than a copper jet.

This section will deal exclusively with the properties of jets from the charge and copper liners discussed in the preceding sections, i.e. liners having an apex angle of 60° and 120°, respectively. Each liner produced jets from two explosive types and two initiation systems. Three charge designs per liner have been studied to determine the effect of liner angle, initiation system, explosive type and explosive crystal size upon jet flight and jet-break-up characteristics.

Double flash X-ray radiographs of the jets from all charges are shown in Figure 119 to Figure 126. The flash-X-ray exposure time (in microseconds) after initiation is noted in Table 29. These times were selected in such a way as to detect the structure of the jet in particulated form. Due to the variance in break-up-times along the jet, the first flash is usually selected with the front portion of the jet being particulated and the second flash is used to show the rear end to be particulated. The pre-determined delay times varied as the charge design varied. Some designs were fully particulated in the first flash already. Corresponding jet particles in the first and second flash of each jet are distinguishable and have been numbered on the X-ray photograph consecutively from tip to rear. Measurements on the individual particles were made via a program called JETP. JETP is a Matlaboratory based software program, an image detection software package designed specifically for digitising flash X-ray jets directly from photographs of the original radiographs. JETP has been improved on two occasions over the phase of this project.

The relative positions of the X-ray tube, jet, and film were arranged to produce only negligible magnification on the film, typically 1.3 times the actual distance in the set-up. However, some error was introduced when the three 300 x 900 mm film panels were placed together to show the complete jet. These panels were enclosed in film holders when exposed and their butting ends produced a gap between adjacent films. These gaps are noticed in JETP and any missed particles may be artificially introduced if it is highly probable for a particle to be in this gap.

The flash X-ray set-up used is presented in Figure 105. A 450 kV flash X-ray system operating at 18 kV and Agfa X-ray film was used. Three X-ray films were housed in X-ray cassettes sandwiched between intensifier screens. A cassette holder manufactured from plywood was built for this specific test allowing all three cassettes to be housed right next to each other. This prevented large gaps between the X-ray films allowing minimum particles to be missed. JETP positions the respective films with the correct distances apart measuring the gap. JETP then statistically analyses the particles on either side of the gap, JETP may then predict if particles were or were not within the gap area and the researcher may decide to artificially add particles to that gap or not. This large gap may incorrectly attribute large break-up-times to particles at the edge of each cassette assuming large spaces between particles.

Effective penetration by a jet ceases when the particle velocity drops slightly below 2 mm/µs [91].

Measurements of jet particles have been made only as far as this lower velocity limit. In some cases where jets were particulated all the way down to the slug, measurements were recorded below 2 mm/µs.

6.2. **Test Set-up**

A typical test set-up is shown in Figure 105 and Figure 106. The cassette holders were manufactured from plywood. Shaped-charges were mounted onto Styrofoam test piece holders and the ruler was typically manufactured from wooden battens with steel welding rods used as the position markers. A steel block was used as a jet stopper. Penetration depths at this high stand-off were not applicable for this study.

Figure 104: Flash X-ray set-up.

Figure 105: Flash X-ray set-up.

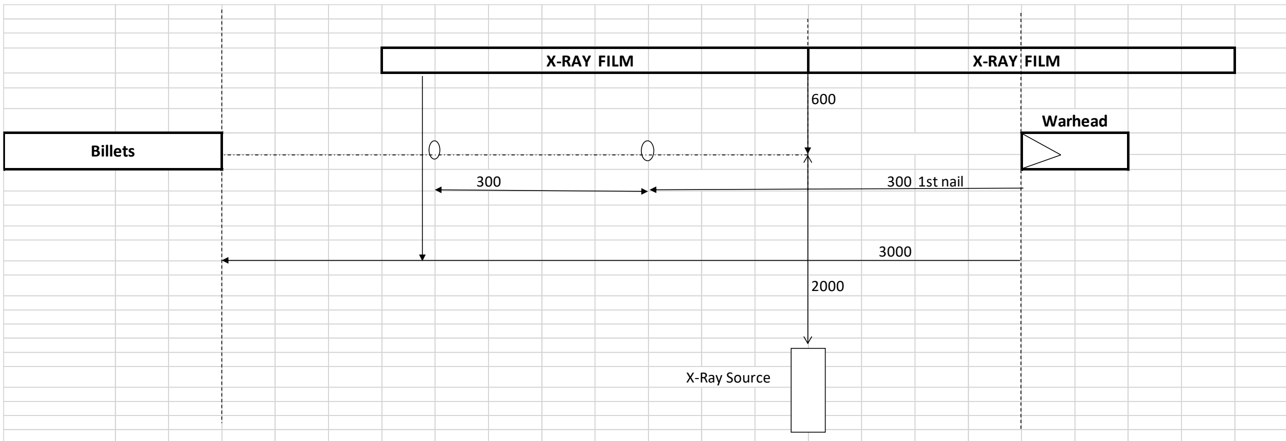

Figure 106: Schematic test set-up.

6.3. Flash X-ray Evaluation

The six concept designs are presented in Figure 107 again as they are referred to in Table 29.

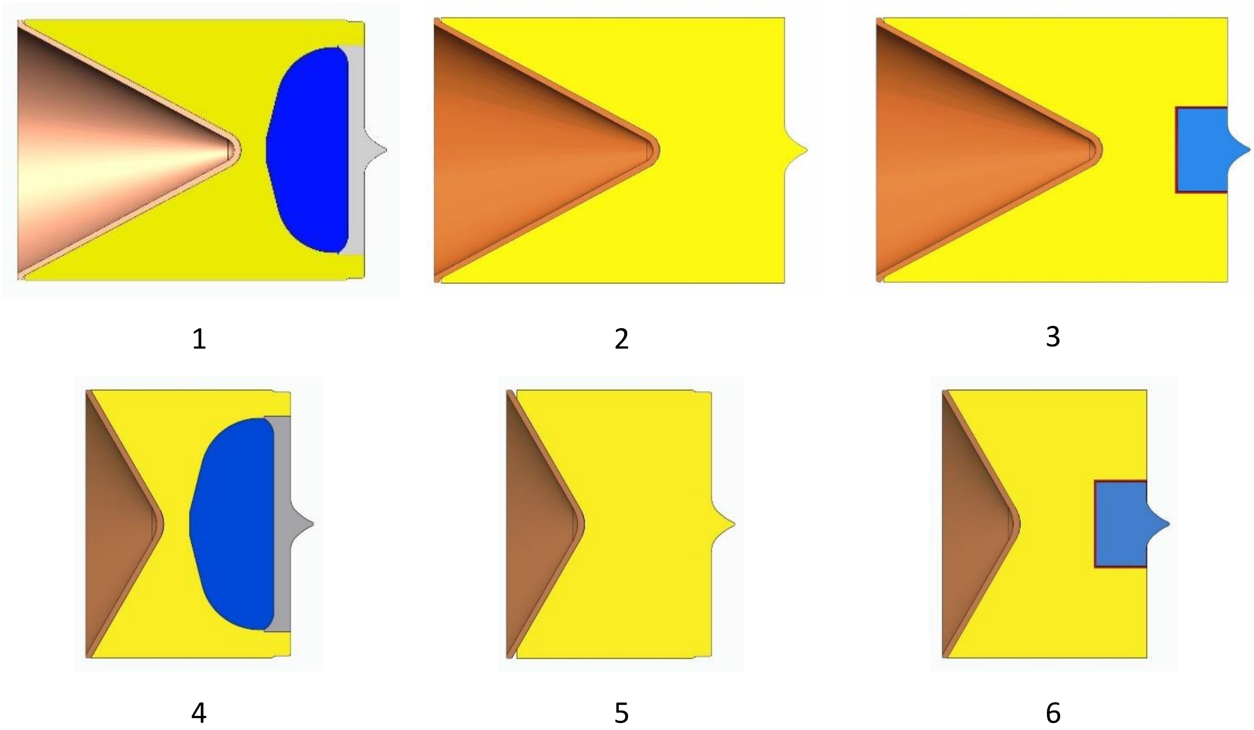

Figure 107: Six shaped-charge warhead concept designs evaluated.

Thirty-three tests were conducted and the matrix of shot selection and calibration marker distances (nail) in the tests, are presented in Table 29. All of these tests were conducted with different objectives leading up to answering the high-level research questions. This section is presented in the sequence of tests taken place to allow the reader to get a feel for the decisions made as the respective tests were conducted. The pre-determined delay times, t_1 and t_2, with each marker position is listed in Table 29. Table 29 will be separated for each design configuration to allow the reader to analyse the data per design as well.

Table 29 Test Summary of all tests.

Shot #	Det #	Initiation Type	Design	HE lot	t_1 (µs)	t_2 (µs)	nail 1 (mm)	nail 2 (mm)	nail 3 (mm)	nail 4 (mm)	nail 5 (mm)	nail 6 (mm)
1	2017-237	Peripheral	1	002-15	226.7	263.2	400	600	1124	1324	1872	2072
2	2017-238	Point	2	002-15	235.7	276.1	104	296	1000	1200	1680	1885
3	2017-239	Peripheral	1	002-15	200.8	235.1	90	290	890	1075	1610	1803
4	2017-240	Peripheral	1	002-15	237.7	271.1	100	300	932	1136	1650	1852
5	2017-241	Peripheral	1	002-15	237.7	271.1	185	370	1012	1215	1560	1745
6	2017-242	Point	2	002-15	266.7	313	200	400	1070	1270	1670	1860
7	2017-243	Point	2	002-15	NA	NA	93	285	985	1190	1690	1895
8	2017-244	Point	2									
9	2017-245	Point	2	002-15	266.7	313	350	550	1070	1270	1670	1860
10	2017-284	point	2	002-15	286.7	507.2	130	330	845	1045	1620	1815
11	2017-285	Peripheral	1	006-17	215.8	446.2	217	417	945	1143	1670	1873
12	2017-286	Peripheral	1	006-17	215.8	446.3	200	400	920	1120	1650	1850
13	2017-287	Peripheral	1	003-17	215.7	446.3	200	400	925	1125	1655	1850
14	2017-288	Peripheral	1	003-17	215.8	446.3	200	407	930	1120	1655	1850
15	2017-289	Peripheral	1	005-17	215.9	446.3	205	405	925	1125	1660	1855
16	2017-290	Peripheral	1	005-17	215.8	446.2	205	405	935	1125	1660	1865
17	2018-19	Point	1	002-15	296.7	517	200	406	927	1124	1647	1850
18	2018-20	Point 120 deg	4	002-15	176.8	516.7	200	405	940	1140	1665	1870
19	2018-21	Point Form F	3	form F	240.8	360.9	205	409	940	1130	1660	1860
20	2018-22	Peripheral 120 deg	4	002-15	130.8	331.9	200	407	945	1145	1660	1875
21	2018-23	Point	2	002-15	296.8	516.8	195	390	934	1134	1650	1850
22	2018-24	Point Form F	3	form F	380.8	445.7	200	400	924	1125	1655	1853
23	2018-25	Point Form F	3	form F	380.7	445.8	200	395	920	1130	1655	1850
24	2018-26	Point 120 deg	5	002-15	225.7	400.7	405	590	1140	1330	1855	2050
26	2018-27	Point 120 deg	5	002-15	225.7	405.8	400	600	1130	1330	1845	2045
27	2018-28	Point 120 deg	5	002-15	225.9	425.8	400	600	1135	1335	1855	2055

28	2018-29	Peripheral 120 deg	4	002-15	131.8	311.9	200	415	937	1145	1665	1860
29	2018-30	Peripheral 120 deg	4	002-15	309.9	403.8	350	555	1067	1270	1805	1995
30	2018-31	Point 120 deg	5	002-15	425.7	555.8	400	605	1130	1330	1860	2052
31	2018-53	Point 120 deg	6	form F	245.7	538.7	400	585	1115	1325		
32	2018-54	Point 120 deg	6	form F	175.8	310.7	350	550	1085	1275		
33	2018-55	Point 120 deg	6	form F	350.7	640.8	550	750	1275	1470		

6.4. Digital Image Analysis

The accurate interpretation of flash X-ray radiographs was extremely important to this research project. Each radiograph was photographed with a digital camera. These radiographs are independently read into the digital analysis tool, JETP, and placed next to each other as shown in Figure 108. A parameter file was prepared for each test as shown in Table 30. This parameter file provides the relevant test parameters and charge design parameters required to analyse this specific test. Each radiograph is then prepared by identifying the position markers and linking them up to the information supplied within the parameter file as shown in Figure 109. The three radiographs are then shown next to each other at their respective positions in Figure 110. The digitised particles are shown in Figure 110 and Figure 111, respectively. Once the jets have been digitised, data is written out in the form shown in Table 31.

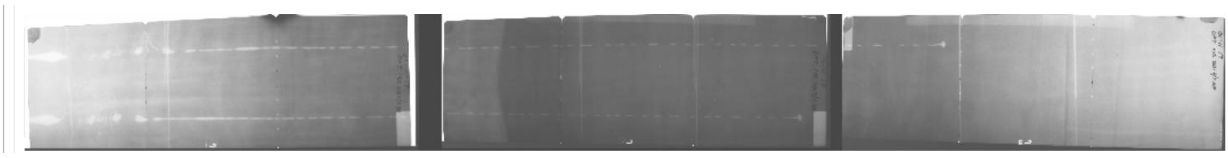

Figure 108: Flash X-ray radiographs as shown in JETP.

Table 30: Generic parameter file prepared per test.

SHOT: 2017-238	
DESIGN: STD	
~~	
CONE_LENGTH_(mm)	79.7
CONE_BASE_TO_VO_FRACTION	0.667
FLASH_1_POSITION_(mm)	
FLASH_2_POSITION_(mm)	
MARKER_1_REF_(mm)	104
MARKER_1_SCA_(mm)	296
MARKER_2_REF_(mm)	1000
MARKER_2_SCA_(mm)	1200
MARKER_3_REF_(mm)	1680
MARKER_3_SCA_(mm)	1885
FILM_POSITION_(mm)	860
TIME_LAG_(microsec)	15
TIME_1_(microsec)	235.7
TIME_2_(microsec)	276.1
~~	

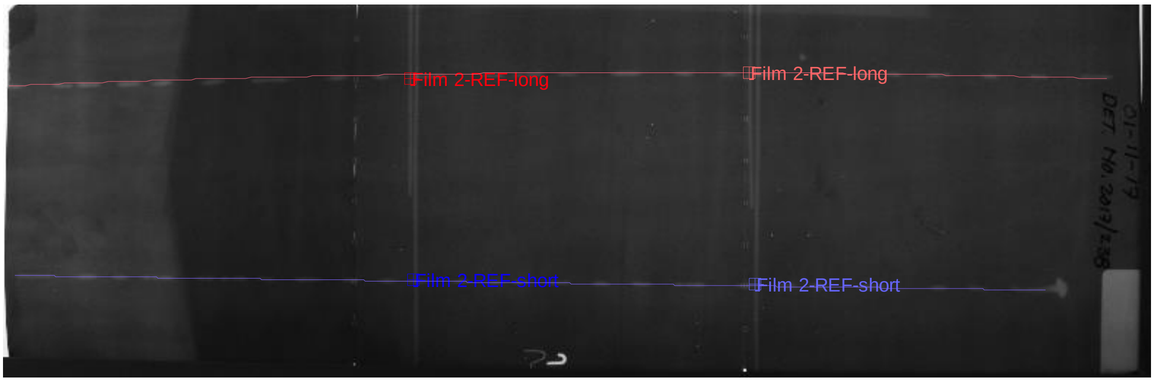

Figure 109: Individual film preparation in terms of position markers and the jet line.

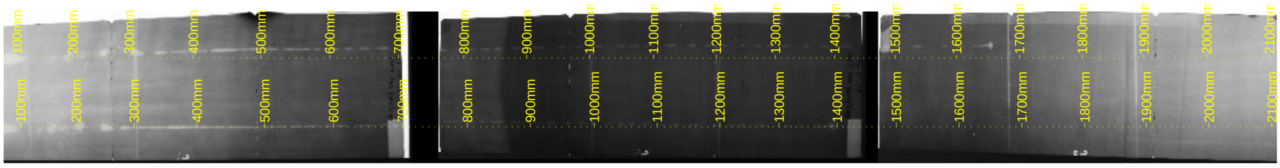

Figure 110: A ruler showing the position of particles along the jet.

Figure 111: An image showing the digitized particles.

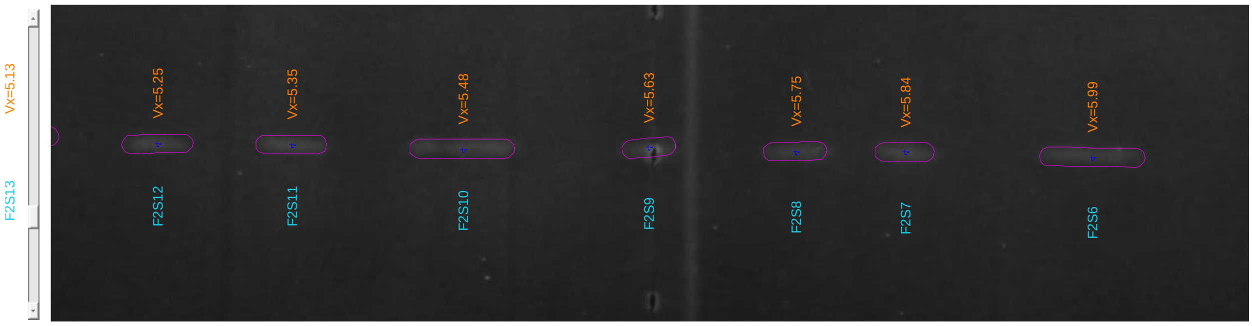

Figure 112: A close-up image showing the digitized particles.

Table 31: Data generated after digitizing the radiographs.

LONG_JET: TRAV_TIME_is 261.1

~~~~~~

Laboratoryel	X_POS	Y_POS	X_VEL	Y_VEL	BU_TIME	LENGTH	CUM_L	WIDTH	AREA	MASS	GAP_L	DELTAV
F3L1	1644	0	6.501	0	122.5	31.7	31.7	2.9	89.49	1.85	16.71	0.15
F3L2	1606	-0.4	6.353	-0.001	84.5	9.9	41.6	2.9	26.92	0.58	15.12	0.1
F3L3	1580	-0.4	6.253	-0.001	61.1	10.7	52.3	2.9	29.1	0.62	29.24	0.17
F3L4	1536	-0.9	6.086	-0.004	73.4	16	68.3	2.9	44.32	0.93	20.88	0.13
F3L5	1502	-1.2	5.957	-0.005	105	7.6	75.9	2.9	20.46	0.45	9.48	0.07
F3L6	1483	-1	5.885	-0.004	68.4	10.3	86.2	2.9	28.51	0.6	30.48	0.18
F2L7	1436	-0.5	5.702	-0.002	100.6	19.4	105.6	2.8	52.86	1.08	18.41	0.14
F2L8	1400	0	5.566	0	87	11.4	117	2.8	30.3	0.63	16.73	0.11
F2L9	1371	0	5.454	0	96.3	11	127.9	2.8	29.12	0.61	17.15	0.12
F2L10	1339	-0.3	5.331	-0.001	111.4	15.7	143.7	2.8	42.9	0.88	12.93	0.1
F2L11	1312	0	5.227	0	132.6	10	153.6	2.8	26.35	0.55	7.45	0.07
F2L12	1293	0.2	5.154	0.001	89.8	11	164.6	2.8	29.14	0.61	15.46	0.11
F2L13	1265	-0.3	5.048	-0.001	84.3	10.7	175.3	2.8	28.54	0.59	18.83	0.12
F2L14	1233	0.1	4.924	0	132	13.4	188.6	2.8	35.84	0.74	9	0.09
F2L15	1210	-0.2	4.837	-0.001	94.9	11.7	200.3	2.8	31.1	0.65	15.6	0.11
F2L16	1181	-0.5	4.727	-0.002	103.4	12.1	212.4	2.8	32.34	0.67	17.99	0.14
F2L17	1145	-0.5	4.591	-0.002	102.8	19.4	231.8	2.8	52.88	1.08	18.41	0.14
F2L18	1109	-0.3	4.452	-0.001	154.5	12.5	244.3	2.8	33.47	0.7	7.59	0.09
F2L19	1085	-0.2	4.358	-0.001	180	18.7	263	2.8	50.92	1.04	4.64	0.08
F2L20	1063	-0.3	4.275	-0.001	103.3	13.4	276.3	2.8	35.84	0.74	20.38	0.15
F2L21	1023	-0.1	4.121	0	134	22.2	298.5	2.5	54.81	1	11.24	0.11
F2L22	994	-0.4	4.011	-0.002	92.9	10.1	308.7	3.2	30.47	0.74	15.18	0.11
F2L23	966	-0.1	3.905	0	115.9	12.2	320.9	3.2	37.45	0.9	17.99	0.15
F2L24	927	0.2	3.754	0.001	132.8	26.3	347.2	2.2	56.24	0.88	14.76	0.14
F2L25	890	0.6	3.611	0.002	102.1	15.3	362.5	3.6	52.15	1.38	16.16	0.12
F2L26	858	0	3.49	0	165.9	12.4	374.9	2.8	33.07	0.69	5.34	0.08
F2L27	838	0.3	3.413	0.001	135.9	14.9	389.8	2.8	40.33	0.83	9.7	0.1
F2L28	813	-0.3	3.316	-0.001	206.8	13.9	403.7	2.8	37.42	0.77	1.69	0.06
F2L29	797	-0.1	3.258	0	85.6	11.7	415.3	2.8	31.12	0.65	16.58	0.11
F2L30	769	-0.2	3.147	-0.001	84.6	10	425.3	2.8	26.35	0.55	18.28	0.12
G1L31	737	0	3.026	0	169	21.7	447	3.4	70.63	1.74	6.27	0.09
G1L32	712	0	2.932	0	177.9	20.2	467.1	3.4	65.63	1.62	5.17	0.09
G1L33	689	0	2.843	0	156.2	21.3	488.4	3.4	69.32	1.7	8.86	0.11
F1L34	660	-0.2	2.731	-0.001	161.4	25.4	513.8	3.7	91.57	2.47	7.75	0.1
F1L35	633	0.3	2.627	0.001	139.4	19.4	533.2	3.7	69.09	1.89	9.14	0.09
F1L36	608	0.7	2.532	0.003	156.3	17.2	550.4	3.7	61.04	1.67	8.37	0.11
F1L37	580	0.9	2.427	0.003	170.1	27	577.4	3.7	97.33	2.63	5.73	0.09
F1L38	558	0.9	2.339	0.003	192.9	12.1	589.4	3.7	42	1.18	5.27	0.12
F1L39	526	0.6	2.216	0.002	193.7	48.5	637.9	3.7	177.47	4.72	6.51	0.15
F1L40	485	0	2.061	0	204.9	28.1	666	3.7	101.38	2.73	3.44	0.11
C1L41	456	0	1.949	0	235.7	29.7	695.7	3.7	107.66	2.9	0	0.1
C1L42	431	0	1.854	0	235.7	25.5	721.3	3.7	92.06	2.49	0	0.11
C1L43	403	0	1.748	0	235.7	35.4	756.7	3.7	128.77	3.45	0	0.11
~~~~~~

C1L44	373	0	1.634	0	235.7	30.7	787.4	3.7	111.21	2.99	0	0.12
C1L45	343	0	1.515	0	197.2	37.8	825.2	3.7	137.52	3.68	4.6	0.12
F1L46	311	0.6	1.396	0.002	110.2	22	847.2	4.4	93.36	3.02	18.13	0.14
F1L47	274	-0.3	1.252	-0.001	52.7	25.3	872.4	8.1	189.64	11.55	36.75	0.2
F1L48	221	-4.4	1.051	-0.017	22.9	17.3	889.8	8.1	141.94	7.91	128.19	0.6
F1L49	64	-1.5	0.448	-0.006	0	74.5	964.3	8.1	586.81	34.07	0	0
SHORT_JET: TRAV_TIME_is	220.7											

~~~~~~

Laboratoryel	X_POS	Y_POS	X_VEL	Y_VEL	BU_TIME	LENGTH	CUM_L	WIDTH	AREA	MASS	GAP_L	DELTAV
F2S1	1403	0	6.6	0	149.9	32.9	32.9	2.8	90.75	1.83	14.76	0.17
F2S2	1365	0	6.428	0	122.4	10.4	43.3	2.8	27.54	0.58	12.23	0.11
F2S3	1342	0	6.32	0	93.4	10.8	54.1	2.8	28.72	0.6	26.84	0.19
F2S4	1300	0	6.131	0	111.1	15.3	69.4	2.8	41.37	0.85	18.13	0.15
F2S5	1268	-0.2	5.985	-0.001	148.2	10	79.4	2.8	26.53	0.55	7.73	0.09
F2S6	1248	0.3	5.897	0.001	118.2	11.9	91.4	2.8	32.22	0.66	14.05	0.12
F2S7	1222	0	5.778	0	124	10.5	101.9	2.8	28.03	0.59	16.44	0.15
F2S8	1189	-0.2	5.63	-0.001	140.7	18.8	120.7	2.8	51.25	1.05	12.65	0.13
F2S9	1160	-0.4	5.497	-0.002	131.5	12.2	133	2.8	32.76	0.68	11.67	0.11
F2S10	1135	0.4	5.385	0.002	135.6	11.8	144.8	2.8	31.53	0.66	12.51	0.12
F2S11	1108	-0.3	5.26	-0.001	154.7	16	160.8	2.8	43.59	0.89	8.15	0.1
F2S12	1086	-0.7	5.16	-0.003	158.6	10.3	171	2.8	27.19	0.57	5.48	0.07
F2S13	1070	-0.4	5.089	-0.002	118.6	8.9	179.9	2.8	23.31	0.49	11.67	0.1
F2S14	1048	-0.7	4.989	-0.003	121.4	10	189.9	2.8	26.53	0.55	13.21	0.12
F2S15	1022	-0.7	4.873	-0.003	177.5	12.5	202.4	2.8	33.47	0.7	4.78	0.08
F2S16	1004	-0.6	4.791	-0.003	141.7	12.6	215	2.8	33.87	0.7	9.84	0.1
F2S17	981	-0.9	4.687	-0.004	143.1	11.9	227	2.8	31.89	0.66	11.1	0.12
F2S18	955	-0.9	4.567	-0.004	136.1	16.6	243.6	2.8	44.93	0.92	11.95	0.12
F2S19	928	-0.9	4.447	-0.004	190	10.3	253.8	2.8	27.19	0.57	3.79	0.08
F2S20	910	-1.1	4.364	-0.005	199.6	17.3	271.1	2.8	47	0.96	2.95	0.08
F2S21	892	-0.9	4.282	-0.004	138.5	11.4	282.5	2.8	30.3	0.63	13.07	0.13
F2S22	862	-1.4	4.147	-0.006	166.3	19.4	301.9	2.8	52.82	1.08	7.17	0.1
F2S23	839	-1.1	4.044	-0.005	152.2	10	311.9	2.8	26.37	0.55	8.29	0.1
F2S24	817	-1.1	3.945	-0.005	180.3	15.5	327.3	2.8	41.79	0.86	7.31	0.13
F2S25	788	-1.5	3.813	-0.007	187.7	25.7	353.1	2.8	70.61	1.43	6.6	0.14
G1S26	758	0	3.675	0	182.7	22.9	376	3.1	69	1.55	6.19	0.12
G1S27	732	0	3.559	0	158.7	21.3	397.3	3.1	64.08	1.44	9.23	0.12
G1S28	706	0	3.439	0	168.6	18.3	415.6	3.1	54.65	1.24	6.39	0.1
F1S29	685	-0.8	3.344	-0.004	202	15	430.6	3.1	44.57	1.02	2.79	0.08
F1S30	667	-1.4	3.261	-0.006	204.8	19.5	450.2	3.1	58.53	1.32	4.03	0.13
F1S31	638	-1.4	3.13	-0.006	158.7	35.6	485.8	3.1	108.44	2.41	13.48	0.18
F1S32	599	-0.9	2.955	-0.004	194.3	22.3	508.1	3.1	67.11	1.51	3.87	0.09
F1S33	578	-1.2	2.862	-0.005	155.1	15.3	523.5	3.1	45.5	1.04	10.07	0.13
F1S34	551	-0.8	2.737	-0.004	196.7	25.1	548.6	3.1	75.76	1.7	4.18	0.11
F1S35	527	-0.9	2.629	-0.004	174.7	18.6	567.2	3.1	55.58	1.26	5.89	0.1
F1S36	506	-0.6	2.533	-0.003	195.7	16.4	583.6	3.1	48.89	1.11	4.03	0.1
F1S37	484	-0.7	2.432	-0.003	198.3	24.3	607.9	3.1	73.38	1.65	3.25	0.09
F1S38	464	-0.3	2.345	-0.001	220.3	11.3	619.3	3.1	33.02	0.76	1.14	0.07
C1S39	448	0	2.271	0	235.7	22.3	641.6	3.1	67.16	1.51	0	0.08
C1S40	431	0	2.193	0	235.7	15.2	656.8	3.1	44.94	1.03	0	0.08
~~~~~~

C1S41	414	0	2.116	0	235.7	22.3	679	3.1	67	1.51	0	0.09
C1S42	394	0	2.024	0	235.7	22.2	701.3	3.1	66.8	1.5	0	0.08
C1S43	375	0	1.94	0	235.7	18.6	719.9	3.1	55.58	1.26	0	0.07
C1S44	359	0	1.868	0	235.7	16.2	736.1	3.1	48.25	1.1	0	0.06
C1S45	345	0	1.805	0	235.7	14.6	750.7	3.1	43.3	0.99	0	0.07
C1S46	330	0	1.735	0	235.7	19.4	770.1	3.1	57.92	1.31	0	0.08
C1S47	311	0	1.65	0	235.7	21.8	791.9	3.1	65.6	1.48	0	0.08
C1S48	294	0	1.574	0	235.7	14.9	806.8	3.1	44.11	1.01	0	0.08
C1S49	278	0	1.498	0	235.7	21.8	828.6	3.1	65.39	1.47	0	0.09
C1S50	258	0	1.41	0	148.6	21	849.5	3.1	62.9	1.42	12.22	0.14
F1S51	227	0	1.27	0	96.8	22.6	872.1	3.1	68.07	1.53	26.29	0.19
F1S52	185	-4.2	1.08	-0.019	60.7	16.5	888.7	3.1	50.99	1.12	100.68	0.58
F1S53	58	1.1	0.505	0.005	0	61.1	949.7	3.1	187.24	4.13	0	0

~~~~~~
~~~~~~

6.5. The Evaluation of the Dynamic Fracture Characteristics of the Jets from a Specific Design and with known Different Initial *Explosive* Crystal Size

6.5.1. Flash X-ray evaluation

The experimental evaluation of the shaped-charges manufactured from Comp A3 with different initial RDX crystal sizes made use of design 1 as shown in Figure 113. Six shots were conducted with three different explosive microstructures as outlined in Table 32. Each test was conducted in duplication with the only variable being the explosive type, more specifically, the RDX crystal variance. All six tests were conducted with the exact same set-up and flashed with the same pre-determined delay times minimizing variables for direct comparison. The FX radiographs are shown in Figure 114 to Figure 119. Results from this work was recently published in [94] and the detailed analysis is presented in this section.

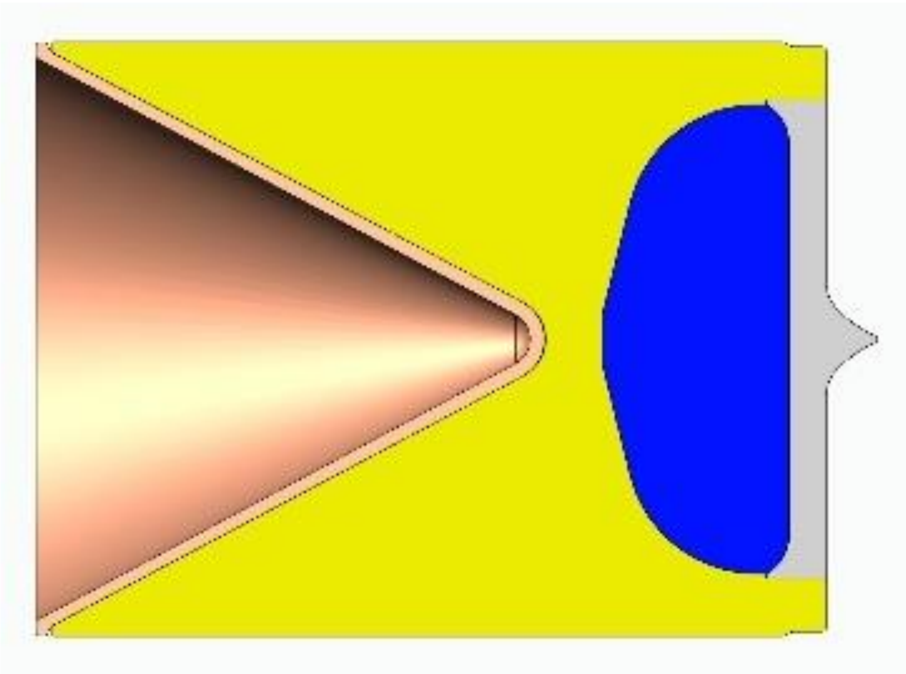

Figure 113: Concept design layout used for the RDX crystal size evaluation.

Table 32: Test parameters for the RDX crystal size evaluation.

Shot #	Det #	Initiation Type	Design	HE lot	T_1 (µs)	T_2 (µs)	nail 1 (mm)	nail 2 (mm)	nail 3 (mm)	nail 4 (mm)	nail 5 (mm)	nail 6 (mm)
11	2017-285	Peripheral	1	006-17	215.8	446.2	217	417	945	1143	1670	1873
12	2017-286	Peripheral	1	006-17	215.8	446.3	200	400	920	1120	1650	1850
13	2017-287	Peripheral	1	003-17	215.7	446.3	200	400	925	1125	1655	1850
14	2017-288	Peripheral	1	003-17	215.8	446.3	200	407	930	1120	1655	1850
15	2017-289	Peripheral	1	005-17	215.9	446.3	205	405	925	1125	1660	1855
16	2017-290	Peripheral	1	005-17	215.8	446.2	205	405	935	1125	1660	1865

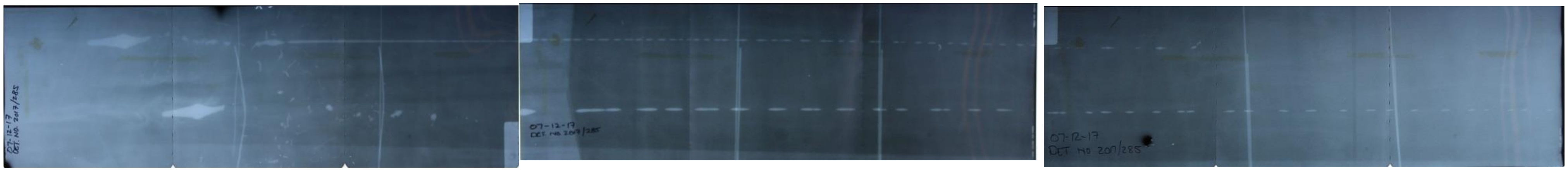

Figure 114: 2017-285 Lot 006.

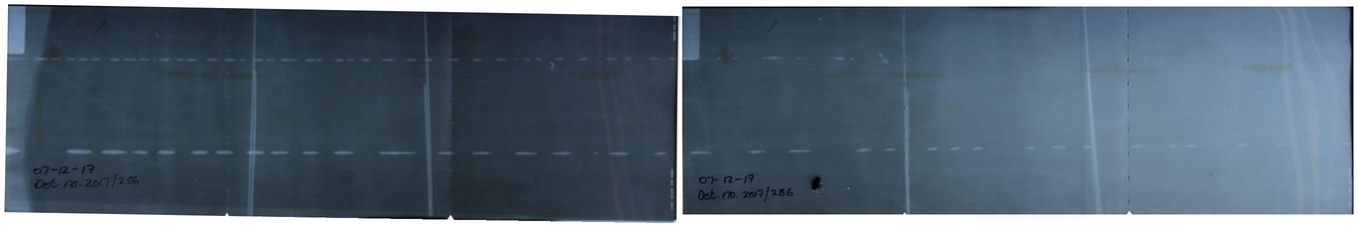

Figure 115: 2017-286 Lot 006.

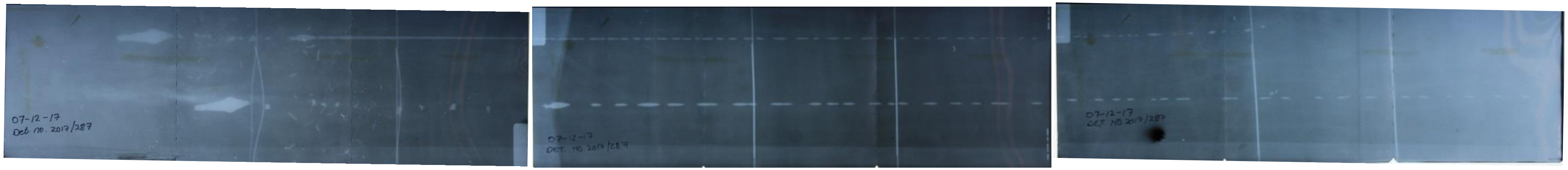

Figure 116: 2017-287 Lot 003.

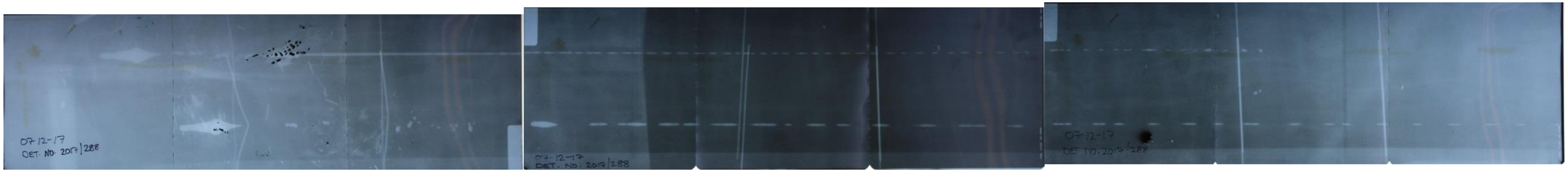

Figure 117: 2017-288 Lot 003.

Figure 118: 2017-289 Lot 005.

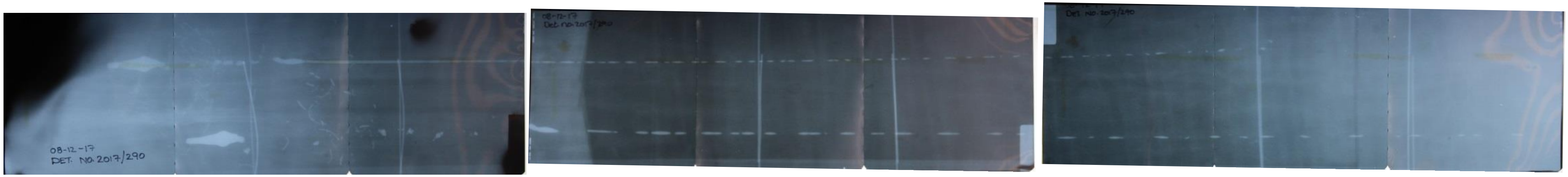

Figure 119: 2019-290 Lot 005.

6.5.2. **Results**

The FX radiographs were accurately digitised as outlined in section 6.4. The tip velocities for each of the tests are presented in Table 33. The cumulative length of the jet can be regarded as one of the most important parameters for the shaped charge jet performance [26], [95]. The influence of the explosive crystal size distribution on this parameter is thus of particular importance in light of the research questions posed in this thesis. The tip velocity measured for each firing was 8.6 ± 0.1 mm/µs. The tip velocities of each jet was measured by double flash X-ray radiographs only. The particle position and particles velocities are shown in Figure 120. This is an interesting figure since the data for all six shots fit perfectly on top of each other. This is due to the exact same times used and nearly identical performance observed in terms of SC jet particle velocity. Figure 121 shows the results for duplicate firings for the cumulative length per jet velocity interval. The graphs depicted show marginal influence of the explosive grain-size distribution on the average cumulative jet length of the combined firings. However, there are differences in the variation of the individual jet length of similar firings. According to Figure 122, Explosive lot 6 (black) had a variation of 20% in cumulative length at 5 mm/µs. Explosive lot 3 (red) showed a variation of less than 10% in cumulative length at 5 mm/µs. Explosive lot 5 (blue) showed a variation of less than 5% in cumulative length at 5 mm/µs. The data suggests that the explosive microstructure has little influence on the overall shaped-charge jet cumulative length. The data rather indicate that an RDX crystal size of 100 µm produces jets that are more consistent, an initial explosive crystal size of 300-400 µm being too coarse and 20-30 µm being too fine. The physical and chemical explanation for this observation is the topic of a continued investigation. The number of particles from jet tip down to 4 mm/µs were 45±2 for the six firings with an average velocity difference of 100±15 m/s between particles. The average break-up-times presented in Figure 124, shows an average break-up-time of 80µs at the tip and approximately 280 µs at 3 mm/µs. The spread of data also verifies the consistency of the RDX crystal size of 100 µm and the variation in break-up-times of the fine and coarse RDX crystals throughout the jet. The break-up-times were calculated by measuring the inter-particle spaces and the velocity difference between those particles. The time was traced back to the point these particles meet. This time is considered the break-up-time. The average break-up-time is the break-up-time of all particles in a 1 mm/µs velocity segment. The break-up-times are averaged for particles in between 6 and 7 mm/µs and similarly for all other jet velocity segments in the jets. The average L/D ratios of the shaped-charge jet particles are presented in Figure 124. The average L/D were also calculated for each 1 mm/µs velocity segment. The graph shows an average

L/D of 2.5 at the jet tip increasing up to 5.5 at 4.5 mm/µs. Average The L/D ratios also confirmed the consistency for the medium sized RDX crystals.

Table 33: Tip velocities and FX delay times for the RDX crystal sizes evaluation.

Shot #	Det #	Comp A3 Explosive LOT	Initiation Type	t_1 (µs)	t_2 (µs)	V_{TIP} (mm/µs)
11	2017-285	006-17	Peripheral	215.8	446.2	8.61
12	2017-286	006-17		215.8	446.3	8.58
13	2017-287	003-17		215.7	446.3	8.58
14	2017-288	003-17		215.8	446.3	8.66
15	2017-289	005-17		215.9	446.3	8.59
16	2017-290	005-17		215.8	446.2	8.61

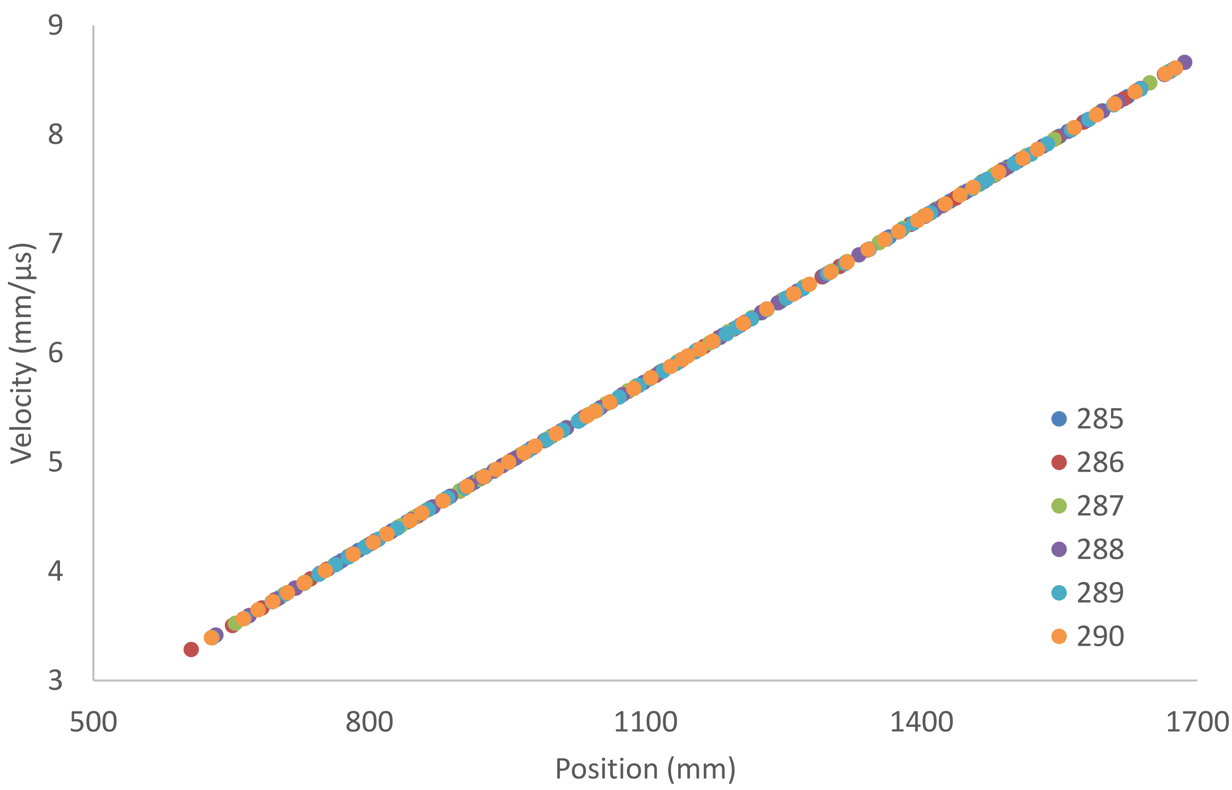

Figure 120: Velocity and particle position for all test conducted for the RDX crystal size evaluation.

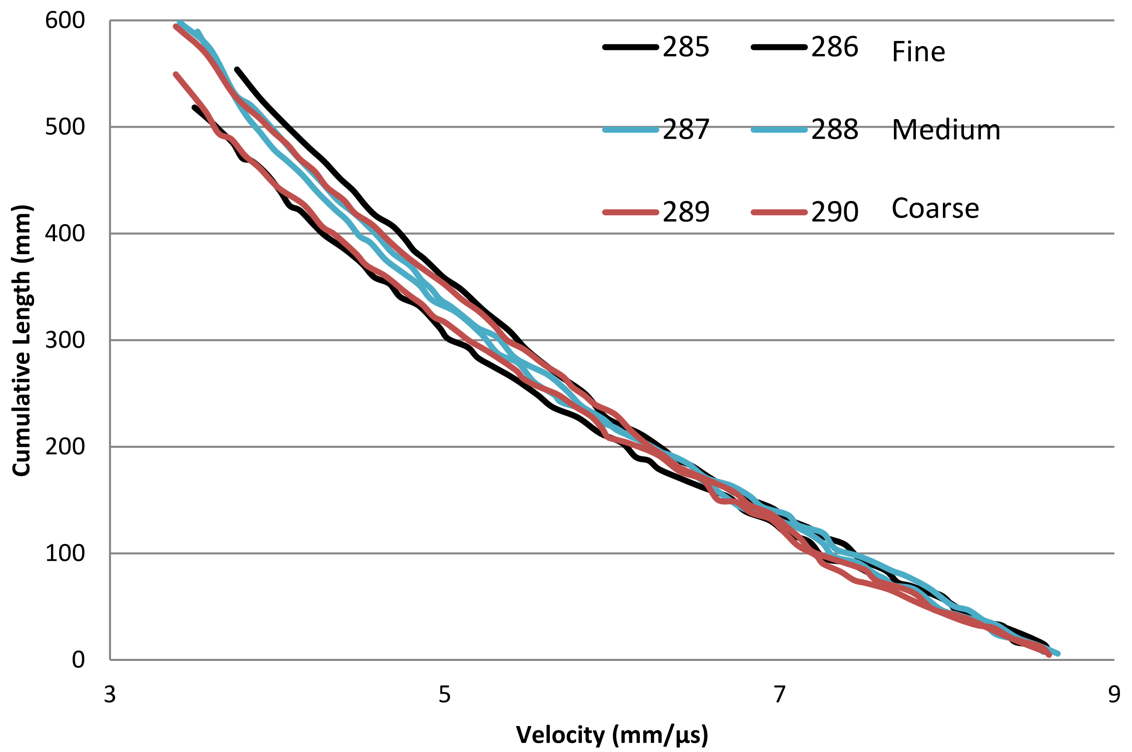

Figure 121: Flash X-ray Analysis – Cumulative length of the overall shaped-charge jet.

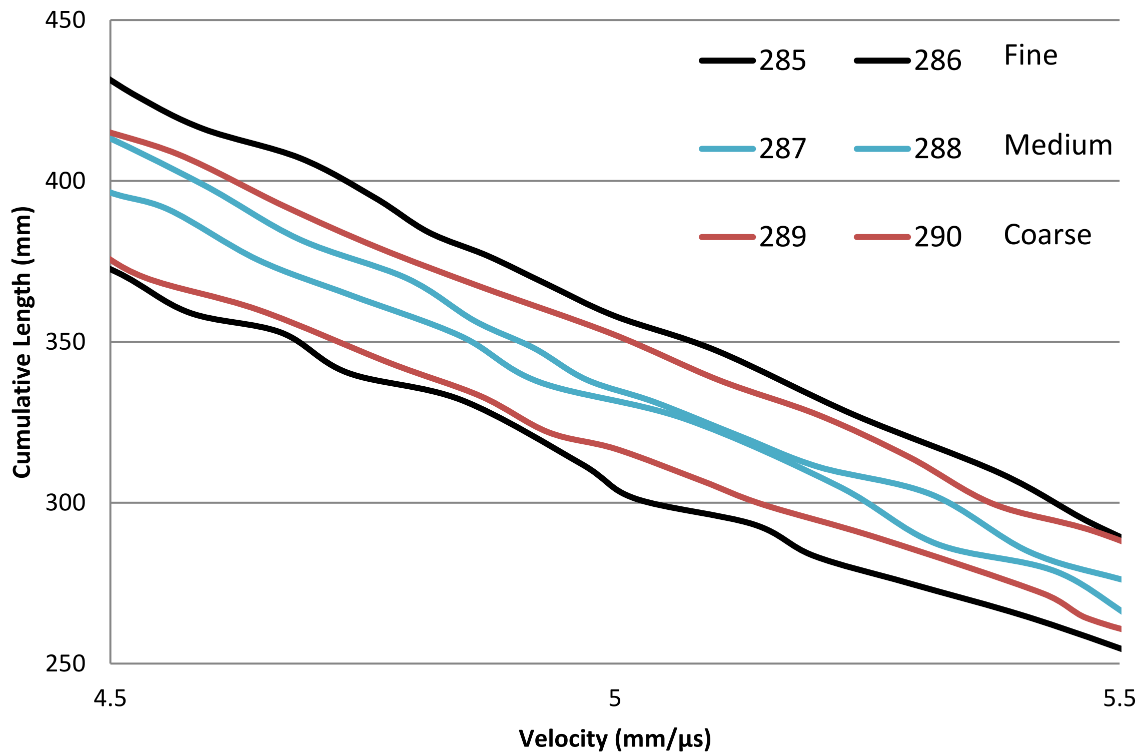

Figure 122: Flash X-ray Analysis – Cumulative length of a section of the shaped-charge jet.

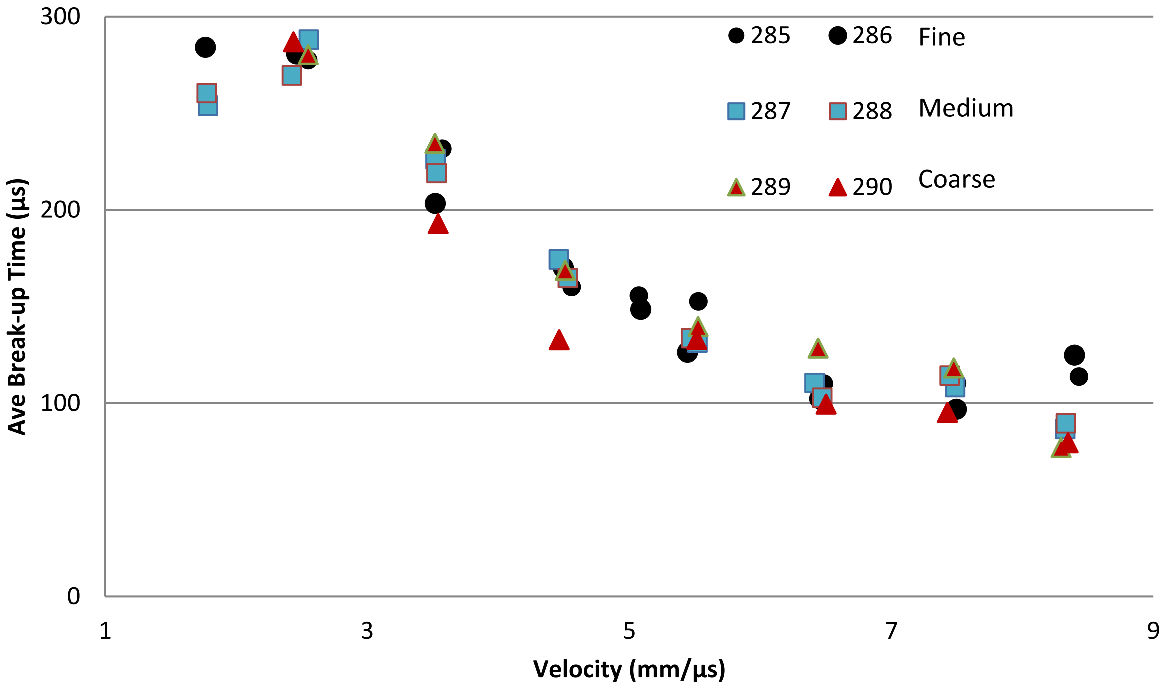

Figure 123: Flash X-ray Analysis - Average break-up-times.

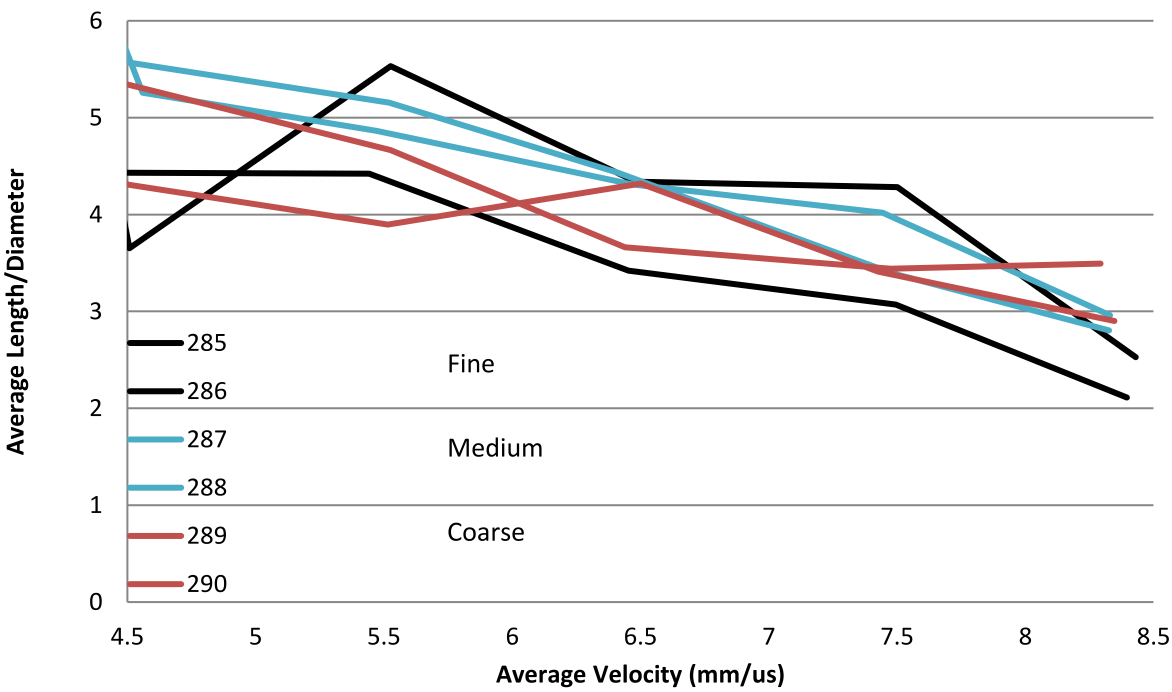

Figure 124: Flash X-ray Analysis - average L/D of particles of shaped-charge jets.

6.6. The Evaluation of the Dynamic Fracture Characteristics of Shaped-charge Jets at different Strain-rates and known initial *LINER MICROSTRUCTURES*

6.6.1. Flash X-ray Evaluation

6.6.1.1. Design 1 – Comp A3 – Peripheral Initiation - 60° liner

The summary of the tests are presented in Table 34. Test 1 was conducted for measuring the tip velocity of the jet for design 1. The design and some hardware are shown in Figure 125. The two flash X-ray pulse times were selected only 40 µs apart such that the first few particles would be observed for both flashes as shown in Figure 126. The selection of the FX discharge times was made possible with the insight obtained from the simulations. The X-ray radiographs in Figure 126 shows two of three radiographs. The third radiograph was damaged during the firing and was not possible to develop it. The test was successful in the sense that the data was used to accurately determine the tip velocity and the formation time of the jet for design 1. The formation time was calculated to be 15 µs including the 5.5 µs electronic delay built into the RP83 precision detonators. It is also clear that the jet is observed in a particulated state, which allows the researcher to measure the jet-break-up times from the tip (8.6 mm/µs) down to 4.2 mm/µs. Test 3 was a repeat of test 1 and the radiographs are presented in Figure 127. This time the jet was observed from the tip down to the appendix. The front portion of the jet was particulated and the rear end was still continuous, even after 235 µs. Test 4 was again an attempt at observing the jet in particulated form from the tip down to the rear of the jet or the section known as the Appendix. The flash X-ray pulse times were selected such that the first flash is observed with the tip on the last FX radiograph and the second flash time was selected with the tip right at the edge of the capturing area of the film. This extended time was selected to allow the rear end of the jet to also particulate. This was partially successful since a portion at the rear was still continuous. The radiographs are presented in Figure 128. The times were considered sufficient since the break-up-times were observed down to a reasonable velocity below 3 mm/µs. Test 3 and 4 was still useful since the statistics were improved in terms of the jet properties of design 1. Test 5 was a repeat of test 4 to improve the statistics and the radiograph is presented in Figure 129.

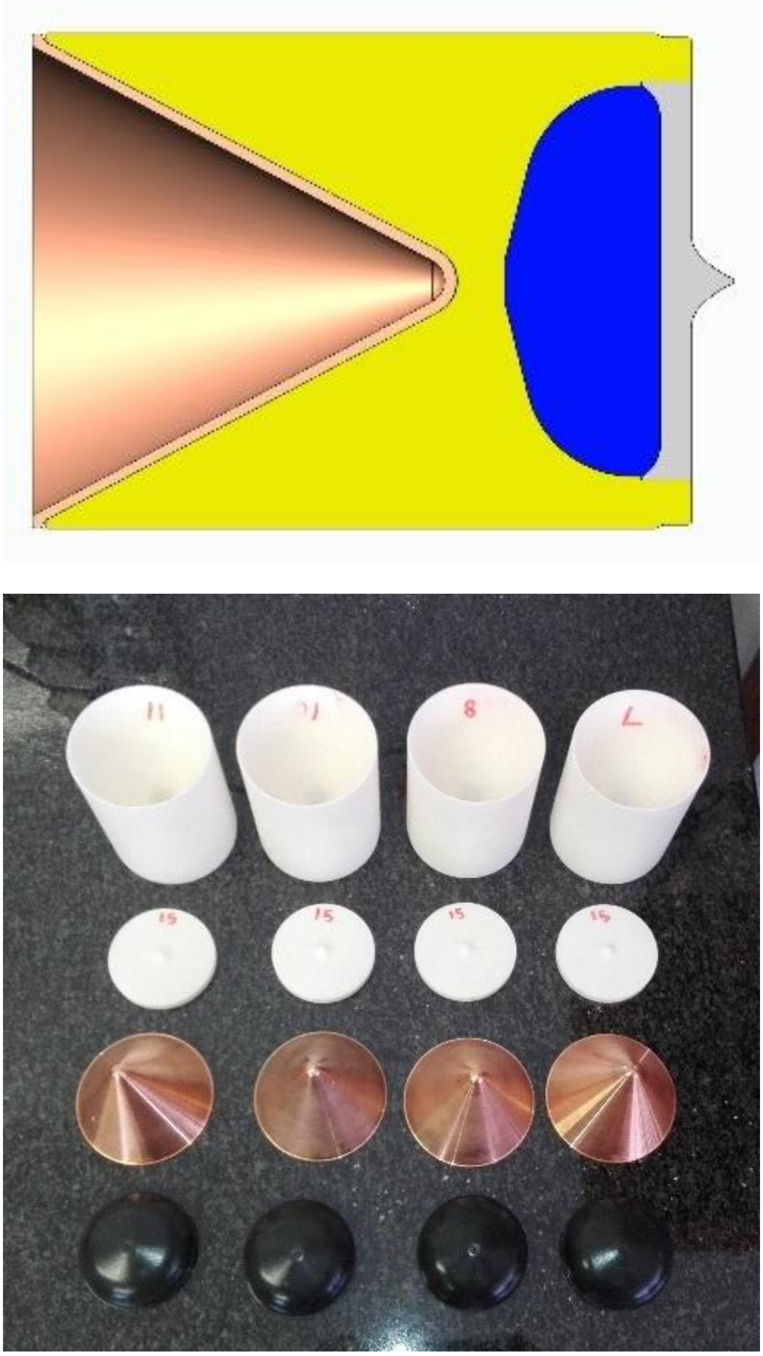

Figure 125: Concept design 1 and matching hardware.

Table 34: Test parameters for design 1.

Shot #	Det #	Initiation Type	HE lot	t1(μs)	t2(μs)	nail 1 (mm)	nail 2 (mm)	nail 3 (mm)	nail 4 (mm)	nail 5 (mm)	nail 6 (mm)
1	2017-237	Peripheral	002-15	226.7	263.2	400	600	1124	1324	1872	2072
3	2017-239	Peripheral	002-15	200.8	235.1	90	290	890	1075	1610	1803
4	2017-240	Peripheral	002-15	237.7	271.1	100	300	932	1136	1650	1852
5	2017-241	Peripheral	002-15	237.7	271.1	185	370	1012	1215	1560	1745

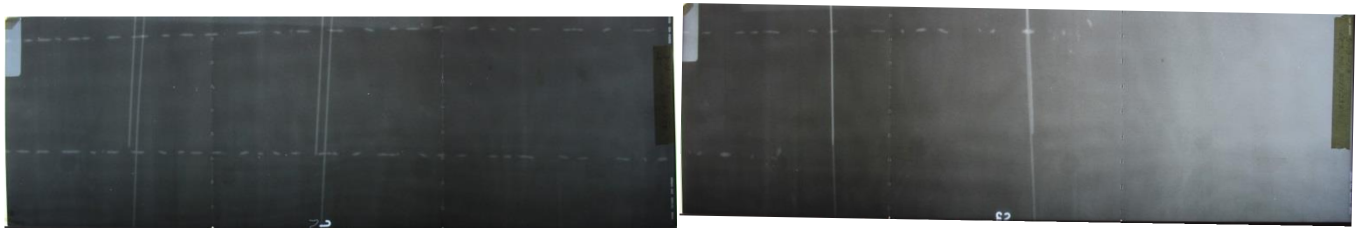

Figure 126: FX radiograph for Detonation No: 2017-237, Shot#1.

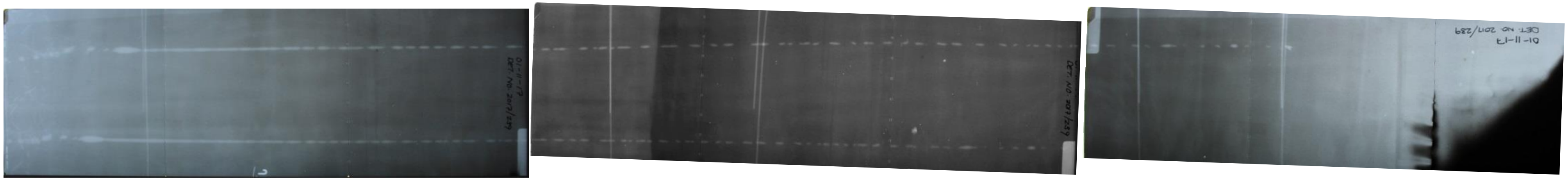

Figure 127: FX radiograph for Detonation No: 2017-239, Shot#3.

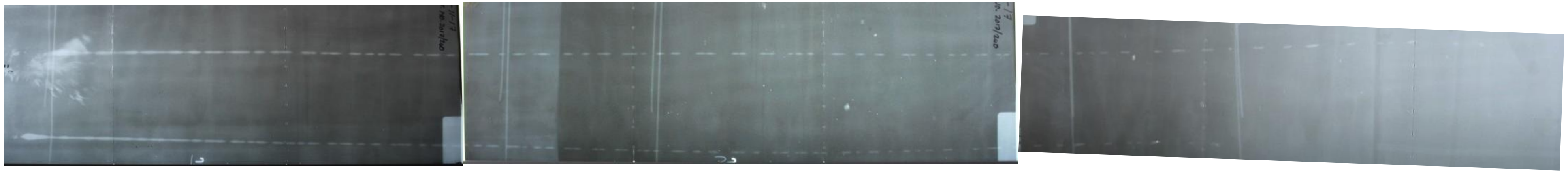

Figure 128: FX radiograph for Detonation No: 2017-240, Shot#4.

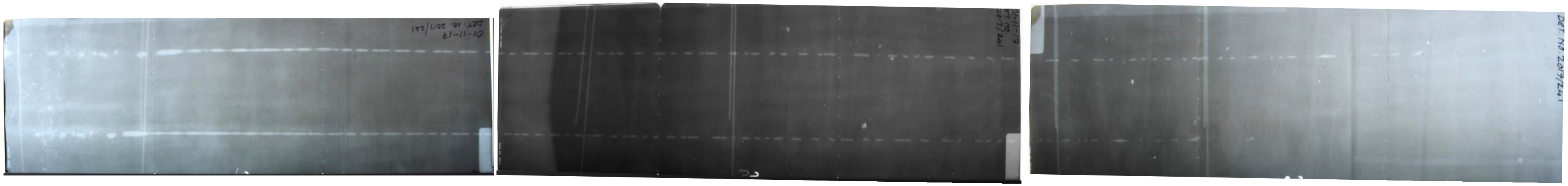

Figure 129: FX radiograph for Detonation No: 2017-241, Shot#5.

6.6.1.2. Design 2 – Comp A3 – Point Initiation - 60° liner

Eight sets of hardware were prepared for design 2. The concept design and an image of some of the hardware is presented in Figure 130. The test parameters are presented in Table 35.

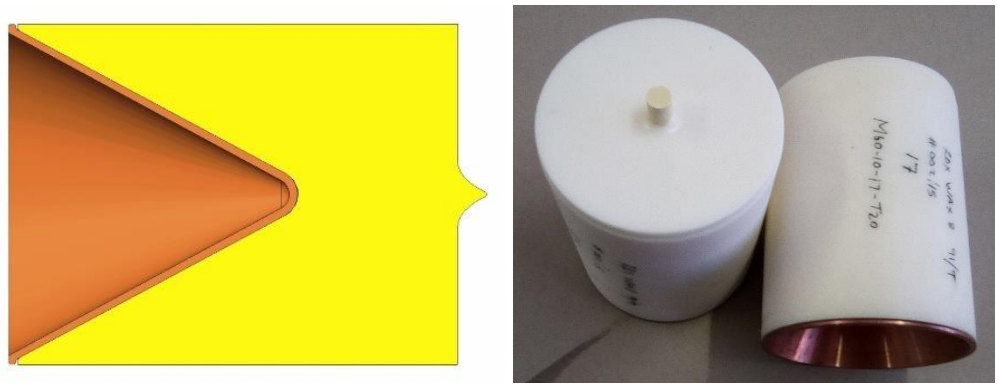

Figure 130: Concept design 2 and matching hardware.

Test 2 was conducted to accurately determine the tip velocity of Design 2. The times selected for this test were good since the jet may be observed from the tip down to the slug in particulated form. This is the case for both flash X-ray pulse times. The radiograph is presented in Figure 131. The author acknowledges that the times could have been extended considering the space available in front of the jet for the second flash. This was acceptable considering it was the first test for this design.

Tests 6 to 9 were additional tests conducted to improve the statistics of the analysis. Test 6 was successful and presented in Figure 132. Test 7 was not since no data was extracted due to a detonator malfunctioning. Test 8 revealed data for one of the flashes as shown in Figure 133 and rather poor contrast making it difficult to analyse. This result was omitted from the data set. An investigation revealed one of the shield plates dropped in front of the FX tube. This was corrected for the next test. Test 9 was successful and the radiograph is presented in Figure 134.

Test 10 was another repeat of design 2, this time selecting a rather larger second flash time. This allowed for the break-up-times of the rear end of the jet to be calculated accurately. The larger separation distances are clearly visible at the rear end of the jet for the second flash as shown in Figure 135. Test 17 and test 21 were again similar to test 10 such that a rather large flash time was selected to allow accurate break-up-times to be determined at the rear of the jet. The radiographs are presented in Figure 136 and Figure 137, respectively.

Table 35: Test parameters for design 2.

Shot #	Det #	Initiation Type	HE lot	t1 (μs)	t2 (μs)	nail 1 (mm)	nail 2 (mm)	nail 3 (mm)	nail 4 (mm)	nail 5 (mm)	nail 6 (mm)
2	2017-238	Point	002-15	235.7	276.1	104	296	1000	1200	1680	1885
6	2017-242	Point	002-15	266.7	313	200	400	1070	1270	1670	1860
7	2017-243	Point	002-15	NA	NA	93	285	985	1190	1690	1895
8	2017-244	Point									
9	2017-245	Point	002-15	266.7	313	350	550	1070	1270	1670	1860
10	2017-284	point	002-15	286.7	507.2	130	330	845	1045	1620	1815
17	2018-19	Point	002-15	296.7	517	200	406	927	1124	1647	1850
21	2018-23	Point	002-15	296.8	516.8	195	390	934	1134	1650	1850

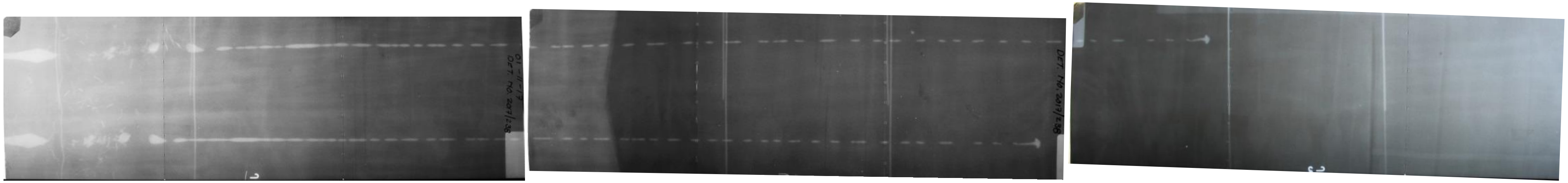

Figure 131: FX radiograph for Detonation No: 2017-238, Shot#2.

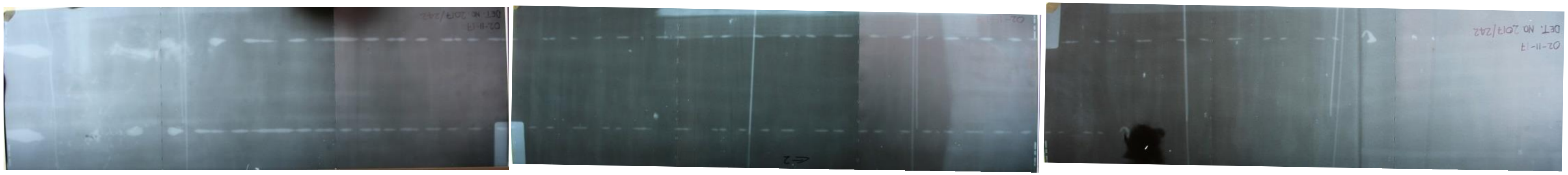

Figure 132: FX radiograph for Detonation No: 2017-242, Shot#6.

Figure 133: FX radiograph for Detonation No: 2017-244, Shot#8.

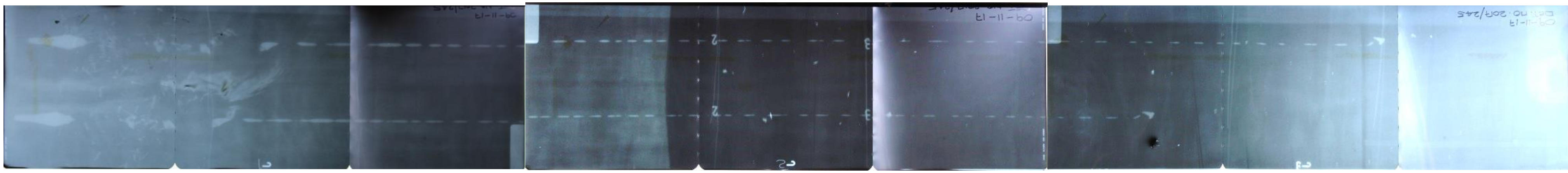

Figure 134: FX radiograph for Detonation No: 2017-245, Shot#9.

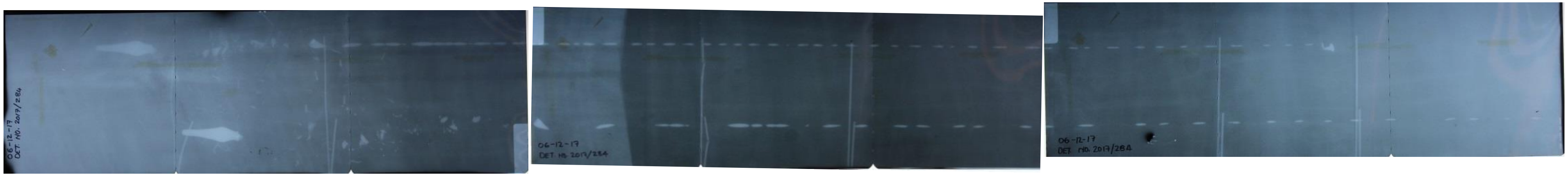

Figure 135: FX radiograph for Detonation No: 2017-284, Shot#10.

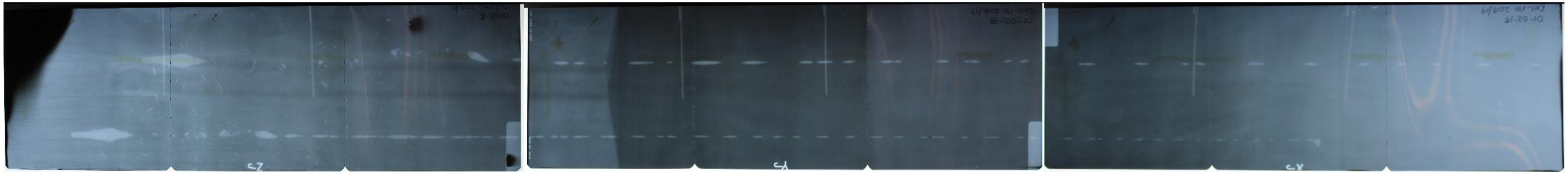

Figure 136: FX radiograph for Detonation No: 2018-19, Shot#17.

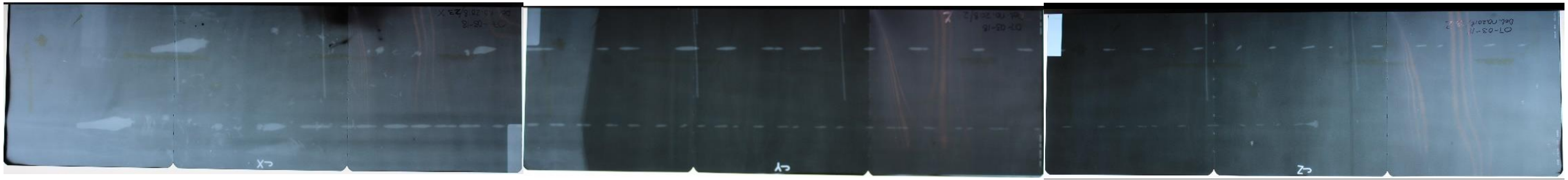

Figure 137: FX radiograph for Detonation No: 2018-23, Shot#21.

6.6.1.3. Design 3 – Formulation F – Point Initiation - 60° liner

Four charges were manufactured to evaluate design 3 with experimental explosive known as Formulation F. The concept design layout and an image of the hardware are presented in Figure 138. Three tests were conducted and the test parameters are presented in Table 36.

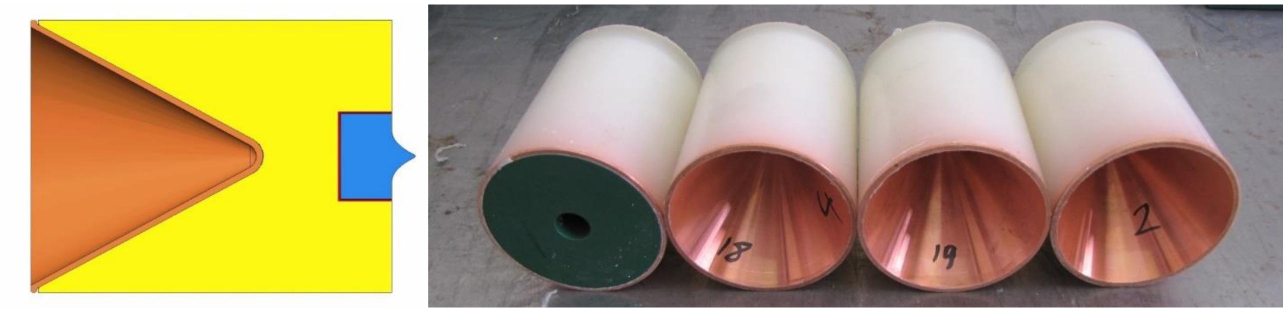

Figure 138: Concept design 3 and matching hardware.

Test 19 was conducted for measuring the tip velocity of the jet for design 3. The time settings on the flash-X-ray apparatus for discharging the X-ray pulses were selected due to the uncertainty about the explosive behaviour correlating to those predicted in simulations. Therefore, the tip of the jet was positioned to the left of the third FX radiograph for the second flash and the tip for the first flash on the second radiograph. This was possible with the insight obtained from simulations. The X-ray radiographs in Figure 139 shows the three FX radiographs. The test was successful since the data could be used to accurately determine the tip velocity and the formation time of the jet for design 3. The formation time was calculated to be 22 µs including the 5.5 µs electronic delay built into the RP83 precision detonators. It is also clear that the jet is observed in a particulated state, which allows for measurement of the jet-break-up times from the tip down to slug. The times selected for this test were effective since the jet may be observed from the tip down to the slug in particulated form. This is the case for both flash X-ray pulse times. The times could be extended considering the space available in front of the jet for the second flash. The times were then extended for test 22 and 23, respectively. The jet tip of the second flash was positioned at the edge of the third film and the jet tip from the first flash was positioned at start of the third film. The radiographs are presented in Figure 140 and Figure 141, respectively.

Table 36: Test parameters for design 3.

Shot #	Det #	Initiation Type	HE lot	t1 (µs)	t2 (µs)	nail 1 (mm)	nail 2 (mm)	nail 3 (mm)	nail 4 (mm)	nail 5 (mm)	nail 6 (mm)
19	2018-21	Point Form F	form F	240.8	360.9	205	409	940	1130	1660	1860
22	2018-24	Point Form F	form F	380.8	445.7	200	400	924	1125	1655	1853
23	2018-25	Point Form F	form F	380.7	445.8	200	395	920	1130	1655	1850

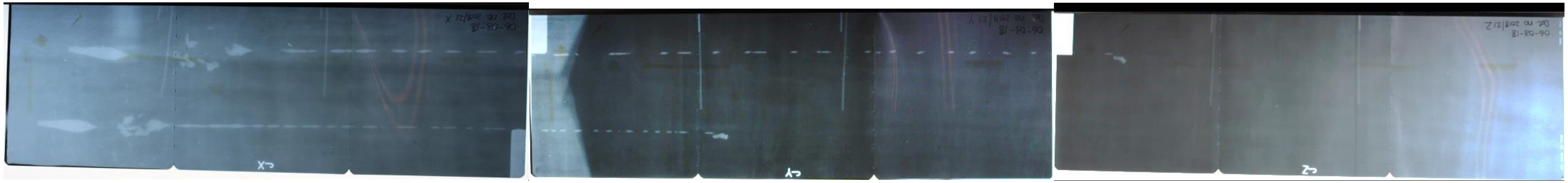

Figure 139: FX radiograph for Detonation No: 2018-21, Shot#19.

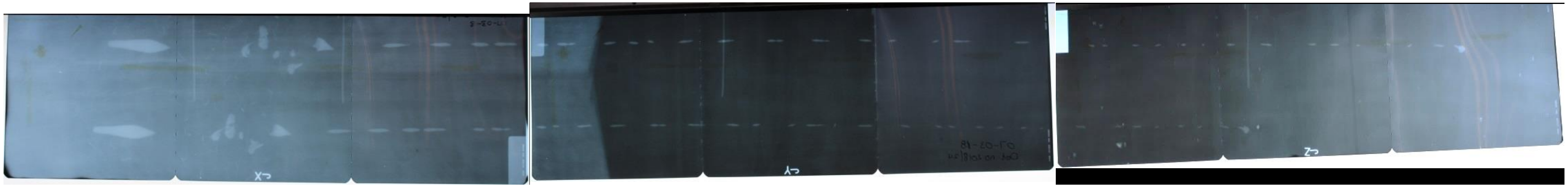

Figure 140: FX radiograph for Detonation No: 2018-24, Shot#22.

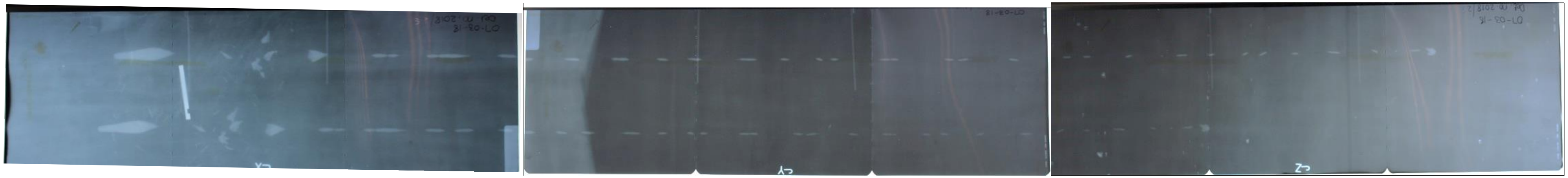

Figure 141: FX radiograph for Detonation No: 2018-25, Shot#23.

6.6.1.4. Design 4 – Comp A3 – Peripheral-initiated - 120° liner

Three charges were manufactured to evaluate design 4. The concept design layout and an image of the hardware are presented in Figure 142. Three tests were conducted and the test parameters are presented in Table 37.

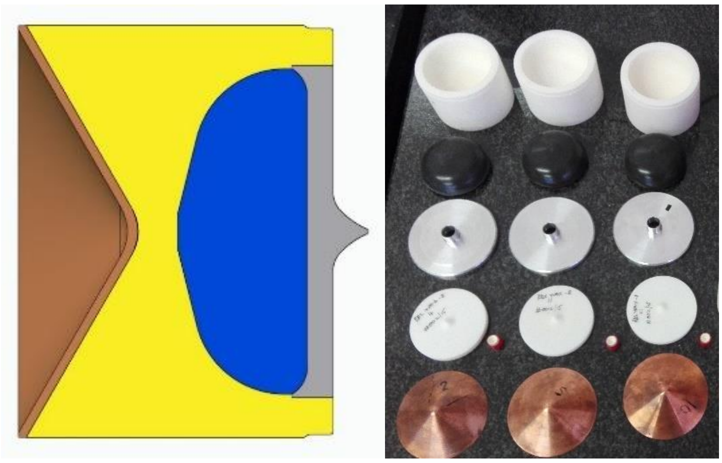
Figure 142: Concept design 4 and matching hardware.

Test 22 was conducted for measuring the tip velocity of the jet for design 4. The liner material for this specific test used copper manufactured from bar material of which the microstructure was not optimised. The tip of the jet was positioned on the edge of the second FX radiograph and the first flash on the first radiograph. This was possible with the insight obtained from simulation. The X-ray radiographs are presented in Figure 143. The test was successful such that the data were used to accurately determine the tip velocity and the formation time of the jet for design 4. The formation time was calculated to be 15 µs including the 5.5 µs electronic delay built into the RP83 precision detonators. It is also clear that the jet is observed in a particulated state for the second flash, which allows the researcher to measure the jet-break-up times from the tip down to slug. The times selected for this test were optimal since the jet may be observed from the tip down to the slug in particulated form. This is case for the second flash time only. The times were repeated for test 28 and the radiograph is presented in Figure 144. The flash time selected for test 29 was such that the jet was particulated for both flash X-ray pulse times. The jet tip of the second flash was positioned at the centre of the third film and the jet tip from the first flash was positioned at the centre of the second film. The radiograph is presented in Figure 145.

Table 37: Test parameters for design 4.

Shot #	Det #	Initiation Type	HE lot	t1 (µs)	t2 (µs)	nail 1 (mm)	nail 2 (mm)	nail 3 (mm)	nail 4 (mm)	nail 5 (mm)	nail 6 (mm)
20	2018-22	Peripheral 120 deg	002-15	130.8	331.9	200	407	945	1145	1660	1875
28	2018-29	Peripheral 120 deg	002-15	131.8	311.9	200	415	937	1145	1665	1860
29	2018-30	Peripheral 120 deg	002-15	309.9	403.8	350	555	1067	1270	1805	1995

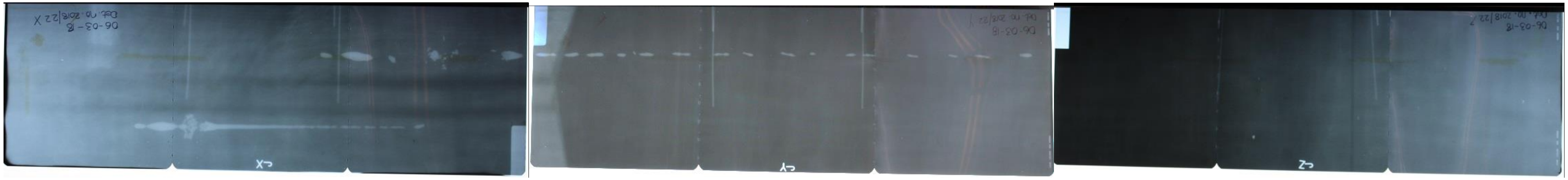

Figure 143: FX radiograph for Detonation No: 2018-22, Shot#20.

Figure 144: FX radiograph for Detonation No: 2018-29, Shot#28.

Figure 145: FX radiograph for Detonation No: 2018-30, Shot#29.

6.6.1.5. Design 5 - Comp A3 – Point-initiated - 120° liner

Five charges were manufactured to evaluate design 5. The concept design layout and an image of the hardware is presented in Figure 146. Five tests were conducted and the test parameters are presented in Table 38.

Figure 146: Concept design 5 and matching hardware.

At this stage of the experimental phase a limited number of 120-degree liners with optimised microstructure were available. It was decided to machine liners from a 100 mm diameter copper bar purely for use in the tip velocity measurement. This copper bar was not processed in any way. Liners manufactured from copper bar were used to verify the jet tip velocity and ensure the test parameters like flash X-ray pulse times were well selected. Test 18 and 24 was conducted with bar liners for measuring the tip velocity of the jet for design 5. The tip of the jet was positioned on the edge of the third FX radiograph for the second flash and the first flash on the first radiograph. This allowed for an observation of the jet in the continuous mode for the first flash and the particulated mode for the second flash. Brittle failure mode of particles is clearly observed for the second flash. The particles observed for test 18 were tumbling when particulated. The X-ray radiographs are presented in Figure 147. The test was successful such that the data were used to accurately determine the tip velocity and the formation time of the jet for design 5. The formation time was calculated to be 15 µs including the 5.5 µs electronic delay built into the RP83 precision detonators. It is also clear that the jet is observed in a particulated state for the second flash, which allows the measurement of the jet-break-up times from the tip down to slug. The times selected for this test were optimal since the jet could be observed from the tip down to the slug in particulated form. This is the case for the second flash time only. The second flash time was reduced for test 24 to allow the jet to be observed in particulated mode before the particles started tumbling. The FX radiograph presented in Figure 148 shows the particles particulated but not tumbling. Now that the set-up and times were known, liners that have been processed to the correct microstructure were used. Test 26 and test 27 were then conducted with the improved flash X-ray pulse times as selected for test 24. The radiographs are presented in Figure 149 and Figure 150, respectively. There was a clear distinction between the jets produced from liners machined from copper bar vs liners machined from copper forgings with fine microstructures. The flash time selected for test 30 was an attempt at obtaining a particulated jet for both flash X-ray pulse times. The radiograph is presented in Figure 151. The jet tip of the second flash was positioned at the centre of the third film and the jet tip from the first flash was positioned at the edge of the second film. The jet particles started tumbling at the later time as well. This test clearly demonstrated improved break-up-times for jets produced from liners with optimised microstructure compared to liners manufactured from bar material, which has not been processed at all.

Table 38: Test parameters for design 5.

Shot #	Det #	Initiation Type	HE lot	t1 (µs)	t2 (µs)	nail 1 (mm)	nail 2 (mm)	nail 3 (mm)	nail 4 (mm)	nail 5 (mm)	nail 6 (mm)
18	2018-20	Point 120 deg	002-15	176.8	516.7	200	405	940	1140	1665	1870
24	2018-26	Point 120 deg	002-15	225.7	400.7	405	590	1140	1330	1855	2050
26	2018-27	Point 120 deg	002-15	225.7	405.8	400	600	1130	1330	1845	2045
27	2018-28	Point 120 deg	002-15	225.9	425.8	400	600	1135	1335	1855	2055
30	2018-31	Point 120 deg	002-15	425.7	555.8	400	605	1130	1330	1860	2052

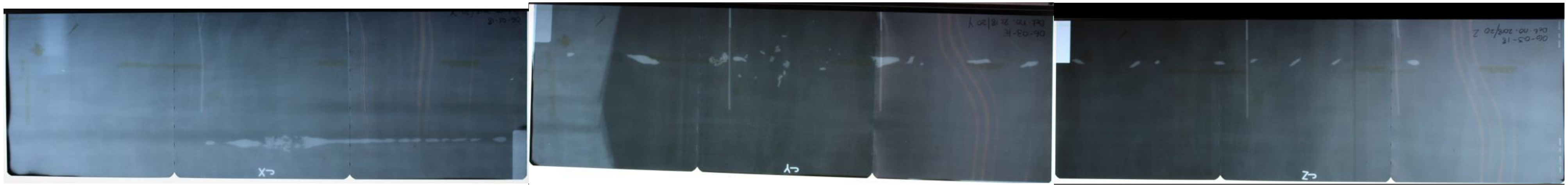

Figure 147: FX radiograph for Detonation No: 2018-20, Shot#18.

Figure 148: FX radiograph for Detonation No: 2018-26, Shot#24.

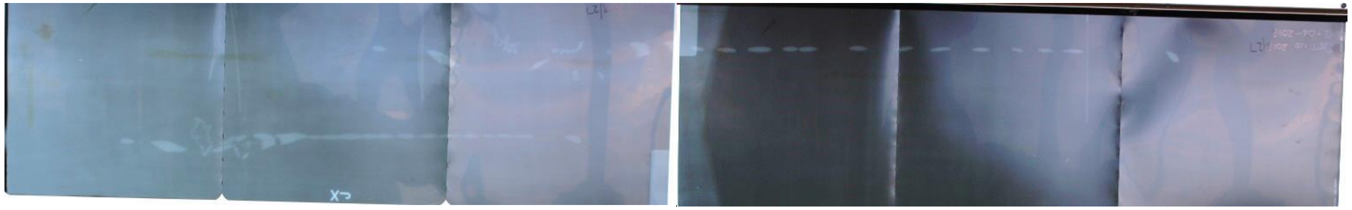

Figure 149: FX radiograph for Detonation No: 2018-27, Shot#26.

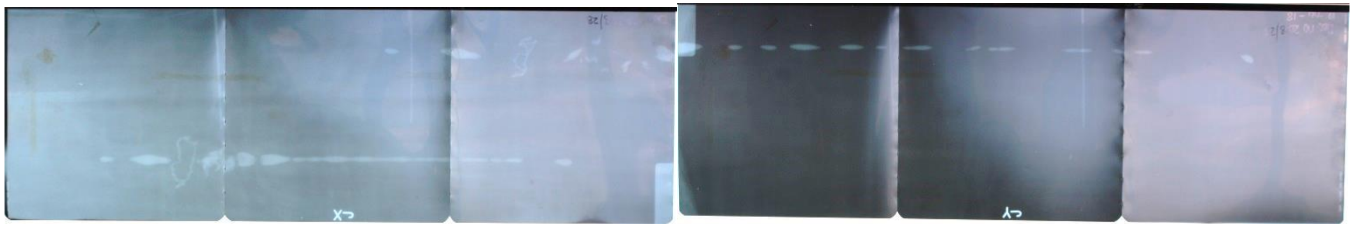

Figure 150: FX radiograph for Detonation No: 2018-28, Shot#27.

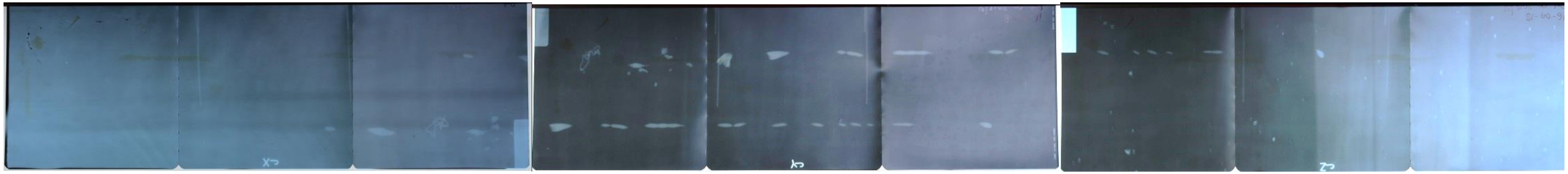

Figure 151: FX radiograph for Detonation No: 2018-31, Shot#30.

6.6.1.6. Design 6 - Formulation F – Point-initiated - 120° liner

Four charges were manufactured to evaluate design 6. The concept design layout and an image of the hardware are presented in Figure 152. Three tests were conducted and the test parameters are presented in Table 39.

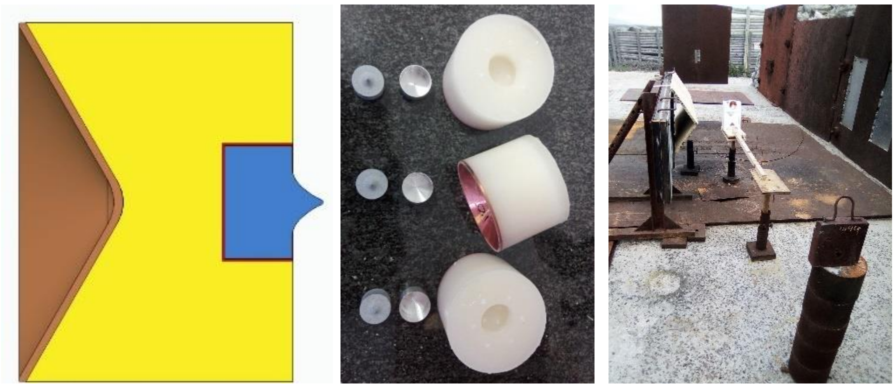

Figure 152: Concept design 6 and matching hardware.

Test 31 was conducted for measuring the tip velocity of the jet for design 6. The times for the first shot were selected for the tip of the jet to be positioned in the centre of the second FX radiograph for the second flash and in the centre of the first film for the first flash. This was possible with the insight obtained from simulation. The radiographs showed the jet in continuous mode and particulated mode. The two FX radiographs are shown in Figure 153. The data were used to accurately determine the tip velocity and the formation time of the jet for design 6. The formation time was calculated to be 22 μs including the 5.5 μs electronic delay built into the RP83 precision detonators. It is also clear that the jet is observed in a particulated state, which allows the researcher to measure the jet-break-up times from the tip down to slug. This is the case for both flash X-ray pulse times. The times were then reduced for test 32 and both jets were captured in one FX radiograph as shown in Figure 154. This test allowed an observation of the jet in continuous mode. The times were again extended in test 33 to allow the jet tip of the second flash to be positioned at the edge of the second film and the jet tip from the first flash was positioned at the edge of the first film. This allowed the jet to be particulated for both flashes. This is useful for tracing multiple particles back to the virtual origin. The FX radiograph is presented in Figure 155.

Table 39: Test parameters for design 6.

Shot #	Det #	Initiation Type	t_1(μs)	t_2(μs)	V_{TIP} (mm/μs)	V_{TIP}-ave (mm/μs)	nail 2 (mm)	nail 3 (mm)	nail 4 (mm)
31	2018-53	Point 120 deg	form F	245.7	538.7	400	585	1115	1325
32	2018-54	Point 120 deg	form F	175.8	310.7	350	550	1085	1275
33	2018-55	Point 120 deg	form F	350.7	640.8	550	750	1275	1470

Figure 153: FX radiograph for Detonation No: 2018-53, Shot#31.

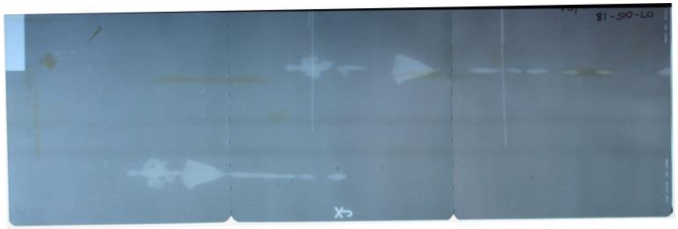

Figure 154: FX radiograph for Detonation No: 2018-54, Shot#32.

Figure 155: FX radiograph for Detonation No: 2018-55, Shot#33.

6.6.2. **Results from Digital Analysis of the Radiographs**

The previous section presented the FX radiographs, the test parameters and an explanation of decisions taken regarding flash X-ray pulse times. This section will present the results after it was analysed by a process outlined in Section 6.4. The results are focused on the jet characteristics of the six shaped-charge concept designs.

6.6.2.1. Design 1

Four tests was conducted with design 1 and the measured flash X-ray pulse times and the tip velocities are shown in Table 40. The averaged tip velocity from the four tests was calculated to be 8.58 mm/µs. This was similar to the tip velocities measured for the test conducted with the different explosive microstructures, namely 8.60 mm/µs. The velocity and position of each particle are presented in Figure 156. The cumulative lengths of the jets are presented in Figure 157. The cumulative lengths were measured for jets of similar delay times and have been highlighted in bold in Table 40. The cumulative lengths were repeatable for all four jets measuring up to approximately 700 mm from the tip down to 3 mm/µs. The averaged break-up-times were measured and shown in Figure 158. The break-up-times were also repeatable for all four tests and may be averaged for this specific design. The averaged velocity difference is presented in Figure 159 and displays a typical velocity difference of 100 m/s as usually observed for copper jets. The data reported for the velocity differences are in line with data reported in [96].

Table 40: Measured tip velocities and FX delay times used for design 1.

Shot #	Det #	Initiation Type	t_1(µs)	t_2(µs)	V_{TIP} (mm/µs)	V_{TIP}-ave (mm/µs)
1	2017-237	Peripheral	**226.7**	263.2	8.57	8.58
3	2017-239		200.8	**235.1**	8.53	
4	2017-240		**237.7**	271.1	8.61	
5	2017-241		**237.7**	271.1	8.61	

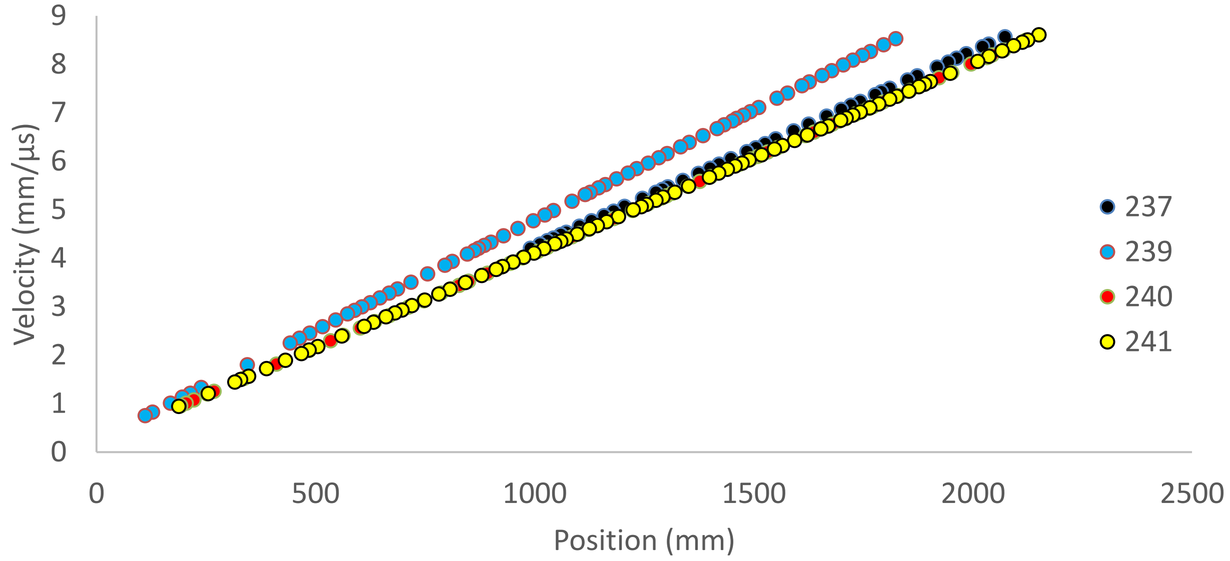

Figure 156: Velocity - Position graph for design 1 – four test firings.

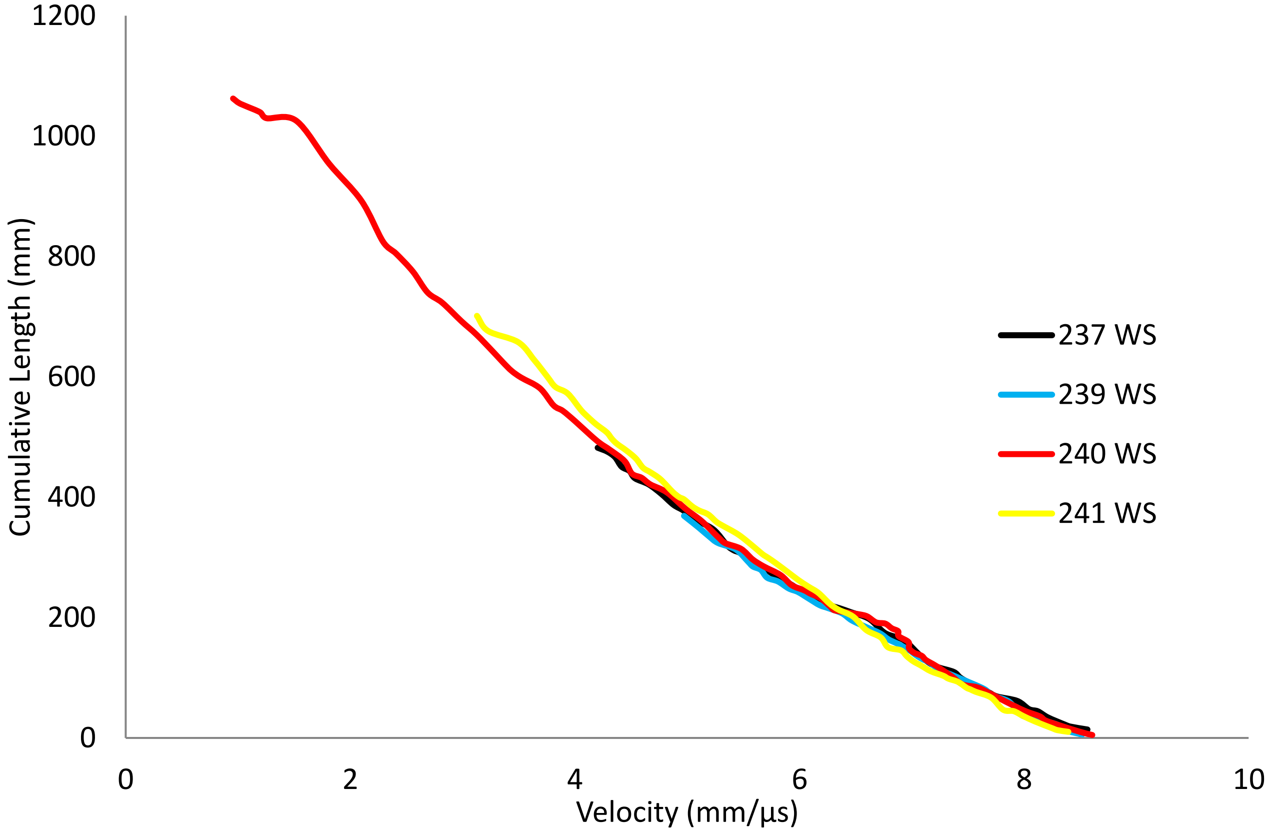

Figure 157: Cumulative Length – Velocity graph for design 1 – four test firings.

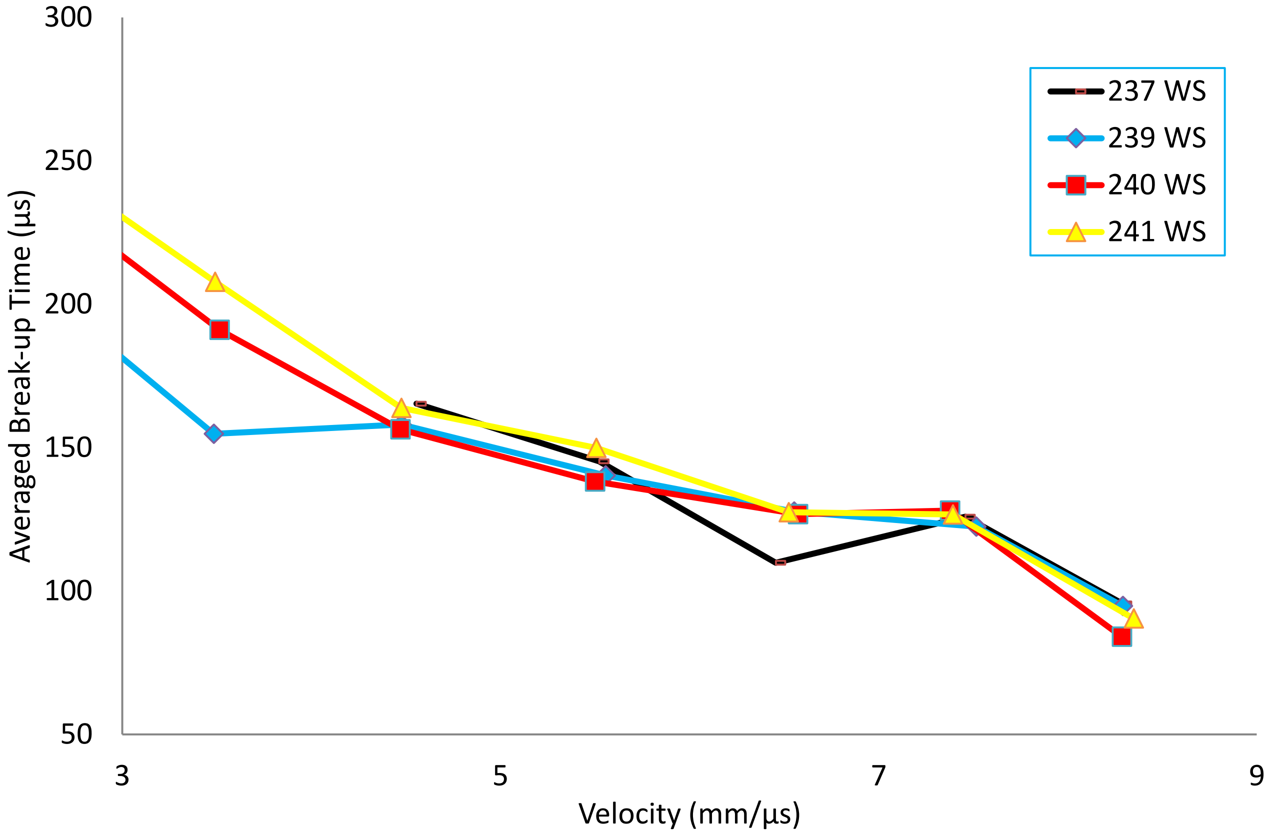

Figure 158: Average break-up-time - Velocity graph for Design 1 - four test firings.

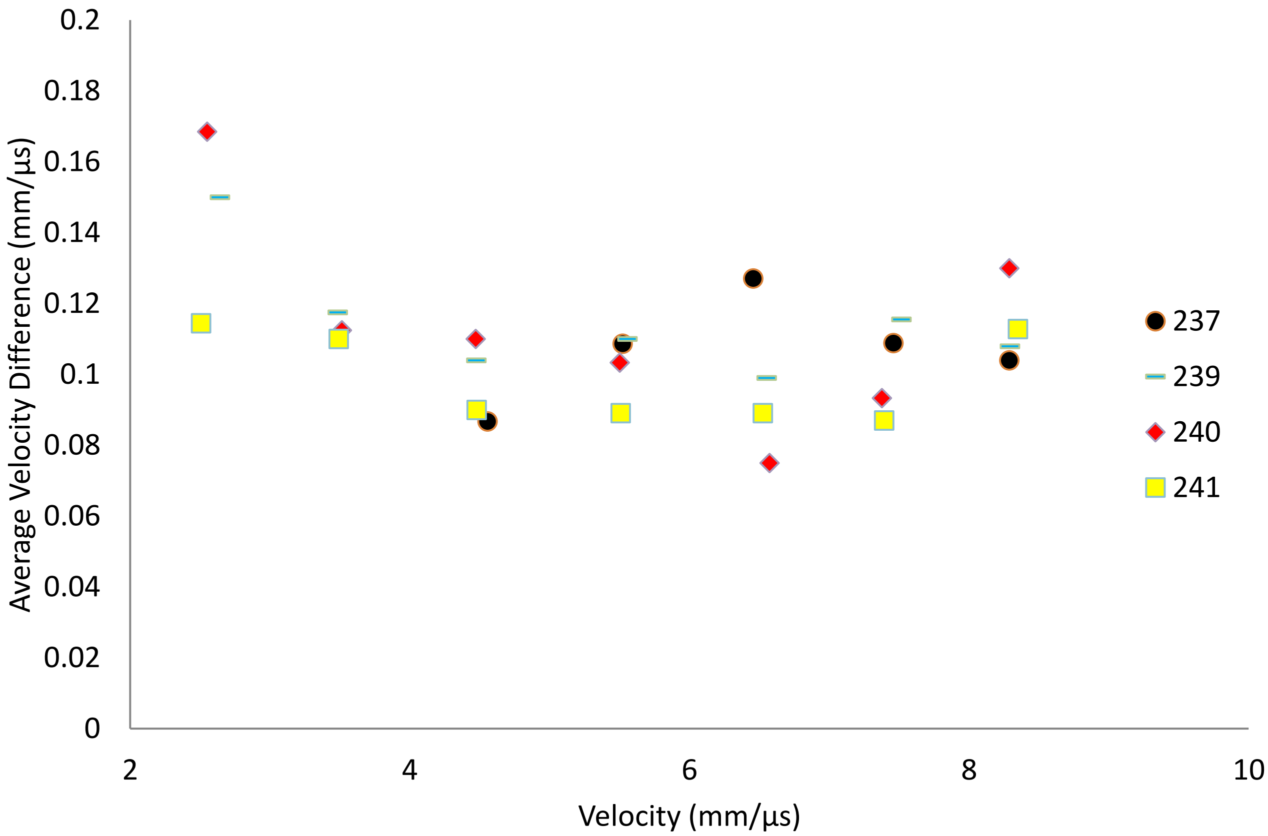

Figure 159: Average velocity difference – Velocity graph for design 1 - four test firings.

6.6.2.2. Design 2

Eight tests were conducted with design 2 of which six provided useful data. The flash X-ray pulse times and the tip velocities are shown in Table 41. The averaged tip velocity from the six tests was calculated to be 6.51 mm/μs. The velocity and position of each particle are presented in Figure 160. The cumulative lengths of the jets are presented Figure 161. The cumulative lengths were measured for jets of similar delay times and have been highlighted in bold in Table 41. The cumulative lengths were repeatable for all six jets measuring up to approximately 500 mm from the tip down to 3 mm/μs. The averaged break-up-times were measured and shown in Figure 162. The averaged break-up-times were also repeatable for all six jets and may be averaged for this specific design.

Table 41: Measured tip velocities and FX delay times used for design 2.

Shot #	Det #	Initiation Type	t_1(μs)	t_2(μs)	V_{TIP} (mm/μs)	V_{TIP}-ave (mm/μs)
2	2017-238	Point	235.7	**276.1**	6.50	6.51
6	2017-242		**266.7**	313.0	6.62	
7	2017-243		NA			
8	2017-244					
9	2017-245		**266.7**	313	6.39	
10	2017-284		**286.7**	507.2	6.73	
17	2018-19		**296.7**	517.0	6.29	
21	2018-23		**296.8**	516.8	6.54	

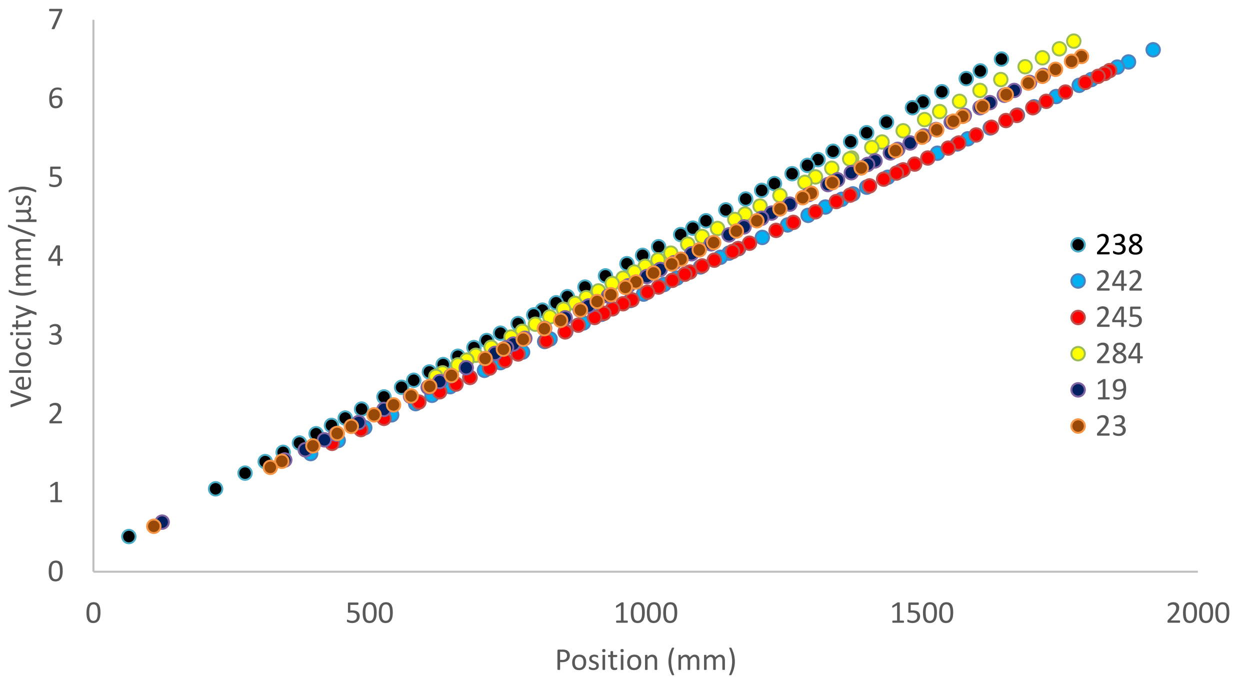

Figure 160: Velocity - Position graph for design 2 – six test firings.

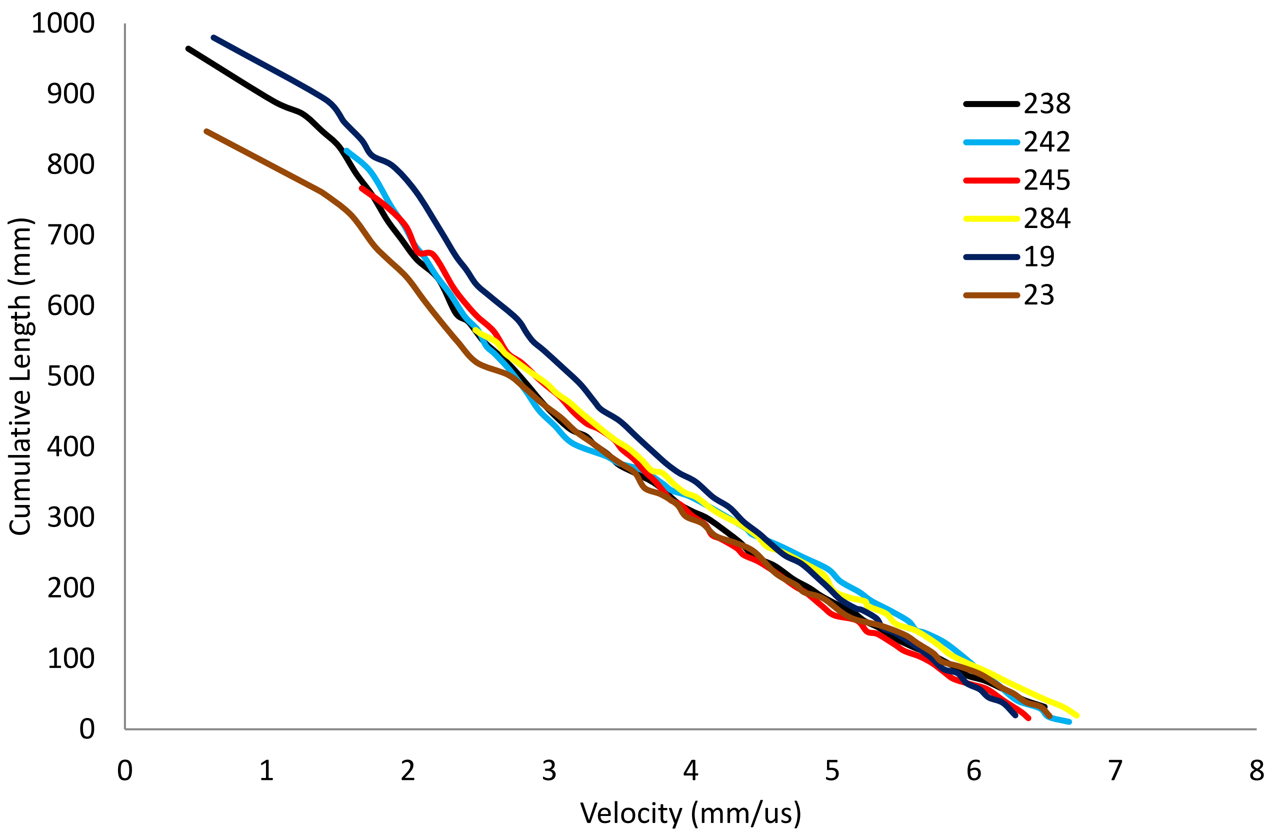

Figure 161: Cumulative Length – Velocity graph for design 2.

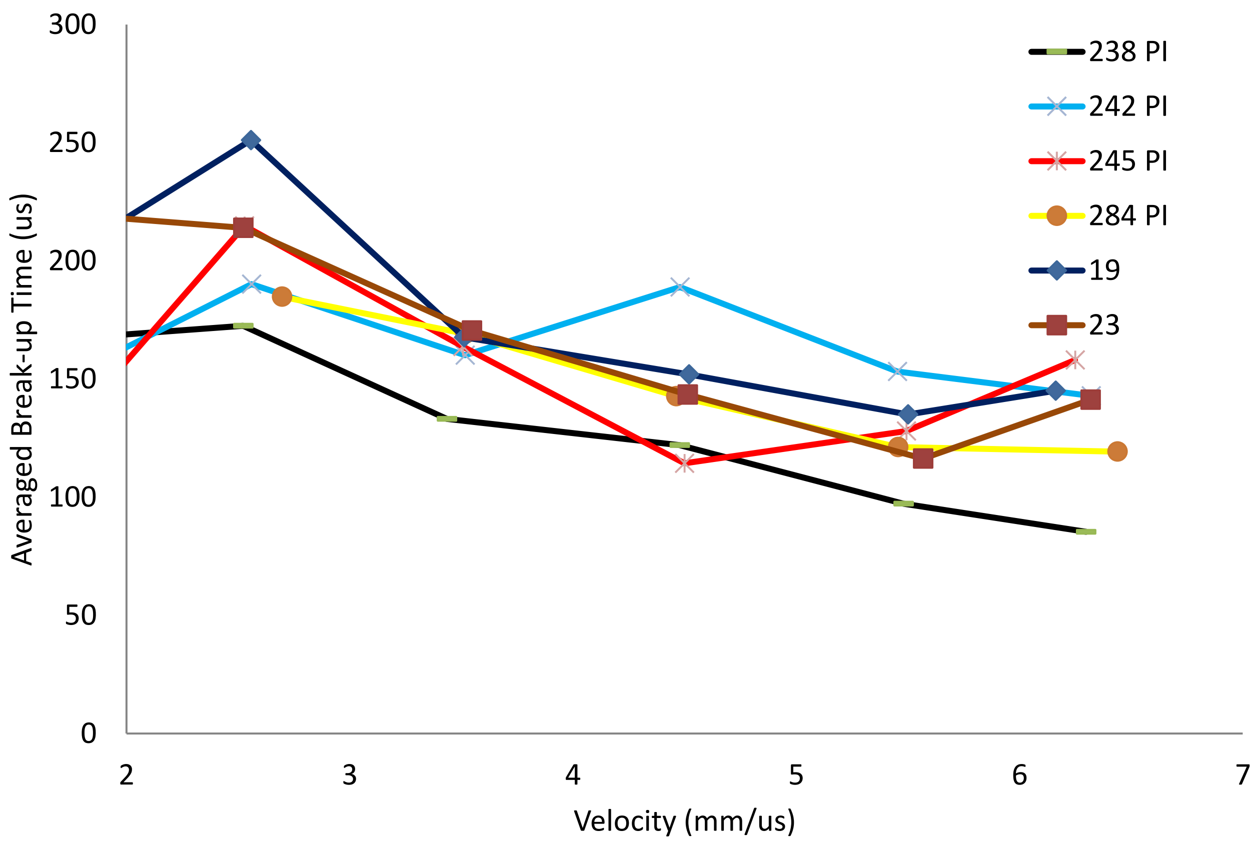

Figure 162: Average break-up-time - Velocity graph for Design 2.

6.6.2.3. Design 3

Three tests were conducted with design 3. The flash X-ray pulse times and the tip velocities are shown in Table 42. The averaged tip velocity from the three tests were calculated to be 4.62 mm/µs. The velocity and position of each particle are presented in Figure 163. The cumulative lengths of the jets are presented Figure 164. The cumulative lengths were measured for jets of similar delay times and have been highlighted in bold in Table 42. The cumulative lengths were repeatable for all three jets measuring up to approximately 200 mm from the tip down to 3 mm/µs. The averaged break-up-times were measured and shown in Figure 165. The break-up-times were also repeatable for all four jets and may be averaged for this specific design.

Table 42: Measured tip velocities and FX delay times used for design 3.

Shot #	Det #	Initiation Type	t_1(µs)	t_2(µs)	V_{TIP} (mm/µs)	V_{TIP}-ave (mm/µs)
19	2018-21	Point	240.8	**360.9**	4.59	4.62
22	2018-24		**380.8**	445.7	4.66	
23	2018-25		**380.7**	445.8	4.61	

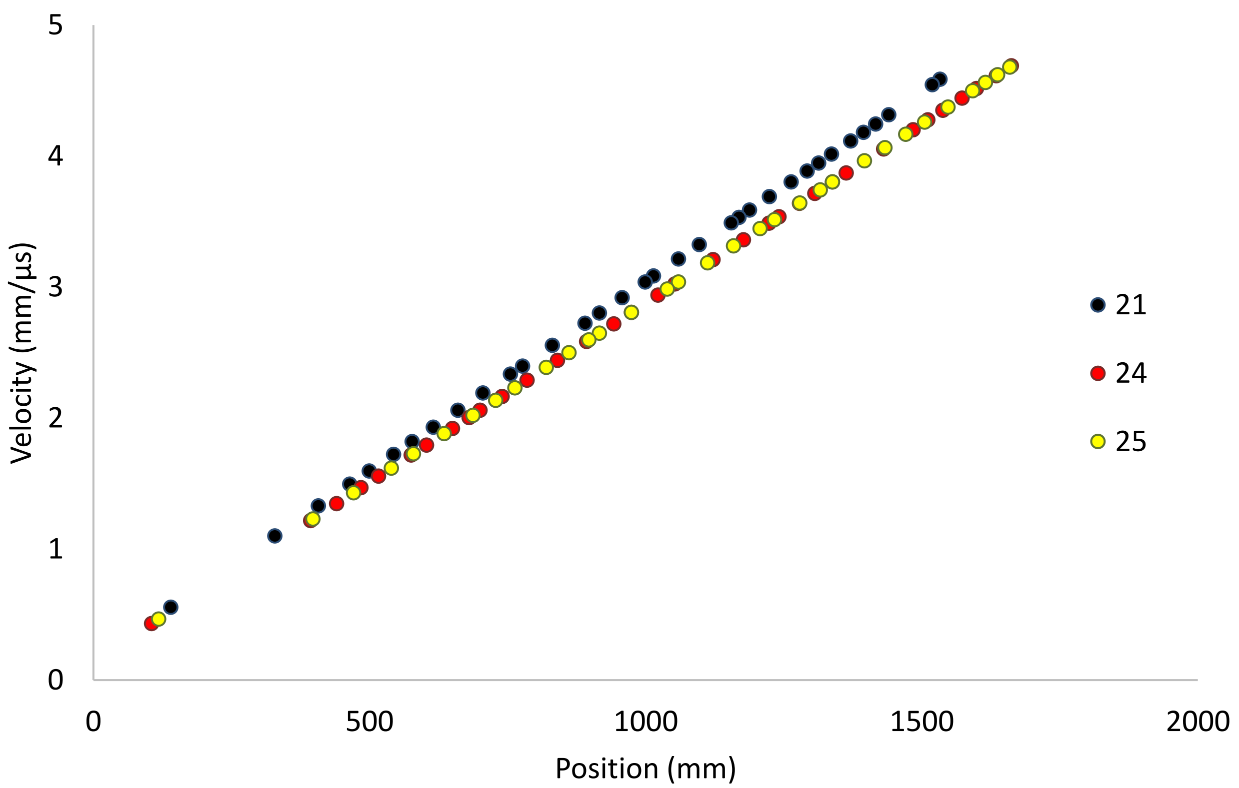

Figure 163: Velocity - Position graph for design 3 – three test firings.

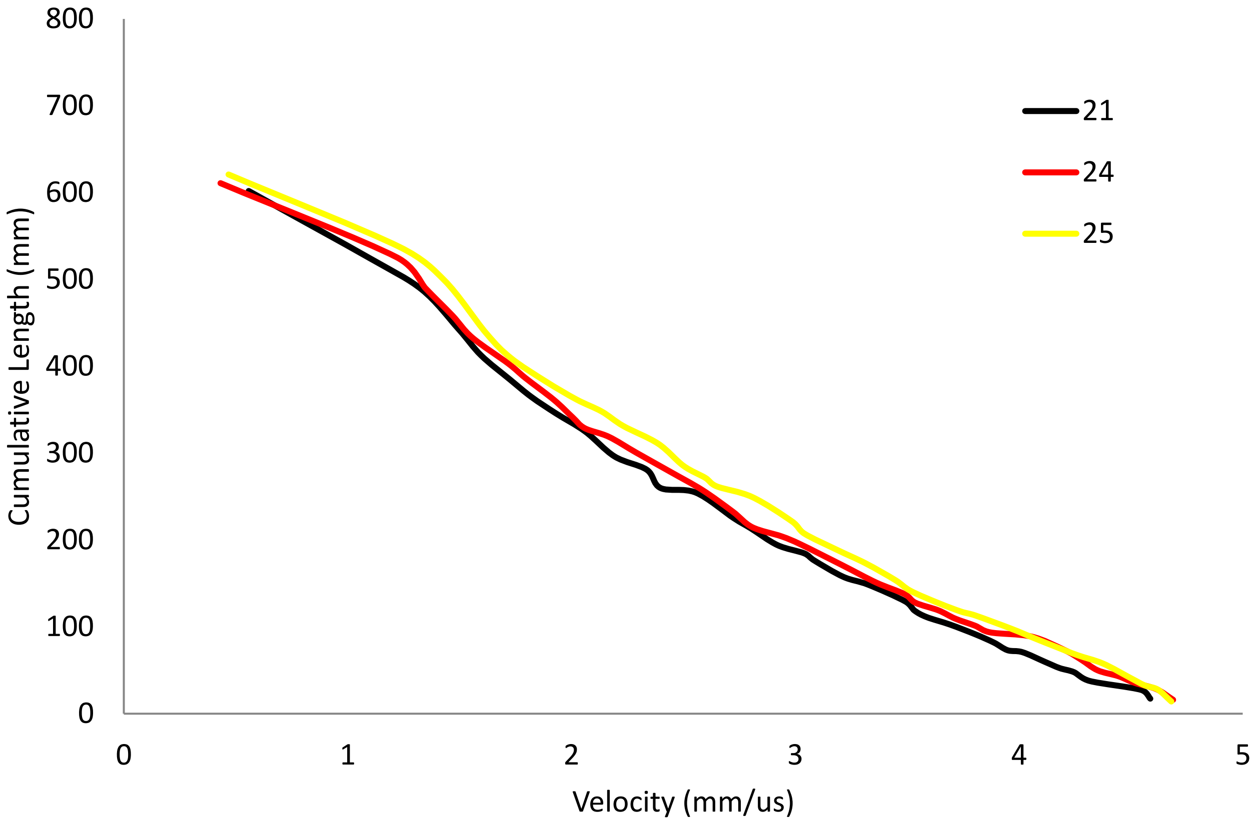

Figure 164: Cumulative Length – Velocity graph for design 3.

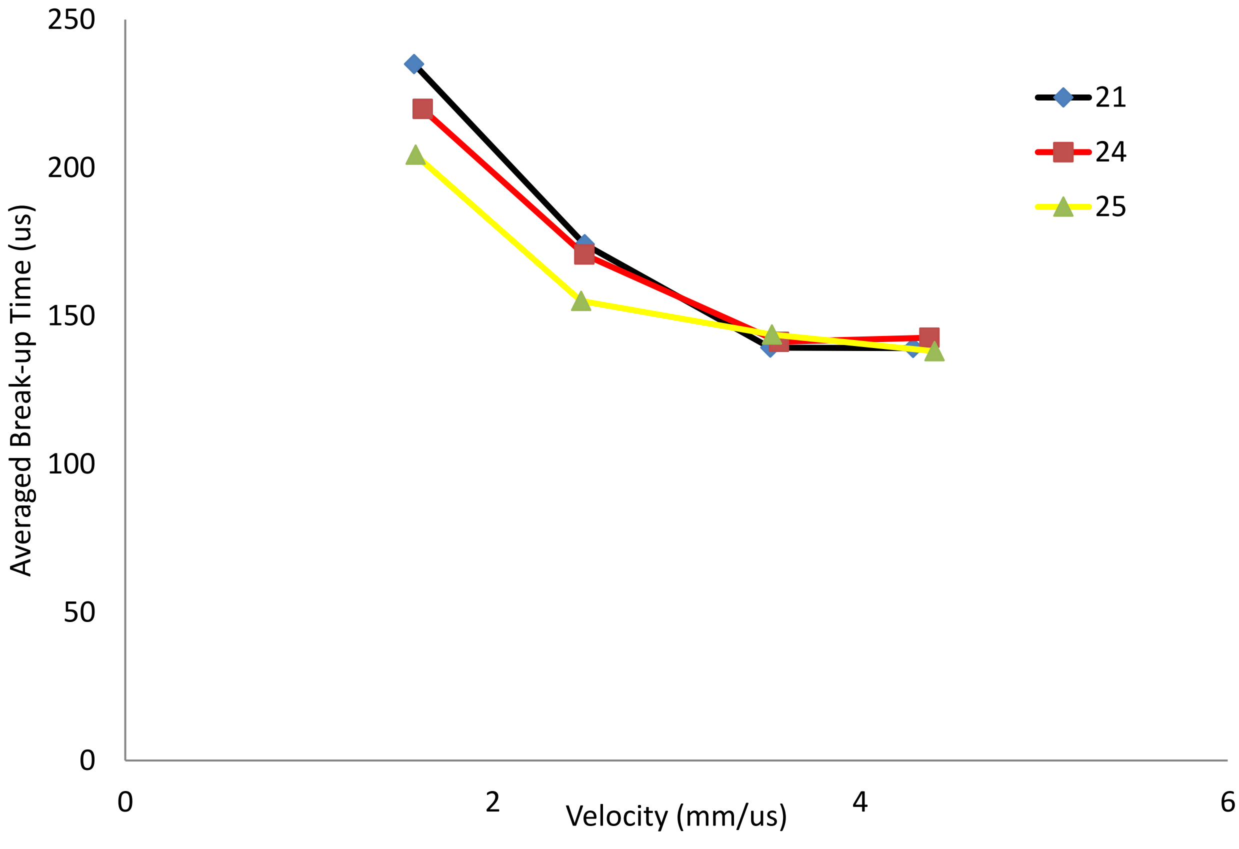

Figure 165: Averaged break-up-time - Velocity graph for Design 3.

6.6.2.4. Design 4

Three tests were conducted for design 4. The flash X-ray pulse times and the tip velocities are shown in Table 43. The averaged tip velocity from the three tests was calculated to be 4.53 mm/µs. The velocity and position of each particle are presented in Figure 166. The cumulative lengths of the jets are presented Figure 167. The cumulative lengths were measured for jets of similar delay times and are highlighted in bold in Table 43. The cumulative lengths were repeatable for two of the three jets measuring up to approximately 250 mm from the tip down to 3 mm/µs (Figure 167). The firing designated as Shot#20 – Det 2018-22, made use of a liner manufactured from bar material and resulted in reduced cumulative lengths compared to jets generated from liners with optimized forgings. The averaged break-up-times were measured and are shown in Figure 168. The break-up-times were also repeatable for the two jets from similar firings. Shot#20 showed reduced break-up-times due to the different liner material used for this firing and is excluded from further analysis.

Table 43: Measured tip velocities and FX delay times used for design 4.

Shot #	Det #	Initiation Type	t_1(µs)	t_2(µs)	V_{TIP} (mm/µs)	V_{TIP}-ave (mm/µs)
20	2018-22	Peripheral 120 deg	130.8	**331.9**	4.50	4.53
28	2018-29		131.8	**311.9**	4.45	
29	2018-30		**309.9**	403.8	4.63	

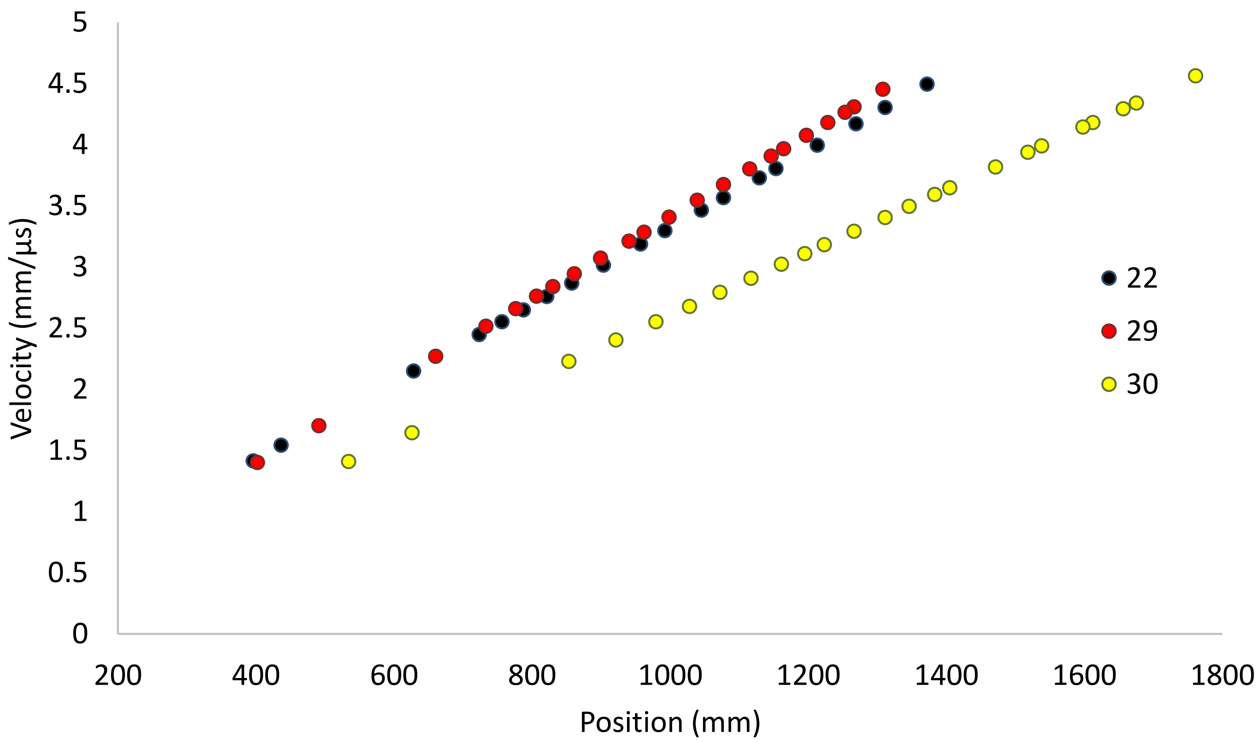

Figure 166: Velocity - Position graph for design 4 – three test firings.

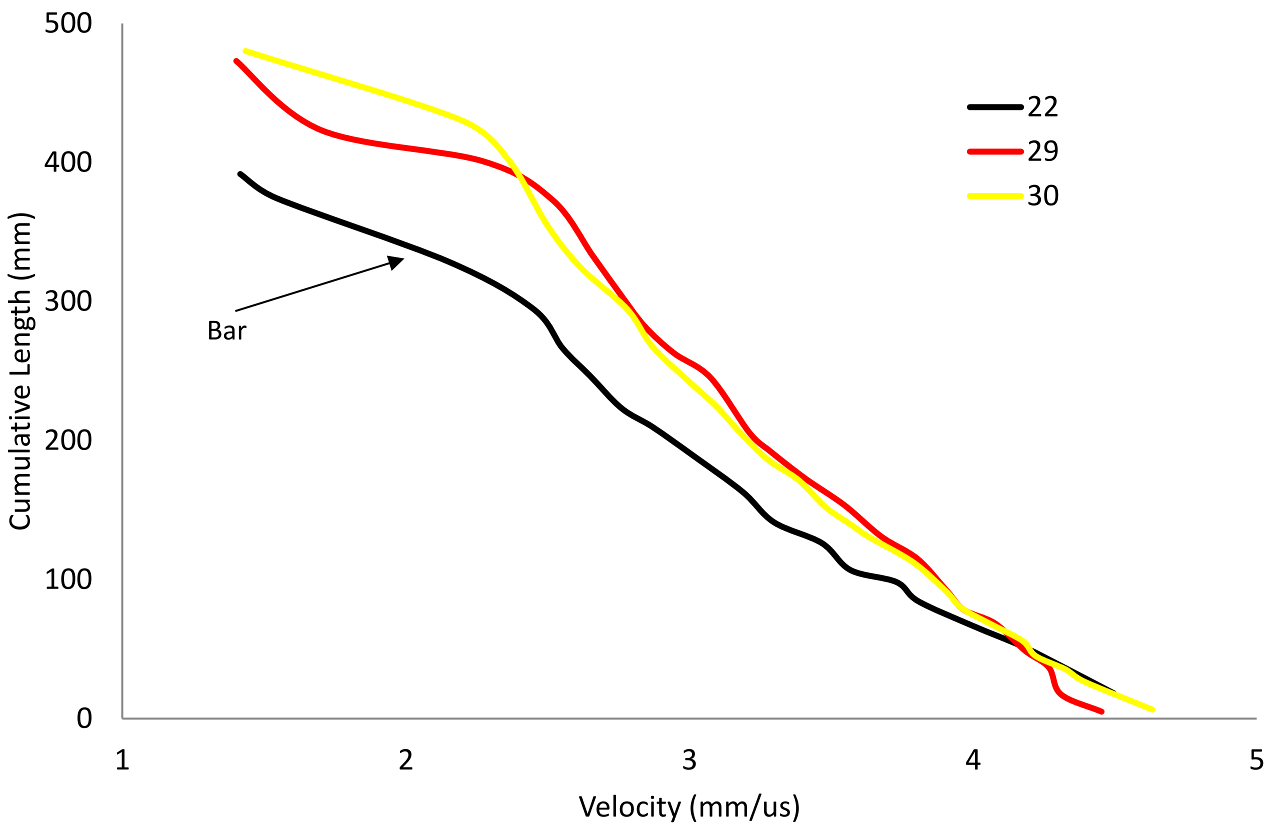

Figure 167: Cumulative Length – Velocity graph for design 4.

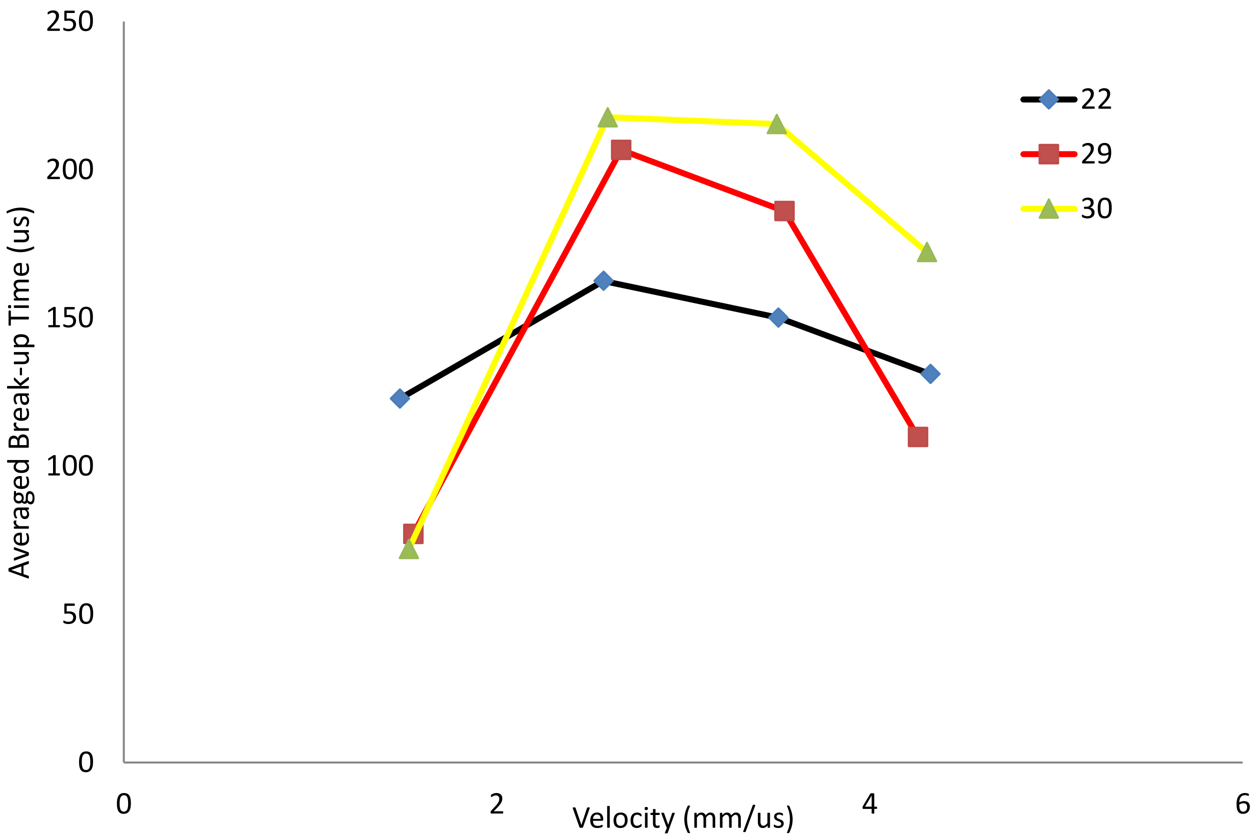

Figure 168: Averaged break-up-time - Velocity graph for Design 4.

6.6.2.5. Design 5

Five tests were conducted with design 5. The flash X-ray pulse times and the tip velocities are shown in Table 44. The averaged tip velocity from the five tests was calculated to be 3.63 mm/µs. The velocity and position of each particle are presented in Figure 169. The cumulative lengths of the jets are presented Figure 170. The cumulative lengths were measured for jets of similar delay times and have been highlighted in bold in Table 44. In Figure 170 the cumulative lengths were repeatable for 3 of the five jets measuring up to approximately 120 mm from the tip down to 3 mm/µs. The cumulative lengths were measured down to 1.5 mm/ µs. Shot#18 (Det # 2018-20) and Shot#24 (Det # 2018-26) made use of liners manufactured from bar material and resulted in reduced cumulative lengths compared to jets generated from liners with optimized forgings. The cumulative length for Test 30 did not show a significant difference in cumulative length compared to other similar firings, even though the FX exposure time used, was much longer. This is due to the jets being captured in the FX recordings in a completely particulated state. The averaged break-up-times were measured and shown in Figure 171. The break-up-times were also repeatable for three of the five jets, Shot#18 and Shot#24 showed reduced break-up-times due to the liner material used for these jets.

Table 44: Measured tip velocities and FX delay times used for design 5.

Shot #	Det #	Initiation Type	t_1(µs)	t_2(µs)	V_{TIP} (mm/µs)	V_{TIP}-ave (mm/µs)
18	2018-20	Point 120 deg	**176.8**	516.7	3.65	3.63
24	2018-26		**225.7**	400.7	3.69	
26	2018-27		**225.7**	405.8	3.60	
27	2018-28		**225.9**	425.8	3.56	
30	2018-31		**425.7**	555.8	3.65	

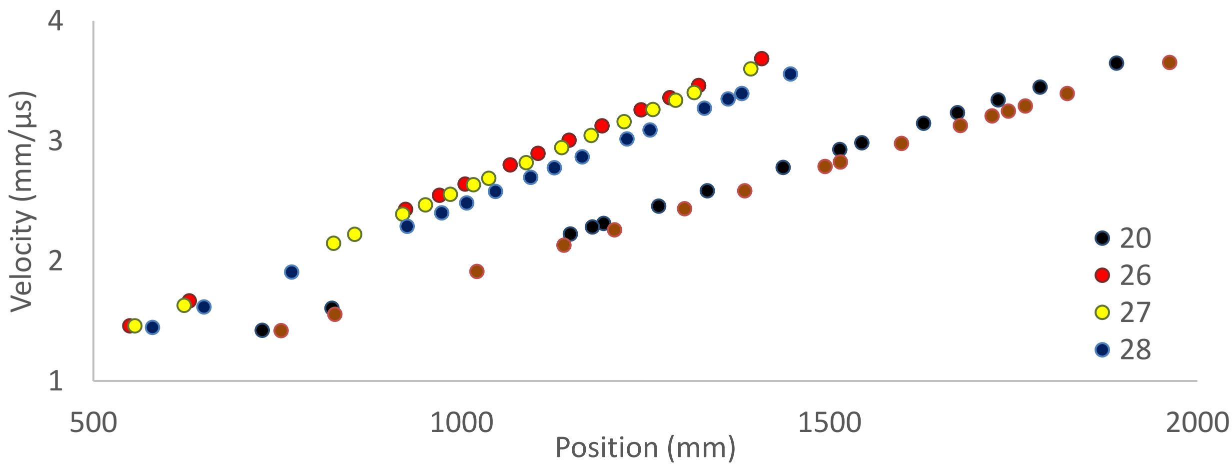

Figure 169: Velocity - Position graph for design 5 – five test firings.

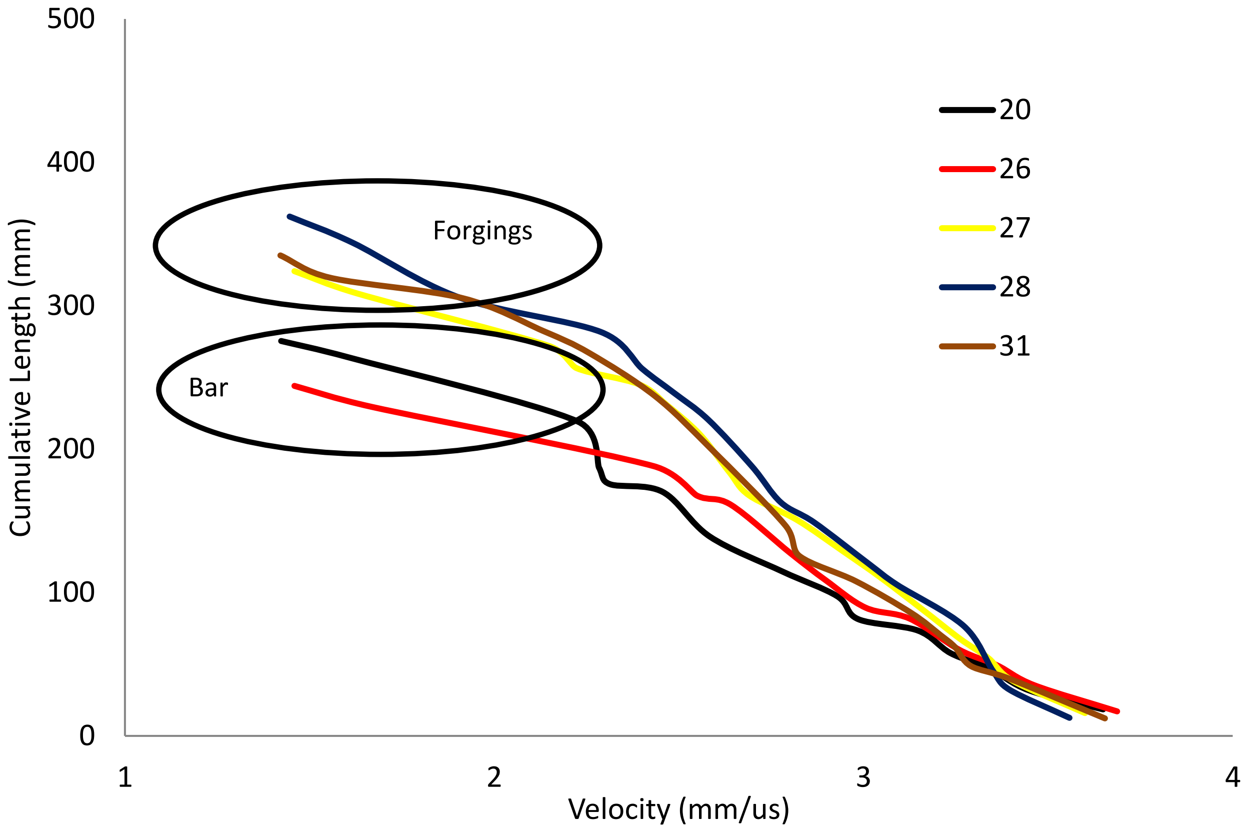

Figure 170: Cumulative Length – Velocity graph for design 5.

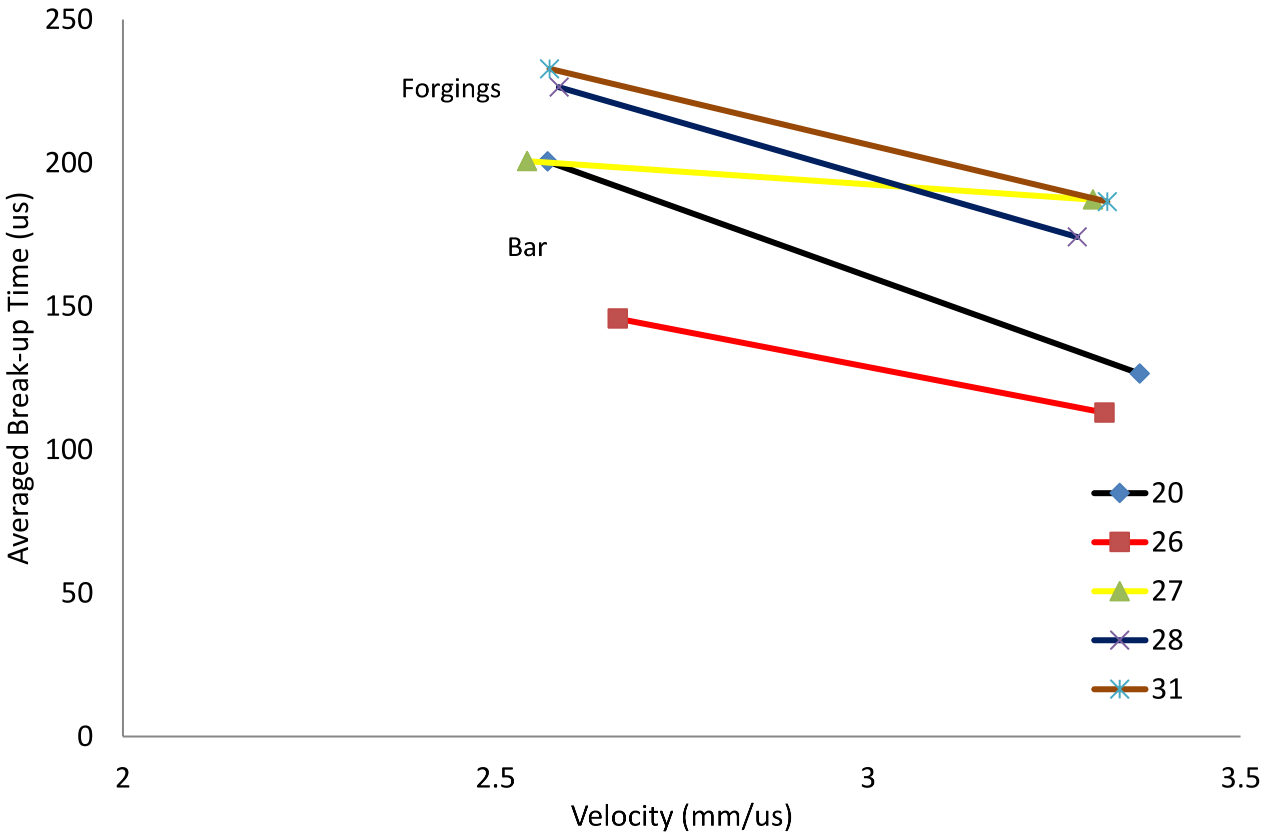

Figure 171: Averaged break-up-time - Velocity graph for Design 5.

6.6.2.6. Design 6

Three tests was conducted with design 6. The flash X-ray pulse times and the tip velocities are shown in Table 45. The averaged tip velocity from the five test was calculated to be 2.57 mm/µs. The velocity and position of each particle are presented in Figure 172. The cumulative lengths of the jets are presented Figure 173. The cumulative lengths were measured for jets of similar delay times and have been highlighted in bold in Table 45. The cumulative lengths were repeatable for all three jets measuring up to approximately 120 mm from the tip down to 2 mm/µs. The cumulative lengths were measured down to 1.5 mm/ µs. The averaged break-up-times were measured and shown in Figure 174.

Table 45: Measured tip velocities and FX delay times used for design 6.

Shot #	Det #	Initiation Type	t_1(µs)	t_2(µs)	V_{TIP} (mm/µs)	V_{TIP}-ave (mm/µs)
31	2018-53	Point 120 deg	**245.7**	538.7	2.54	2.57
32	2018-54		175.8	**310.7**	2.57	
33	2018-55		**350.7**	640.8	2.59	

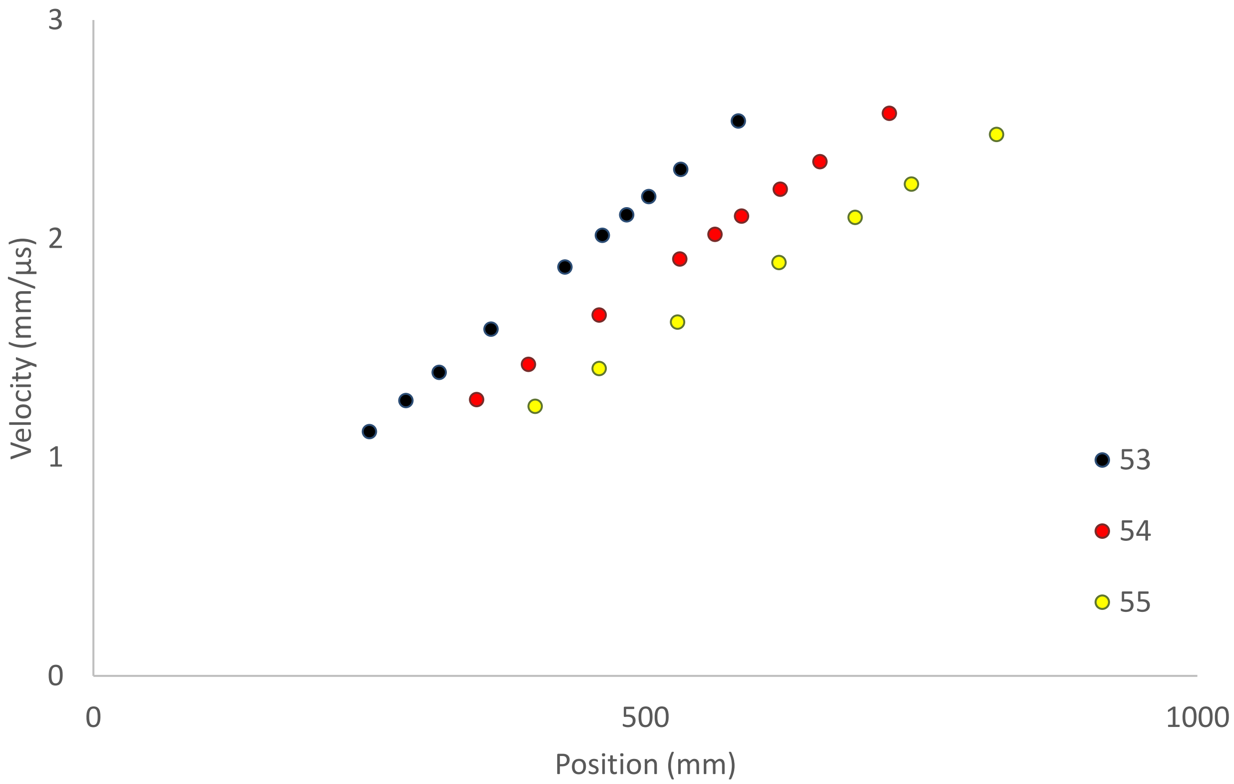

Figure 172: Velocity - Position graph for design 6 – three test firings.

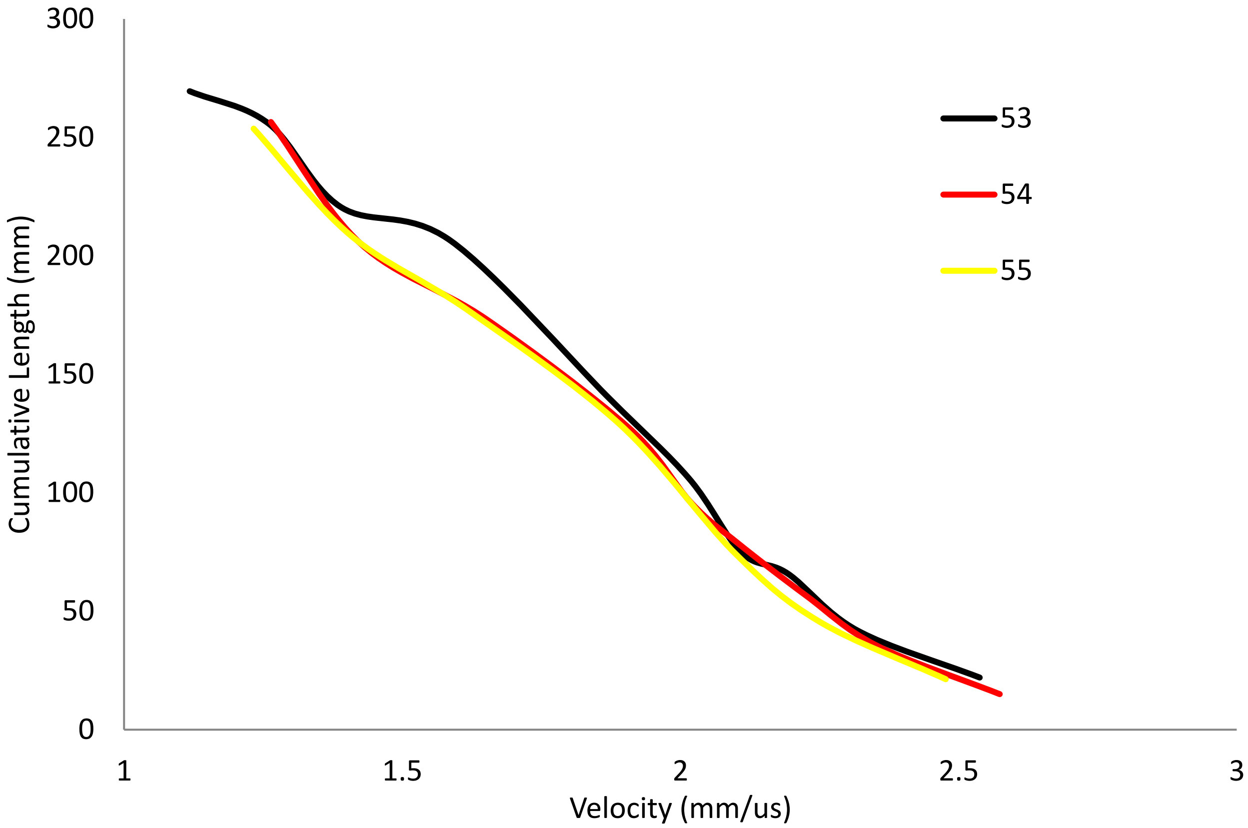

Figure 173: Cumulative Length – Velocity graph for design 6.

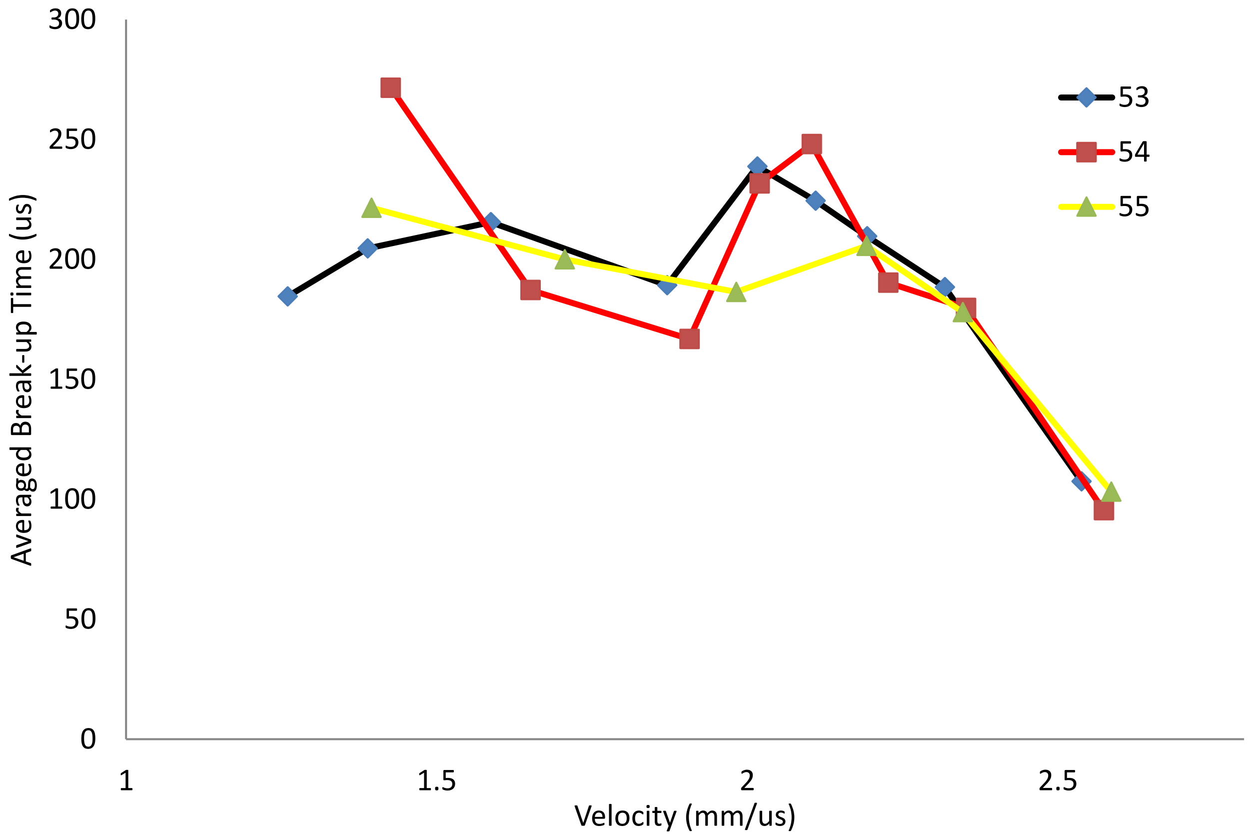

Figure 174: Averaged break-up-time - Velocity graph for Design 6.

6.6.2.7. **Data Summary**

The data from the different individual groups of firings were averaged. This enables a more effective comparison between the respective designs. This section presents a single data set per design, that is, the data for a number of firings are averaged presenting a single cumulative mass distribution and break-up-time distribution as a single data set per design. This simplifies comparison between the designs. **The average data only includes tests for which optimized copper forgings were used as liner material**. The data sets presented here is not only used to compare individual parameters between designs, but also to compare experimental data to well established analytical models. The averaged data for all six designs are presented inTable 46 to Table 51, respectively. The variables listed in Table 46 to Table 51 are described below:

- **V_{ave}:** Averaged velocity in a 1 mm/µs jet segment and further averaged for a number of tests
- **T_b:** Averaged break-up-time in a 1 mm/µs jet segment and further averaged for a number of tests
- **ΔV:** Averaged velocity difference in a 1 mm/µs jet segment and further averaged for a number of tests
- **$r_j(t_b)$:** Averaged shaped-charge jet radius in a 1 mm/µs jet segment and further averaged for a number of tests
- **Cum. Mass:** Averaged cumulative mass in a 1 mm/µs jet segment and further averaged for a number of tests
- **Length:** Averaged particle length in a 1 mm/µs jet segment and further averaged for a number of tests
- **Ave. No. of Particles:** Averaged number of particles in a 1 mm/µs jet segment and further averaged for a number of tests
- **V_{tip}:** Averaged tip velocity for a number of tests

The total number of particles are highlighted in bold in each table below the average number of particles column.

Table 46: Averaged experimental data extracted from FX analysis for design 1.

Design 1							
V_{ave} (mm/µs)	**T_b (µs)**	**ΔV (mm/µs)**	**$r_j(t_b)$ (mm)**	**Cum. Mass (g)**	**Length (mm)**	**Ave. No. Particles**	**V_{tip} (mm/µs)**
8.31	89.7	0.12	1.47	3.49	7.68	5.0	8.58
7.43	125.7	0.10	1.45	9.97	10.46	9.3	
6.55	127.4	0.09	1.35	15.32	8.73	11.7	**V_{Pl}**
5.52	142.8	0.10	1.41	21.94	11.93	9.7	0.093
4.47	159.5	0.10	1.42	30.34	13.86	10.7	
3.50	184.6	0.11	1.65	43.82	19.54	8.3	
2.57	231.2	0.14	1.97	69.15	27.35	8.0	
1.39	145.6	0.16	2.63	104.98	21.41	5.7	
						68.3	

Table 47: Averaged experimental data extracted from FX analysis for design 2.

Design 2							
V_{ave} (mm/µs)	**T_b (µs)**	**ΔV (mm/µs)**	**$r_j(t_b)$ (mm)**	**Cum. Mass (g)**	**Length (mm)**	**Ave. No. Particles**	**V_{tip} (mm/µs)**
6.29	128.76	0.11	1.66	6.93	13.97	4.0	6.55
5.48	126.14	0.11	1.34	12.96	12.05	9.7	
4.49	141.77	0.10	1.34	20.11	14.11	9.3	**V_{Pl}**
3.49	152.34	0.10	1.38	28.40	13.98	10.7	0.090
2.54	192.51	0.11	1.99	53.08	22.42	8.7	
1.70	150.67	0.14	2.88	90.66	33.70	5.0	
						47.3	

Table 48: Averaged experimental data extracted from FX analysis for design 3.

Design 3							
V_{ave} (mm/µs)	**T_b (µs)**	**ΔV (mm/µs)**	**$r_j(t_b)$ (mm)**	**Cum. Mass (g)**	**Length (mm)**	**Ave. No. Particles**	**V_{tip} (mm/µs)**
4.36	139.95	0.09	1.44	6.54	10.52	6.7	4.65
3.53	141.47	0.11	1.28	11.68	11.19	9.7	
2.49	166.68	0.15	1.61	19.58	17.41	8.0	**V_{Pl}**
1.59	205.00	0.12	1.27	43.52	27.81	7.0	0.089
						31.4	

Table 49: Averaged experimental data extracted from FX analysis for design 4.

Design 4							
V_{ave} (mm/µs)	**T_b (µs)**	**ΔV (mm/µs)**	**$r_j(t_b)$ (mm)**	**Cum. Mass (g)**	**Length (mm)**	**Ave. No. Particles**	**V_{tip} (mm/µs)**
4.32	137.27	0.14	1.56	5.17	13.48	5.0	4.67
3.53	175.65	0.11	1.66	19.33	17.37	9.3	
2.60	188.12	0.18	2.63	53.75	22.91	6.7	**V_{PI}**
1.54	83.13	0.22	4.32	71.96	31.53	3.3	0.091
						24.3	

Table 50: Averaged experimental data extracted from FX analysis for design 5.

Design 5							
V_{ave} (mm/µs)	**T_b (µs)**	**ΔV (mm/µs)**	**$r_j(t_b)$ (mm)**	**Cum. Mass (g)**	**Length (mm)**	**Ave. No. Particles**	**V_{tip} (mm/µs)**
3.25	153.7	0.11	2.07	9.51	16.79	3.7	3.63
2.58	199.5	0.13	2.44	47.66	23.15	9.0	
1.61	79.4	0.14	2.94	59.14	23.49	2.7	**V_{PI}**
							0.130
						15.3	

Table 51: Averaged experimental data extracted from FX analysis for design 6.

Design 6							
V_{ave} (mm/µs)	**T_b (µs)**	**ΔV (mm/µs)**	**$r_j(t_b)$ (mm)**	**Cum. Mass (g)**	**Length (mm)**	**Ave. No. Particles**	**V_{tip} (mm/µs)**
2.26	170.0	0.15	2.42	14.51	21.49	3.0	2.58
1.51	215.0	0.17	3.02	60.78	37.75	4.7	**V_{PI}**
						7.7	0.139

The average cumulative lengths of all six designs are shown in Figure 175. This graphs clearly shows the incremental changes in tip velocity, the similar trends observed in cumulative mass distributions for similar liners and how the lengths increases as the strain and strain rate of a design increases. Similar trends are observed in the cumulative masses for each design as shown in Figure 176. The averaged breakup times may be compared in Figure 177. Again the trends in breakup times correlated based on the liner design and the higher strain and strain rate designs results in higher breakup times.

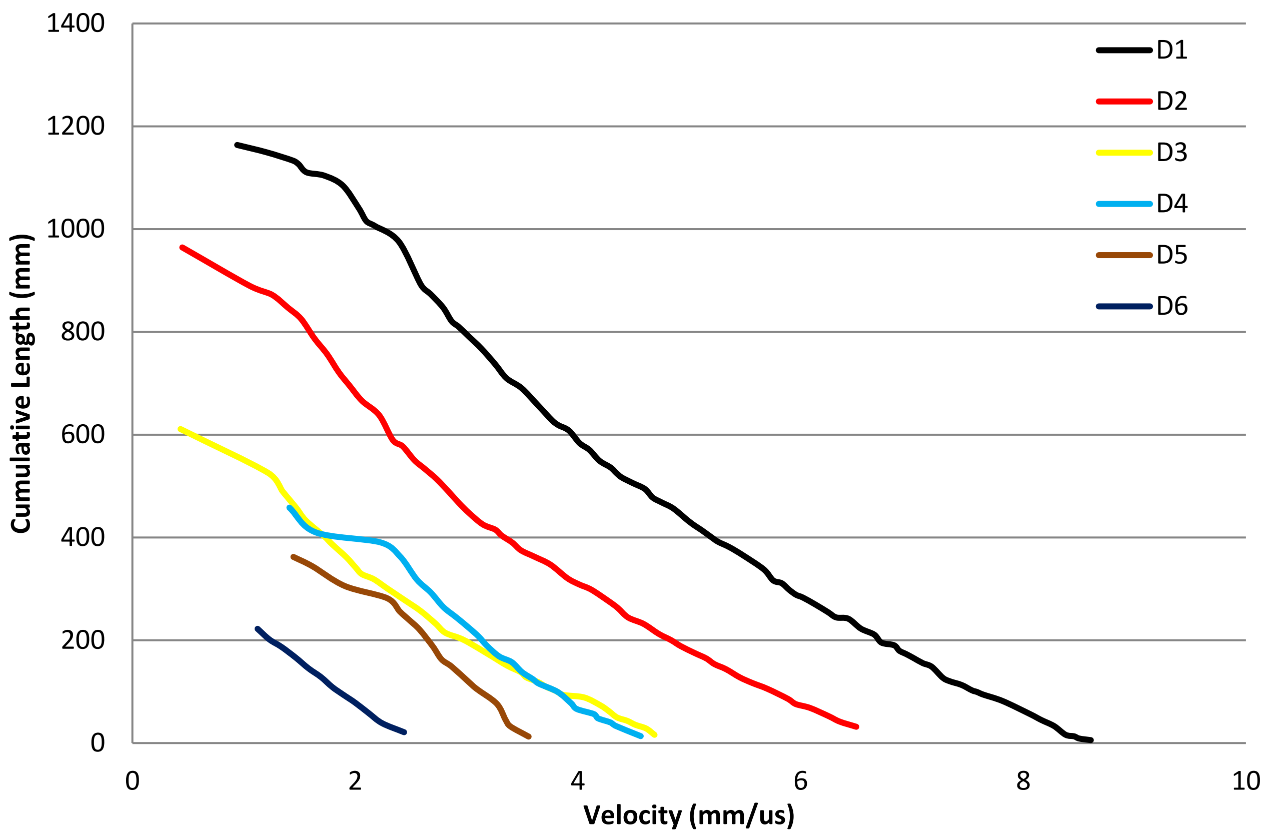

Figure 175: An illustration of the cumulative length for each particular design.

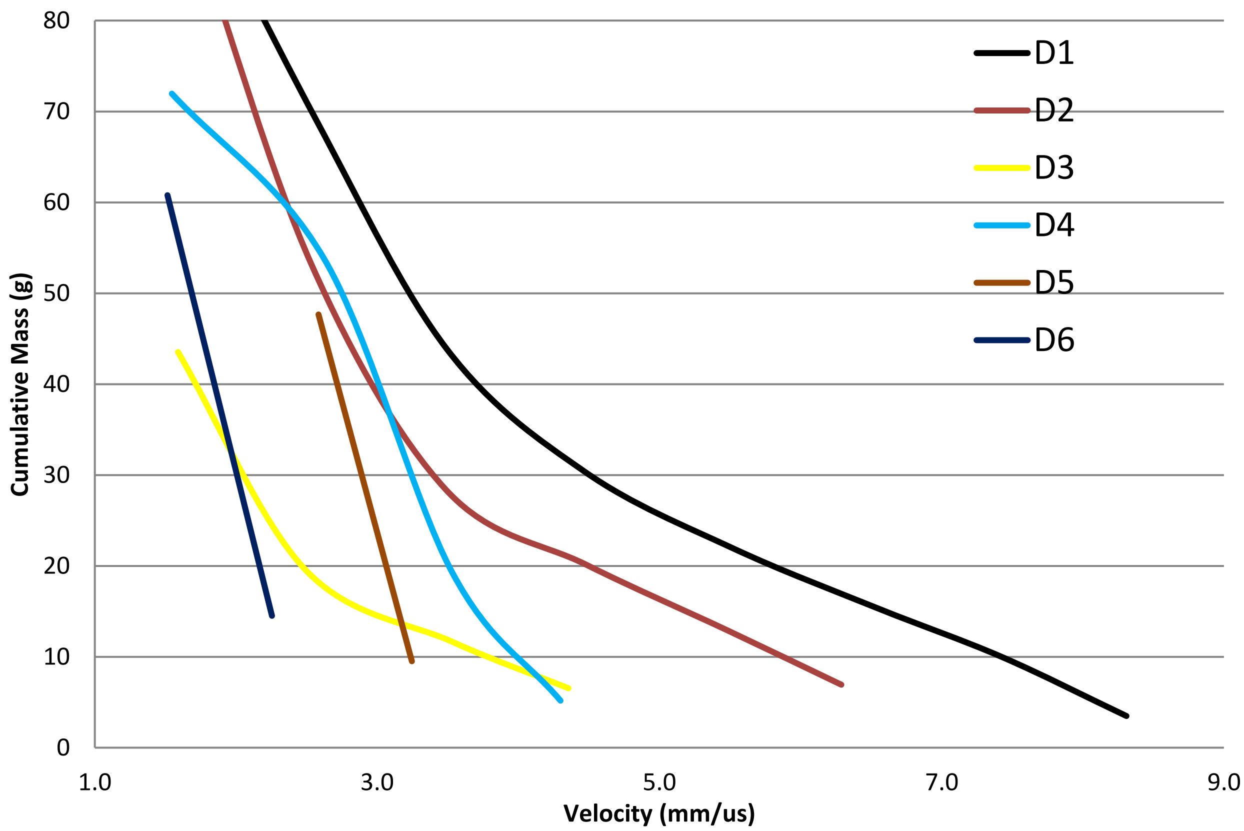

Figure 176: An illustration of the cumulative mass for each particular design.

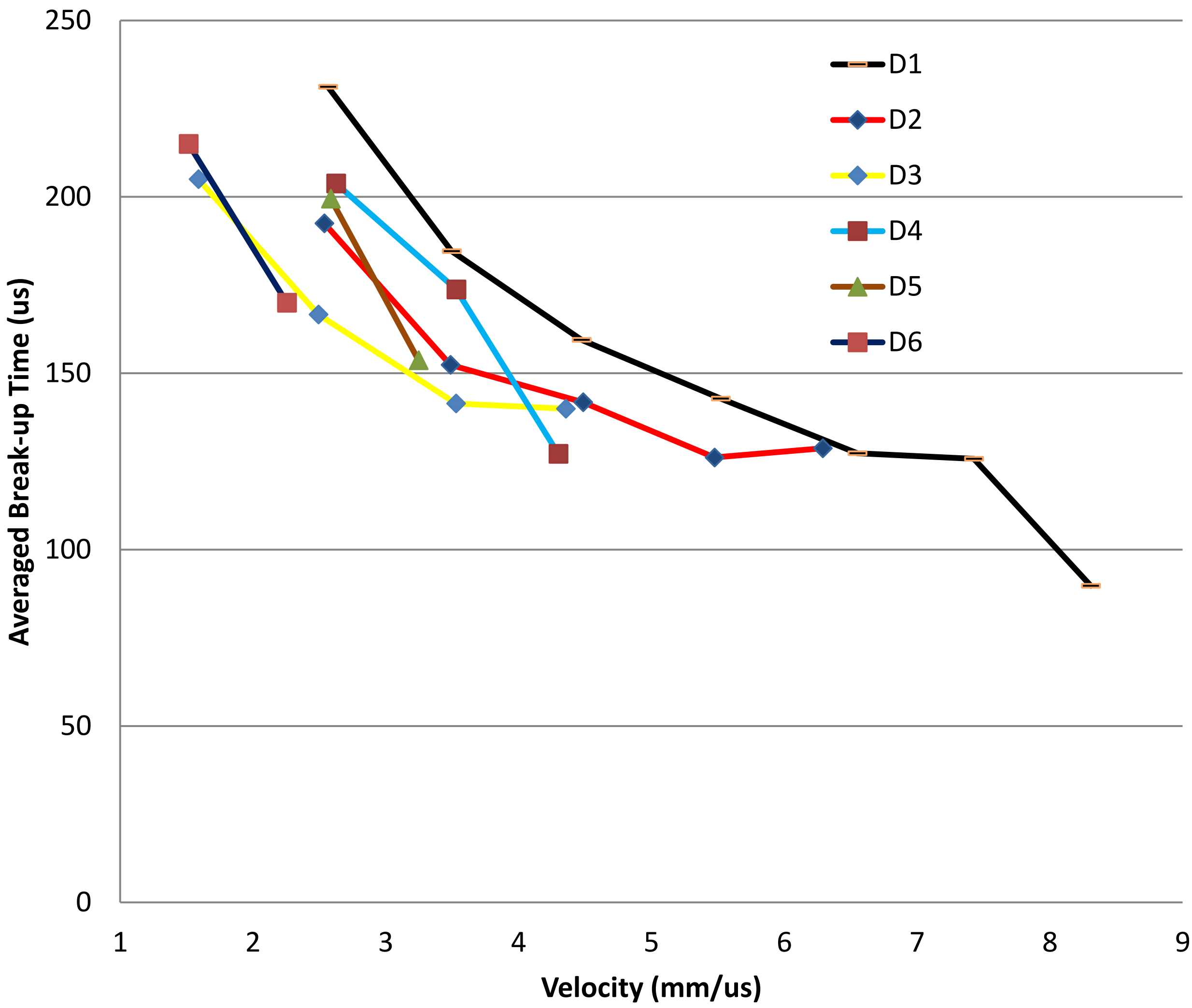

Figure 177: A comparison of the averaged break-up-times for each design.

7. DISCUSSION

7.1. Introduction

The break-up phenomena in shaped-charge jets have been studied for many designs over numerous decades [46], [48], [60], [75], [83], [97]. Most of this work have centred on the break-up of copper jets. There is consensus that the copper jets dynamically elongate to strains far exceeding that of the virgin material at lower strain-rates, but the physics behind this behaviour, is still obscure. While many comparative studies have been performed, few compared experimental results that were obtained with exactly the same starting material conditions. The main focus of the current research was to demonstrate the influence of varying strain and strain-rate behaviour on shaped-charge jet break-up times with copper liners which have the same initial microstructures, more specifically, to investigate the nature of the true plasticity of the jets. A detailed experimental study was performed on forging manufacture with microstructural analysis performed in each forging process in order to manufacture copper forgings of different angles with comparable microstructures.

The overall jet strain and strain-rate was varied by changing the liner angle and the use of different initiation systems. Two liner designs (60° and 120°, respectively) with similar microstructures were evaluated. The jet strain and strain-rate was further modified by the utilisation of two initiation systems (point initiation and peripheral initiation)

The section below lists some of the well-known empirical formulae used to predict break-up-times of shaped-charge jets. The experimental dataset associated with the shaped-charge designs were used to evaluate some of the empirical formulae. Each shaped-charge design was simulated in Ansys AUTODYN for the respective desired jet properties. Each design was manufactured and tested three times by means of flash X-ray radiography. The flash X-ray results from data analyses to be compared to the respective models. Some of these analysis were reported in [98]. The extension of work in this chapter is the addition of two concept designs using the experimental explosive formulation F and comparisons to AUTODYN simulations.

7.2. Strain and Strain-rate determination

Six shaped-charge designs were simulated, manufactured and tested. The charge diameter for all designs was 80 mm and the liner thickness was kept constant at 1.7 mm. A change in the initiation system was further incorporated to vary the overall jet strain and strain-rate. This section mainly focuses on the experimental evaluation. The data accumulated from the respective designs were used to test models or check correspondence between model predictions and experimental data. The design parameters are presented in Table 52.

Table 52: Shaped-charge warhead design parameters.

Design	Explosive	Initiation Mode	Liner Angle (deg)	Tip Velocity (mm/µs)	Slug Velocity (mm/µs)
1	Comp A3	Peripheral	60	8.58	0.45
2	Comp A3	Point	60	6.55	0.45
3	Form F	Point	60	4.65	0.50
4	Comp A3	Peripheral	120	4.67	1.43
5	Comp A3	Point	120	3.63	1.42
6	Form F	Point	120	2.58	1.23

7.2.1. **Strain Determination from Eq. 23**

The strain-rates are calculated for each design after jet-break-up. The strain-rates were calculated according to Eq. 18 in this section. The subjectivity about this equation is the allocation of L_0. L_0 is defined as the initial length measured from the jet tip down to the jet tail. The subjectivity amongst authors is the selection of the tail velocity. Some authors makes use of the cut-off velocity. Cut-off velocity is the velocity of the slowest particle contributing to penetration within a semi-infinitely thick target. The problem with this selection is that cut-off velocity is a function of the stand-off. As stand-off increases, the cut-off velocity increases and so therefore the strain-rate is not constant for a particulated-jet.

The author has decided to calculate L_0 according to Eq. 23, assuming a final strain of 2.3 at jet-break-up. The cumulative lengths were measured down to velocity of 2 mm/µs and down to the slug for all six-concept designs. This final strain correlates to a constant strain of 9 according to Eq. 17. The final lengths were measured from the FX radiographs. The total cumulative length was used as the final length. L_0 was calculated according to Eq. 23 and the strain-rate was calculated according to Eq. 18.

$$\varepsilon_F = ln\left(\frac{L}{L_0}\right) \approx 2.3 \qquad \text{Eq. 23}$$

$$\varepsilon = \frac{L - L_0}{L_0} = \frac{\Delta L}{L_0} \qquad \text{Eq. 17}$$

$$\dot{\varepsilon} = \frac{d\varepsilon}{d\tau} = \frac{d}{d\tau}\left(\frac{\Delta L}{L_0}\right) = \frac{(v_t - v_r)}{L_0}$$ Eq. 18

Table 53: Strain-rate determination for a constant final strain, ε_F, of 2.3 from jet tip down to the slug.

Design	V_{Tip} (mm/µs)	V_{Rear} (mm/µs)	L (mm)	ε_F	L_0 (mm)	ε	$\dot{\varepsilon}$ (s^{-1})
1	8.58	0.45	1160	2.3	116	9	70100
2	6.55	0.45	964		96		63300
3	4.65	0.50	620		62		66900
4	4.67	1.43	480		48		67500
5	3.63	1.42	360		36		61400
6	2.58	1.23	250		25		54000

Table 54: Strain-rate determination for a constant final strain, ε_F, of 2.3 from jet tip down to the 2 mm/µs.

Design	V_{Tip} (mm/µs)	V_{Rear} (mm/µs)	L (mm)	ε_F	L_0 (mm)	ε	$\dot{\varepsilon}$ (s^{-1})
1	8.58	2.00	892	2.3	89.2	9	73800
2	6.55		700		70.0		65000
3	4.65		340		34.0		77900
4	4.67		440		44.0		60700
5	3.63		305		30.5		53400
6	2.58		100		10.0		54700

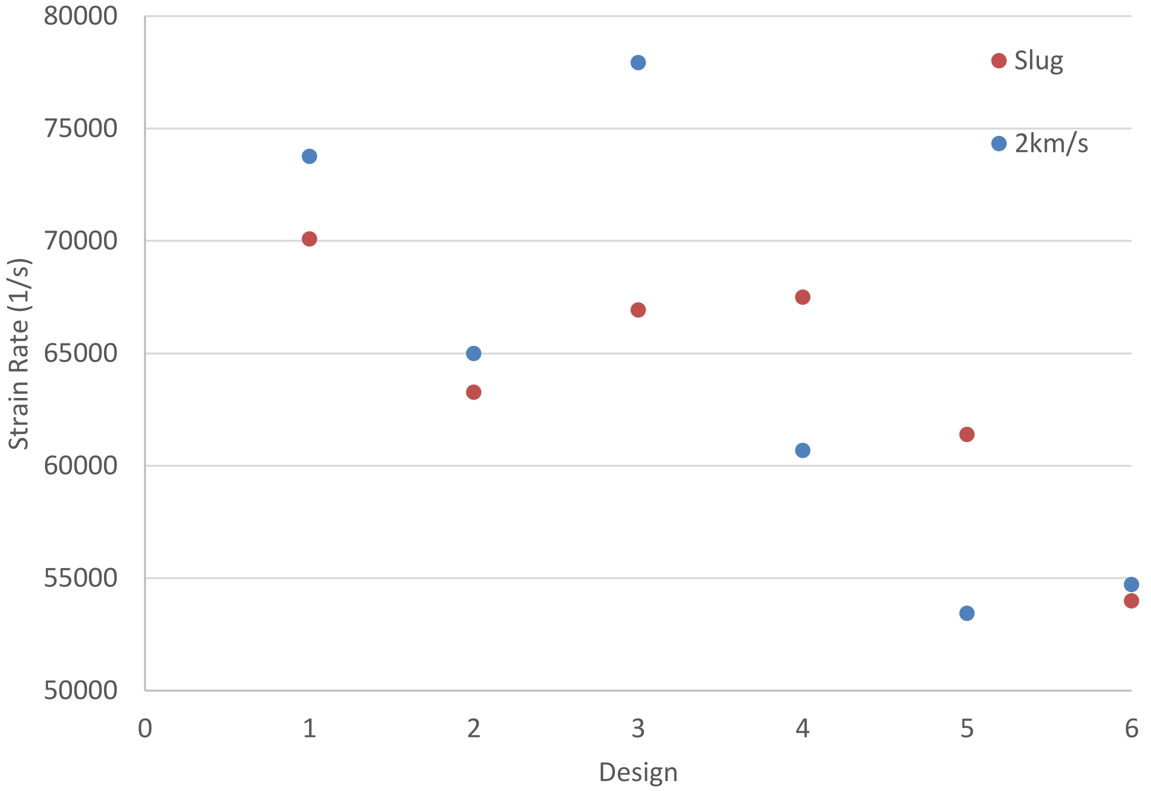

Figure 178: Strain-rate determination from an initial length determined from a constant final strain assumption of 2.3.

After calculating the strain-rates for a constant final strain rate 2.3, it seems the strain-rates for the "lower strain-rate designs" are artificially increased. This is so due to a rather low initial length allocation based on the measured total cumulative lengths from experiments. The analysis was repeated with inputs from the simulations of each concept design and presented below.

7.2.2. L_0 Determination from Simulation

The initial length of the jets for the respective concept designs were measured in figures from AUTODYN simulations. The lengths were measured when the jet was formed down to 2 mm/µs. The measurements were read from the jet tip down to 2 mm/µs and from the jet tip down to the slug, respectively. The strain and strain-rates were calculated, using Eq. 17 and Eq. 18, from images graphically presented in Figure 179 to Figure 190 and summarized in Table 55 and Table 56, respectively. The strain-rates are graphically summarised in Figure 191.

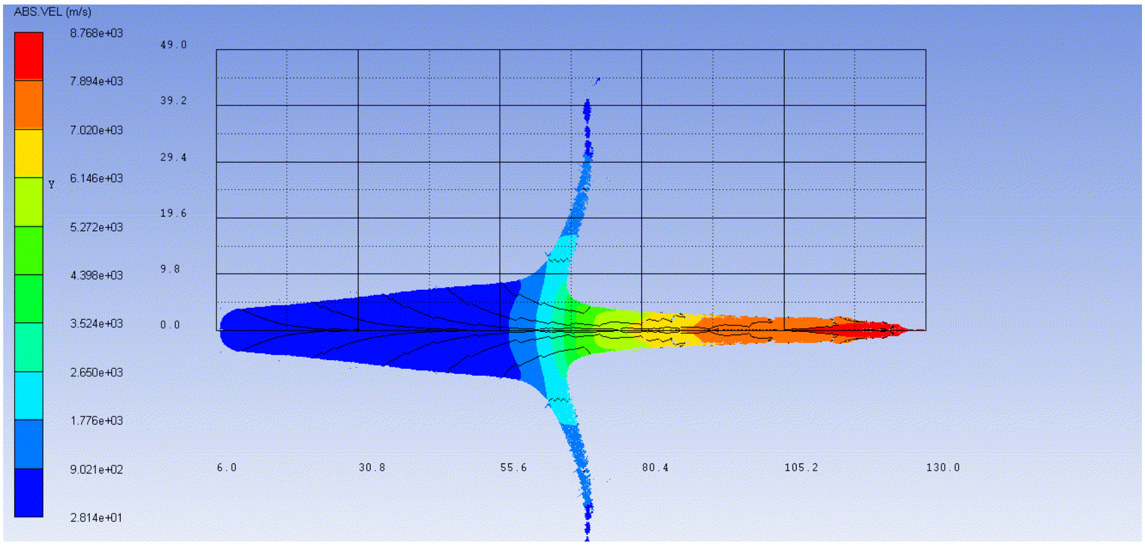

Figure 179: L_0 determination for Design 1 down to the slug.

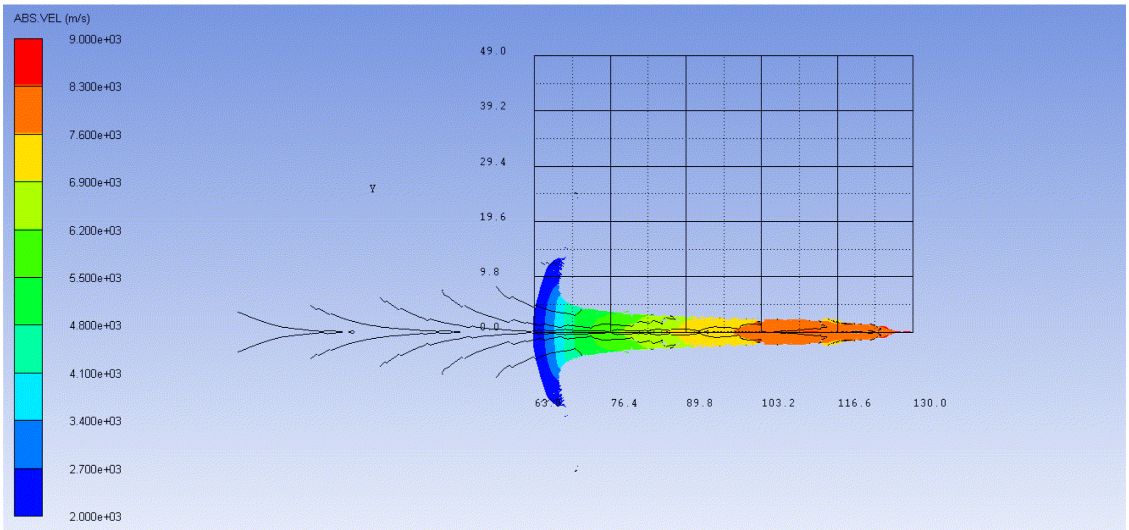

Figure 180: L_0 determination for Design 1 down to the 2 mm/µs.

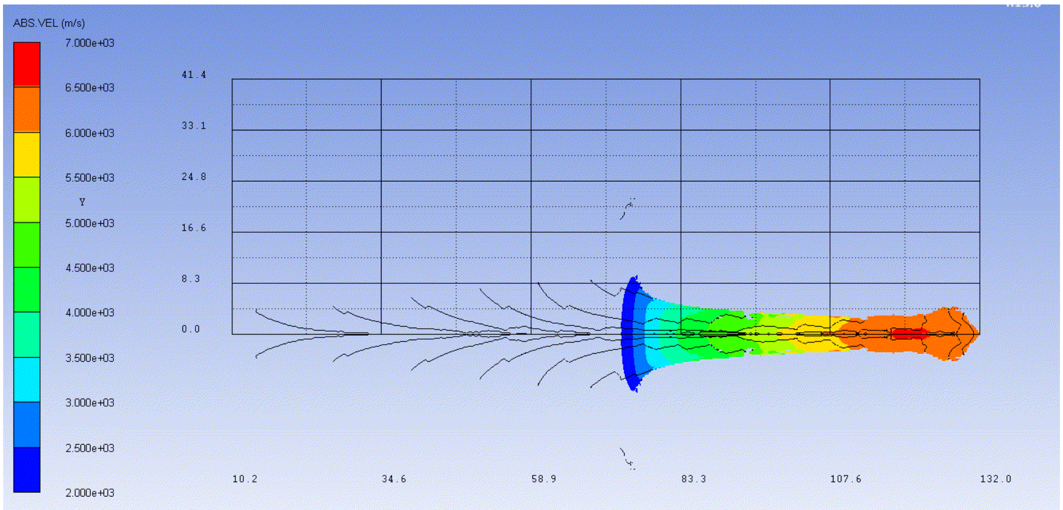

Figure 181: L_0 determination for Design 2 down to the slug.

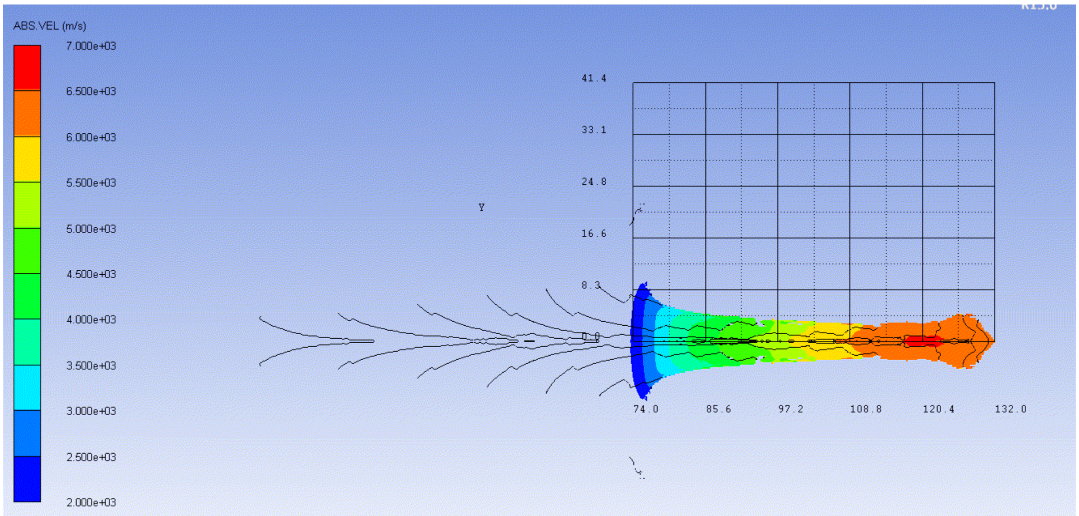

Figure 182: L_0 determination for Design 2 down to the 2 mm/µs.

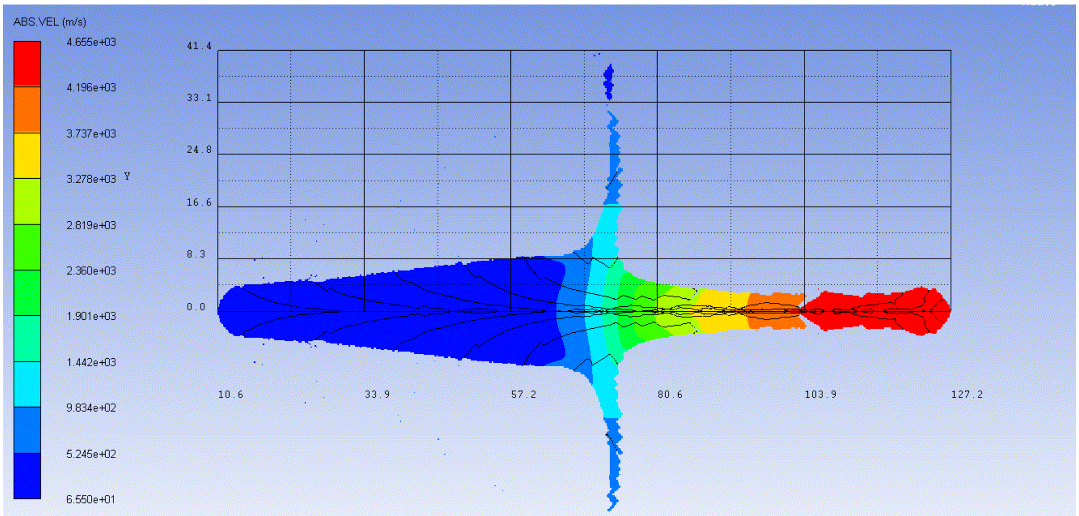

Figure 183: L_0 determination for Design 3 down to the slug.

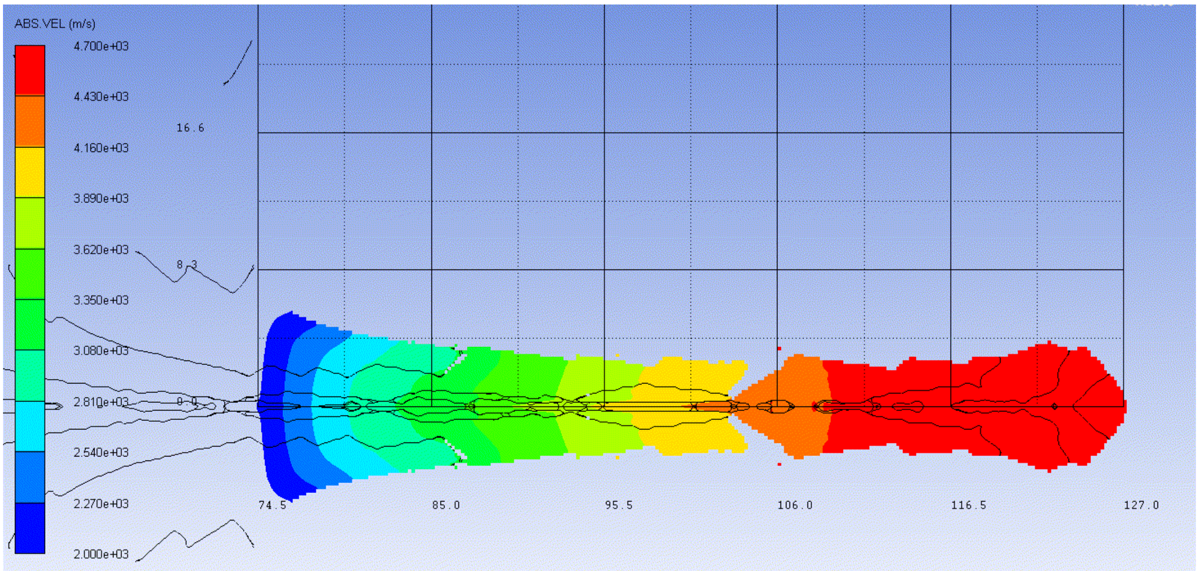

Figure 184: L_0 determination for Design 3 down to the 2 mm/µs.

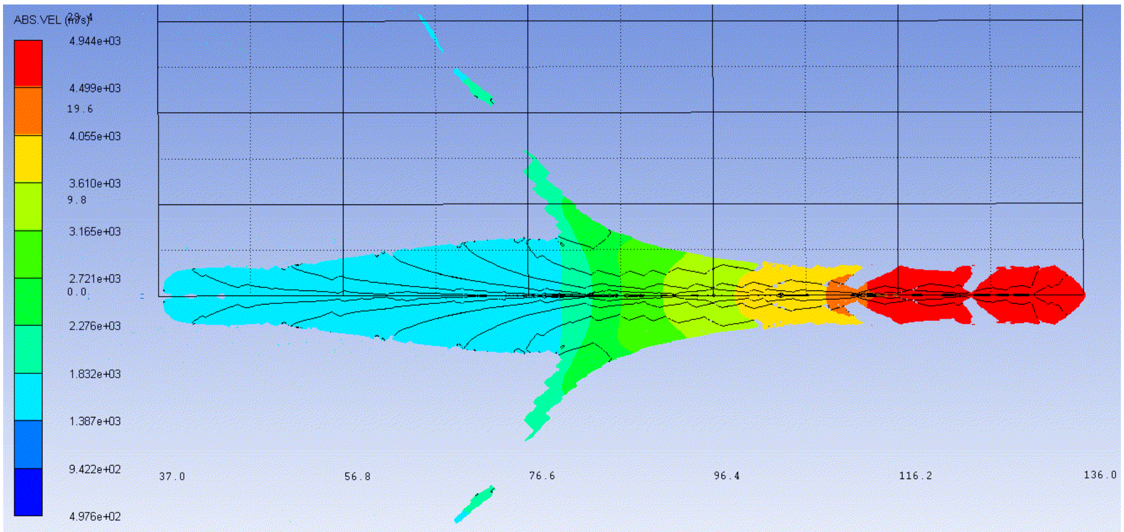

Figure 185: L_0 determination for Design 4 down to the slug.

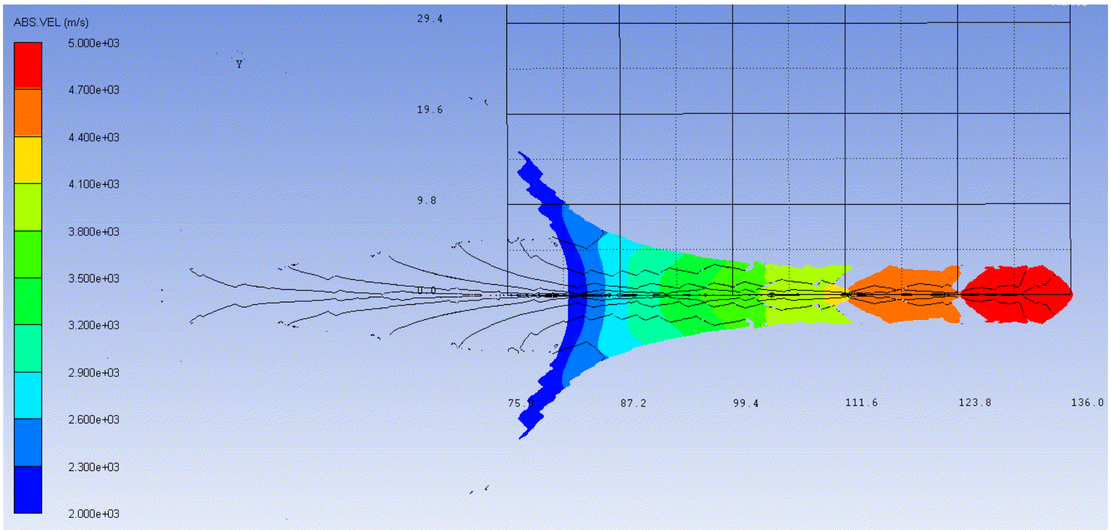

Figure 186: L_0 determination for Design 4 down to the 2 mm/µs.

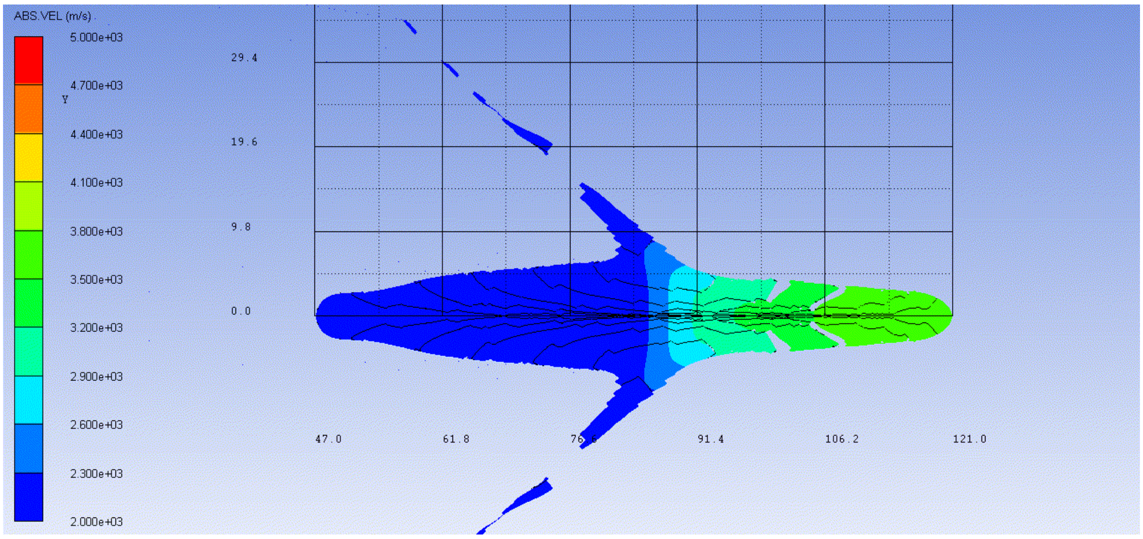

Figure 187: L_0 determination for Design 5 down to the slug.

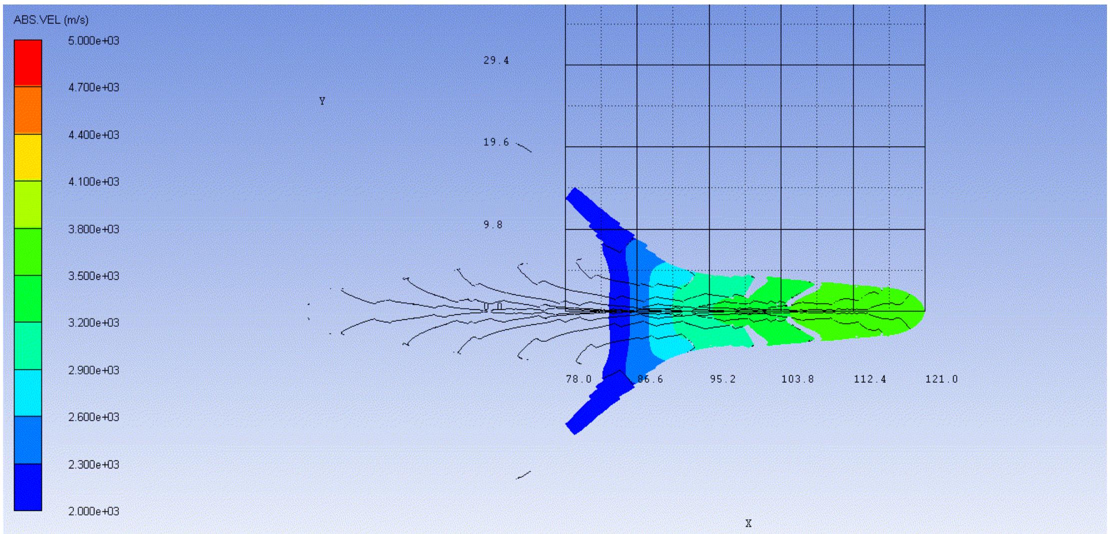

Figure 188: L_0 determination for Design 5 down to the 2 mm/μs.

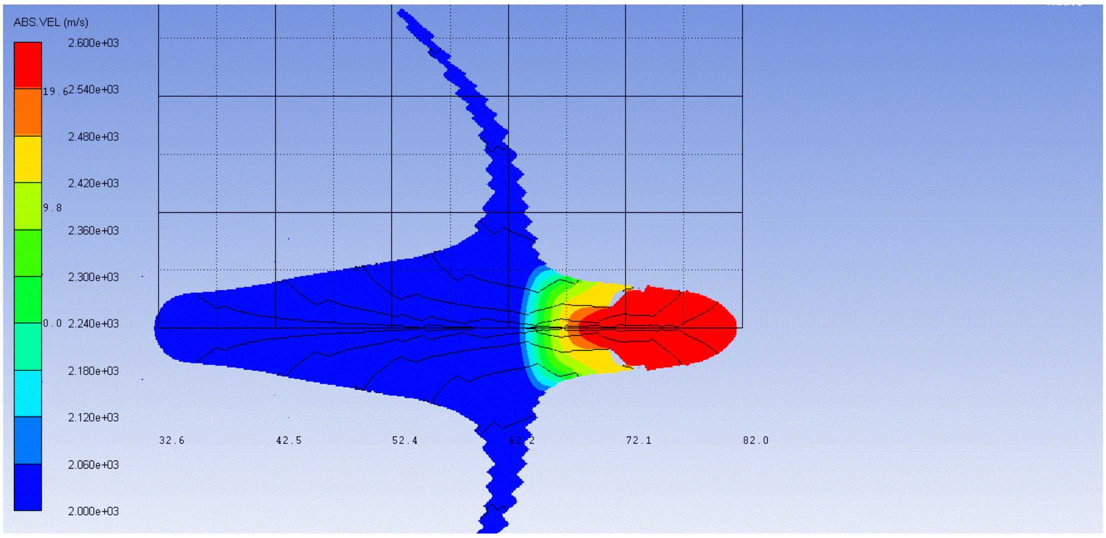

Figure 189: L_0 determination for Design 6 down to the slug.

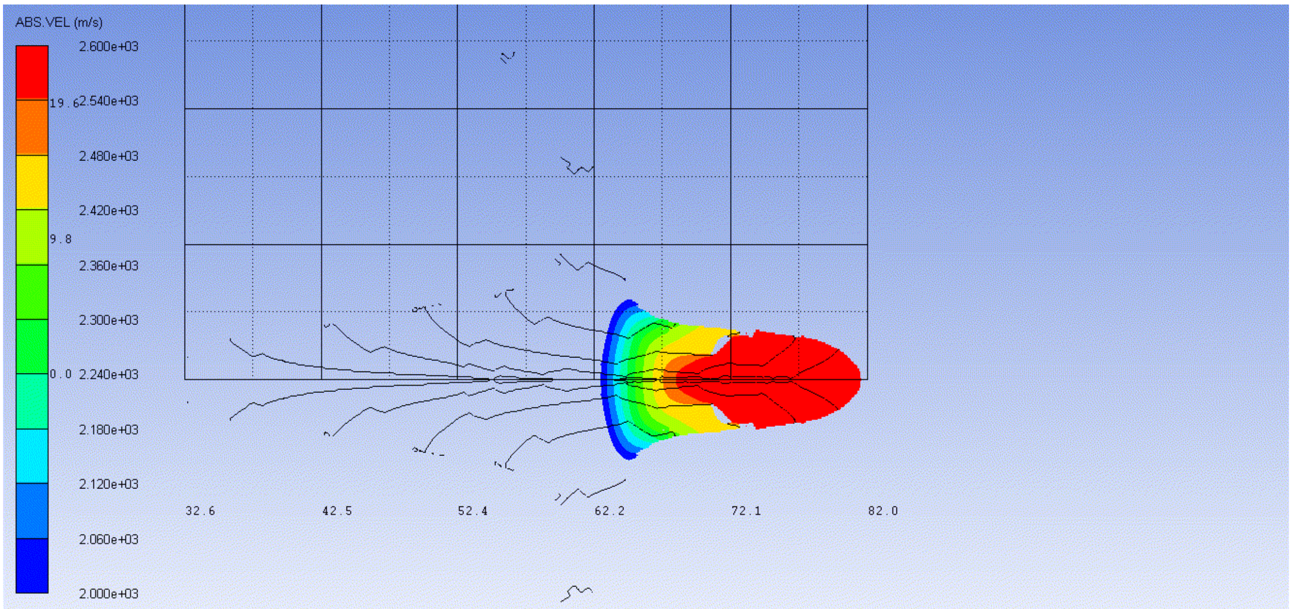

Figure 190: L_0 determination for Design 6 down to the 2 mm/µs.

Table 55: Strain and Strain-rate calculations for six concept designs from simulation with L_0 measured down to a velocity of 2 mm/µs.

Design	V_{Tip} (mm/µs)	V_{Rear} (mm/µs)	L (mm)	L_0 (mm)	$\acute{\varepsilon}$ (s^{-1})	strain
1	8.58	0.45	1160	67	121343	16.3
2	6.55	0.45	964	58	105172	15.6
3	4.65	0.50	620	53	79048	10.8
4	4.67	1.43	480	61	53115	6.9
5	3.63	1.42	360	43	51395	7.4
6	2.58	1.23	250	19	71053	12.2

Table 56: Strain and Strain-rate calculations for six concept designs from simulation with L_0 measured down to the slug.

Design	V_{Tip} (mm/µs)	V_{Rear} (mm/µs)	L (mm)	L_0 (mm)	$\acute{\varepsilon}$ (s^{-1})	strain
1	8.58	0.45	1160	124	65565	8.4
2	6.55	0.45	964	122	50000	6.9
3	4.65	0.50	620	116	35776	4.3
4	4.67	1.43	480	99	32727	3.8
5	3.63	1.42	360	74	29865	3.9
6	2.58	1.23	250	49	27551	4.1

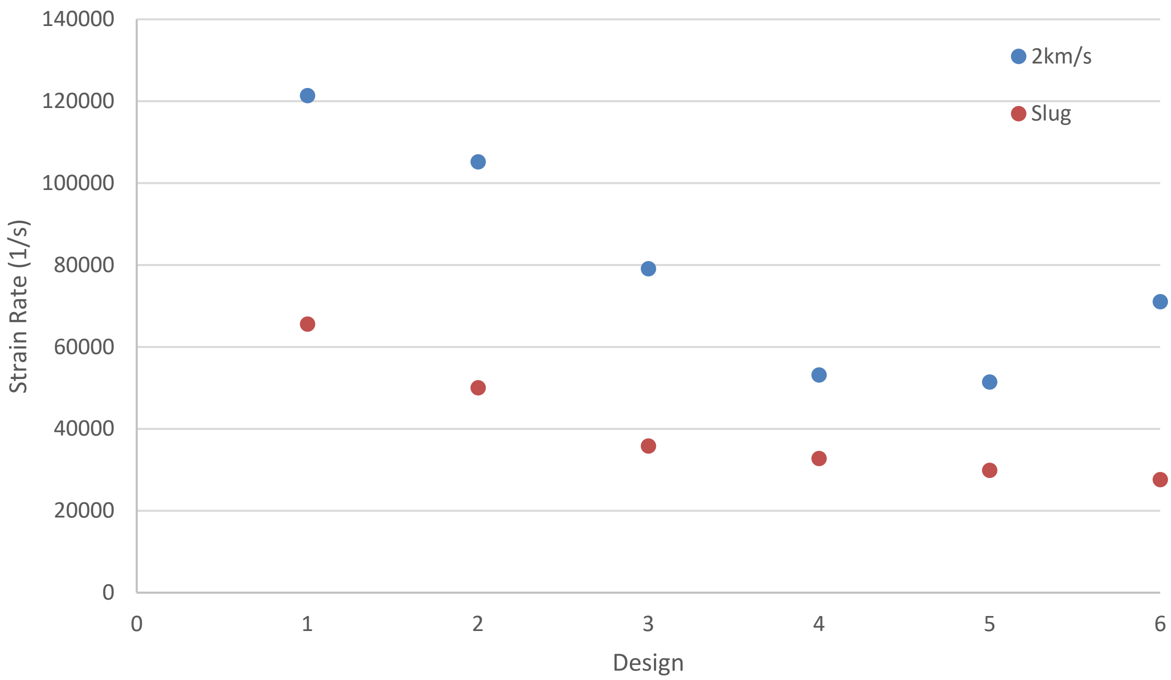

Figure 191: Graphic representation of strain-rates presented in Table 55 and Table 56, respectively.

7.3. Correlation between numerous analytical models to the experimental data set

7.3.1. Breakup times

The jet-break-up time t_{nB} presents the time at which the separation between any two adjacent jet particles n and n-1 is zero. The formulae used for calculating the experimental average break-up-time of a jet particle uses the initiation time of the charge, i.e. trigger signal, as reference time. The formulae used to calculate this value is The equations relating to breakup quoted in this paragraph were discussed in Section 3.3.1:

$$t_{nB} = \frac{\left(P_{n-1}(t_{FX1}) - L_{n-1} - P_n(t_{FX1})\right)}{V_{n-1} - V_n} \qquad \text{Eq. 6}$$

The data presented for the numerous designs are essentially the average break-up-times per velocity segment. Furthermore, the average break-up-time per velocity segment was measured for three firings and the average of three firings are presented below.

The other parameters like the velocity difference between neighbouring jet particles, the cumulative jet particle length as function of velocity are self-explanatory and need no further discussion.

A few empirical formulae are presented below:

Hirsch [46] suggested a phenomenological formulae for the jet-break-up time. This formula calculates the break-up-time (t_B) as:

$$t_B = \frac{D_o}{V_{Pl}} \qquad \text{Eq. 14}$$

where D_o is the initial diameter of the jet element when the elongation starts and V_{PL} is the characteristic plastic velocity, manifesting as the velocity difference between successive fragments. Hirsch [50] further used the SCAN code and a set of experiments with charges of varying liner thicknesses to study the break-up-time, in which V_{PL} was found to be a function of liner thickness and charge diameter. $1/V_{PL}$ was named as reasonable break-up-time of the jet and was given by:

$$\frac{1}{V_{PL}} = 13.886 - 101.49\frac{T_L}{C_D} \qquad \text{Eq. 7}$$

where C_D is the charge diameter and T_L is the liner element thickness. Eq. 35 predicts reasonable jet-break-up times for certain shaped-charges.

$$V_{Pl} = \frac{v_{max} - v_{min}}{\text{number } of\ particles} \qquad V_{Pl} \approx \Delta V \qquad \text{Eq. 8}$$

where ΔV is the average interparticle velocity difference measured from FX radiographs and V_{Pl} is the plastic velocity taking the tip and tail velocities of the jets. The reader should take note that there are slight differences between the V_{Pl} and ΔV and some models are sensitive to those differences which will come out of the analysis.

Chou and Carleone [51] deduced a formula predicting the break-up-time. The formula yielded results that compared well with measured data and has the following expression:

$$t_b = \frac{r_0}{C_p}\left[3.75 - 0.125\frac{r_0\eta_0}{C_p} + \frac{C_p}{r_0\eta_0}\right] \qquad \text{Eq. 9}$$

where t_B is the break-up-time, r_0 is the initial jet radius, η_0 is the initial strain-rate of the jet, $C_P = \sqrt{\frac{Y}{\rho_0}}$, where ρ_0 is the initial jet density, Y is the jet material static yield strength (270 MPa for OFHC copper) [16]. Held [38] defined the average break-up-time of several shaped-charges using flash X-rays to calculate the fragments length. He defined the break-up-time by

$$t_b = \frac{\sum l}{V_{TIP} - V_{cut-off}} \qquad \text{Eq. 10}$$

where Σl. is the summation of broken-up jet element lengths, V_{TIP} and $V_{CUT\text{-}Off}$ are the velocities of the jet tip and the cut-off element (i.e. the velocity of last penetrating element), respectively. Helds' model was not used in this study since the cut-off velocities of each design was not measured yet.
Baker mentions in [52] that Walsh, J.M. (1984), theorized that the dependence of jet length would take a particular form based on his determination of a dimensionless parameter for the problem and numerical experiments in which initial perturbation strengths were varied [53]. Baker further discusses that Mostert (1995) [54], suggested that break-up-time is proportional to $\left(\frac{\Delta m}{\Delta v}\right)^{\frac{1}{3}}$. Baker then assigns a proportionality constant linked to the jet plasticity/jet ductility by [99] :

$$t_b = Q\left(\frac{\Delta m}{\Delta v}\right)^{\frac{1}{3}} \qquad \text{Eq. 11}$$

The expression for t_b from the Mostert-König Model originally published in 1987 [10], and then in 2016 [55] is presented below:

$$t_b^{\frac{3}{2}} = \frac{\alpha r_0 l_0^{\frac{1}{2}}}{\gamma \Delta v^{\frac{1}{2}}} ln\left(\frac{N(x)}{N_c}\right) \qquad \text{Eq. 12}$$

where α,γ and N_c are constants and N is the initial dislocation density, r_0 is the initial radius of the jet, l_0 is the initial jet length and t_b is the break-up time of the shaped-charge jet.
The Mostert-König model expression rewritten as Baker presents it below is an attempt at deciphering the physics of this constant. According to Mostert & König, this constant may be attributed to dislocation theory. According to Baker it is attributed to jet plasticity [28], [99]. The expression is:

$$t_b = C\left(\frac{\acute{\Delta m}}{\Delta v}\right)^{\frac{1}{3}} \qquad \text{Eq. 13}$$

where C is a proportionality constant, Δm is the cumulative mass and Δv is described in Eq. 36.
In the following figures, the experimental results are shown together with predictions of Hirsch (Eq. 37), Chou (Eq. 38) and Baker (Eq. 39). The uncertainties presented in
Figure 192 to Figure 197 were calculated from the standard deviation of the mean; of the break-up times per velocity segment for each design. The break-up times **per velocity segment** were compared for each design, the mean calculated as shown in the figures below. The standard deviation calculated from the mean for the respective number of firings are presented as the uncertainty below.

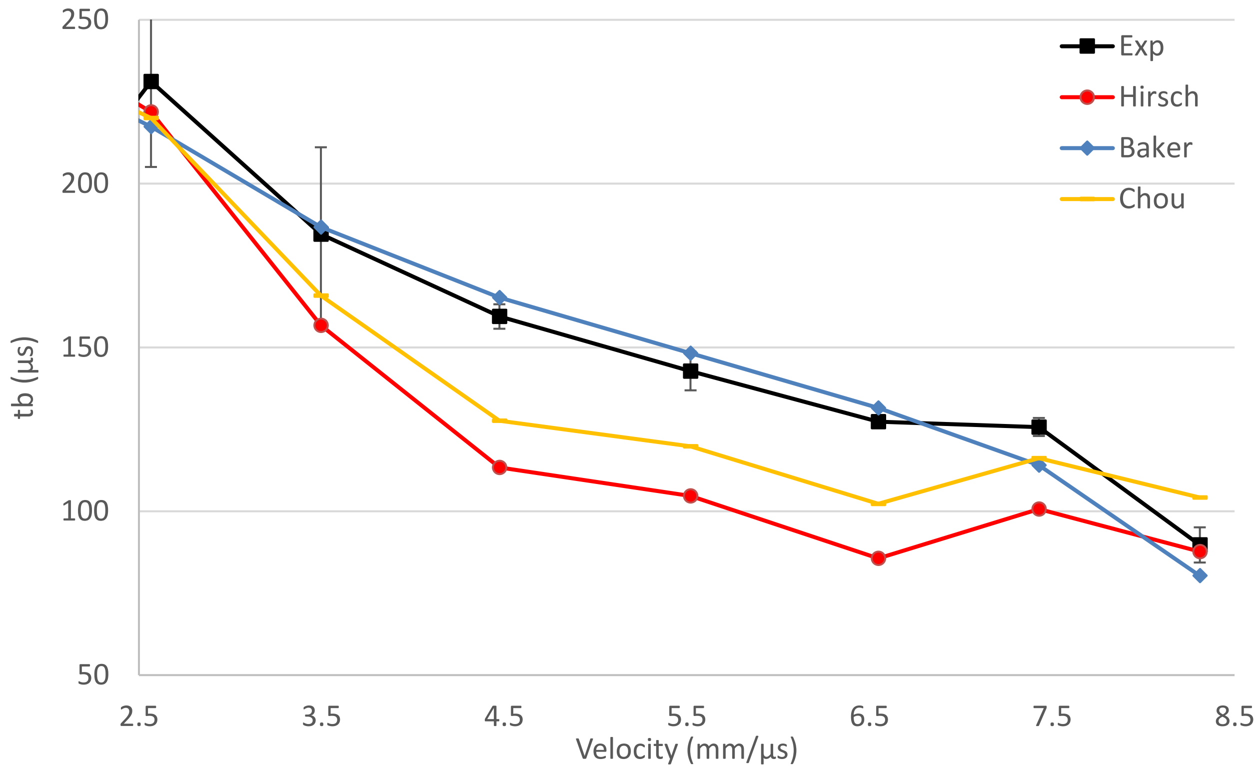

Figure 192: Measured experimental break-up-times and analytical predictions for design 1.

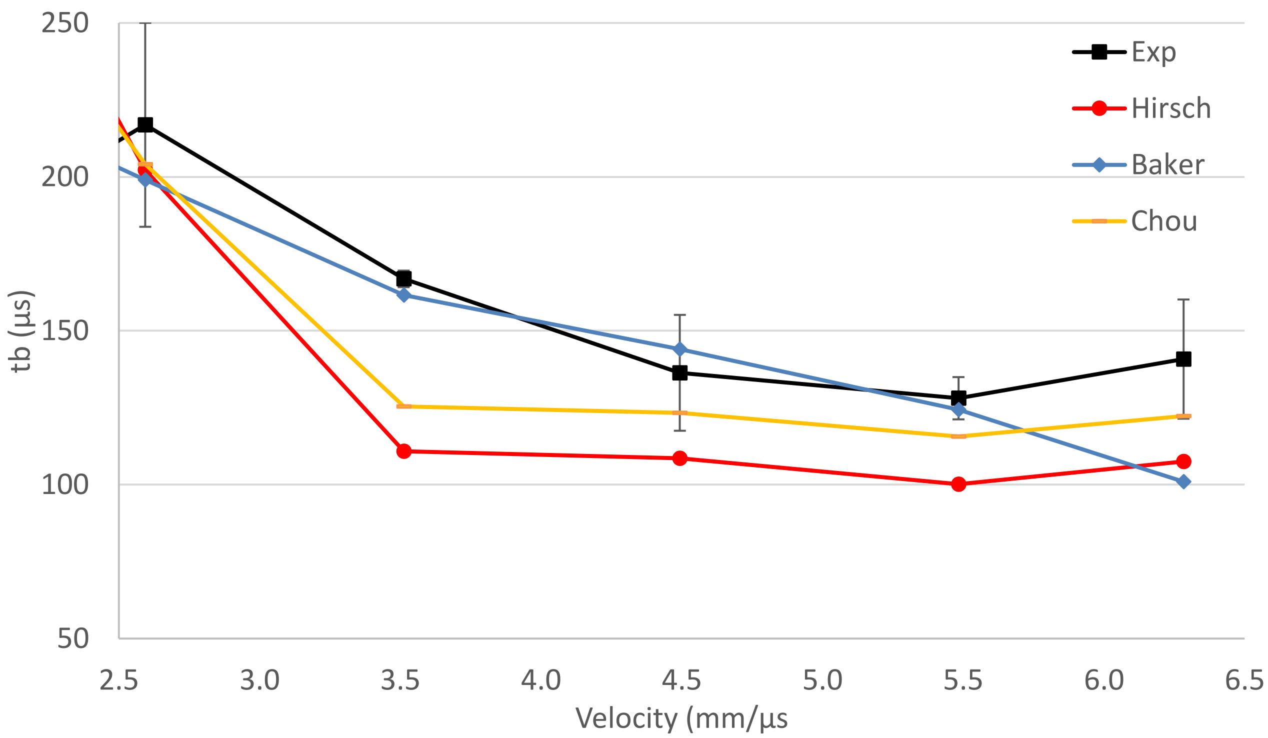

Figure 193: Measured experimental break-up-times and analytical predictions for design 2.

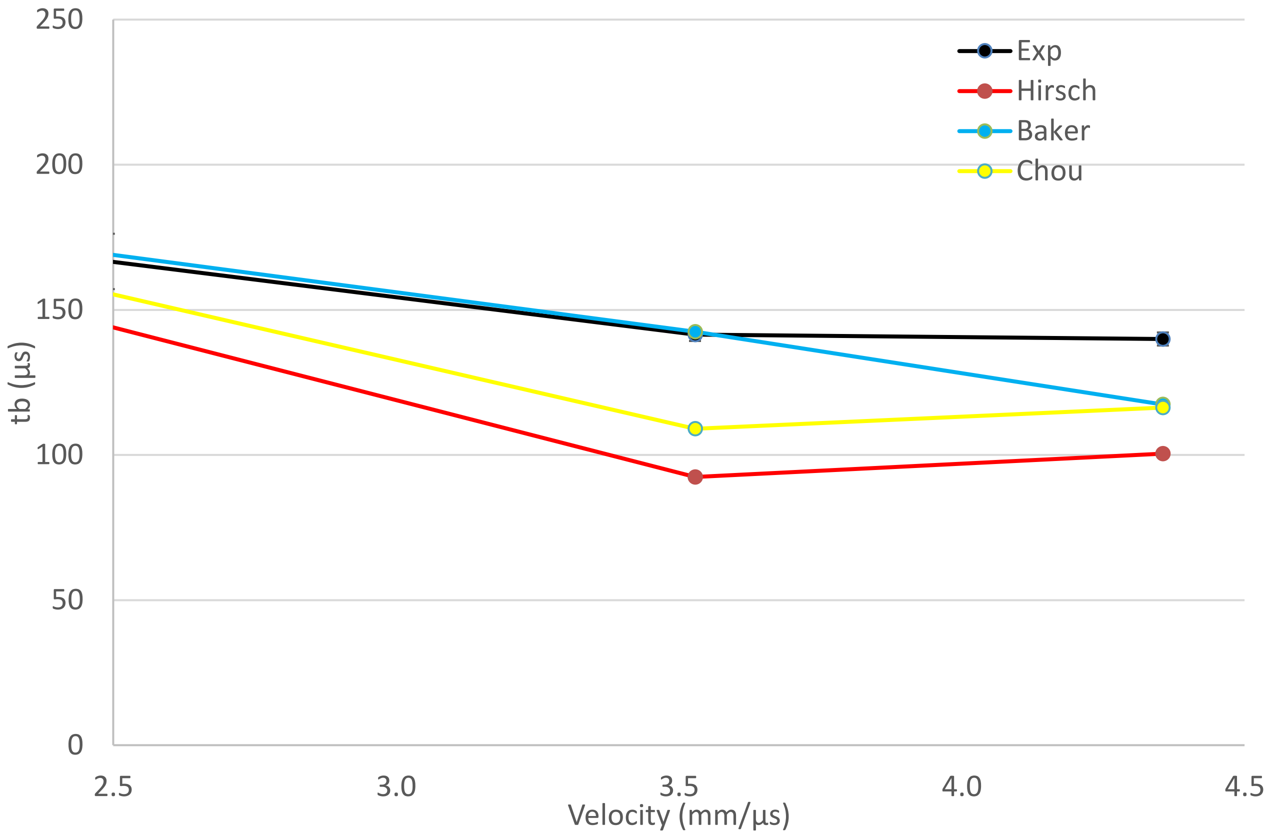

Figure 194: Measured experimental break-up-times and analytical predictions for design 3.

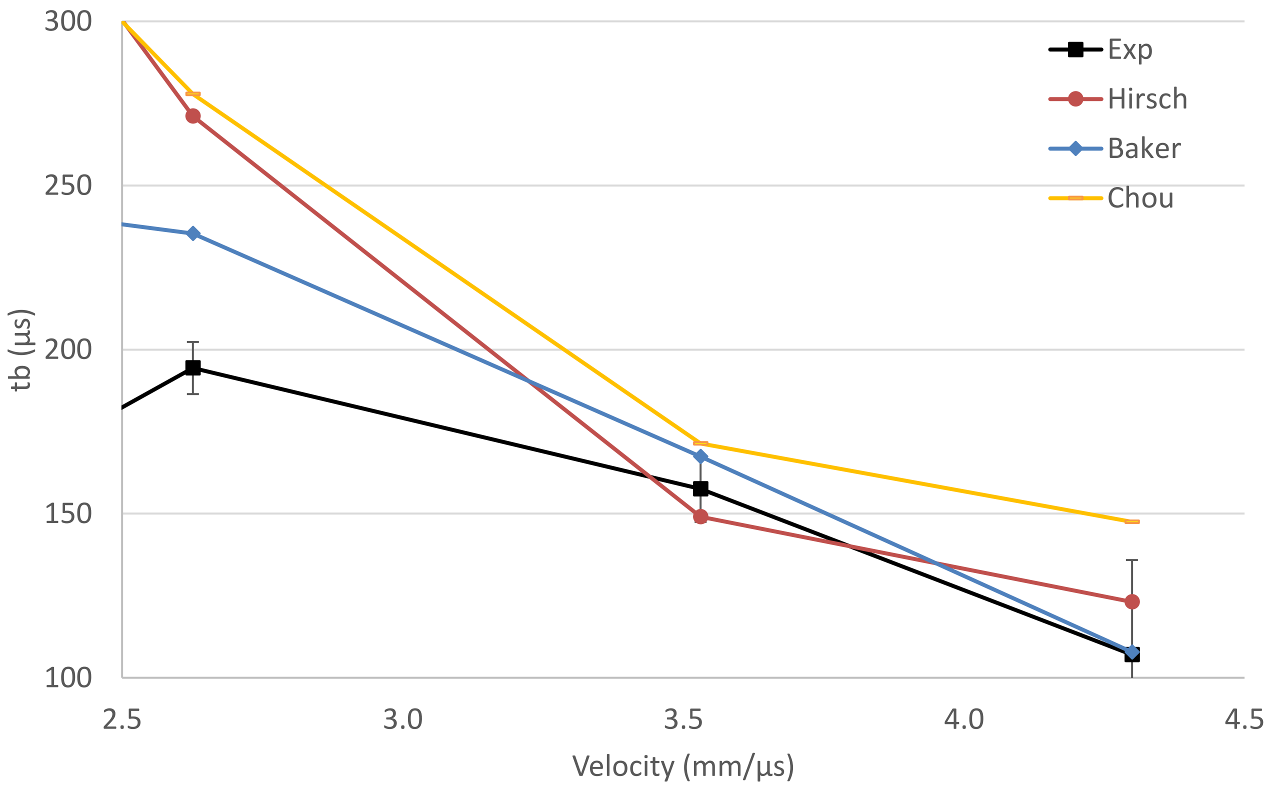

Figure 195: Measured experimental break-up-times and analytical predictions for design 4.

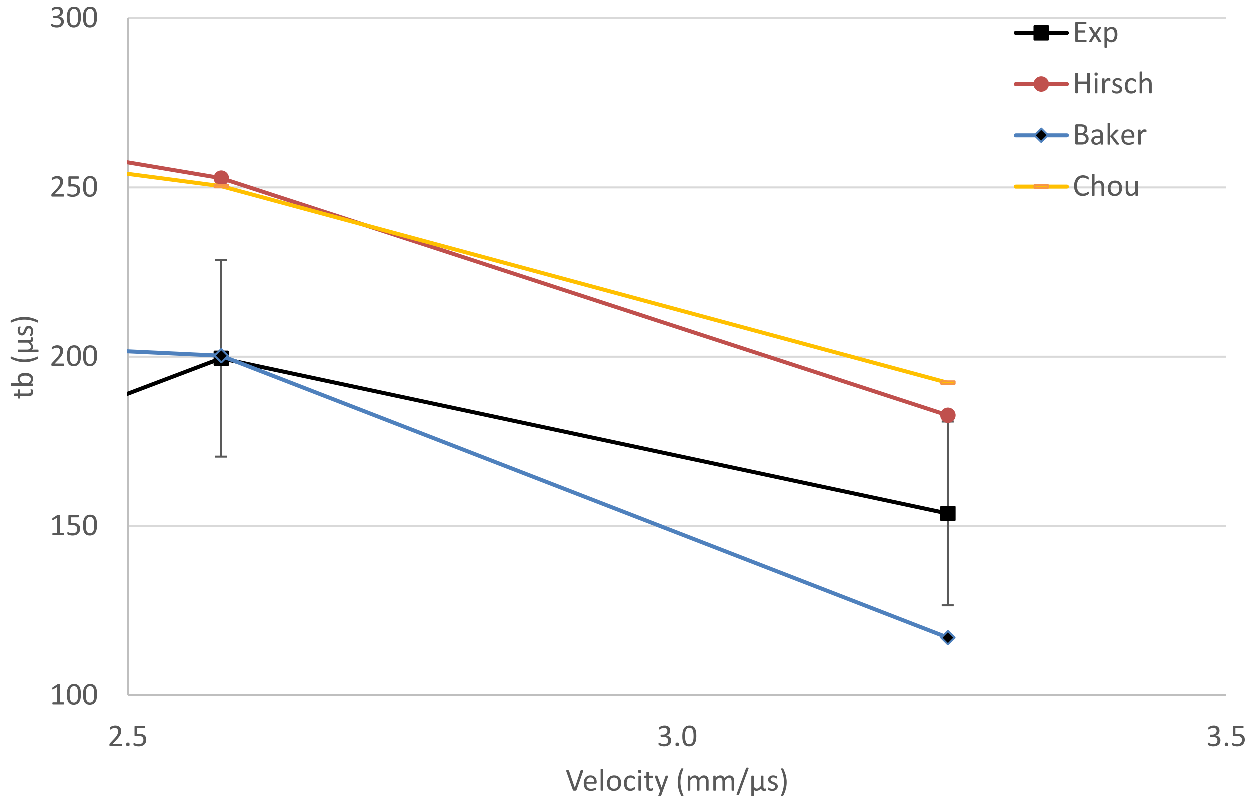

Figure 196: Measured experimental break-up-times and analytical predictions for design 5.

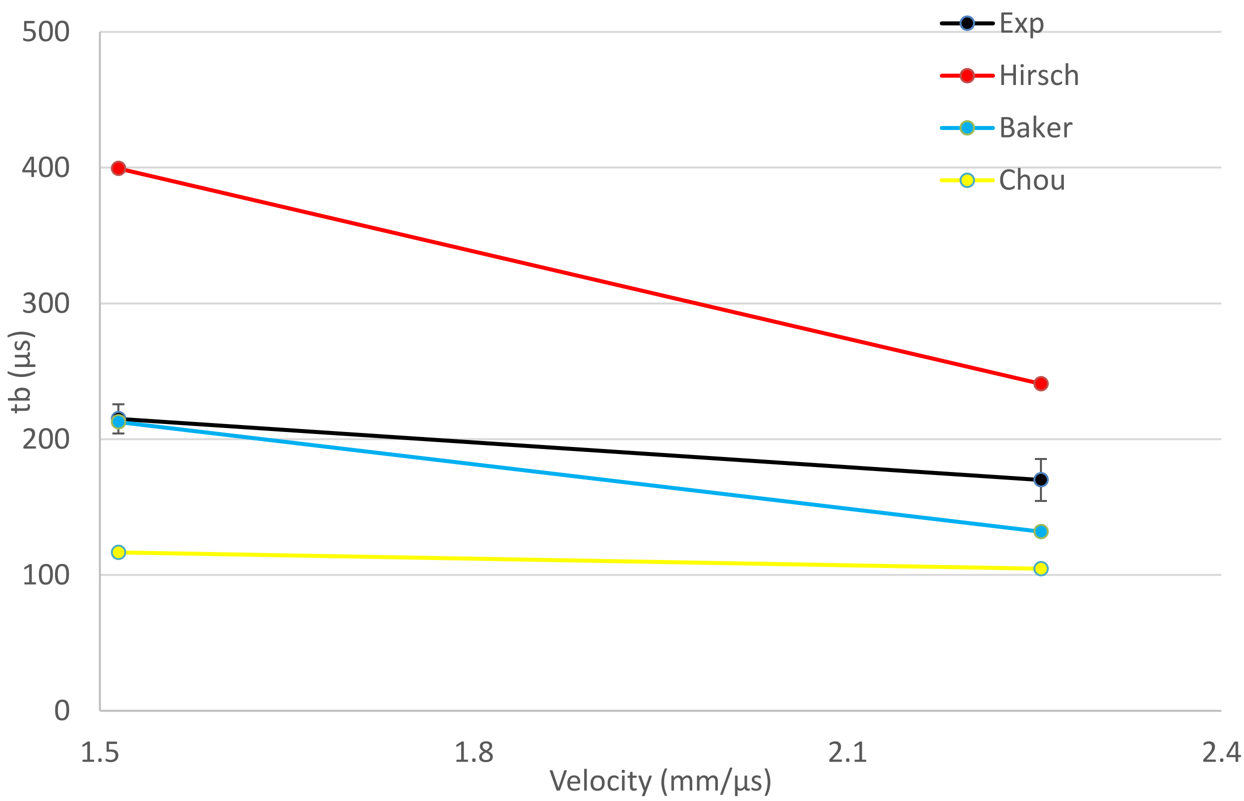

Figure 197: Measured experimental break-up-times and analytical predictions for design 6.

The six designs were used in controlled in terms of varying the strain and strain-rate with the benefit of controlling the variables like explosive selection and liner microstructure. The data clearly shows that an increase in strain and strain-rate increases the break-up-times and increases the number of particles. The data also shows a constant "plastic velocity" in the region of 100 m/s for jets from all six designs.

The model which best predicts the experimental data is that of the Baker-approach (or alternatively, the Mostert-König model), since it may be controlled by varying a proportionality constant. The constant used for design 1 was 24, and the constant used for designs 2 to 6 was 28. The Hirsch model does not include a constant but this model did produce fair break-up-time predictions. The Chou and Carleone (C&C) model produced break-up-times that closely match those predicted by the Hirsch model. The C&C model did however produce better fits to this set of experimental data compared to that of Hirsch. The overall initial strain-rates were measured from the respective simulations conducted in AUTODYN. The Baker model showed the best trends, in

Figure 192 to Figure 197, for the break-up-times along the entire velocity range.

It should be noted that the analysis for both Hirsch and Baker, which is strongly dependent on whether V_{Pl} or ΔV is used in the models, was calculated for both parameters. V_{Pl} produced better fits to the data compared to the average inter-particle velocity differences, calculated using the Hirsch model. When using the averaged inter-particle velocities for Hirsch, poor break-up-times are predicted. The break-up-times for the Baker model was not affected by changes in velocity differences. The Baker model had good fits when using a constant V_{Pl} or ΔV as well. The best-fit data for both the Hirsch and Baker models is presented above in

Figure 192 to Figure 197.

7.3.2. Plasticity

The procedure of determining the plasticity parameter as indicated in [55] by Baker was to plot the specific breakup time ($\frac{t_B}{D}$) against $\frac{\left(\frac{\Delta m}{\Delta v}\right)^{\frac{1}{3}}}{D}$. The slope is the constant C or Q known as the plasticity constant.

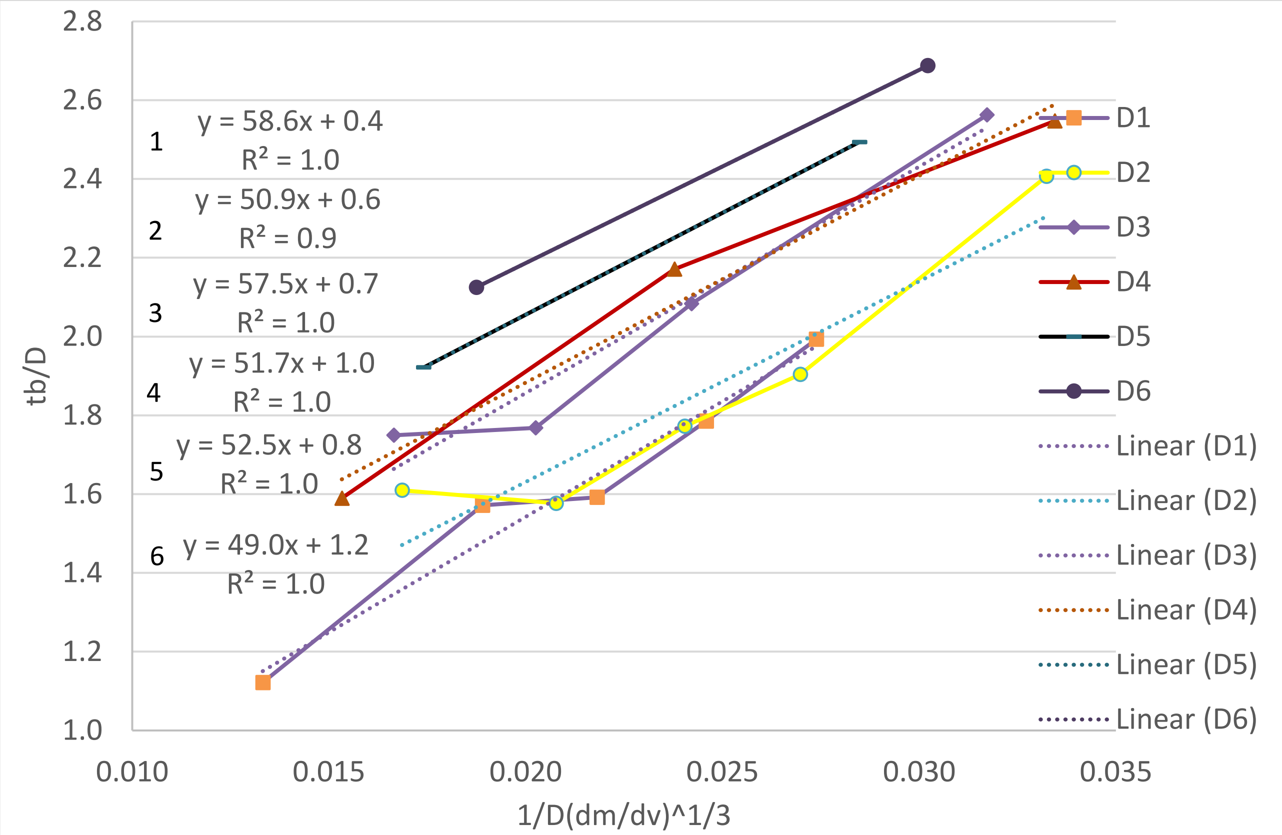

Figure 198: Plasticity determination of all six designs.

The data shows that the "plasticity parameter" (as defined by Baker) is nearly constant for all six designs. This is demonstrated by looking at the slope of each trend line in Figure 198 for all six designs. The value of the plasticity parameter is approximately ***50*** $\left(\frac{s}{(kg.s/m)^{\frac{1}{3}}}\right)$. This constant value may be attributed to the control of the liner microstructure and the use of a single explosive. The data shows that the initial microstructure (for a particular explosive) dictates the underlying physics of shaped-charge jet-break-up behaviour. An important finding from this work is thus that, whilst the strain and strain-rate affects the break-up-time, it does not alter the plasticity parameter of the jet. Furthermore, whilst perturbation theory could account for the onset of initial disturbances on the jet surfaces, it does not dictate the plasticity parameter.

7.4. The Evaluation of the Dynamic Fracture Characteristics of Shaped-charge Jets at single Strain-rate and known initial *Explosive* crystal size

Three batches of Comp A3 (RDX: WAX-91:9) were manufactured with different initial RDX crystal sizes. A range of 30, 100 and 300 µm was selected for the evaluation. Chemical analysis showed all three batches conformed to the 91:9 RDX: WAX ratio within 1% tolerance. The pressing analysis showed all three press charge densities (ρ=1.63 g/cc) to be comparable within 0.25% g/cm^3. Precision shaped-charge warheads were manufactured with copper liners with an average grain-size of 30 µm. Six flash X-ray firings were conducted to quantify the influence of the RDX crystal size on the cumulative length of jets produced. The data showed a rather equal trend in terms of break-up-times and cumulative length for the average of similar firings. The variation of these parameters between the similar firings, however, differed. The conclusion drawn from the data generated is rather that an optimum RDX crystal size exists for such composition that will produce more consistent jet parameters. In the case of this investigation, the 100 µm RDX-105 produced more consistent shaped-charge jets over and above that of the RDX 104 (20-30 µm) and RDX 107 (300-400 µm) mixtures

7.5. Conclusion

An investigation was performed with different shaped-charge designs with copper liners, where care was taken to obtain the same starting microstructure in the liners. Experimental results from numerous firings with flash-X-ray diagnostics were analysed and used to obtain jet parameters to a high degree of accuracy. These parameters were used to evaluate a dynamic "plasticity" parameter of the jets. It was found that this plasticity parameter was similar for all the jets. It is concluded from this study that, for a particular explosive, whilst the strain and strain-rate will influence the break-up-times of metallic shaped-charge jets, the underlying physics of jet plasticity is dictated by liner microstructural properties.

The experimental data were compared to predictions from four analytical models of which all predict the break-up-times of the shaped-charge jets at different strains and strain-rates. The Baker and Mostert-König model taking $\left(\frac{\Delta m}{\Delta v}\right)^{\frac{1}{3}}$ into account with a constant V_{Pl} yielded break-up times that best fitted the experimental data.

8. CONCLUSION

This research covers a wide range of parametric studies based on AUTODYN hydro code simulations and experiments for a range of precision shaped-charge concepts with different liner designs, initiation systems and explosive types in order to investigate the influence of strain and strain-rate on the fracture dynamics of the produced jets.

The research covered a wide variety of literature, an in depth evaluation of shaped-charge manufacture, flash X-ray experimentation and the analysis of associated data.

The data produced from flash X-ray analysis regarding break-up-times from experimentation was compared with predictions from a wide range of models. It was proven that break-up-times correlate best with $\left(\frac{\Delta m}{\Delta v}\right)^{\frac{1}{3}}$, that is the cube root of the ratio of the cumulative mass to plastic velocity of a particular design.

This research also revealed quantitative data distinguishing between the plasticity of jets and the break-up-times of jets. More importantly, it was proved that the underlying mechanism controlling break-up-times lies within the microstructure of the liner, not the explosive material. This is further motivated by the fact that jets produced from electromagnetic energy in [39] have shown jets of comparable break-up-times to those of explosives. The data showed that a change in explosive crystal size does not affect the break-up-times of the jets, rather the variation in that break-up-times to marginal extent. The data also showed that the plasticity of jets are constant for two completely different explosives. That is an explosive containing 91% RDX versus an explosive containing 55% RDX and also a pressed explosive versus a cast explosive. The break-up-times differ, but this is due to the variation in detonation pressure causing a different strain and strain-rate.

9. FUTURE WORK

The following future research studies may be pursued:

- the experimental data set may be used to extend on the current virtual origin models;
- an investigation is being pursued correlating the normalised cumulative mass distribution with experimental break-up-times;
- the plasticity parameter should be quantified with different types of explosive compositions, that is RDX, HMX, HNS, CL20 and more; and
- the variation in shaped-charge performance should also be evaluated with different explosive molecules of different crystal sizes.

10. REFERENCES

[1] W. P. Walters and J. A. Zukas, *Fundamentals of shaped charges*. John Wiley, 1989.

[2] M. Mayseless and E. Hirsch, "The Appendix," in *Proceedings of the 24th International Symposium on Ballistics*, 2008, vol. 2, pp. 1069–1076.

[3] K. S. Vecchio, U. Andrade, M. A. Meyers, and L. W. Meyer, "MICROSTRUCTURAL EVOLUTION IN HIGH STRAIN, HIGH STRAIN-RATE DEFORMATION," in *Shock Compression of Condensed Matter–1991*, Elsevier, 1992, pp. 527–530.

[4] M. A. Meyers, U. R. Andrade, and A. H. Chokshi, "The effect of grain size on the high-strain, high-strain-rate behavior of copper," *Metallurgical and materials transactions A*, vol. 26, no. 11, pp. 2881–2893, 1995.

[5] P. C. Chou, J. Carleone, and R. R. Karpp, "Criteria for jet formation from impinging shells and plates," *Journal of Applied Physics*, vol. 47, no. 7, pp. 2975–2981, 1976.

[6] P. C. Chou and W. J. Flis, "Recent developments in shaped charge technology," *Propellants, Explosives, Pyrotechnics*, vol. 11, no. 4, pp. 99–114, 1986.

[7] E. Hirsch and M. Mayseless, "THE MAXIMUM MACH NUMBER OF COHERENT COPPER JET."

[8] J. Brown, J. P. Curtis, and D. D. Cook, "The formation of jets from shaped charges in the presence of asymmetry," *Journal of applied physics*, vol. 72, no. 6, pp. 2136–2143, 1992.

[9] F. E. Allison and G. M. Bryan, "Cratering by a train of hypervelocity fragments," in *Proceeding of 2nd Hypervelocity Impact Effects Symposium*, 1957, vol. 1, p. 81.

[10] F. E. Allison and R. Vitali, "A new method of computing penetration variables for shaped-charge jets," ARMY BALLISTIC RESEARCH LAB ABERDEEN PROVING GROUND MD, 1963.

[11] J. Simon, R. Dipersio, and A. B. Merendino, "Penetration of Shaped-charge Jets into Metallic Targets, Ballistic Research Laboratory Memorandum," Report, 1965.

[12] W. P. Walters, W. J. Flis, and P. C. Chou, "A survey of shaped-charge jet penetration models," *International journal of impact engineering*, vol. 7, no. 3, pp. 307–325, 1988.

[13] T. A. E. Elshenawy, "Criteria of design improvement of shaped charges used as oil well perforators," The University of Manchester (United Kingdom), 2012.

[14] L. A. Glenn, J. B. Chase, J. Barker, and D. J. Leidel, "Experiments in Support of Pressure Enhanced Penetration with Shaped Charge Perforators," Lawrence Livermore National Lab., CA (US), 1999.

[15] M. Held, *Hydrodynamic theory of shaped charge jet penetration*. Messerschmitt-Bölkow-Blohm, 1991.

[16] W. P. Walters and J. A. Zukas, *Fundamentals of shaped charges*. John Wiley, 1989.

[17] Ansys, *Autodyn Theory Manual*. Century Dynamics Concord, CA, 2005.

[18] W. H. Lee, “Oil well perforator design using 2D Eulerian code,” *International Journal of Impact Engineering*, vol. 27, no. 5, pp. 535–559, 2002.

[19] D. Davison and D. Pratt, “A Hydrocode-Designed well perforator with Exceptional performance,” 1998.

[20] P. Y. Chanteret and A. Lichtenberger, “About varying shaped charge liner thickness,” in *17th International Symposium on Ballistics*, 1998, vol. 2, pp. 2–365.

[21] M. Defourneaux, “Theorie Hydrodynamique des Charges Creuses,” *Mem. l’artillerie Francaise*, vol. 44, no. 2, pp. 293–334, 1970.

[22] D. R. Scheffler and W. P. Walters, “A method to increase the tip velocity of a shaped charge jet using a hollow cavity,” *Computational Ballistics III*, vol. 45, p. 11199, 2007.

[23] J. Brown, P. J. Edwards, and P. R. Lee, “Studies of shaped charges with built-in asymmetries. Part II: Modelling,” *Propellants, explosives, pyrotechnics*, vol. 21, no. 2, pp. 59–63, 1996.

[24] M. Moyses, “Penetration by Shaped Charge Jets with Varying Off-Axis Velocity Distributions,” 1998.

[25] M. Held, “Liners for shaped charges,” *Journal of battlefield technology*, vol. 4, pp. 1–7, 2001.

[26] W. Guo, S. K. Li, F. C. Wang, and M. Wang, “Dynamic recrystallization of tungsten in a shaped charge liner,” *Scripta Materialia*, vol. 60, no. 5, pp. 329–332, 2009.

[27] S. L. Renfro, *Liner and improved shaped charge especially for use in a well pipe perforating gun*. Google Patents, 1996.

[28] A. S. Daniels and E. L. Baker, “HIGH PERFORMANCE TRUMPET LINED SHAPED CHARGE TECHNOLOGY,” *28th International Ballistics Symposium*, 2014.

[29] B. Bourne, K. G. Cowan, and J. P. Curtis, “Shaped charge warheads containing low melt energy metal liners,” in *Proc. 19th Int. Symp. Ballistics, Switzerland*, 2001, pp. 583–589.

[30] B. Bourne, P. N. Jones, and R. H. Warren, “Grain size and crystallographic texture effects on the performance of shaped charges,” in *14th Internatioanl Symposium on Ballistics, Quebec Canada*, 1993, vol. 1, pp. 19–124.

[31] A. J. Schwartz, M. Kumar, and D. H. Lassila, “Analysis of intergranular impurity concentration and the effects on the ductility of copper-shaped charge jets,” *Metallurgical and Materials Transactions A*, vol. 35, no. 9, pp. 2567–2573, 2004.

[32] S. Fujiwara and K. Abiko, "Ductility of ultra high purity copper," *Le Journal de Physique IV*, vol. 5, no. C7, pp. C7-295-C7-300, 1995.

[33] V. Y. Gertsman, M. Hoffmann, H. Gleiter, and R. Birringer, "The study of grain size dependence of yield stress of copper for a wide grain size range," *Acta metallurgica et materialia*, vol. 42, no. 10, pp. 3539–3544, 1994.

[34] E. Hirsch, "The Effect of the Liner Metallurgical State on the shaped charge jet break-up time," *Propellants, explosives, pyrotechnics*, vol. 15, no. 4, pp. 166–176, 1990.

[35] F. J. Zerilli and R. W. Armstrong, "Constitutive relations for the plastic deformation of metals," in *AIP conference proceedings*, 1994, vol. 309, pp. 989–992.

[36] J. P. Curtis, M. Moyses, A. J. Arlow, and K. G. Cowan, "A break-up model for shaped charge jets," 1996.

[37] W. H. Tian, A. L. Fan, H. Y. Gao, J. Luo, and Z. Wang, "Comparison of microstructures in electroformed copper liners of shaped charges before and after plastic deformation at different strain rates," *Materials Science and Engineering: A*, vol. 350, no. 1–2, pp. 160–167, 2003.

[38] M. Held, "Determination of the material quality of copper shaped charge liners," *Propellants, explosives, pyrotechnics*, vol. 10, no. 5, pp. 125–128, 1985.

[39] F. J. Mostert and Konig, P, J, "A link between liner metallurgy and shaped charge jet ductility," *South African Journal of physics*, vol. 10, no. 3, pp. 127–131, 1987.

[40] M. L. Duffy and S. K. Golaski, "Effect of liner grain size on shaped charge jet performance and characteristics," *US Army Ballistic Research Laboratory Technical Report No. BRL-TR-2800*, 1987.

[41] A. H. Chokshi and M. Meyers, "The prospects for superplasticity at high strain rates: preliminary considerations and an example," *Scr. Metall. Mater.*, vol. 24, no. 4, pp. 605–610, 1990.

[42] E. Hirsch, "Internal Shearing during Shaped Charge Jet Formation and Break-up," *Propellants, explosives, pyrotechnics*, vol. 17, no. 1, pp. 27–33, 1992.

[43] L. Lu, S. X. Li, and K. Lu, "An abnormal strain rate effect on tensile behavior in nanocrystalline copper," *Scripta Materialia*, vol. 45, no. 10, pp. 1163–1169, 2001.

[44] S. H. LEE, S. LEE, S. YANG, H. KIM, and L. J. PARK, "Penetration Performance of Ultrafine-Grained Copper Shaped Charge Liner," 2017.

[45] K. G. Cowan and B. Bourne, "Further analytical modelling of shaped charge jet break-up phenomena," in *Proc. 19th Int. Symp. Ballistics, Switzerland*, 2001, pp. 803–810.

[46] E. Hirsch, "A Formula for the Shaped Charge Jet Breakup-Time," *Propellants, Explosives, Pyrotechnics*, vol. 4, no. 5, pp. 89–94, 1979.

[47] E. Hennequin, "Modelling of the Shaped Charge Jet Break-Up," *Propellants, explosives, pyrotechnics*, vol. 21, no. 4, pp. 181–185, 1996.

[48] W. P. Walters and R. L. Summers, "A review of jet breakup time models," *Propellants, explosives, pyrotechnics*, vol. 18, no. 5, pp. 241–246, 1993.

[49] M. Maritz, "JETP Documentation, Dynamic Jet Modelling." 2014.

[50] E. Hirsch, "Scaling of the Shaped Charge Jet Break-Up Time," *Propellants, Explosives, Pyrotechnics: An International Journal Dealing with Scientific and Technological Aspects of Energetic Materials*, vol. 31, no. 3, pp. 230–233, 2006.

[51] P. C. Chou and J. Carleone, "Calculation of Shaped Charge Jet Strain, Radius, and Breakup Time," *BRL CR*, vol. 246, 1975.

[52] Ernest L. Baker and James Pham, "AN EMPIRICAL SHAPED CHARGE JET BREAKUP MODEL." U.S. ARMY ARMAMENT RESEARCH, DEVELOPMENT AND ENGINEERING CENTER, Jul. 2014.

[53] J. M. Walsh, "Plastic instability and particulation in stretching metal jets," *Journal of applied physics*, vol. 56, no. 7, pp. 1997–2006, 1984.

[54] F. J. Mostert, G. J. F. Smit, and K. D. Werneyer, "Analysis of jet properties of different liner materials manufactured under various conditions," 1995.

[55] F. J. Mostert, I. M. Snyman, and P. KÖNIG, "Towards a Unified Dislocation-Based Model for Shaped Charge Jet Break-Up," 2016.

[56] N. F. Mott, "Fragmentation of shell cases," *Proceedings of the Royal Society of London. Series A. Mathematical and physical sciences*, vol. 189, no. 1018, pp. 300–308, 1947.

[57] E. Hirsch, "A Formula for the Shaped Charge Jet Breakup-Time," *Propellants, Explosives, Pyrotechnics*, vol. 4, no. 5, pp. 89–94, 1979.

[58] E. Hirsch, "A model explaining the Rule for Calculating the Break-up Time of homogeneous ductile metals," *Propellants, Explosives, Pyrotechnics*, vol. 6, no. 1, pp. 11–14, 1981.

[59] B. S. Welsh, "High speed deformation and break-up of shaped charge jets," University of Nottingham, 1993.

[60] P. C. Chou and J. Carleone, "The stability of shaped-charge jets," *Journal of Applied Physics*, vol. 48, no. 10, pp. 4187–4195, 1977.

[61] P. C. Chou and J. Carleone, "The Effect of Compressibility on the Formation of Shaped Charge Jets," *1st International Symposium on Ballistics*, 1983.

[62] C. W. Miller, "A New Approach to the Numerical Analysis of Shaped Charge Jets," 1981.

[63] M. Mayseless, E. Hirsch, O. Dolev, and A. Schwartz, “THE EFFECT OF INITIATION METHOD ON THE BREAK-UP TIME OF SHAPED-CHARGE JETS,” *International Symposium of Ballistics*.

[64] N. Ridley and J. Pilling, *Superplasticity in crystalline solids*. Institute of metals London, 1989.

[65] G. E. Dieter, “Elements of the theory of plasticity,” *Mechanical metallurgy*, pp. 76–79, 1988.

[66] G. E. Dieter, “Metallurgical effects of high velocity shock waves in metals,” *Response of Metals to High Velocity Deformation*, pp. 409–422, 1960.

[67] A. H. Holtzman and G. R. Cowan, “The strengthening of austenitic manganese steel by plane shock waves,” *Response of Metals to High Velocity Deformation, Interscience Publishers*, p. 447, 1961.

[68] F. Jamet, “Investigation of shaped charge jets using flash X-ray diffraction,” 1984.

[69] B. Derby and M. F. Ashby, “On dynamic recrystallisation,” *Scripta Metallurgica*, vol. 21, no. 6, pp. 879–884, 1987.

[70] J. Carleone and P. C. Chou, “A one-dimensional theory to predict the strain and radius of shaped charge jets,” 1974.

[71] C. Miller, “Generation of Necks in an Elongating Shaped Charge Jet,” 1982.

[72] J. E. Backofen, “The use of analytical computer models in shaped charge design,” *Propellants, explosives, pyrotechnics*, vol. 18, no. 5, pp. 247–254, 1993.

[73] J. Simon, “The effect of explosive detonation characteristics on shaped charge performance,” ARMY BALLISTIC RESEARCH LAB ABERDEEN PROVING GROUND MD, 1974.

[74] E. Hirsch, “The Mott Fragmentation Model and the Vpl break-up parameter,” *Propellants, Explosives, Pyrotechnics*, vol. 14, no. 1, pp. 31–38, 1989.

[75] M. Held, *Particulation of Shaped Charge Jets: Proceedings of the 11th International Symposium on Ballistics, Brussels Congress Centre, Brussels-Belgium, May 09-10-11, 1989; Volume II: Warhead Mechanisms Terminal Ballistics*. Messerschmitt-Bölkow-Blohm, 1989.

[76] S. Pappu and L. E. Murr, “Hydrocode and microstructural analysis of explosively formed penetrators,” *Journal of materials science*, vol. 37, no. 2, pp. 233–248, 2002.

[77] Malcolm S, “Autodyn theory manual, R 3.0.” Century Dynamics, USA, 1997.

[78] G. Birkhoff, D. P. MacDougall, E. M. Pugh, and S. G. Taylor, “Explosives with lined cavities,” *Journal of Applied Physics*, vol. 19, no. 6, pp. 563–582, 1948.

[79] E. M. Pugh, R. J. Eichelberger, and N. Rostoker, “Theory of jet formation by charges with lined conical cavities,” *Journal of Applied Physics*, vol. 23, no. 5, pp. 532–536, 1952.

[80] P. W. Cooper, “Estimating detonation properties,” *Explosives engineering*, pp. 159–162, 1996.

[81] P. C. Chou and J. Carleone, "Breakup of Shaped-Charge Jets," 1976.

[82] R. R. Karpp and J. Simon, "An estimate of the strength of a copper shaped charge jet and the effect of strength on the breakup of a stretching jet," *US Army Ballistic Research Laboratory Report*, no. 1893, 1976.

[83] J. Petit, V. Jeanclaude, and C. Fressengeas, "Breakup of Copper shaped-charge jets: Experiment, numerical simulations, and analytical modeling," *Journal of applied physics*, vol. 98, no. 12, p. 123521, 2005.

[84] G. Baudin and R. Serradeill, "Review of Jones-Wilkins-Lee equation of state," in *EPJ Web of Conferences*, 2010, vol. 10, p. 00021.

[85] E. L. Lee, H. C. Hornig, and J. W. Kury, "Adiabatic expansion of high explosive detonation products," Univ. of California Radiation Lab. at Livermore, Livermore, CA (United States), 1968.

[86] C. M. Tarver, W. C. Tao, and C. G. Lee, "Sideways plate push test for detonating solid explosives," *Propellants, Explosives, Pyrotechnics*, vol. 21, no. 5, pp. 238–246, 1996.

[87] S. G. Cochran and M. W. Guinan, "Bauschinger effect in uranium," California Univ., 1976.

[88] A. E. Gardner, *Process for desensitizing solid explosive particles by coating with wax*. Google Patents, 1970.

[89] P. S. Han and D. Jordan, *Coating process for plastic bonded explosive*. Google Patents, 2002.

[90] V. D. Ringbloom, *Process for coating crystalline explosives with polyethylene wax*. Google Patents, 1982.

[91] R. DiPersio, J. Simon, and T. H. Martin, "A study of jets from scaled conical shaped charge liners," ARMY BALLISTIC RESEARCH LAB ABERDEEN PROVING GROUND MD, 1960.

[92] E. C. Zurey Jr, "Facilities requirements for a flash X-ray machine," NAVAL POSTGRADUATE SCHOOL MONTEREY CA, 1985.

[93] M. Held, "Analysis of a shaped charge jet with the double-orthogonal-synchro-streak technique," *Propellants, explosives, pyrotechnics*, vol. 20, no. 3, pp. 116–122, 1995.

[94] F. Majiet and F. J. Mostert, "Investigation on the influence of the initial RDX crystal size on the performance of shaped charge warheads," *Defence Technology*, vol. 15, no. 5, pp. 802–807, 2019.

[95] A. Barua and M. Zhou, "A Lagrangian framework for analyzing microstructural level response of polymer-bonded explosives," *Modelling and Simulation in Materials Science and Engineering*, vol. 19, no. 5, p. 055001, 2011.

[96] T. Elshenawy, "Determination of the velocity difference between jet fragments for a range of copper liners with different small grain sizes," *Propellants, Explosives, Pyrotechnics*, vol. 41, no. 1, pp. 69–75, 2016.

[97] P. Y. Chanteret, "Considerations about the analytical modelling of shaped charges," *Propellants, explosives, pyrotechnics*, vol. 18, no. 6, pp. 337–344, 1993.

[98] F. Majiet and F. J. Mostert, "Evaluation of the Dynamic Fracture Characteristics (Plasticity) of Shaped Charge Jets at Different Strain Rates and Characterized Initial Liner Microstructure," presented at the 31st International Symposium on Ballistics, 2019.

[99] E. L. Baker, A. Daniels, J. Pham, T. Vuong, and S. DeFisher, "Jet break-up characterization of Molybdenum shaped charge liners," *US Army, Armament Research, Development and Engineering Center*.